UNIVERSIDAD NACIONAL AUTÓNOMA DE MÉXICO
PROGRAMA DE POSGRADO EN ASTROFÍSICA
INSTITUTO DE ASTRONOMÍA

Towards a Complete Study of the Initial Mass Function and Early Kinematics Evolution of the 25 Orionis Stellar Group

TESIS

Para Optar por el Grado de:
Doctor en Ciencias (Astrofísica)

Presenta:

Genaro Suárez Castro

Asesores:

Dr. Carlos G. Román Zúñiga
Instituto de Astronomía - UNAM, México

Dr. Juan José Downes Wallace
Centro Universitario Regional del Este,
Universidad de la República, Uruguay

Ensenada, BC., Febrero, 2019

This dissertation is approved by the Dissertation Committee:

Dr. Jesús Hernández
Instituto de Astronomía, UNAM, México

Dr. Luis Salas
Instituto de Astronomía, UNAM, México

Dra. Aina Palau
Instituto de Radioastronomía y Astrofísica, UNAM, México

Dr. Javier Ballesteros
Instituto de Radioastronomía y Astrofísica, UNAM, México

Dra. Amelia Bayo
Instituto de Física y Astronomía, Universidad de Valparaíso, Chile

A mi familia y a mi prometida

AGRADECIMIENTOS

Es para mí un privilegio comenzar a escribir estas palabras de agradecimiento justo para dar por terminada mi tesis doctoral. Es un momento muy especial puesto que voy a apuntar, no solo a recordar, a las personas que me han permitido llegar hasta aquí, al igual que a las instituciones que me han brindado su apoyo. Por sí solos, estos agradecimientos ameritan un texto tan o más extenso que la misma disertación pero intentaré incluirlos en las siguientes líneas.

Comienzo por agradecer a la UNAM, en específico, al Instituto de Astronomía por haberme abierto las puertas para llegar a trabajar desde lo que fue mi tesis de licenciatura, haber pasado la etapa de maestría y estar a punto de culminar la etapa de doctorado. Agradezco todas las facilidades/comodidades que me brindó esta universidad; espacio para trabajar con una increible vista al mar, equipo de cómputo, salas y espacios para información y discusión, área de recreación, etc. Asimismo, agradezco el apoyo que recibí a través de diversos proyecto para participar en una gran cantidad de eventos nacionales e internacionales. Sin duda, la gran mayoría de mi preparación profesional como astrónomo se la debo a la Máxima Casa de Estudios.

Igualmente, agradezco a CONACYT el apoyo otorgado durante los 6 años anteriores (incluidos los 2 de maestría) para que me enfocara de tiempo completo en hacer lo que más me gusta: estudiar el Universo. También agradezco el apoyo que recibí de esta institución para asistir a eventos académicos y por brindarme herramientas indispensables para esta profesión, como lo es la computadora personal con la que estoy escribiendo esta tesis y la que me acompañó a largo de esta etapa. Contar con este tipo de apoyos por parte de CONACYT hizo posible que llegara hasta este nivel.

Es un gran privilegio haber tenido como asesores de tesis a Carlos Román y a Juan José Downes, dos excelentes investigadores de quienes aprendí y sigo aprendiendo lo maravillosa que es la Astronomía. Recuerdo cuando estaba por terminar mi etapa de maestría y que se reunieron conmigo para presentarme/ofrecerme un proyecto que, por el tema que sale a relucir en el título y por lo que recordaba de mis cursos de maestría, reconozco que no me causó la mejor impresión. Luego de adentrarnos en la discusión fui aclarando mis preocupaciones y, al final, decidí que era el proyecto perfecto para la etapa que estaba por iniciar. Cuatro años después reafirmo la calidad de proyecto que me ofrecieron y la visión que tuvieron para lograr lo que ahora presento en esta disertación y lo que continuaré haciendo por muchos años más. De cada uno de mis asesores aprendí cosas valiosas de esta profesión. De Carlos aprendí a trabajar en paralelo, a hablar y a presentar mis resultados ante cualquier público, a poner en un contexto más general cada cosa que iba aprendiendo, a aventurarse a aprender nuevas herramientas y un sinfín de habilidades para ser capaz de resolver problemas por sí mismo. De Juan aprendí lo importante que son lo detalles en cada paso, en cada cálculo, en cada suposición, a organizar y estructurar cada archivo y cada idea por sencilla que parezca e incluso a organizar el tiempo, a estar trabajando en una cosa e ir pensando en lo siguiente, y una gran cantidad de capacidades para lograr uno de los objetivos principales de este nivel; hacer investigación de manera independiente. Sin duda, la sinergia que logramos los tres fue crucial para sacar adelante el proyecto.

También agradezco a cada investigador que me orientó y que me ayudó a resolver alguna duda, así como a quienes mostraron interés por mi desempeño académico. En especial, agradezco a Marco Moreno por haberme recibido cuando inicié este camino de ser astrónomo, por sus consejos y por estar pendiente de mis avances. Igualmente, agradezco a Luis Aguilar por todo su conocimiento transmitido en el aula así como en su oficina. A Mauricio Tapia por seguir de cerca los avances de mi proyecto, lo cual me ayudó a enfocarme y sacarlo adelante. A Jesús Hernández por cada asesoría y por cada consejo que se ve reflejado en este trabajo. A Michael Richer por su disponibilidad para resolver cada duda que tuve, al igual que a William Schuster. A Raúl Michel por sus enseñanzas

sobre la obtención y manejo de datos. A Alejandro González por lo que fueron mis primeros cursos de astronomía y por estar pendiente de mi preparación profesional. Agradezco a todos los profesores de quienes aprendí que la astronomía no es solo en lo que trabajo y que, al igual, son temas muy interesante. También agradezco a Luis Carlos, Roy, Gerardo, Carmen, Héctor, Diego, Nicole, Isaac, Javier, Valeria, Verónica y demás compañeros de oficina y del instituto por cada plática, cada discusión, cada broma y cada momento que hicieron de esta etapa una grandiosa aventura.

Si duda, un pilar fundamental en todo esto es mi familia, la cual me ha mostrado su apoyo incondicional. Especialmente agradezco a mi madre y a mi padre, Lola y Genaro, por impulsarme y darme todo su apoyo para seguir adelante, así como por estar pendientes de cada paso que doy. Gracias a mi madre por esperar cada noche mi llamada para platicarle sobre mi día; es motivante esperar ese momento. Agradezco a mis hermanos, Cristina y Eberardo, por estar allí cuando los he necesitado. A mis abuelitos, Elena y José (Nena y Pepe), porque siempre me han mostrado su apoyo, cariño y sus buenos deseos. A mis tíos, Cheto y Chita, y a mis primos, por darme ánimos y ofrecerme su tiempo para cualquier situación, así como por su amabilidad.

Por último, pero no menos importante, quiero agradecer el apoyo infinito que me ha brindado la persona indicada para ser mi pareja de vida, mi prometida Hilda. Le estoy enormemente agradecido por haber estado al pendiente desde que decidí emprender este viaje llamado "ser astrónomo". Gracias por tus mensajes para alegrar mi día e impulsarme a avanzar en mis tareas. Gracias por tu llamada de cada noche (incluso la de hoy justo antes de escribir este párrafo), por tu interés en aprender y darme consejos, y por tus motivaciones que me ayudaron a salir adelante. Gracias por tu comprensión cuando el trabajo me ha absorbido. Este logro es de los dos.

Contents

List of Figures

List of Tables

Abbreviations

25 Ori 25 Orionis Stellar Group

2MASS Two Micron All Sky Survey (Skrutskie et al., 2006)

APOGEE-2 Apache Point Observatory Galactic Evolution Experiment 2 (Blanton et al., 2017)

ASPCAP APOGEE Stellar Parameter and Chemical Abundances Pipeline (García Pérez et al., 2016)

BD Brown Dwarf

BGM Besançon Galactic Model (Robin et al., 2003)

BOSS Baryon Oscillation Spectroscopic Survey (Dawson et al., 2013)

BT-Settl Baraffe et al. (2015)

CDSO CIDA Deep Survey of Orion (Downes et al., 2014)

CMD Color-Magnitude Diagram

CTTS Classical T-Tauri Star

CVSO CIDA Variability Survey of Orion (Briceño et al., 2019)

DECam Dark Energy Camera (Flaugher et al., 2015)

FOV Field of View

FSFR Fossil Star Forming Regions

FWHM Full Width at Half Maximum

Gaia DR1 Gaia Collaboration et al. (2016)

Gaia DR2 Gaia Collaboration et al. (2018)

H-R Hertzsprung-Russell

IMF Initial Mass Function

KDE Kernel Density Estimate

LF Luminosity Function

LMS Low-Mass Star (0.2-0.8 $M_{\odot}$)

MES Manchester Echelle Spectrograph (Meaburn et al., 1984, 2003)

MS Main Sequence

NIR Near-Infrared

OAN-SPM Observatorio Astronómico Nacional at San Pedro Mártir

ONC Orion Nebula Cluster

OSIRIS Optical System for Imaging and low Resolution Integrated Spectroscopy (Cepa et al., 2000, 2003)

PARSEC Bressan et al. (2012) and Chen et al. (2014)

PARSEC-COLIBRI Marigo et al. (2017)

PDMF Present Day Mass Function

PHOENIX Husser et al. (2013)

PMS Pre-Main Sequence

RMS Root Mean Square

RV Radial Velocity

SAS Science Archive Sever

SDSS Sloan Digital Sky Survey (Gunn et al., 2006)

SED Spectral Energy Distribution

SNR Signal-to-Noise Ratio

TDC Transitional Disk Candidate

UCAC4 USNO CCD Astrograph Catalog (Zacharias et al., 2013)

USNO United States Naval Observatory (Monet et al., 2003)

VISTA Visible and Infrared Survey Telescope for Astronomy (Emerson et al., 2004)

VOSA Virtual Observatory SED Analyzer (Bayo et al., 2008)

WISE Wide-field Infrared Survey Explorer (Cutri & et al., 2013)

WTTS Weak T-Tauri Star

YNMG Young Nearby Moving Group

YSO Young Stellar Object

Nomenclature

L_{bol} Bolometric luminosity

m_c Characteristic mass of a lognormal form

T_{eff} Effective temperature

ξ Initial Mass Function

m_p Mass peak of a tapered power-law form

$\bar{A_V}$ Mean visual extinction

Z Metallicity

σ_{RV} Radial velocity dispersion

Γ Slope of a power-law function in logarithmic mass units

R Spectral resolution

σ Standard deviation

β Tapering exponent of a taper power-law form

M_{Jup} Units of a Jupiter mass

$M_{\odot}$ Units of solar mass

A_V Visual extinction

Resumen

Las asociaciones estelares jóvenes son lugares donde podemos estudiar el proceso por el cual se formaron casi todas las estrellas de la Galaxia. La mayoría de los grupos de estrellas jóvenes se dispersan durante las primera decenas de millones de años y solo algunos sobreviven como entidades ligadas gravitacionalmente para convertirse en cúmulos estelares abiertos. Este fenómeno se entiende comúnmente como una rápida evolución de los sistemas estelares jóvenes cuando se dispersa la nube progenitora, sin embargo, también hay evidencia que sugiere que estas asociaciones estelares no ligadas se forman en procesos estructurados. Para entender cómo se forman las estrellas y cómo evolucionan los sistemas estelares jóvenes, es esencial estimar la masa total de la asociación, lo cual se puede lograr a través del análisis de la función de masa inicial (IMF, por sus siglas en inglés). Aunque existen bastantes contribuciones al estudio de la IMF, con solo unas pocas en el rango completo de masas de la población, aún es incierta su dependencia con las condiciones ambientales y/o el tiempo. Por su cercanía, baja extinción, densidad estelar y estado evolutivo, un excelente lugar para estudiar la IMF, desde las masas planetarias hasta estrellas de masa intermedia/alta, y la evolución temprana de un sistema estelar joven que acaba de emerger de su fase embebida, es el grupo estelar 25 Orionis (25 Ori).

Combinando nueva fotometría profunda en el óptico con datos de la literatura en el óptico e infrarrojo cercano, seleccionamos 1687 miembros a candidatos de 25 Ori con magnitudes en la banda I_c entre 5 y 23.3 mag en una área de 1.1° de radio. Con esta muestra determinamos la IMF del sistema de 25 Ori que va desde las 0.012 hasta 13.1 $M_\odot$. La IMF resultante está bien descrita por una función doble ley de potencias y por una forma de ley de potencias para masas altas con un comportamiento exponencial para masas bajas. También reportamos la parametrización lognormal que mejor ajusta. La IMF obtenida no presenta variaciones significantes dentro de un radio de aproximadamente 7 pc, lo cual indica que las estrellas y las enanas cafés en 25 Ori no presentan alguna distribución espacial preferencial. Comparamos la IMF de 25 Ori y la proporción entre objetos subestelares y estelares con los reportados en una gran diversidad de poblaciones estelares y no encontramos diferencias significativas, lo cual soporta la hipótesis sobre que el mecanismo de formación estelar es en gran medida insensible a las condiciones ambientales.

Para confirmar la membresía de cada candidato en nuestra muestra, tenemos en marcha un sondeo espectroscópico usando varios instrumentos. Hemos obtenido espectros de alta resolución ($R \sim 22000$) de 77 candidatos con masas intermedias/altas (1.3-11 $M_\odot$) usando OAN-SPM/MES y de 1185 candidatos con masas intermedias (0.3-5.2 $M_\odot$) usando SDSS-IV/APOGEE-2. Adicionalmente, tenemos espectros de baja resolución ($R \approx 1000-2000$) de 400 candidatos con masas bajas (0.25-0.8 $M_\odot$) usando MMT/Hectospec, de 172 candidatos con masas bajas (0.09-0.7 $M_\odot$) usando SDSS-III/BOSS y de 66 candidatas a enanas cafés (0.01-0.08 $M_\odot$) usando GTC/OSIRIS. Considerando diversos criterios de membresía, hemos confirmado 530 miembros en nuestra muestra espectroscópica, de los cuales 290 están dentro del área de 25 Ori y 208 de éstos han sido confirmados por primera vez. Con esta muestra de miembros confirmados, más los disponibles en la literatura, estimamos que 25 Ori es una población con 6.5 ± 2.5 millones de años localizada a 356 ± 47 pc de distancia y que presenta una baja extinción de 0.29 ± 0.26 mag. También, estimamos que la velocidad radial promedio de 25 Ori es 20.9 ± 2.0 km s^{-1}. Utilizando estos parámetros encontramos que 25 Ori es un grupo dinámicamente joven que no ha tenido el tiempo suficiente para estar relajado y confirmamos que es una asociación estelar no ligada gravitacionalmente.

Considerando los miembros confirmados, así como los disponibles en la literatura, el sondeo espectroscópico está completo en un ∼75%, con la mayoría de los candidatos por observar con masas estimadas alrededor del límite subestelar. Tenemos observaciones en marcha para completar este sondeo espectroscópico en 25 Ori.

Abstract

Young stellar aggregates are the laboratories where we study the process by which almost every star in the Galaxy has formed. Most of the young stellar groups break up in at most a few tens of Myr and only a few of them survive as gravitational bound entities to become open clusters. This phenomenon is usually understood as a rapid evolution of young stellar systems when the parental molecular gas is expelled, however, there is also evidence suggesting that these unbound stellar associations are formed in a structured process. To understand how stars are formed and how young stellar systems evolve, it is essential to estimate the total mass of the association, which can be achieved through the analysis of the stellar initial mass function (IMF). Despite many contributions to the study of the IMF, only a few of them over the whole cluster mass range, it is still unclear how it depends on environmental conditions and/or time. Due to its closeness, low extinction, stellar density and evolutionary status, an excellent place to study the IMF, from planetary-mass objects to intermediate/high-mass stars, and the early evolution of a young stellar system that just emerged from its embedded phase, is the 25 Orionis stellar group (25 Ori).

Combining new deep optical photometry from DECam with optical and NIR data from the literature, we selected 1687 member candidates of 25 Ori with I_c-band magnitudes between 5 and 23.3 mag in an area of 1.1° radius. With this sample we derived the system IMF of 25 Ori from 0.012 to 13.1 $M_\odot$, which is one of the few IMFs across the entire mass range of a stellar association. The resultant system IMF is well-described by a two-part power-law function and by a tapered power-law form. We also report its best lognormal parameterization. This system IMF do not present significant variations within a radius of about 7 pc, which indicates that the substellar and stellar objects in 25 Ori do not have any preferential spatial distribution. We compared the reported system IMF as well as the BD/star ratio with those of a large diversity of stellar populations and did not find any significant discrepancies, which strongly supports the hypothesis that the star formation mechanism is largely insensitive to environmental conditions.

In order to confirm the membership of each candidate in our sample, we have an ongoing spectroscopic survey using several world-wide facilities. We have obtained high-resolution ($R \sim 22000$) spectra of 77 intermediate/high-mass (1.3-11 $M_\odot$) candidates with OAN-SPM/MES and of 1185 intermediate-mass (0.3-5.2 $M_\odot$) candidates with SDSS-IV/APOGEE-2. Additionally, we have low-resolution ($R \approx 1000 - 2000$) spectra of 400 low-mass (0.25-0.8 $M_\odot$) candidates with MMT/Hectospec, of 172 low-mass (0.09-0.7 $M_\odot$) candidates with SDSS-III/BOSS and of 66 brown dwarf (0.01-0.08 $M_\odot$) candidates with GTC/OSIRIS. After applying diverse membership criteria, we have so far confirmed 530 members from the spectroscopic sample, out of which 290 lie inside the 25 Ori area and 208 of them are confirmed for the first time. With this sample of confirmed member, plus those in the literature, we estimated that 25 Ori is a 6.5 ± 2.5 Myr old population located at 356 ± 47 pc and presenting a low extinction of 0.29 ± 0.26 mag. Also, we estimated that the 25 Ori mean radial velocity is 20.9 ± 2.0 km s^{-1}. Using these parameters we found that 25 Ori is a dynamically young group without time enough to be relaxed and confirmed that it is, in fact, a gravitationally unbound association that will be part of the Galactic Disk population.

Considering the observed and confirmed members as well as those already confirmed in the literature, the spectroscopic follow-up is ∼75% complete, with most of the remaining candidates to be observed with estimated masses around the substellar mass limit. We have ongoing observations to complete the spectroscopic survey of 25 Ori.

1 Introduction

Star formation is a complex process that can be structured on a wide range of scales; from small compact clusters or, even, single stars, to star-forming complexes (e.g. Larson, 1994; Elmegreen & Efremov, 1996; Parker & Goodwin, 2007; Bonnell et al., 2011; Bressert et al., 2012; Feigelson et al., 2013; Vázquez-Semadeni et al., 2017; Gouliermis, 2018). However, only a small fraction ($\sim 10\%$) of young stellar groups reaches ages larger than few tens of Myr, which is usually understood as a dynamical evolution of young embedded associations after the molecular cloud is expelled by stellar feedback (Lada & Lada, 2003; Kuhn et al., 2019) or it could be an indicative that stars are born in a diversity of structures where not all of them are bound clusters (Schweizer, 2009; Ward & Kruijssen, 2018; Gouliermis, 2018). To distinguish between these scenarios and to understand if a young stellar group will become an open cluster or will disperse to be part of the Galactic Disk population, it is important to study the distribution of masses of the group and its kinematics.

1.1 Initial Mass Function

The stellar initial mass function (IMF, ξ) is the distribution of masses at birth in a stellar population and is a fundamental product of star formation, as well as an essential input for a diversity of astrophysical studies (see the review by Hopkins, 2018). The IMF is defined as Equation 1, where m is the mass of a star and N is the number of stars in the logarithmic mass interval between $\log m$ and $\log m + d(\log m)$.

$$\xi(\log m) = \frac{dN}{d(\log m)} \tag{1}$$

The origin of the IMF is commonly referred to the formation of prestellar cores of different masses by a rather poorly understood process of fragmentation in molecular clouds which, then, scale to form stars roughly keeping the distribution of the core masses (e.g. Padoan & Nordlund, 2002; Alves et al., 2007; Chabrier & Hennebelle, 2010; Hennebelle & Chabrier, 2013). However, additional ideas that explained the origin of the IMF are discussed in Hennebelle & Chabrier (2011) and Offner et al. (2014), which we mentioned in the context of the parameterizations of the IMF in the next section.

1.1.1 IMF Parameterization

To make comparisons of the IMF of different stellar populations, it is appropriate to parameterize the IMF using a functional form, which, among other things, allows the study of integrated properties of unresolved populations.

The pioneering IMF work was done by Salpeter (1955) studying stars in the solar neighborhood. He provided an IMF parameterization as a power-law function in the form of Equation 2, with slope Γ=1.35 for $m > 0.5\ M_{\odot}$.

$$\xi(\log m) \propto m^{-\Gamma} \tag{2}$$

This power-law form, with a similar slope ($\Gamma = 1$), is predicted by star formation models due to the fragmentation of a collapsing cloud where competitive accretion occurs in the protostellar cores (Larson, 1978; Zinnecker, 1982).

The IMF parameterization proposed by Salpeter (1955) diverges as the mass decreases. A functional form that describes well the decreasing behavior observed for low-mass stars (LMSs) and very LMSs in the solar neighborhood was introduced by Miller & Scalo (1979) as a lognormal

function. This representation has a theoretical explanation invoking the central limit theorem and considering the star formation process as a complex combination of several possible independent variables (Larson, 1973; Zinnecker, 1984; Adams & Fatuzzo, 1996). This lognormal function is shown in Equation 3, where m_c is the characteristic mass and σ the standard deviation. However, it is found that this functional form underestimates the number of massive stars ($> 20\ M_\odot$) with respect to the slope behavior (e.g. Bastian et al., 2010).

$$\xi(\log m) \propto e^{-\frac{(\log m - \log m_c)^2}{2\sigma^2}} \tag{3}$$

A functional form that corrects the underestimation of massive stars by the lognormal function is a three-part power-law with break masses at 0.08 and 0.5 $M_\odot$, proposed by Kroupa et al. (1991, 1993) and updated by Kroupa (2001, 2002). This form describes well the behavior observed in a sample of stellar populations (the solar neighborhood, stellar associations, stellar clusters and extragalactic resolved clusters) discussed in Scalo (1986), which has a steeper slope ($\Gamma = 1.7$) than the Salpeter (1955) value.

An additional form that represents the IMF of various components of the Galaxy (disk, spheroid, young and globular clusters) is a power-law form for $m \gtrsim 1\ M_\odot$ with a lognormal form for lower masses (Chabrier, 2001, 2003a, 2005), which is predicted by theories based on turbulence (e.g. Hennebelle & Chabrier, 2008). This functional form is mostly observational indistinguishable from a dual power-law function with break at 0.5 $M_\odot$ (Dabringhausen et al., 2008; Kroupa et al., 2013). However, a lognormal function can overestimate the number of very LMSs and brown dwarfs (BDs) (Hoffmann et al., 2018), as reported in σ Ori (Peña Ramírez et al., 2012) and Upper Sco (Lodieu, 2013), and as we found in Section 2.4.2.4.

A functional form that describes well the IMF across the entire cluster mass range is the "tapered" power-law presented by de Marchi & Paresce (2001) and De Marchi et al. (2005), which has a slope form for high masses with an exponential truncation for lower masses. This parameterization is shown in Equation 4, where m_p is the peak mass (similar to m_c in Equation 3), Γ the power law index which describes the massive range and β the tapering exponent in the low-mass domain. This parameterization described well the IMF of a large sample of Galactic clusters and of the Galactic Disk (Bastian et al., 2010; De Marchi et al., 2010; Parravano et al., 2011).

$$\xi(\log m) \propto m^{-\Gamma}\left[1 - e^{-(m/m_p)^\beta}\right] \tag{4}$$

Additional recent proposed forms to parameterize the IMF are two power-laws smoothly joined by a lognormal (Maschberger, 2013), a modified lognormal power-law distribution (Basu et al., 2015) and a dual power-law probability distribution (Hoffmann et al., 2018). In Figure 1 we show a scheme of some of the parameterizations discussed in this section.

1.1.2 System IMF

In the context of the IMF, it is important to distinguish between the *single-star* IMF, where multiple stellar systems are resolved, and the *system* IMF as the opposite case (e.g. Chabrier, 2003b). Most of the above discussed contributions, mainly those studying the solar neighborhood, refer to the single-star IMF. In contrast, in studies of the low-mass population of distant clusters, a correction by binarity is often necessary to obtain the single-star IMF. As the binarity properties for substellar objects are poorly understood, most studies report the system IMF to avoid the introduction of additional uncertainties. However, there are some efforts to study the effects of unresolved binarity system in the mass distribution. Luhman et al. (1998) found that, in the case

of the IC 348 population, the changes in the system IMF slopes due to the correction for unresolved binaries are small between 0.6 and 2.5 $M_\odot$ but significant, by about 0.5, for the mass range from 0.05 to 0.6 $M_\odot$, which results in a larger account of objects with masses in this range. Chabrier (2003b) showed that the m_c of the single-star IMF of the disk moves towards larger values by a factor of ~ 2 if the binaries were not resolved, with small changes in the σ parameter. Similar conclusions about the change of the m_c parameter when resolving binary systems were obtained by Moraux et al. (2003) studying the Pleiades mass distribution. More recently, Mužić et al. (2017) found that both ends of the system IMF become slightly steeper if unresolved binary systems are taken into account, which is also obtained in Kroupa (2001) for the slopes of the stellar objects.

Working with the system IMF allows comparisons between several stellar populations, assuming similar binary properties (Duchêne et al., 2018), to analyze how sensitive or not it can be to local conditions.

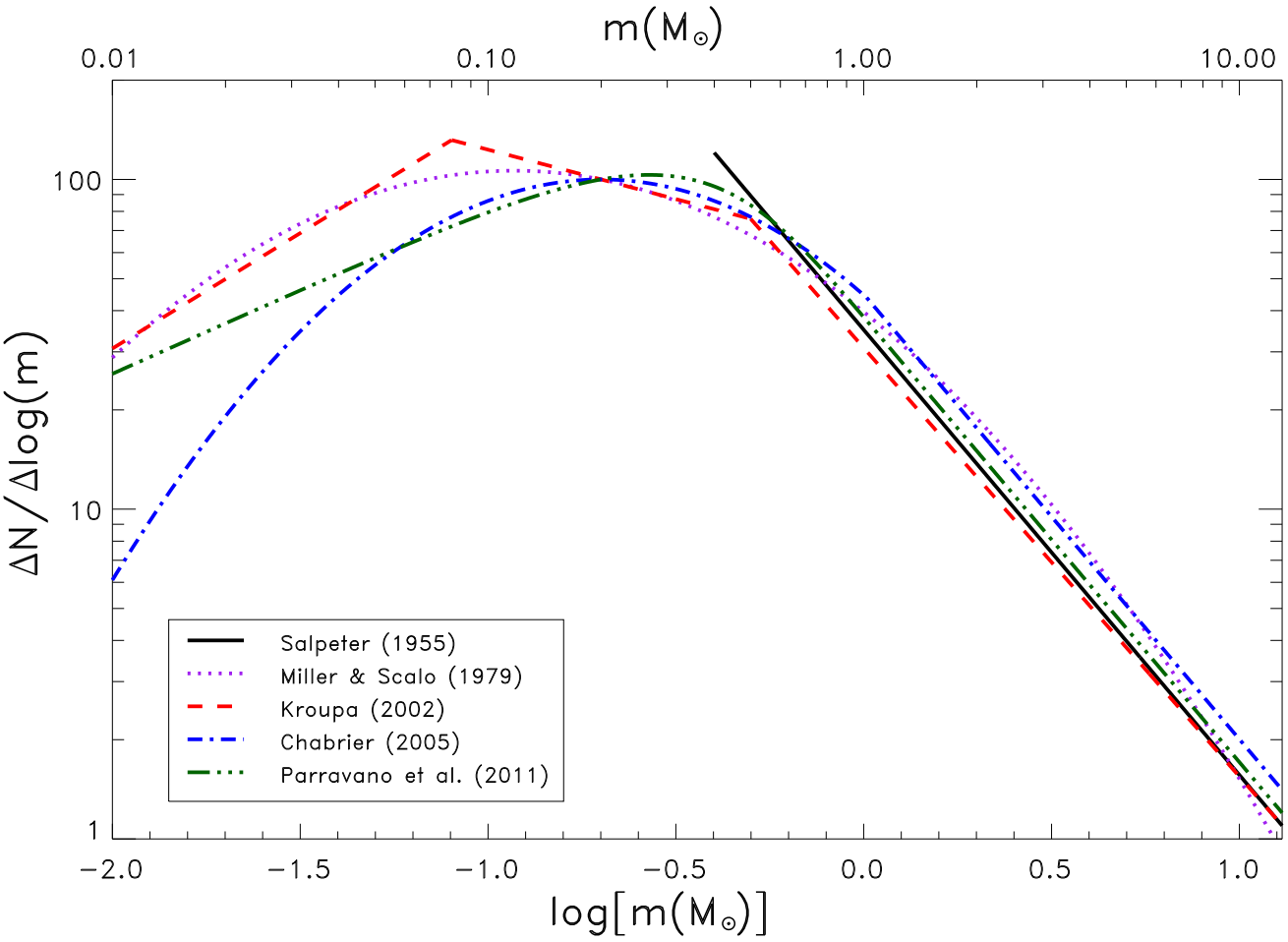

Figure 1: Functional forms representing the IMF of several stellar populations by the studies indicated in the label. All functions are normalized at 0.2 $M_\odot$, except for the Salpeter (1955) slope.

1.1.3 Universality of the IMF

One of the most challenging problems in modern astrophysics is the so-called *universality* of the IMF, which refers to a possible null dependence of the IMF with the environmental conditions and/or time. Despite the diverse IMF functional forms mentioned in last section, the IMF of a

vast diversity of stellar populations (dense clusters, associations, open clusters, globular clusters and field population) is well-described by a single representation, as found by Bastian et al. (2010), working with the compilation from De Marchi et al. (2010). Nevertheless, significant scatter arise for the substellar regime, which can be due to uncertainties and/or incompleteness in the surveys. Similar results are found by Offner et al. (2014), who focused on theories of the origin of the IMF and mostly comparing with regions in extreme circumstances where evidence of variations were presented. However, there are some studies showing significant variations of the IMF in the massive range such Weisz et al. (2015), for a large sample of clusters in M31, and Dib et al. (2017), by comparing the massive population of various young Galactic clusters with synthetic clusters from diverse IMF parameters. In a more general context, the study by Weidner & Kroupa (2005) shows that the distribution of stellar masses across several entire galaxies is steeper than the stellar IMF.

These results in an apparent disagreement call for additional studies, specifically in the low-mass regime, for more robust conclusions about the nature of the IMF. As an example of the importance of the last phrase, one of the stellar associations most dispersed from the single underlying IMF by Bastian et al. (2010) is the Taurus Star-forming region, which exhibits an excess of LMSs, which disappears in the recent study by Luhman (2018), working with data from Gaia DR2 (Gaia Collaboration et al., 2018).

To observationally determine the IMF of a stellar population, it is necessary to obtain first the luminosity function (LF) of a sample of stars in a defined volume. Then, the LF is converted to the present day mass function (PDMF) by assuming a mass-magnitude relationship. Finally, the PDMF is corrected by the star formation history, stellar evolution, cluster dynamical evolution, galactic structure and binarity to obtain the IMF. Each of these steps present difficulties on their own, which makes the IMF determination a non straightforward task (e.g. Zinnecker, 2005; Maíz Apellániz & Úbeda, 2005; Ascenso, 2011; Jeffries, 2012; Stassun et al., 2014).

Various of the aforementioned difficulties in IMF studies are minimized when working with stellar clusters, in which, if young enough, the PDMF approximates to the IMF. However, an important issue to be taken into account in the analysis of stellar clusters is their dynamical evolution, which can produce a significant loss of members.

1.2 Evolution of Young Clusters

As mentioned at the beginning of this section, only a small fraction of young stellar systems keep as gravitational bound clusters after few tens of Myr. In fact, Lada & Lada (2003) and Bonatto & Bica (2011) found that only $\sim 10\%$ of the young stellar systems remains as bound clusters for ages larger than 10 Myr. The evolution of these young systems could depend on the variations of the gravitational potential when the parental cloud is expelled (e.g. Baumgardt & Kroupa, 2007) and on their dynamical state (contracting, expanding or in equilibrium, e.g. Kuhn et al., 2019) as well as to tidal perturbations by nearby and dense giant molecular clouds (Kruijssen, 2012).

The molecular gas present in embedded clusters is an important component than can be comparable in mass with the stellar content (in the DR21 region; Schneider et al., 2010) or, even, can dominate the gravitational potential (in the Orion Nebula Cluster, ONC, except in the inner region; Stutz, 2018). Gas expulsion due to stellar feedback (outflows, stellar winds, supernovae and photoionizing radiation) produces a decrease of the gravitational potential of the stellar systems, which in turn result in an expansion of the groups due to the velocity dispersion of the stars (Baumgardt & Kroupa, 2007). This process can result in an expanding unbound association if the gas remotion is fast (Goodwin & Bastian, 2006), explaining the deficit of observed clusters with ages larger than few tens of Myr (Lada & Lada, 2003). However, in more recent simulations, it is

found that the gas expulsion effect is less important during the cluster disruption (Parker & Dale, 2013; Dale et al., 2015). Recently, Sills et al. (2018) found that the evolution of embedded clusters is more influenced by gravitational interactions between stars, with a small contribution from the surrounding gas.

However, recent studies in OB associations by Wright & Mamajek (2018) and Ward & Kruijssen (2018) show no clear evidence of expansion that can indicate that these associations had a more compact configuration in the past, which suggests they were not formed by the disruption of young stellar systems. These results support the idea that the star formation process is a structured process where the different components are formed *in situ* i.e. a hierarchically process, more than in a monolithic scenario (see the review by Gouliermis, 2018).

However, additional evidence of expansion was presented by Getman et al. (2018) in young stellar populations in several star-forming regions and by Kuhn et al. (2019) in various young stellar clusters and associations as well as by Román-Zúñiga et al. (2019) in the Perseus Arm in the vecinity of the W3/W4/W5 complex. Also, Kounkel et al. (2018) found that the large stellar group structures that emerged from the molecular gas in the Orion Complex are preferentially expanding, but specific analysis are encouraged to determine the gravitational state (bound or not) of individual stellar systems in the complex.

Gravitational bound clusters are stellar systems with a total energy (kinematic energy plus gravitational energy) that is negative. A study to know if a stellar system is gravitationally bound can be done by comparisons of its velocity dispersion with the velocity dispersion necessary for a virial equilibrium (e.g. Kuhn et al., 2019). The important quantities for this analysis are 1D velocity dispersion which can be obtained from the radial velocity (RV) and the total mass and its distribution that can be obtained from the determination of the IMF.

In this dissertation I present a characterization of the substellar and stellar population of a group that just emerged from its embedded phase. We focus on the determination of its mass spectrum over the whole mass range of the population, from planetary-mass objects to intermediate/high-mass stars, together with a follow-up spectroscopy using several world-wide facilities, which allow us to determine if the group is gravitationally bound or not.

1.3 25 Orionis Stellar Group

An excellent stellar group to carry out the proposed study is 25 Orionis (25 Ori), the most prominent overdensity in Orion OB1a (Briceño et al., 2005, 2007; Downes et al., 2014; Briceño et al., 2019). The physical properties that 25 Ori present allow a detailed analysis of its entire population. First, it is relatively close and has a low extinction (365 ± 47 pc and 0.29 ± 0.26 mag; Suárez et al., 2019), which makes it possible to observe members with estimated masses lower than the deuterium burning limit (0.013 $M_{\odot}$). Also, it is young enough (6.1±2.4; Briceño et al., 2019, and references therein) to have lost massive members due to stellar evolution and to appear spatially concentrated to survey its entire spatial distribution, but old enough to have dispersed its parental cloud and have formed all its members as well as to keep a small fraction of members harboring circumstellar disks (Briceño et al., 2005; Hernández et al., 2007b; Downes et al., 2014). More details about 25 Ori are found in Sections 2.1, 2.4.2.1 and 3.4.1.

2 System IMF of 25 Ori (Suárez et al., 2019)

The analysis presented in this section constitutes the publication "System IMF of the 25 Ori Group from Planetary-mass Objects to Intermediate/High-mass Stars" by Suárez et al. (2019), which was carried out as part of this dissertation.

Abstract. The stellar initial mass function (IMF) is an essential input for many astrophysical studies but only in a few cases it has been determined over the whole cluster mass range, limiting the conclusions about the nature of its complete shape. The 25 Orionis group (25 Ori) is an excellent laboratory to investigate the IMF across the entire mass range of the population, from planetary-mass objects to intermediate/high-mass stars. We combine new deep optical photometry with optical and near-infrared data from the literature to select 1687 member candidates covering a 1.1° radius area in 25 Ori. With this sample we derived the 25 Ori system IMF from 0.012 to 13.1 $M_{\odot}$. This system IMF is well described by a two-segment power-law with $\Gamma = -0.74 \pm 0.04$ for $m < 0.4$ $M_{\odot}$ and $\Gamma = 1.50 \pm 0.11$ for $m \geq 0.4$ $M_{\odot}$. It is also well described over the whole mass range by a tapered power-law function with $\Gamma = 1.10 \pm 0.09$, $m_p = 0.31 \pm 0.03$ and $\beta = 2.11 \pm 0.09$. The best lognormal representation of the system IMF has $m_c = 0.31 \pm 0.04$ and $\sigma = 0.46 \pm 0.05$ for $m < 1$ $M_{\odot}$. This system IMF does not present significant variations with the radii. We compared the resultant system IMF as well as the BD/star ratio of 0.15 ± 0.03 we estimated for 25 Ori with that of other stellar regions with diverse conditions and found no significant discrepancies. These results support the idea that general star formation mechanisms are probably not strongly dependent to environmental conditions. We found that the substellar and stellar objects in 25 Ori have similar spatial distributions and confirmed that 25 Ori is a gravitationally unbound stellar association.

2.1 Introduction

The mass spectrum of the members of a stellar population at birth is known as initial mass function (IMF). The IMF is the main product of the star formation process and is one of the fundamental astrophysical quantities. Since the seminal IMF study by Salpeter (1955), there have been many contributions to this topic to understand the origin and behavior of the IMF, but only few of them focus on the whole mass range of the populations, which limits the conclusions about its complete shape (e.g. Bastian et al., 2010, and references therein).

Observational IMF studies in a complete range of masses, from planetary-mass objects to massive star scales, allow to analyze the continuity of the star formation process over about three orders of magnitude of mass and help to constrain initial conditions of star formation models. These kind of studies are also important to understand if the star formation process is sensitive or not to environmental conditions and if it changes in time, which is the nature of the so-called *universality of the IMF* (e.g. Kroupa et al., 2013; Offner et al., 2014).

Young stellar clusters ($\lesssim 10$ Myr) are useful laboratories for observational studies of the IMF in a wide range of masses because objects are brighter in the pre-main sequence (PMS) phase than on the main sequence (MS), none or minimum correction by the stellar evolution of their members is necessary, their spatial distributions are relatively small (for groups beyond the solar neighborhood) and their members have basically the same age, metallicity (Z) and distance. However, an important issue to be taken into account when working with embedded clusters ($\lesssim 3$ Myr; Lada & Lada, 2003) is dust extinction, which, on one hand, complicates the detection of the least massive objects but, on the other hand, helps to separate the cluster population from the background contamination. An additional issue that can affect IMF determinations is the loss of low-mass members in dynamically evolved clusters caused by the preferential escape of these

Table 1: System IMF parameterizations over a wide mass range in several young clusters.

Cluster	Age	Lognormal			Power Law				Model	Ref
		m_c	σ	m range	Γ_1^a	m range	Γ_2^b	m range		
	[Myr]	[$M_\odot$]		[$M_\odot$]		[$M_\odot$]		[$M_\odot$]		
RCW 38	1[c]				-0.29±0.11	0.02-0.50	0.60±0.13	0.50-20	BT-Settl+PARSEC	1
					-0.58±0.18	0.02-0.20	0.48±0.08	0.20-20		
ONC	2	0.35±0.02[d]	0.44±0.05[d]	0.025-3	-1.12±0.90[d]	0.025-0.30	0.60±0.33[d]	0.30-3	NextGen	2
		0.28±0.02	0.38±0.01		-2.41±0.25	0.025-0.17	1.30±0.09	0.17-3	DM98	
σ Ori	∼3[e]	0.24±0.09[f]	0.53±0.19[f]	0.006-1	-0.40±0.20	0.006-0.35	0.70±0.20	0.35-19	Siess+Lyon	3
		0.27±0.09[f]	0.63±0.15[f]	0.006-19						
Collinder 69	5[g]				-0.71±0.10[h]	0.01-0.65	0.82±0.05[h]	0.65-25	Siess+COND	4
Blanco 1	100-150	0.36±0.07	0.58±0.06	0.03-3	-0.31±0.15	0.03-0.60			NextGen+DUSTY	5
Pleiades	125[i]	0.25	0.52	0.03-10	-0.40±0.11	0.03-0.48	1.7	1.5-10	NextGen	6

[a] For LMSs and BDs.
[b] For intermediate/high-mass stars.
[c] Getman et al. (2014).
[d] For sources older than 1 Myr.
[e] Zapatero Osorio et al. (2002) and Caballero (2008).
[f] Mean values of the two set of parameters obtained combining Baraffe et al. (1998) and Siess et al. (2000) models at different cutoffs (0.3 and 1 $M_\odot$).
[g] Dolan & Mathieu (1999) and Bayo et al. (2011).
[h] Mean value of the six reported values and the error as the standard deviation.
[i] Stauffer et al. (1998).

NextGen: Baraffe et al. (1998), DM98: D'Antona & Mazzitelli (1998), Siess: Siess et al. (2000), DUSTY: (Chabrier et al., 2000), COND: (Baraffe et al., 2003), Lyon: NextGen, DUSTY and COND, BT-Settl: Baraffe et al. (2015), and PARSEC: Bressan et al. (2012) and Chen et al. (2014).

References: (1) Mužić et al. (2017), (2) Da Rio et al. (2012), (3) Peña Ramírez et al. (2012), (4) Bayo et al. (2011), (5) Moraux et al. (2007a), and (6) Moraux et al. (2003).

members and/or by the BD photospheric cooling (de La Fuente Marcos & de La Fuente Marcos, 2000). Therefore, we should look for stellar clusters that are old enough to diminish extinction effects but are also young enough to allow a complete determination of the IMF.

The best studied clusters in the literature in terms of their IMFs over a wide mass range are: Pleiades (0.03 - 10 $M_\odot$; Moraux et al., 2003), Blanco 1 (0.03 - 3 $M_\odot$; Moraux et al., 2007a), σ Ori (0.006 - 19 $M_\odot$; Peña Ramírez et al., 2012), the Orion Nebula Cluster (ONC; 0.025 - 3 $M_\odot$, ≈0.005 - 1 $M_\odot$; Da Rio et al., 2012; Drass et al., 2016, respectively), and RCW 38 (0.02 - 20 $M_\odot$; Mužić et al., 2017). Additionally to these studies based on photometric data, a detailed determination of the IMF of Collinder 69 based on spectroscopically confirmed members across more than three orders of magnitude of mass (0.016 - 20 $M_\odot$) was presented by Bayo et al. (2011). All these studies reported the IMF not corrected by unresolved multiple systems, also referred as *system* IMF (Chabrier, 2003a). Additionally, Moraux et al. (2003) and Mužić et al. (2017) also presented the single-star IMF, in which a correction by multiple systems is applied. In Table 1 we summarize the resulting parameterizations of these system IMFs as well as the employed theoretical models for mass determination. For parameterizations of a larger sample of clusters but in smaller mass ranges see Table 1 from De Marchi et al. (2010) and Table 4 from Mužić et al. (2017), mainly, for LMSs. Although the tables indicated above show some differences between the various IMFs, more complete and systematic observational studies are needed in populations with different environments and evolutionary stages before any claim concerning variations of the IMF, as suggested by Bastian et al. (2010) and Offner et al. (2014).

An interesting young stellar group for studying the IMF over its whole mass range and full spatial extent is 25 Ori, the most prominent spatial overdensity of PMS stars in Orion OB1a, originally detected by Briceño et al. (2005) and kinematically confirmed by Briceño et al. (2007). The estimated area of this group have radii of 1.0° (Briceño et al., 2005, 2007), 0.5° (hereafter referred as the 25 Ori overdensity; Downes et al., 2014) and 0.7° (Briceño et al., 2019), centred

at $\alpha_{J2000} = 81.2°$ and $\delta_{J2000} = 1.7°$. This makes it feasible to perform an observational study covering the full spatial extent of this group. 25 Ori is a 7-10 Myr population located at 356±47 pc and presents a low visual extinction (A_V) of 0.29±0.26 mag (see Appendix B.3), which facilitates the detection of members down to planetary-masses (Downes et al., 2015). Several previous studies have focused on characterizing the 25 Ori population; Kharchenko et al. (2005, 2013) for intermediate/high-mass stars, Briceño et al. (2005); McGehee (2006); Briceño et al. (2007); Hernández et al. (2007b); Biazzo et al. (2011); Downes et al. (2014); Suárez et al. (2017c); Briceño et al. (2019) for LMSs and Downes et al. (2015) for BDs.

In 2014, Downes et al. reported the first and only available determination of the system IMF of 25 Ori in the mass range $0.02 \lesssim m/M_\odot \lesssim 0.8$ working with a sample of photometric member candidates inside an area of 3x3 deg^2 around 25 Ori. In this work we improve the 25 Ori system IMF by including optical and near-infrared (NIR) photometry spanning from intermediate/high-mass stars down to planetary-mass objects ($0.012 \leq m/M_\odot \leq 13.1$) and also covering its full spatial extent. In Section 2.2, we present our observations and public catalogs used in this study. The selection of the photometric member candidates and a discussion of different issues that could affect the determination of the IMF, in the particular case of 25 Ori, and how we deal with them are presented in Section 2.3. In Section 2.4, we present the derivation of the 25 Ori system IMF and the comparisons with other associations, and the analysis of the spatial distribution, BD frequency and gravitational state of 25 Ori. Finally, a summary and conclusions are given in Section 2.5.

2.2 Photometric Data

2.2.1 DECam observations

This work includes new very deep optical i-band photometry of 25 Ori obtained using the Dark Energy Camera (DECam) mounted on the 4m Victor M. Blanco telescope at CTIO. DECam is a 570 Megapixel camera with an array of 62 2kx4k detectors with a plate scale of 0.263″ pixel^{-1}, covering a field of view (FOV) of 1.1° radius (Flaugher et al., 2015). Our DECam observations were performed on Feb 24, 2016 (NOAO2016A-0337, PI: G. Suárez). We obtained 11x300s exposures in the i-band centered at $\alpha_{J2000} = 05^h25^m04^s.8$ and $\delta_{J2000} = +01°37'48''.6$ with an airmass < 1.3 and a mean seeing of $\sim 0.9''$. During our observations two DECam detectors were not functional, reducing the array to 60 usable detectors. In Section 2.3.2.1 we discuss how this fact, together with the gaps and the non circular configuration of the detectors, affect the spatial coverage of the DECam observations. In Figure 2 we show the spatial coverage of our DECam data.

The reduced and calibrated data were produced by the DECam Community Pipeline (Valdes et al., 2014) and downloaded from the NOAO Science Archive[1]. The resulting data have processing level of 2, which means they are single reduced frames after removing the instrument signature and applying the WCS and photometric calibrations, as explained in the NOAO Data Handbook[2].

We combined the individual frames using the `imcombine` routine of IRAF[3], considering a ccdclip value of 3.5-σ and correcting the offset of the individual images using the WCS solutions provided by the NOAO pipeline. The accuracy of the astrometry with respect to the the Sloan Digital Sky Survey (SDSS) Data Release 9 (Ahn et al., 2012) catalog is 0.1″ for bright sources and decays to 0.2″ for the faintest sources in the DECam catalog. The photometry was made using a modification of the *PinkPack* pipeline (Levine, 2006) to work with the DECam data, which uses the SExtractor software (Bertin & Arnouts, 1996) for the detections, IRAF/APPHOT for the aperture photometry

[1] http://archive.noao.edu/

[2] http://ast.noao.edu/sites/default/files/NOAO_DHB_v2.2.pdf

[3] IRAF is distributed by NOAO, which is operated by AURA, Inc., under cooperative agreement with the NSF.

and IRAF/DAOPHOT for the PSF photometry. To calibrate the resulting i-band photometry we added the zero point of 25.18 mag for our DECam observations and an offset of 0.637 mag with respect to the i-band photometry in the DECam system obtained from the Sloan Digital Sky Survey (SDSS) Data Release 9 (DR9) (Ahn et al., 2012) catalog. More details about this calibration are found in Appendix B.1. The mean value of the residuals between our calibrated data and those in the DECam system using photometry from SDSS is -0.001 mag with a root mean square (RMS) of 0.038 mag.

2.2.2 CIDA Deep Survey of Orion

Additional optical I_c-band photometry for sources brighter that the DECam saturation limit (see Section 2.3.2.2) was obtained from the CIDA Deep Survey of Orion (CDSO; Downes et al., 2014). This catalog was constructed by coading the photometry from the CIDA Variability Survey of Orion (CVSO; Briceño et al., 2005; Mateu et al., 2012; Briceño et al., 2019), obtained at the National Astronomical Observatory of Venezuela. The area covered by this survey extends beyond the limits of our DECam data.

2.2.3 VISTA Orion Survey

The deep Z, J and K near-infrared photometry for this study is from the VISTA (Visible and Infrared Survey Telescope for Astronomy) survey in Orion (Petr-Gotzens et al., 2011), which was carried out as part of the VISTA science verification program (Arnaboldi et al., 2010) with the near-infrared camera (VIRCAM) mounted on the 4.2m telescope at Paranal Observatory.

2.2.4 Photometry from Literature

2.2.4.1 Optical Photometry

The optical data from DECam and the CDSO were complemented with the i-band photometry from the fourth USNO (United States Naval Observatory) CCD Astrograph Catalog UCAC4 (Zacharias et al., 2013) as well as the I_c-band photometry from the *Hipparcos* catalog (Perryman et al., 1997) for the brightest sources in 25 Ori.

2.2.4.2 Near-IR Photometry

We complemented the VISTA near-infrared photometry with J and Ks-band photometry from the Two Micron All Sky Survey (2MASS) catalog (Skrutskie et al., 2006).

In Table 2 we summarized the spatial coverage of 25 Ori (for an area of 0.7° radius, see Section 2.3.2.1), the spatial resolution and the photometric sensitivities (see Section 2.3.2.2) of the optical and NIR catalogs used in this study. The masses corresponding to the saturation and completeness magnitudes are obtained using the mass-luminosity relation explained in Section 2.4.2.1.

2.2.5 Merged Optical-NIR Catalog

From the individual catalogs with optical and NIR data we constructed one single general catalog, as explained in this section.

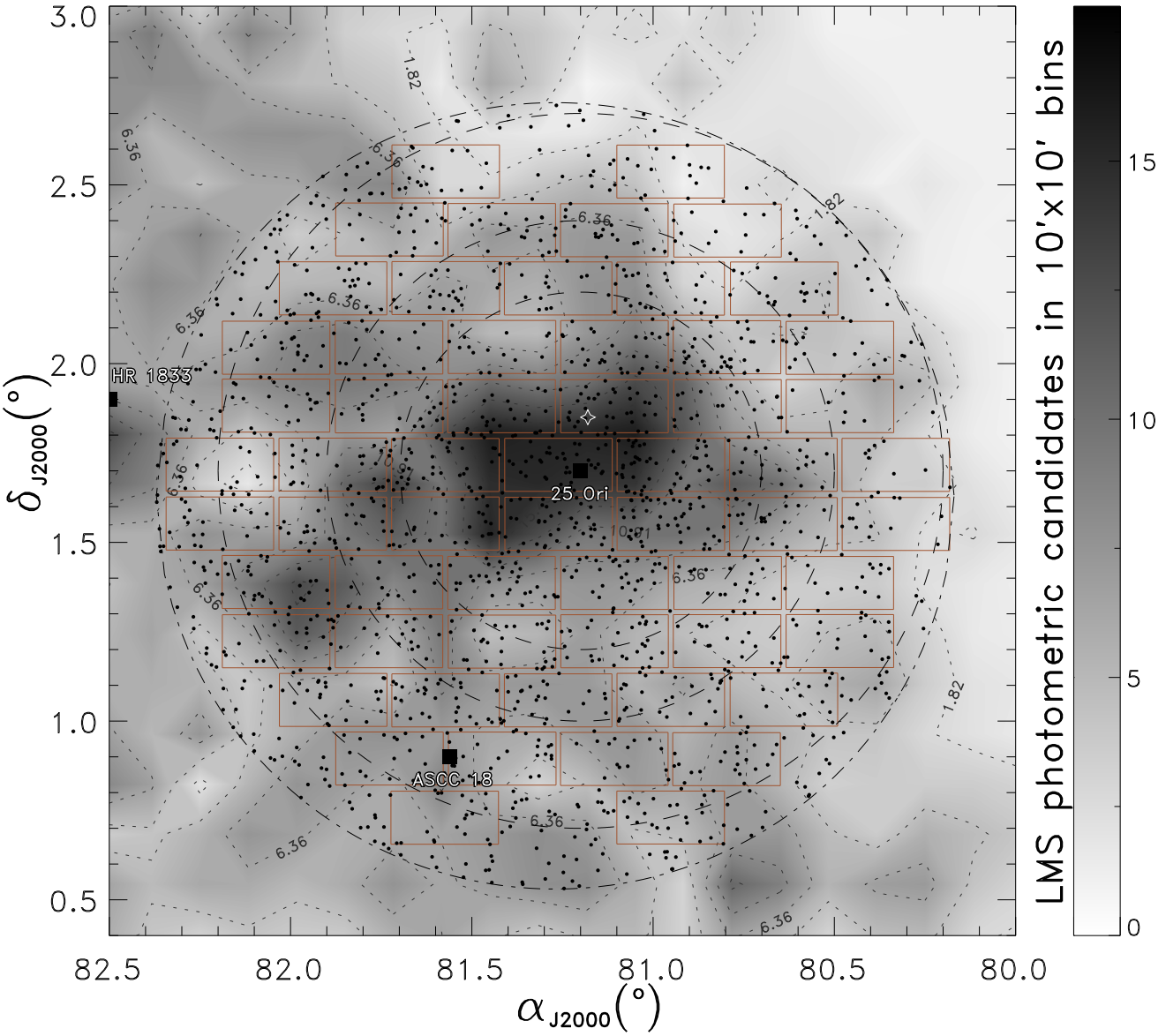

Figure 2: Spatial distribution of our photometric member candidates (black points; see Section 2.3). The dash-dotted circle shows the FOV of our DECam observations obtained with the array of detectors indicated by the brown boxes. The dashed circles indicate, from the center outwards, the 25 Ori estimated areas by Downes et al. (0.5° radius; 2014), Briceño et al. (0.7° radius; 2019) and Briceño et al. (1.0° radius; 2005, 2007) centered at $\alpha_{J2000} = 81.2°$ and $\delta_{J2000} = 1.7°$. The black squares indicate the labeled stellar groups (25 Ori by Briceño et al. 2005, ASCC 18 and ASCC 20 by Kharchenko et al. 2013 and HR 1833 by Briceño et al. 2019). The gray background map indicates the density of LMS and BD photometric member candidates of Orion OB1a, computed as the number of sources in bins of 10'x10' using the selection of Downes et al. (2014). The white star symbol shows the position of the 25 Ori star.

2.2.5.1 Transformation of optical photometry into Cousins system

We transformed the i-band photometry from UCAC4 and DECam to the Cousin system I_c-band, which is a photometric band predicted by the BT-Settl (Baraffe et al., 2015) and PARSEC-COLIBRI (Marigo et al., 2017) isochrones used to estimate masses to later construct the system

Table 2: Spatial coverage of 25 Ori[1] and photometric sensitivities of the catalogs used in this study.

Survey	**Phot. Band**	**FWHM** (arcsec)	**Area** (%)	**Satur.** (mag)	**Comp.** (mag)	**Satur.** ($M_\odot$)	**Comp.** ($M_\odot$)	**Ref.**
DECam	I_c	0.9	≈ 86	16.0	22.50	0.16	0.012	a
CDSO	I_c	2.9	100	13.0	19.75	0.86	0.020	b
UCAC4	I_c	1.9	100	7.0	14.75	6.33	0.340	c
Hipparcos	I_c	—	100	<5.0	—	>13.5	—	d
VISTA	J	0.9	100	12.0	20.25	0.85	<0.010	e
2MASS	J	2.5	100	4.0	16.25	19.3	0.287	f

[a]Considering an area of 0.7° radius.
References: (a) This work; (b) Downes et al. (2014); (c) Zacharias et al. (2013); (d) Perryman et al. (1997); (e) Petr-Gotzens et al. (2011); (d) Skrutskie et al. (2006)

IMF in Section 2.4.2.1. To obtain the I_c magnitudes from UCAC4 we used the empirical transformations by Jordi et al. (2006), which relate SDSS photometry with other photometric systems included the Cousins system. For the DECam photometry we derived directly from our data color-dependent transformations to convert the calibrated DECam magnitudes to the SDSS system and then to the Cousins system. The RMS we obtained when comparing the I_c magnitudes from the CDSO and those from UCAC4 and from DECam after the transformation are 0.07 and 0.04 mag, respectively. The details about these transformations are described in Appendix B.2. Because the Cousins photometric system is already used by the CDSO and *Hipparcos* catalogs, after the transformation of the DECam and UCAC4 photometries, the complete sample of optical observations are all in the same photometric system.

2.2.5.2 Photometric uncertainties

Before we define the brightness ranges where each catalog will be used, we fitted exponential functions to the photometric uncertainties of the optical and NIR catalogs with respect to the magnitude ($\delta I_c(I_c)$ for the optical data and $\delta J(J)$ for the NIR data). This way we can estimate the uncertainties of the data as a function of the photometric magnitudes, which will allow us to combine the catalogs considering the typical photometric uncertainties at each brightness point where the catalogs are joined. In Figure 3 we show the photometric uncertainties of the catalogs we used and in Table 3 we list the parameters of the functions fitted to these uncertainties working with magnitudes inside their saturation and completeness limits (see Section 2.3.2.2).

2.2.5.3 Cutoffs and merged catalogs

The brightness ranges where each photometric catalog was used are related to their photometric sensitivities, which are described in Section 2.3.2.2 and reported in Table 2. The I_c-band photometry we used to have a combined optical catalog are as follows: *i*) UCAC4 for $I_c < 13.0 + \delta I_c(13.0)$, *ii*) CDSO for $13.0 - \delta I_c(13.0) \leq I_c < 17.0 + \delta I_c(17.0)$, and *iii*) DECam for $I_c \geq 17.0 - \delta I_c(17.0)$. We also added 25 stars (including 25 Ori) from the *Hipparcos* catalog, which are too bright to have I_c magnitudes from UCAC4. The J-band photometry used to have a combined NIR catalog are as follows: *i*) 2MASS for $J < 13.0 + \delta J(13.0)$, and *ii*) VISTA for $J \geq 13.0 - \delta J(13.0)$. Then, we removed 3″ duplicates from the optical and NIR catalogs and kept the sources with smaller photometric uncertainties. To join the optical and NIR catalogs we did a cross-match between

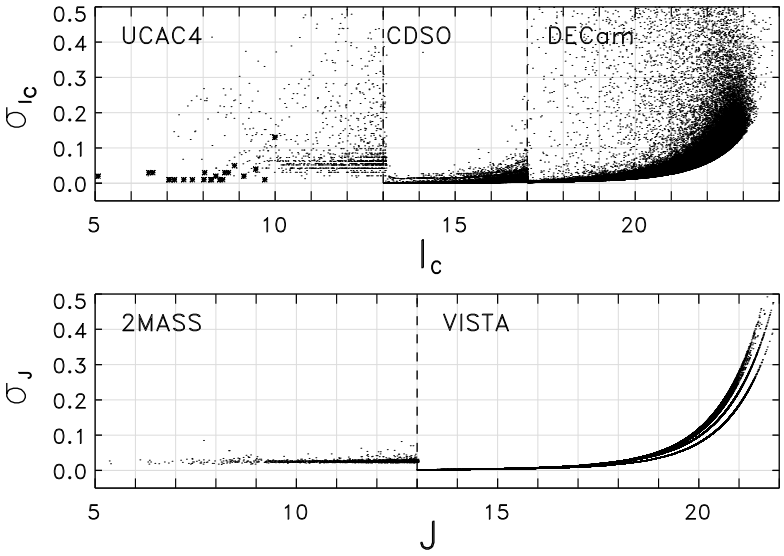

Figure 3: Photometric uncertainties as a function of magnitude for the merged optical (top) and NIR (bottom) catalogs. The labeled names indicate the catalogs used in each magnitude range separated by the dashed lines. The few *Hipparcos* sources in the optical catalog are indicated by the asterisks.

Table 3: Parameters of the exponentials fitted to the photometric uncertainties of the optical and NIR catalogs used in this study.

Catalog	**Photometric Band**	a	b	c
DECam	I_c	0.005	25.861	1.042
CDSO	I_c	0.002	22.175	0.999
UCAC4	I_c	0.037	8.993	0.453
VISTA	J	0.002	16.870	0.732
2MASS	J	0.024	20.240	1.105

Note. The exponentials have the form $f(x) = a + e^{(cx-b)}$, where x is the magnitude in the corresponding photometric band.

them with a tolerance of 3″ using STILTS[4] (Taylor, 2006).

The final optical and NIR catalog has 110527 detections inside an area of 1.1° radius in 25 Ori, being most of them (about 85%) from the DECam and VISTA catalogs.

2.3 Selection of Photometric Candidates

2.3.1 PMS Locus

The use of color-magnitude diagrams (CMDs) combining optical and NIR data has been successfully tested for identifying young stellar objects (e.g. Downes et al., 2014, and references therein). We selected photometric member candidates from the merged optical and NIR catalog according to their position in the I_c vs $I_c - J$ diagram shown in Figure 4.

To define the PMS locus in which the member candidates lie, we plotted a large set of 355 spectroscopically confirmed low-mass members of 25 Ori from Briceño et al. (2005, 2007); Downes et al. (2014); Suárez et al. (2017c); Briceño et al. (2019) and 15 spectroscopically confirmed BD members of 25 Ori and Orion OB1a from Downes et al. (2015). Most of these members were

[4] http://www.star.bris.ac.uk/~mbt/stilts/

confirmed through similar spectroscopic procedures, which makes the sample more homogeneous. Additionally to the confirmed members, we also plotted 38 highly probable intermediate/high-mass members from Kharchenko et al. (2005). The final sample of 408 spectroscopically confirmed members and highly probable members covers the spectral type range from B2 to M9 and trace a clear sequence in the I_c vs $I_c - J$ diagram. This sequence corresponds to the empirical isochrone of 25 Ori, which was defined averaging the $I_c - J$ colors per I_c-bin (red dashed curve in Figure 4). The resulting empirical isochrone is roughly consistent with the PARSEC-COLIBRI and BT-Settl 7 Myr isochrones, confirming the 25 Ori age (6.1±2.4; Briceño et al., 2019, and references therein). This empirical isochrone was our starting point to define the PMS locus considering the following uncertainties and effects:

i) *Distance uncertainty.* From the sample of spectroscopically confirmed members of 25 Ori by Briceño et al. (2005, 2007); Downes et al. (2014, 2015); Suárez et al. (2017c); Briceño et al. (2019), we obtained a mean distance of 356 pc with a standard deviation, σ, of 47 pc, considering the distance estimates we calculated from the Gaia parallaxes (Gaia DR2; Gaia Collaboration et al., 2018) with uncertainties of $\leq 20\%$ using the method implemented by Bailer-Jones (2015) and Bailer-Jones et al. (BJ18; 2018), as explained in Appendix B.3.1. Then, we broaden vertically the edges of the PMS locus in the CMD by adding the 1-σ uncertainty in distance, which corresponds to upwards and downwards offsets of 0.31 and 0.27 mag, respectively.

ii) *Age uncertainty.* To estimate the change in the I_c brightness (ΔI_c) as a function of the $I_c - J$ color due to the uncertainty of the 25 Ori age (6.1±2.4 Myr; Briceño et al., 2019, and references therein), we worked with the PARSEC-COLIBRI and BT-Settl isochrones. We obtained ΔI_c^I between the isochrone corresponding to the age of 25 Ori and that for the 25 Ori age minus the error. Similarly, we obtained ΔI_c^{II} considering the age of 25 Ori and the age plus the error. In most of the color range considered (-0.5-4.5 mag), ΔI_c^I is larger than ΔI_c^{II}. We used ΔI_c^I to move upwards the upper edge of the locus and ΔI_c^{II} to move downwards the lower edge.

iii) *Unresolved binarity.* According to Briceño et al. (2007), the observed spread in the CMD of young stars in the 25 Ori field is roughly consistent with the upper limit of 0.75 mag expected from unresolved binaries. Thus, we used this limit to move upward the upper edge of the locus.

iv) *Mean intrinsic variability.* We characterized the I_c-amplitude variations as a function of the magnitude for the 25 Ori member candidates from Downes et al. (2014) using the CVSO catalog. These amplitude variations increase with the I_c magnitudes from 0.2 to 0.9 mag in the brightness range between 13.0 to 19.0 mag. For brighter and fainter I_c magnitudes we assumed these minimum and maximum variation limits, respectively. Thus, we used these I_c-amplitude variations to move upwards and downwards the upper and lower edges of the locus, respectively. For the J-band, Scholz et al. (2009) reported the low-level amplitude variations of about 0.2 mag for young LMSs and BDs. Assuming that when occurs a maximum or a minimum in the I_c-brightness of a variable source also takes place the maximum or minimum in the J-band brightness, we considered $I_c - J$ amplitude variations as the difference between the I_c-amplitude variations and the representative 0.2 mag variations in the J-band to move leftwards and rightwards the blue (lower) and red (upper) edges of the locus, respectively.

v) *Photometric uncertainties.* We considered the exponentials fitted to the uncertainties of the optical and NIR catalogs as a function of the magnitudes to move both edges of the locus. The upper and lower edges were moved upwards and downwards, respectively, according to the uncertainty corresponding to each I_c-magnitude of the optical catalogs used in the different ranges. The blue (lower) and red (upper) edges of the locus were moved leftwards and rightwards, respectively, considering the uncertainties added in quadrature for each I_c and J-magnitude from the catalogs used in the different ranges.

The sources lying inside this resulting PMS locus were selected as photometric member can-

Table 4: List of photometric member candidates used in this study.

ID	α_{J2000}	δ_{J2000}	I_c	eI_c	J	eJ	H	eH	K	eK	Source I_c	Source JHK	Ref
25Ori_1	81.186774	1.846467	5.08	0.02	5.349	0.027	5.417	0.027	5.355	0.02	Hipparcos	2MASS	b
25Ori_20	81.208733	0.766291	8.569	0.217	8.761	0.026	8.805	0.055	8.826	0.019	UCAC4	2MASS	c
25Ori_734	81.166427	1.361305	13.384	0.001	12.278	0.023	11.609	0.022	11.436	0.026	CDSO	2MASS	g
25Ori_898	81.664442	1.20085	14.309	0.001	13.008	0.002	12.399	0.002	12.187	0.002	CDSO	VISTA	k
25Ori_1642	81.243645	1.733347	20.154	0.032	17.358	0.012	16.762	0.012	16.241	0.025	DECam	VISTA	i
25Ori_1685	80.573212	1.435463	22.602	0.137	19.257	0.055	18.442	0.06	18.108	0.075	DECam	VISTA	p

References:
(a) Briceño et al. (2005); spectroscopically confirmed members.
(b) Hernández et al. (2005); member candidates using kinematic and photometric data.
(c) Kharchenko et al. (2005); highly probable candidates.
(d) Kharchenko et al. (2005); low-probability candidates.
(e) Briceño et al. (2007); spectroscopically confirmed members.
(f) Hernández et al. (2007b); member candidates using infrared and optical photometric data.
(g) Downes et al. (2014); spectroscopically confirmed members.
(h) Downes et al. (2014); photometric member candidates using optical and NIR data.
(i) Downes et al. (2015); spectroscopically confirmed members.
(j) Downes et al. (2015); sources rejected as members.
(k) Suárez et al. (2017c); spectroscopically confirmed members.
(l) Suárez et al. (2017c); sources rejected as members.
(m) Kounkel et al. (2018); highly problable members using kinematic data.
(n) Kounkel et al. (2018); candidates from Cottle et al. (2018) rejected as members.
(o) Briceño et al. (2019); spectroscopically confirmed members.
(p) This work.

(This table is available in its entirety in machine-readable form.)

didates of 25 Ori. We selected 1694 candidates inside the DECam FOV having I_c magnitudes from 5.08 to 23.3 mag. In Table 4 we provide the list of our member candidates together with the optical and NIR photometry used in this study after removing potential extragalactic sources in Section 2.3.2.4. We also included in this table the corresponding citation for the cases when a candidate has been studied in previous contributions.

The locus defined this way contains about 95% of the confirmed members and highly probable members of 25 Ori. From the members lying out, on the left side, of the PMS locus, about 75% of them have $> 99\%$ probability of being variable stars in the CVSO. In Section 2.3.2.8 we estimated that the fraction of 25 Ori members we can lose in our photometric selection is $\sim 3.1\%$.

It is important to notice in Figure 4 that in the I_c range roughly between 9 and 13 mag, the giant and subgiant branches cross the PMS locus, which increases the contamination by these sources in this brightness range. We discussed in Section 2.3.2.3 how to deal with this contamination.

2.3.2 Sources of Uncertainty, Contamination and Biases

Several previous works have studied the uncertainties and biases implicit in the observational determination of the IMF (e.g. Moraux et al., 2003, 2007a,b; Ascenso, 2011; Bayo et al., 2011; Jeffries, 2012; Dib et al., 2017). In this section we characterize these effects in the case of 25 Ori and show how we corrected them.

2.3.2.1 Spatial Completeness

The CDSO and VISTA catalogs and all the public catalogs considered in this work have a full spatial coverage of the FOV of the DECam observations.

As explained in Section 2.2.1, our DECam observations were obtained with an array of 60 detectors configured as shown in Figure 2 (brown boxes), therefore, part of the area in a FOV is lost by the gaps and because the array is not circular. To compute what fraction of a FOV

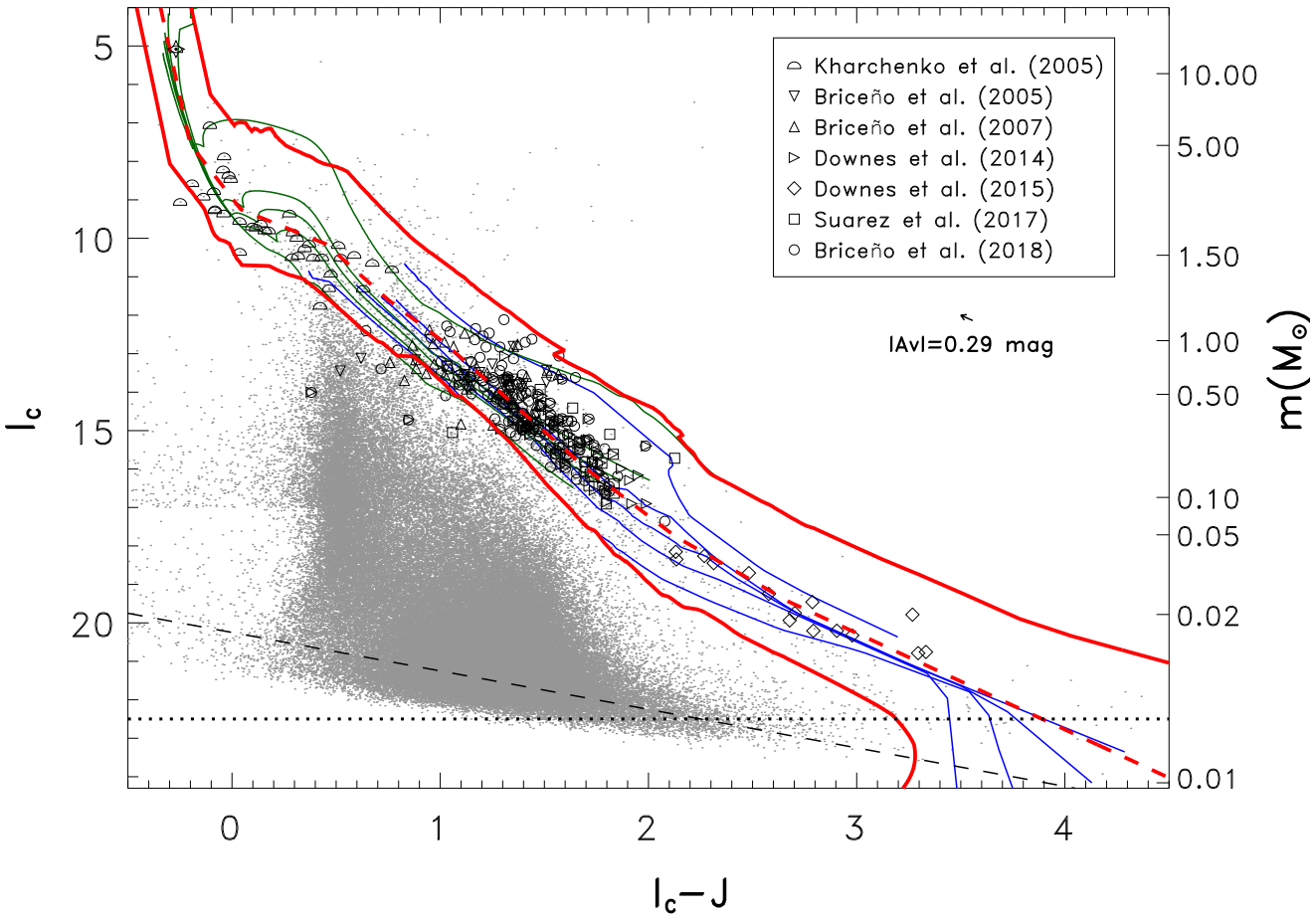

Figure 4: CMD used for the selection of photometric member candidates of 25 Ori. The red solid curves show the PMS locus defined considering the empirical isochrone (red dashed curve) and several issues that may affect the position of the sources in this plot. The open symbols represent the known spectroscopically confirmed members (Briceño et al., 2005, 2007; Downes et al., 2014, 2015; Suárez et al., 2017c; Briceño et al., 2019) and high-probable members (Kharchenko et al., 2005) of 25 Ori, as shown in the label, which trace the empirical isochrone. The gray dots indicate all the detections in our combined optical and NIR catalog. The black dotted and black dashed lines show the I_c/DECam and J/VISTA completeness magnitudes, respectively. The blue and green curves indicate, respectively, the BT-Settl and PARSEC-COLIBRI isochrones for ages, from top to bottom, of 1, 5, 7, 10 and 20 Myr. The arrow shows the dereddening vector for the mean extinction of 25 Ori. The right axis indicates the corresponding masses from the PARSEC-COLIBRI 7 Myr isochrone for $m > 1$ $M_\odot$ and from the BT-Settl 7 Myr isochrone for lower masses, considering a distance of 356 pc and a visual extinction of 0.29 mag. The giants and subgiants branches cross the PMS locus close to (0.9, 13) and (0.5, 11), respectively.

is covered by the DECam data, we used the Monte Carlo method to generate a list of sources randomly distributed inside the FOV and counting those lying inside the detectors. We found this way that for the DECam FOV, the DECam data cover ≈ 70% of the area. If we consider the previously estimated areas of 25 Ori, the DECam observations have a coverage of ≈ 79% when considering Briceño et al. (1.0° radius; 2005, 2007) and ≈ 86% when considering Briceño et al. (0.7° radius; 2019) or Downes et al. (0.5° radius; 2014). These fractions will allow us to correct the luminosity function (LF) and system IMF of 25 Ori by the spatial coverage of the DECam data

considering that the LMSs and BDs in 25 Ori do not present any preferential spatial distribution (see Section 2.4.4). In Table 2 we report the spatial coverage of 25 Ori for all the catalogs used in this study.

In Table 5 we list the number of member candidates inside the DECam FOV after applying the correction by the spatial coverage of the DECam data. If we had a full coverage of the DECam observations, we would expect 1782 photometric member candidates in the I_c range from 5.08 to 23.3 mag. The mass range corresponding to this brightness range is obtained in Section 2.4.2.2.

2.3.2.2 Photometric Sensitivity

The saturation and completeness magnitudes for the optical and NIR catalogs were determined, respectively, as the brightest and faintest magnitudes between which the logarithmic number of sources per magnitude bin do not deviate from a linear behavior. We estimated the masses corresponding to these magnitudes using the PARSEC-COLIBRI 7 Myr isochrone for $m > 1\ M_{\odot}$ and the BT-Settl 7 Myr isochrone for lower masses. In Table 2 we summarize these values, where we can see how the optical and NIR catalogs complement each other. Therefore, in the determination of the LF and system IMF of 25 Ori, for the sources more massive than the DECam completeness mass (0.012 M_{Jup}), it is not necessary to make any correction due to the photometric sensitivity of the catalogs.

2.3.2.3 Contamination by Field Stars

Though the use of optical-NIR CMDs allows a clear selection of young sources, a contamination of $\sim$ 20% by field stars is expected for the low-mass domain (Downes et al., 2014) and $\sim$ 30% for the very low-mass and BD regime (Downes et al., 2015) in our sample of photometric member candidates. Furthermore, a higher degree of contamination is expected in the intermediate-mass range of our candidate sample due to giant and subgiant stars.

We estimated the number of field stars inside the PMS locus following two procedures: First, by means of a simulation of the expected galactic stellar population using the Besançon Galactic model (hereafter BGM; Robin et al., 2003). Second, empirically, by a fiducial selection of photometric candidates from an observed control field with similar galactic latitude.

For the BGM approach we performed four simulations[5] in an area of 2x2 deg^2 in 25 Ori and considering the photometric uncertainties of our joined optical and NIR catalogs shown in Figure 3 and listed in Table 3. The simulated populations combined the optical and NIR photometric errors from UCAC4 and 2MASS (simulation 1), CDSO and 2MASS (simulation 2), CDSO and VISTA (simulation 3), and DECam and VISTA (simulation 4). Then, we joined the resulting simulations by keeping the sources brighter than $I_c = 13$ mag from simulation 1, the sources in the range 13 mag$\leq I_c <$15 mag from simulation 2, the sources with magnitudes 15 mag$\leq I_c <$17 mag from simulation 3, and sources with $I_c \geq 17$ mag from simulation 4. This way we have a simulated stellar population compatible with our observational joined optical-NIR catalog.

For the control field approach, we estimated the field star contamination in our candidate sample by means of direct counting on selected regions as follows: *i*) For the optical CDSO, UCAC4 and *Hipparcos*, and NIR 2MASS catalogs, we considered a control field of 1.0° radius FOV placed at the same galactic latitude of 25 Ori in a direction moving away from the Orion's Belt ($\alpha_{J2000} = 05^{\rm h}19^{\rm m}03^{\rm s}.6$ and $\delta_{J2000} = +04°18'17''.1$). *ii*) Since we do not have neither DECam nor VISTA specific observations in this region, we used for these catalogs the areas of the eight north-westernmost and westernmost detectors of the DECam array as control fields, because a)

[5] http://model2016.obs-besancon.fr

they mostly lie outside the larger estimated area of 25 Ori, b) they have the lesser number of Orion OB1a reported members (Briceño et al., 2019; Kounkel et al., 2018) and c) the density of LMS and BD candidates in the regions covered by these detectors falls to about 10% of the density in the 25 Ori core (Downes et al., 2014). Then, we joined all the photometric catalogs from both control fields in the same way we did for the 25 Ori observations.

We applied our procedure for selecting photometric member candidates to the BGM and control field samples in order to account the sources lying inside the PMS locus, which we defined as contaminants. The number of contaminants in both samples are consistent for magnitudes brighter than $I_c \sim 17$ mag, as discussed in Section 2.4.1. In Table 5 we list the number of member candidates and contaminants after applying the spatial coverage corrections for the DECam data as well as their complete brightness and mass ranges. Using the control field we estimated that the fraction of contaminants present in our candidate sample, in the I_c brightness range between 13 and 20 mag, is about 30%, which is somewhat higher than the 20% estimated, and spectroscopically proven, by Downes et al. (2014) in the same brightness range for their candidate selection working with similar CMDs but using a narrower PMS locus. In Section 2.3.3 we compared both samples.

As mentioned in Section 2.3.1 and shown in Figure 4, there is a high contamination by giant and subgiant stars in the I_c range between ∼9 and ∼13 mag in our candidate sample. Even, the contaminants estimated by the control field or the BGM can be as numerous as the member candidates in this particular brightness range, which do not allow us to remove the contamination in this range using only the control field or BGM. Fortunately, we can take advantage of Gaia DR2 because about 92% of the candidates brighter than $I_c = 13$ mag have parallaxes with errors of $\leq 20\%$. The same fraction is obtained for candidates with brightness up to about 17.5 mag, but for fainter sources Gaia DR2 starts presenting significant incompleteness issues. Thus, we did a subset of the member candidates with $I_c < 17.5$ mag and having distances and proper motions within 3-σ of the mean values of 25 Ori (356±47 pc and $\mu_\alpha = 1.33 \pm 0.46$ mas yr^{-1} and $\mu_\delta = -0.23 \pm 0.55$ mas yr^{-1}; see Appendix B.3). Additionally, we removed the sources with deviant radial velocities (<15 km s^{-1} or >40 km s^{-1}; Briceño et al., 2007) from Kounkel et al. (2018). With these criteria we recover about 90% of the confirmed members. Hereafter, we are going to refer to this subset of highly probable 25 Ori members as the filtered sample of candidates.

From the member candidates in the I_c brightness range between 9 and 13 mag, only ≈11% of them satisfy the distance and proper motion criteria. About 70% of the sources contaminating this brightness range and having parallax errors of $\leq 20\%$ have distances significantly larger than those of the 25 Ori members. Thus, we checked that these contaminants are, in fact, giant or subgiant stars, as predicted by the BGM.

Field stars are the main, but not the only, contamination present in our candidate sample. After applying the correction for the DECam spatial coverage, we have only one BGM contaminant fainter than $I_c = 19.6$ mag, while there are about 32 contaminants using the control field in the same brightness range. As the BGM does not include extragalactic sources, this difference between the contaminants counted in both samples suggests that most of the contamination present in the faintest range of our candidate sample is due to extragalactic sources.

2.3.2.4 Contamination by Extragalactic Sources

As 25 Ori is out of the galactic plane ($b = 18.4°$) and has a low visual extinction of 0.29±0.26 mag, we expect extragalactic sources in any deep photometric sample in that direction. We suggest in the previous section that the contamination by extragalactic sources dominates the contamination in the faintest range of our member candidate sample. To remove the most likely extragalactic sources from this sample we used the $J - K$ vs $Z - J$ color-color diagram shown in Figure 5. We

Table 5: Number, I_c brightness and mass ranges of the member candidates and contaminants in an area of 1.1° radius in 25 Ori after correcting by the spatial coverage of the DECam data.

Origin	**Number of Sources**	I_c **Range** (mag)	**Mass Range** ($M_\odot$)
25 Ori FOV	1782	5.08-23.3	0.011-13.1
Control Field FOV	1030	6.51-23.3	0.011-7.74
BGM	840	7.67-19.6[a]	0.021[a]-4.76

[a]There is a fainter dwarf star contaminant with $I_c = 23.5$ (0.011 $M_\odot$).

plotted a sample of ≈ 500 spectroscopically confirmed galaxies and quasars in the direction of 25 Ori with I_c-brightness between 13.5 and 20.0 mag from Suárez et al. (2017c). Also, we plotted our member candidates and the previously confirmed members of 25 Ori. Similarly to what we did for the CMD, we defined the empirical isochrone traced by the low-mass and BD confirmed members. Then, we defined the sequence centered on this isochrone and containing over 90% of the confirmed members. This sequence is clearly distinct from the region where are located more than 80% of the galaxies and quasars. About 1% (7 sources) of the member candidates plotted in this color-color diagram (those having VISTA photometry) lie in the region defined by the galaxy/quasar sample and have I_c magnitudes between 15.2 and 18.2 mag. We considered these 7 sources as contaminants and removed them from our member candidate sample, keeping the rest of the candidates selected in the CMD. The resultant sample has 1687 member candidates and is provided in Table 4. This is the list of candidates we used to derive the LF and system IMF of 25 Ori in Sections 2.4.1 and 2.4.2, respectively.

We used a similar color-color diagram to that in Figure 5 to remove potential extragalactic sources present in the contaminants from the control field.

In Figure 5, only four (∼1%) of the spectroscopically confirmed members lie in the region where most of the galaxies and quasars are located. Two of these peculiar members are classical T-Tauri stars (CTTSs) harboring circumstellar disks and having an intense H_α emission (41 and 53 Å; Suárez et al., 2017c), while the other two have low H_α emission, one being a CTTS and the other one a weak T-Tauri star (WTTS; Briceño et al., 2007). These four members are highly probable to be variable stars according to the CVSO, which could explain their position in the color-color diagram.

After we removed from our member candidate sample and from the control field contaminants the potential extragalactic sources, we used the control field to statistically remove the extragalactic and galactic contamination from the LF and system IMF of 25 Ori in Section 2.4.1 and 2.4.2.

2.3.2.5 IR excesses

Possible excesses in the J-band, due to disks, can bias the candidate selection because members showing such excesses could lie outside, on the red side, of the PMS locus. In Figure 4 there are 60 sources lying on the right side of the PMS locus, which have $I_c < 12.7$ mag. The simulations performed with the BGM show that the positions of these sources are consistent with those of giant stars. Additionally, we checked the distances of these sources and compared them with the currently estimated 25 Ori distance. 97% of the sources having parallaxes with errors of ≤ 20 per cent have distances not consistent with those of the 25 Ori members, of which most of them

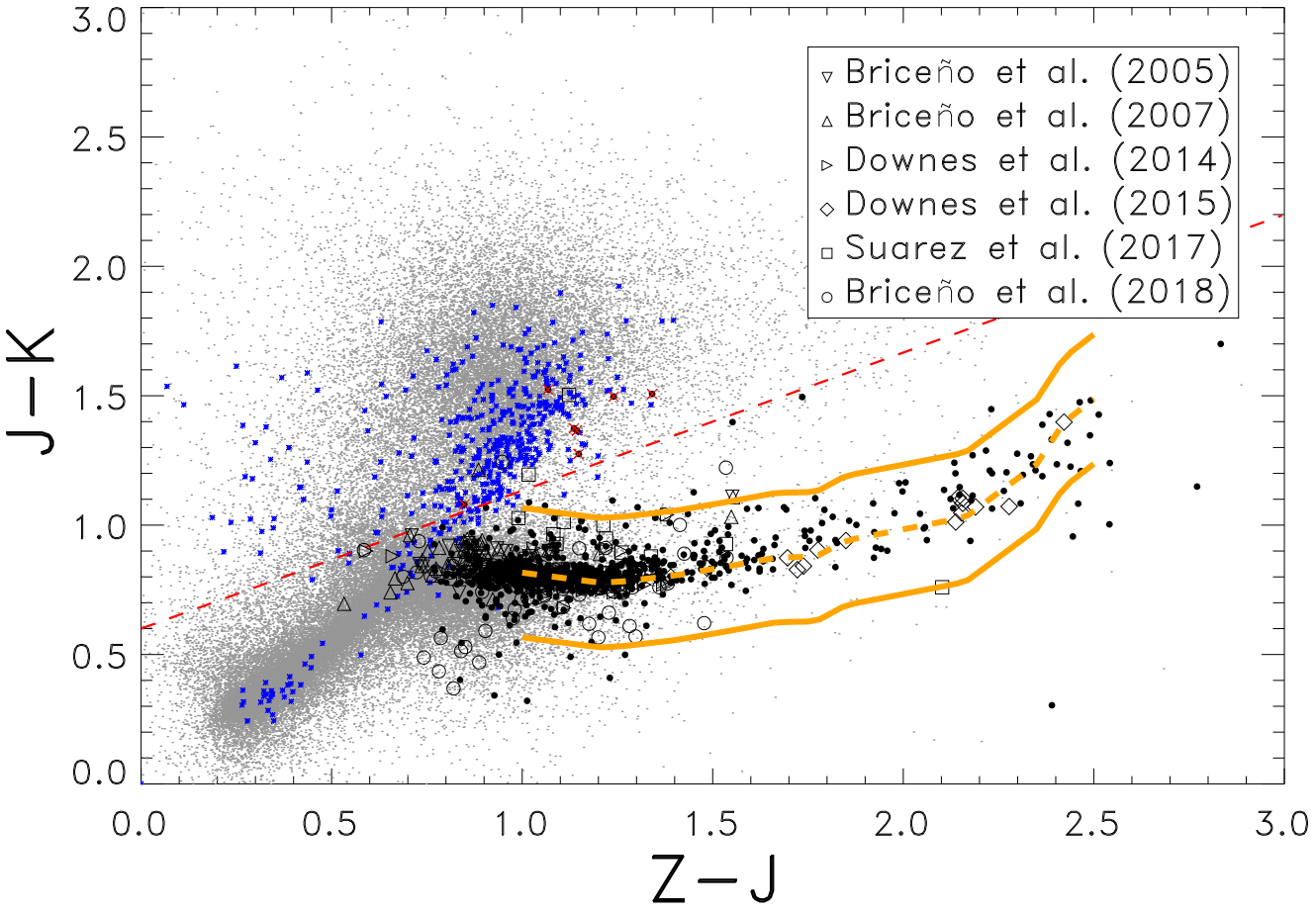

Figure 5: Color-color diagram used to remove highly probable extragalactic contaminants (red crosses) from our member candidate sample (black dots). The blue asterisks represent a sample of spectroscopically confirmed galaxies and quasars in the direction of 25 Ori (Suárez et al., 2017c). The red dashed line separates more than 80% of the sample of extragalactic sources from the member candidates. The orange dashed curve shows the empirical isochrone traced by the low-mass and BD confirmed members of 25 Ori by the studies indicated in the label, which are mostly contained in the sequence defined by the orange solid curves. The gray dots are the same as in Figure 4.

(91%) have larger distances, suggesting these are, in fact, giant stars. Only two sources have distances consistent with 25 Ori, but these sources have unexpected photometric uncertainties from the UCAC4 catalog (0.146 and 0.234 mag), which could explain, in part, their location in the CMD. Thus, most of the sources left out, on the red side, of the PMS locus are behind the 25 Ori population, indicating that in our photometric selection we do not lose 25 Ori members due to the presence of IR excesses.

Additionally, if the magnitudes used to obtain the masses were affected by the IR excesses, the masses could be overestimated. However, at the age of 25 Ori, only a fraction of ∼5% of the LMSs harbor circumstellar disks (Briceño et al., 2005, 2007; Hernández et al., 2007b; Downes et al., 2014; Briceño et al., 2019), which produce IR excesses starting at the $WISE$ 3.4 μm band or longer wavelengths (Suárez et al., 2017c). Even for the BDs in 25 Ori, which have a larger disk fraction of $\sim$ 30%, the IR excesses start beyond the K-band (Downes et al., 2015). In this study we used the I_c and J-band magnitudes which are not expected to be affected by IR excesses. In any event, we

worked with the I_c magnitudes to estimate masses to avoid any overestimation due to IR excesses.

2.3.2.6 Effects of Chromospheric Activity

Active LMSs suppress the effective temperature (T_{eff}) by $\sim$ 5% and inflate the radius by $\sim$ 10% with respect to inactive objects (e.g. López-Morales, 2007). These effects roughly cancel themselves, which preserves the bolometric luminosity (Stassun et al., 2012).

Due to the effective temperature suppression, the masses of active LMSs estimated from the Hertzsprung-Russell (H-R) diagram are underestimated, but if masses are estimated from luminosities (or absolute magnitudes), the effect would be much smaller (Jeffries et al., 2017). According to Stassun et al. (2012), when the effective temperature is used to estimate masses from model isochrones, the resultant masses are systematically lower than the true masses by factors of ~ 3 and ~ 2 for LMSs and BDs with intense chromospheric activity of $\log L_{H_\alpha}/L_{bol} = -3.3$, respectively. This level of chromospheric activity corresponds to the saturation limit in young LMSs, which separates the CTTSs from WTTSs (Barrado y Navascués & Martín, 2003). For LMSs and BDs with low levels of magnetic activity ($\log L_{H_\alpha}/L_{bol} = -4.5$), the masses estimated using the effective temperature are systematically lower than true values by factors of ~ 2 and ~ 1.5, respectively. Instead, when masses are estimated using the bolometric luminosities derived from the K-band absolute magnitudes and considering model isochrones, the resulting masses are $\sim$ 5% smaller than true values for LMSs and BDs with high chromospheric activity and roughly unaffected for LMSs and BDs with low chromospheric activity (Stassun et al., 2012). This small bias is introduced by the effective temperature dependence of the bolometric corrections that Stassun et al. (2012) used to convert absolute magnitudes to bolometric luminosities.

In our case, as explained in Section 2.4.2.1, we used absolute magnitudes and model isochrones to obtain the masses of the member candidates which, according to Stassun et al. (2012), minimize the underestimation bias of masses of active stars introduced when the bolometric luminosities of the models are transformed to absolute magnitudes. Additionally, the fraction of active stars in 25 Ori is $\sim$ 5% (Briceño et al., 2005, 2007; Hernández et al., 2007b; Downes et al., 2014; Briceño et al., 2019). Considering the expected $\sim$5% underestimation of masses for the expected $\sim$5% of active stars in our candidate sample, we estimated that the change in the system IMF of 25 Ori is smaller than the Poisson noise of the distribution.

2.3.2.7 Spatial Resolution and Binaries

Most of the mass distributions of stellar clusters available in the literature do not take into account unresolved binaries or multiple systems and are, in fact, the system IMFs (e.g. Table 1 and Bastian et al., 2010).

A revision and treatment of the effect of unresolved binary systems in the IMF parameterization is found in Mužić et al. (2017). They found that the mass distribution becomes steeper in the low-mass and high-mass sides when correcting the system IMF by binary systems to obtain the single-star IMF, but the changes in the slopes agree within the uncertainties. A similar effect on the IMF due to binary systems is reported in Kroupa (2001).

In this study we reported the system IMF of 25 Ori, which will allow us to directly compare it with all the system IMFs in Table 1, assuming that the binarity properties are similar for these populations and a similar spatial resolutions of the data used in the different studies. The conversion of the 25 Ori system IMF to the single-star IMF is beyond the scope of this study.

2.3.2.8 Estimation of the Missed Members

As explained in previous sections, in our estimation of the system IMF we corrected the possible over-counting of individual stars and/or stellar systems belonging to 25 Ori by considering several sources of contamination in the photometric sample. An additional improvement of our procedure is to estimate possible under-counting of members by estimating the number of 25 Ori individual stars and/or stellar systems that could lie outside the PMS locus defined in the CMD.

We made this estimation through a simple simulation of the expected distribution of the cluster members in the I_c vs $I_c - J$ diagram and computing the fraction of these that falls outside the PMS locus. The simulation was performed as follows, in which we refer as *synthetic members* to those individual stars and/or stellar systems obtained from a realization of the system IMF:

(*i*) We made a random realization of the 25 Ori system IMF by drawing masses for 1000 synthetic members from a lognormal distribution with $m_c = 0.31$ and $\sigma = 0.46$. These parameters matches the resulting system IMF that will be discussed in Section 2.4.2.3.

(*ii*) The I_c and J-band absolute magnitudes of each synthetic member were computed by interpolating their masses into the mass-luminosity relation using the 7 Myr isochrones of BT-Settl and PARSEC-COLIBRI, as explained in Section 2.4.2.1.

(*iii*) The absolute magnitudes were converted into apparent magnitudes by adding the distance moduli and the corresponding extinctions. The distances and visual extinctions were generated for each synthetic member by creating random realizations considering the inversion of the cumulative distributions of the distances from the Gaia DR2 parallaxes and visual extinctions from spectroscopically confirmed members of 25 Ori (see Figure 42). Visual extinctions were converted into extinctions in I_c and J bands through the Rieke & Lebofsky (1985) extinction law with R_V=3.02.

(*iv*) We randomly labeled 25% of the synthetic members as photometrically variables in both I_c and J bands. To each of the variables we assigned a variation, ΔI_c, drawn at random from a normal distribution with zero mean and standard deviation, σ_{I_c}, equal to 0.3. The fraction of variables as well as σ_{I_c} were obtained by matching the catalog of member candidates with the CVSO, which includes stars and BDs with K and M spectral types. A total of 840 candidates (∼50% of the candidate sample) fainter than $I_c = 13$ mag (saturation of the CVSO) have a counterpart in the CVSO and we considered as variable the 220 candidates having a probability $> 99\%$ of being variables in the I_c-band. The J-band variation was computed by multiplying the ΔI_c by the ratio between the amplitude variations in the I_c and J-bands from Scholz et al. (2009). Both variations were added to the corresponding apparent magnitudes computed in (*iii*).

(*v*) We assumed no IR excesses in the J-band because at the 25 Ori age they are observed at larger wavelengths, as explained in Section 2.3.2.5.

(*vi*) Finally, we simulated the photometric uncertainties in the I_c and J-bands by adding to the corresponding apparent magnitude a random error based on an estimation of the photometric errors present in our data. Such estimations were obtained through the fit we did to the mean errors as a function of the mean magnitudes and a fit of the standard deviation of errors as a function of the mean magnitude. Then, for each source, the final apparent magnitude is computed by extracting a magnitude from a normal distribution which is centered at the mean apparent magnitude resulting from (*v*) with a standard deviation equal to the standard deviation of errors that corresponds to such mean apparent magnitude.

We generated 1000 random realizations of the cluster and obtained that a mean fraction of $\sim 3.1\%$ of the synthetic members fall outside the PMS locus, with most of them ($\sim 3.0\%$) lying on the left side and mainly having I_c magnitudes between 13 and 17 mag. This preferential loss of members does not represent an issue in our system IMF determination because corresponds to changes contained within the uncertainties. We found that this fraction and distribution are

consistent with the fraction of confirmed members lying outside the PMS locus shown in Figure 4. In Figure 6 we show the result of a characteristic simulation.

Through the variation of the input parameters within values representative of 25 Ori, we found that the main effects that can move synthetic members outside the PMS locus is the photometric variability. As expected, within reasonable values, the system IMF parameters m_c and σ do not affect the number of synthetic members falling outside the PMS locus, so our estimation of the under-counting is not affected by the assumed system IMF.

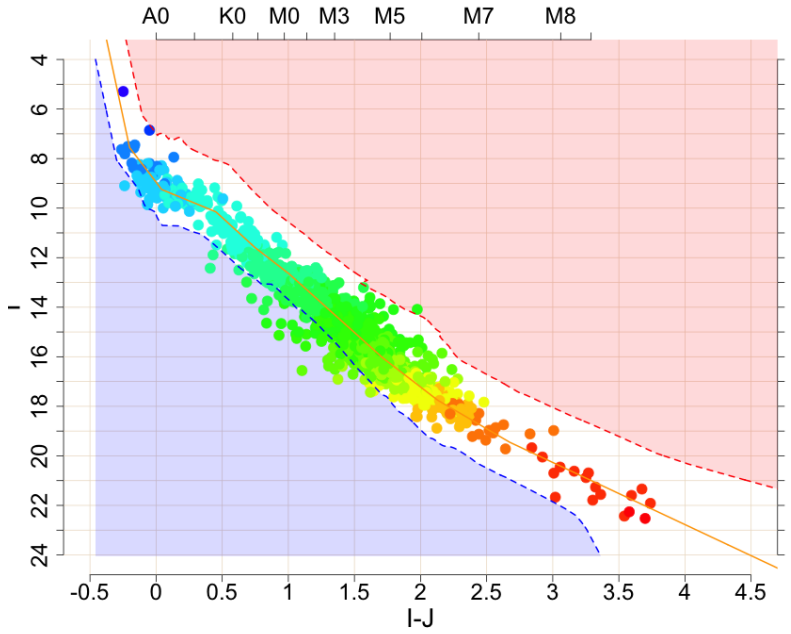

Figure 6: Simulated I_c vs $I_c - J$ diagram for the estimation of the number of members missed by our candidate selection procedure. Dashed lines indicate the PMS locus and solid line the empiric isochrone. The colored scale indicates the mass of the synthetic members.

2.3.3 Resulting Sample of Member Candidates

The resultant sample selected from the PMS locus in the CMD and after removing potential extragalactic contaminants in the color-color diagram has 1687 photometric member candidates with I_c magnitudes between 5.08 and 23.3 mag ($0.011 - 13.1\ M_{\odot}$) and covering an area of 1.1° radius in 25 Ori. The completeness of this sample is at $I_c = 22.5$ mag ($12\ M_{Jup}$) and the brightest sources in 25 Ori are also included. For a statistical removal of the field star and extragalactic contaminants in this sample, when constructing the LF and system IMF in Sections 2.4.1 and 2.4.2.2, respectively, we used the control field and, as a comparison for the galactic contamination, the BGM. The contamination present in our sample depends of the brightness range but it can be roughly characterized into three ranges. The extragalactic contamination starts to be significant for I_c magnitudes fainter than ∼17 mag. For the bright I_c range, between ∼9 to 13 mag, there is a high level of contamination by giant and subgiant stars (reason why we applied distance and proper motion criteria to filter the sample). In the brightness range between these kind of contaminants, the PMS population is clearly distinguished from the old dwarf stars and the contamination decreases. We estimated, using the control field and/or the BGM, a contamination of ∼ 20% in our sample in the range between 13 and 17 mag. Actually, in this brightness range is where most of the 25 Ori members has been spectroscopically confirmed, as shown in Figure 4.

With our sample we confirmed the low stellar density in 25 Ori. We obtained values between 8.6 and 4.8 stars pc^{-3} for areas with radii between 0.5 and 1.0, while the substellar density ranges from 1.3 to 0.7 BDs pc^{-3} for the same areas, considering the 25 Ori distance estimated in this study

and assuming a spherical group. This stellar density values are roughly consistent with Briceño et al. (2007); Downes et al. (2014); Briceño et al. (2019).

We compared our candidate sample with the candidate selection done by Downes et al. (2014) using a similar procedure and the CDSO and VISTA catalogs. Their sample includes candidates with masses in a smaller range ($0.02 \leq M/M_{\odot} \leq 0.80$) but covering a larger area (about 3x3 deg^2 around 25 Ori). If we consider the same area as in the present work, there are about 750 candidates in their selection. Our sample contains 924 member candidates in the same mass range and includes 91% of their candidates. From the remaining 9% not included in our sample and with $I_c > 17$ mag (brightness limit from which we used the DECam photometry), about 85% of them lie outside the DECam detectors, making it imposible to recover those sources in our selection. Thus, where we have full spatial coverage, we recover more than 97% of the member candidates by Downes et al. (2014) and, additionally, we reported 242 new candidates in the same mass range covered by their study. We estimated that the contamination in our candidate sample, in the I_c brightness range between 13 to 20 mag, is about 30%, which is somewhat higher than the 20% estimated and spectroscopically proven by them in their sample. This difference is due, mainly, because our PMS locus is somewhat wider.

2.4 Results and Discussion

2.4.1 Luminosity Function

In order to construct the LF we calculated the absolute magnitudes of the member candidates and contaminants considering they are real members of 25 Ori. This consideration allow us to analyze properties of the candidate sample as a whole, such as the LF and the system IMF after correcting the contamination effect.

The absolute magnitudes were obtained using our joined I_c-band catalog and, as only 18% of the candidates (those spectroscopically confirmed as members) have visual extinctions from previous studies and 86% of the sample has Gaia DR2 parallaxes with errors of $\leq 20\%$, we assigned distance and visual extinction values to the whole sample as follow: From a list of 334 spectroscopically confirmed members of 25 Ori (Briceño et al., 2005, 2007; Downes et al., 2014, 2015; Suárez et al., 2017c; Briceño et al., 2019), we constructed the normalized cumulative distributions of their distances and reported visual extinctions. Then, we used the inversion of these observed distributions to create random realizations to assign values of these parameters to each member candidate, even those already having parallaxes with errors of $\leq 20\%$ or visual extinctions from previous spectroscopic studies in order to have a sample with all values consistent with those of the 25 Ori members. A detailed explanation of this procedure is found in Appendix B.4. With these distances and extinctions, together with the I_c photometry, we computed the corresponding absolute magnitudes, M_{I_c}, for all the member candidates. We made 10^4 repetitions of this experiment in order to obtain a robust simulation, which produced 10^4 artificial distributions in the M_{I_c} range from -2.8 to 15.4 mag.

In a similar way we obtained 10^4 M_{I_c} magnitudes for each candidate in the filtered sample. The resultant M_{I_c} range of this subset is between -2.8 and 9.6 mag, assuming the distance and extinction of 25 Ori, and includes to the region mostly affected by giant and subgiant stars.

For the contaminants from the control field and BGM, we estimated their fiducial M_{I_c} magnitudes following the same procedure we used for the member candidates. This way, we can estimate the contamination in the M_{I_c} distribution of the member candidates to then obtain the LF.

Using the simulation just described, we constructed the 10^4 M_{I_c} distributions of the member candidate and contaminant samples. To correct each distribution by the DECam spatial coverage

factor explained in Section 2.3.2.1, we first made the M_{I_c} distributions of the sources from the DECam catalog and applied them the correction. Then, we added to these distributions those from the rest of the data.

With the 10^4 M_{I_c} distributions of the member candidate sample, we defined the distribution using the mean values and assigning uncertainties of 1-σ. The errors for the more massive bins, which do not have more than two candidates, are very small because these sources have similar M_{I_c} values for all the repetitions. For these bins we replaced the uncertaintites by the Poisson errors. In a similar way, we defined the distribution of mean values for the candidates in the filtered sample and for the contaminants. The resultant distributions of the contaminants from the control field and the BGM are consistent, within the uncertainties, for M_{I_c} magnitudes brighter than ~ 9 mag, even where the giant and subgiant stars lie, which indicates that the contamination in our sample in this range is due mainly to field stars. For fainter sources, a significant discrepancy arises between both samples of contaminants, which increases with the magnitude, suggesting the presence of extragalactic sources. We decided to work with the contaminants estimated from the control field because this also allow us to remove these extragalactic sources.

To the M_{I_c} distribution of the member candidates we subtracted the distribution of the contaminants from the control field and by adding the errors in quadrature. The resultant distribution is very consistent with that from the filtered sample, excluding the M_{I_c} interval ($\sim 1-5$ mag) that corresponds to the region presenting a high degree of contamination by giant and subgiant stars. This indicates that the adopted Gaia DR2 thresholds are well-suited. Thus, to obtain the LF of 25 Ori, in the distribution of the member candidates minus the contaminants from the control field we replaced the range $M_{I_c} > 5$ mag by the distribution of the candidates in the filtered sample.

In the procedure described above we worked with histograms (with bins of 1 mag) to construct the 25 Ori LF. Additionally, we built the continuous LF of 25 Ori using a kernel density estimate (KDE) and the M_{I_c} magnitudes computed in this section. We obtained the KDEs of the member candidates and contaminants using a bandwidth of 0.4 mag and an Epanechnikov kernel (Silverman, 1986). Similarly than for the case of histograms, we first obtained the KDE of the member candidates from the DECam catalog to apply the correction by the DECam spatial coverage. This KDE was normalized to the histogram of the member candidates at $M_{I_c} = 10.5$ mag. Then, we obtained the KDE of the rest of candidates normalized to the same histogram at $M_{I_c} = 7.5$ mag. These normalizations allow us to compare the KDEs directly with the histograms. Both KDEs were joined to obtain the KDE of the member candidates for each of the 10^4 repetitions of the experiment to assign the M_{I_c} magnitudes. Finally, we defined the KDE of the member candidates with the mean values over all the repetitions and assigned uncertainties of 1-σ. Similarly, we obtained the KDEs of the contaminants from the control field and of the candidates in the filtered sample. The final continuous LF of 25 Ori was obtained subtracting from the KDE of the member candidates the KDE of the contaminants and replacing the KDE of the filtered sample of candidates for $M_{I_c} > 5$ mag.

We constructed continuous and discrete LFs for different areas with radius between 0.5 and 1.1°. In Figure 7 we show the LFs for the 25 Ori estimated areas. These LFs have very similar morphologies, within the uncertainties, regardless the considered area. Also, the KDEs are very consistent with the histograms, specially where we have more than two counts ($M_{I_c} \sim 0-14$ mag).

2.4.2 System IMF

The main purpose of this study is to determine the system IMF of 25 Ori. Therefore, we need to estimate through a mass-luminosity relationship, the corresponding masses for our member candidates and contaminants under the consideration that both are true members of 25 Ori.

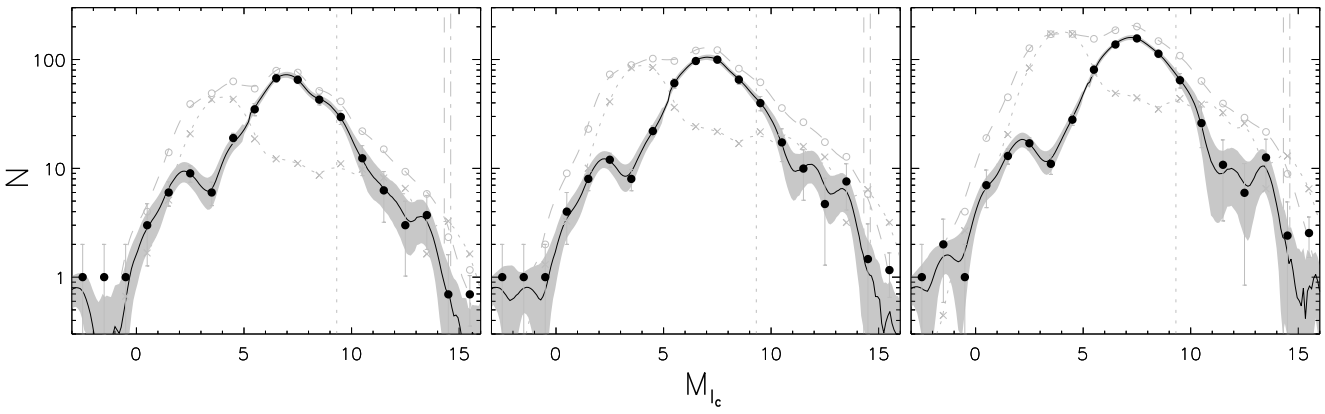

Figure 7: LFs of 25 Ori (black points and black solid curves) after correcting by the galactic and extragalactic contamination (gray crosses and dotted curves) in our member candidate sample (gray open circles and dashed curves) inside the 25 Ori estimated areas. The panels from left to right correspond to the 25 Ori area by Downes et al. (0.5° radius; 2014), Briceño et al. (0.7° radius; 2019) and Briceño et al. (1.0° radius; 2005, 2007). The vertical lines, from left to right, indicate the substellar limit (H burning limit), the BD-planetary object limit (D burning limit) and the completeness limit of our DECam observations.

2.4.2.1 Mass-Luminosity Relationship

At the age of 25 Ori (7-10 Myr; Briceño et al., 2005, 2007; Downes et al., 2014; Briceño et al., 2019), stars with masses between $\sim$ 2 and $\sim$ 15 $M_{\odot}$ should be already in the MS, while less massive objects are still in the PMS and more massive stars are in post-MS stages (Prialnik, 2000). The most massive star in 25 Ori is the star with the same name, classified as a peculiar B1V star with broad lines (Houk & Swift, 1999), which roughly corresponds to $\sim$ 10 $M_{\odot}$ using the Schmidt-Kaler (1982) empirical mass-luminosity relationship. Therefore, we do not expect in our candidate sample members of 25 Ori being in post-MS but we do expect PMS and MS members. We estimated that $\sim$ 7% of our candidates have masses larger than 2 $M_{\odot}$, considering the system IMF by Downes et al. (2014).

In order to cover the large M_{I_c} range in our candidate sample (from -2.8 to 15.4 mag), we worked with two sets of mass-luminosity relationships for PMS and MS stellar models at the age of 25 Ori. We considered the 7 Myr isochrones of PARSEC-COLIBRI for masses higher than 1.0 $M_{\odot}$ and of BT-Settl for lower masses. These isochrones were obtained assuming solar metallicity (Biazzo et al., 2011). In Figure 8 we show the resulting mass-luminosity relation from high-mass stars to very low-mass objects (from 0.01 to 15 $M_{\odot}$). We stress the soft transition between both isochrones at the selected cutoff (1 $M_{\odot}$).

2.4.2.2 System IMF Determination

By interpolation of the M_{I_c} magnitudes into the mass-luminosity relationship explained in the previous section, we estimated the masses that correspond to each member candidate as well as to each contaminant considering they are members of 25 Ori. Thus, we obtained 10^4 masses for each source. The resulting mass range covered by the member candidates is between 0.011 and 13.1 $M_{\odot}$. In Table 5 we list this mass range along with those for the samples of contaminants.

With these masses we constructed the mass distributions of the member candidates and contaminants. Similarly than for the M_{I_c} distributions, we corrected the distributions by the spatial completeness of DECam and then we defined the mass distribution using the mean values and as-

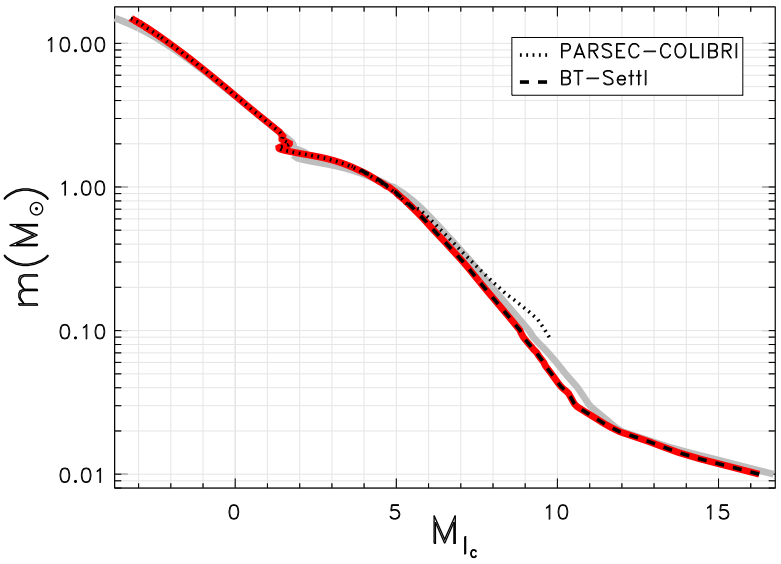

Figure 8: Mass-luminosity relation used to estimate the masses of the member candidates and contaminants (red solid curve). This relation is a combination of the 7 Myr isochrones of BT-Settl and PARSEC-COLIBRI, which are indicated by the dashed curve and the dotted curve, respectively. As a reference, the mass-luminosity relation considering instead the 10 Myr isochrones is represented by the gray solid curve, which is mostly contained into the thickness of the mass-luminosity relation for 7 Myr.

signing errors of 1 σ. For the massive bins, which do not have more than two sources, we replaced the uncertainties by the Poisson errors. From the mass distribution of the member candidates we subtracted that of the control field contaminants adding the errors in quadrature. The resultant distribution is very consistent with that of the candidates in the filtered sample, avoiding the region ($\sim 0.8 - 3\ M_\odot$) with a high degree of contamination by giant and subgiant stars. Thus, we obtained the system IMF of 25 Ori by replacing in the mass distribution of the member candidates minus the contaminants from the control field the range $m > 0.8\ M_\odot$ by the distribution of the filtered sample. The derived 25 Ori system IMF is complete from 0.012 to 13.1 $M_\odot$ (corresponding to the 25 Ori star).

Additionally to the discrete determination of the system IMF of 25 Ori, we built the continuous system IMF using a KDE and the masses determined in this section. We assumed a bandwidth of 0.1 dex (in logarithmic scale of mass) and an Epanechnikov kernel (Silverman, 1986) to obtain the KDEs of the member candidates and contaminants. These KDEs were obtained similarly than for the continuous LFs, normalizing to the mass histograms at 0.03 and 0.3 $M_\odot$ when working with the sources (candidates or contaminants, depending the KDE to be derived) from the DECam catalog or from the rest of catalogs, respectively. The final continuous system IMF of 25 Ori was obtained subtracting from the KDE of the candidates the KDE of the contaminants and replacing the KDE of the filtered sample of candidates for $m > 0.8\ M_\odot$.

In Figure 9 we show the system IMFs for the 25 Ori estimated areas. The least massive bin (at $\log m = -1.9$) is partially affected by the completeness of our DECam data in the magnitude range between about 21 and 24 mag (DECam completeness at $I_c = 22.5$ mag). Then, we corrected the counts in this magnitude range by a factor of ~ 2.5, which results from the ratio between the expected number of sources (from extrapolation of the linear behavior of the I_c magnitude distribution in logarithmic scale of the DECam data; see Section 2.3.2.2) and those observed with DECam in that magnitude range. We did not correct the least massive interval of the KDE by the DECam incompleteness due to the edges of a KDE are influenced by a boundary effect that occurs in nonparametric curve estimation problems (Silverman, 1986). This is not an issue for us because the parametrizations of the system IMF are done considering the discrete determinations. However, we point out the consistency of the histogram and KDE determinations of the system IMF of 25 Ori for the different areas.

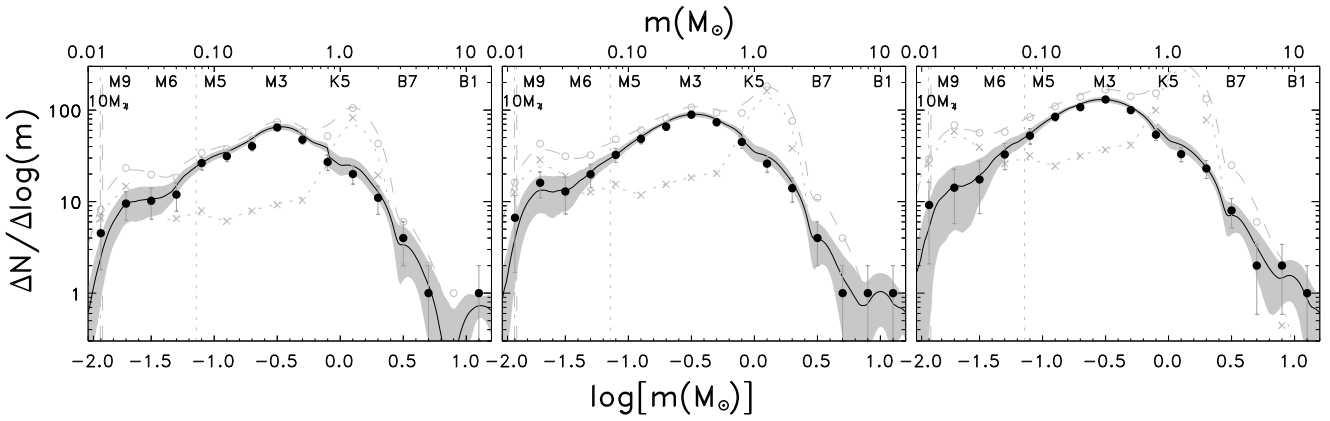

Figure 9: System IMFs of 25 Ori (black points and black solid curves) after correcting by the galactic and extragalactic contamination (gray crosses and dotted curves) in our member candidate sample (gray open circles and dashed curves). The panels, from left to right, correspond to the 25 Ori areas by Downes et al. (0.5° radius; 2014), Briceño et al. (0.7° radius; 2019) and Briceño et al. (1.0° radius; 2005, 2007). The vertical lines are the same as in Figure 7. The spectral type scale is a combination of the Pecaut & Mamajek (2013) relation and the mass-luminosity relation explained in Section 2.4.2.1. The size of the bin for the discrete distributions is 0.2 dex.

2.4.2.3 Parameterizations

We described the derived system IMF of 25 Ori using the following parameterizations:

i) A two-part power-law distribution in the form:

$$\xi(\log m) \propto m^{-\Gamma_i} \tag{5}$$

where Γ_1 and Γ_2 are the slopes for masses $m < 0.40\ M_\odot$ and $m \geq 0.4\ M_\odot$, respectively. Such parameterization is inspired by that of the Galactic-field IMF proposed by Kroupa (2001, 2002) and by the dual power-law distribution of Hoffmann et al. (2018), but with a different break mass because these parameterizations are for the single-star IMF.

ii) A lognormal distribution for masses $m \leq 1 M_\odot$, according to Chabrier (2003a,b):

$$\xi(\log m) \propto e^{-\frac{(\log m - \log m_c)^2}{2\sigma^2}} \tag{6}$$

where m_c is the characteristic mass and σ the standard deviation. If we consider the lognormal fit up to 13.1 $M_\odot$, the resultant parameters are in agreement, within the errors, with those when the fit is done for masses $m \leq 1\ M_\odot$.

iii) A tapered power-law function over the whole mass range of the system IMF (0.012 − 13.1 $M_\odot$):

$$\xi(\log m) \propto m^{-\Gamma}\left[1 - e^{-(m/m_p)^\beta}\right] \tag{7}$$

where m_p is the peak mass, Γ the power law index and β the tapering exponent. This function, introduced by De Marchi et al. (2005), has a power law behavior for high masses and an exponential truncation for lower masses.

The fits were done in the discrete determination of the system IMF, as mentioned in Section 2.4.2.2. In Figure 10 we show the parameterizations of the 25 Ori system IMF and in Table 6 we summarize the parameters with their uncertainties.

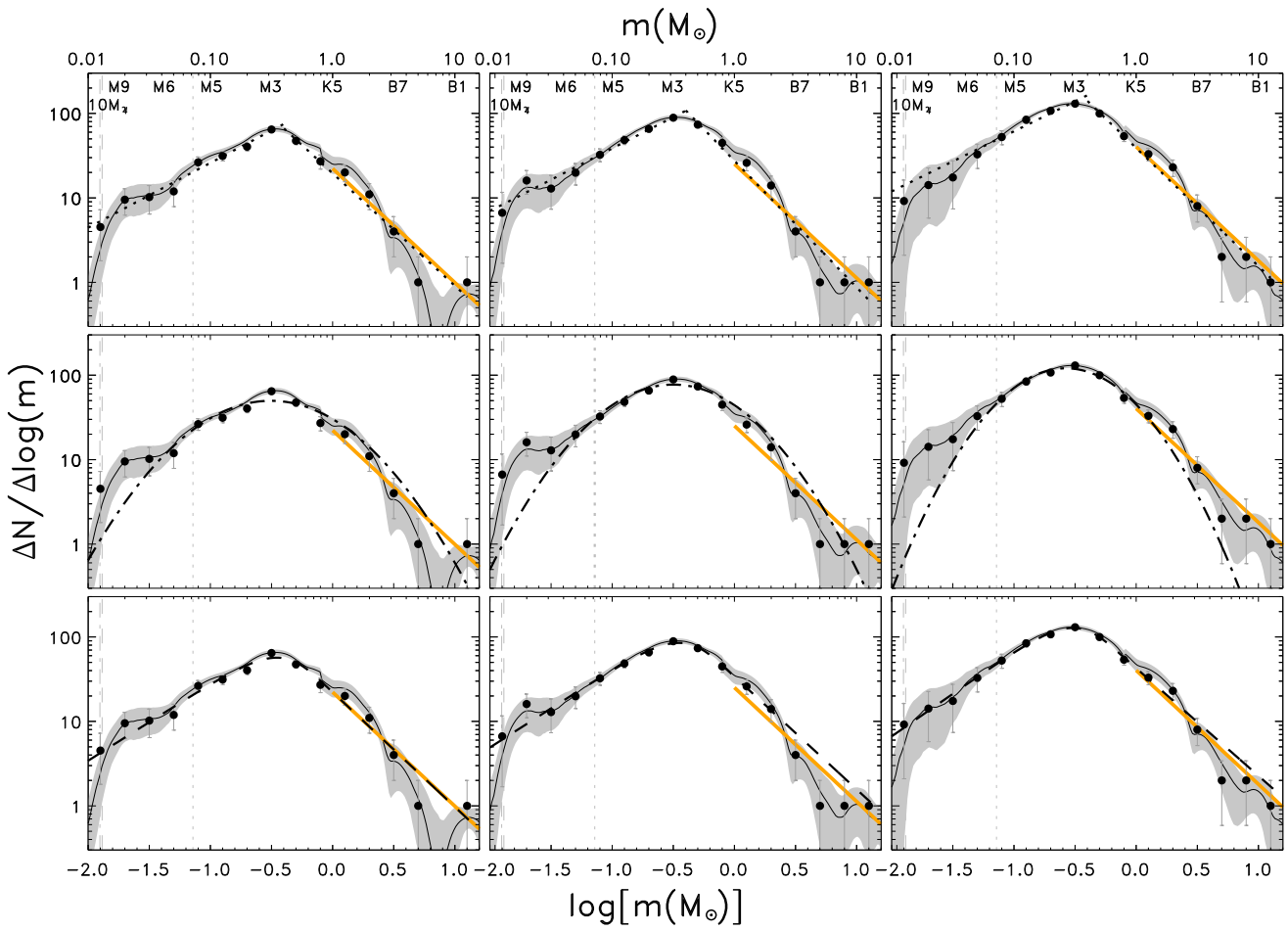

Figure 10: Parameterizations fitted to the 25 Ori system IMFs. Left, central and right panels are the system IMFs considering the areas by Downes et al. (0.5° radius; 2014), Briceño et al. (0.7° radius; 2019) and Briceño et al. (1.0° radius; 2005, 2007), respectively. Top, middle and bottom panels show the two-segment power-law, lognormal and tapered power-law functions, respectively, fitted to the system IMFs. As a reference, the orange line shows the Salpeter (1955) slope ($\Gamma = 1.35$). The rest of the symbols and lines are the same as in Figure 9.

2.4.2.4 Comparison of the 25 Ori system IMF with Other Studies

Before comparing the system IMF reported here with that in other regions, we considered the 25 Ori system IMF obtained by Downes et al. (2014). They found that the system IMF in their entire survey (3x3 deg^2 around 25 Ori) is well described by either two power laws with slopes $\Gamma_a = -2.73 \pm 0.31$ and $\Gamma_b = -0.32 \pm 0.41$ for the mass ranges $0.02 \leq m/M_\odot \leq 0.08$ and $0.08 \leq m/M_\odot \leq 0.5$, respectively, or a lognormal function with parameters $m_c = 0.21 \pm 0.02$ and $\sigma = 0.36 \pm 0.03$ over the whole studied mass range. Additionally, for the system IMF of the overdensity (0.5° radius), they obtained $\Gamma_a = -2.97 \pm 0.02$ and $\Gamma_b = -0.63 \pm 0.04$, and $m_c = 0.22 \pm 0.02$ and $\sigma = 0.42 \pm 0.05$ in the corresponding mass ranges. Those m_c and σ values are slightly lower and the slope for substellar masses is quite steeper than those reported here. We mainly attribute these differences between both system IMFs to differences in the corresponding samples and also in the procedures used in both works. Here, we considered the mass range $0.01 < M/M_\odot < 13$ against $0.03 < M/M_\odot < 0.8$ from Downes et al. (2014), in which some level of incompleteness was expected in the less and more massive system IMF bins. Particularly,

Table 6: Parameterizations fitted to the 25 Ori system IMF.

Area	**Lognormal**		**Two-Segment Power Law**		**Tapered Power-Law**		
radius	m_c	σ	Γ_1 ($m < 0.4\ M_\odot$)	Γ_2 ($m \geq 0.4\ M_\odot$)	Γ	m_p	β
(°)	($M_\odot$)					($M_\odot$)	
0.5[a]	0.31±0.06	0.51±0.08	-0.77±0.06	1.33±0.12	1.36±0.39	0.36±0.07	2.27±0.33
0.7[b]	0.32±0.04	0.47±0.06	-0.74±0.04	1.50±0.11	1.34±0.14	0.36±0.03	2.26±0.11
1.0[c]	0.27±0.02	0.41±0.03	-0.71±0.07	1.40±0.09	1.28±0.07	0.30±0.02	2.28±0.07

[a]By Downes et al. (2014).
[b]By Briceño et al. (2005, 2007).
[c]By Briceño et al. (2019).

we estimated that ∼10% of our member candidates with I_c magnitudes between 17 and 19 mag are unresolved sources in the CDSO catalog used by Downes et al. (2014), which could result in that fraction of missed candidates in their selection in this brightness range due to the spatial resolution differences between the DECam and CDSO catalogs, as shown in Table 2. Additionally, both system IMF estimations followed different procedures: Downes et al. (2014) interpolates masses simultaneously from T_{eff} and L_{bol} in the H-R diagram while here we obtained the system IMF using the mass-luminosity relationship explained in Section 2.4.2.1. Thus, in this work we present the updated version of the system IMF of 25 Ori over its whole mass range, which allows us to rule-out the possible low number of BDs suggested by Downes et al. (2014) when comparing with the Galactic-disk IMF from Chabrier (2003b).

In order to contribute to the understanding of the origin of the IMF and its relation with environmental conditions, we compared the parameters of the two-segment power-law and lognormal functions fitted to the 25 Ori system IMF with those in Table 1, mainly because those IMFs cover a wide mass range as that presented here, and with other studies of interest to include as well the tapered power-law parameterizations. In these comparisons we assumed similar binarity properties for the different clusters and similar spatial resolutions of the surveys.

The best fitted lognormal function to the 25 Ori system IMF are roughly consistent, within the uncertainties, with those obtained in the clusters mentioned in Table 1. The values of m_c range from 0.25 to 0.36 $M_\odot$, with the most widely varying values in the oldest associations (Blanco 1 and Pleiades). σ takes values between 0.44 and 0.58 (considering the parameterizations of σ Ori for m <1 $M_\odot$ and of the ONC with the full sample by Da Rio et al. 2012). Also, these values are consistent with a set of young clusters in Bayo et al. (2011). Though we compared the best fitting lognormal function, we point out that this functional form tends to underestimate the number of BDs in 25 Ori. A similar result was reported in σ Ori by Peña Ramírez et al. (2012) and Upper Sco by Lodieu (2013), and are predicted by Hoffmann et al. (2018).

From the power-law fit, the slope we obtained for LMSs and intermediate/high-mass stars is very consistent with the Salpeter (1955) slope ($\Gamma = 1.35$) and with the most representative slope for $m \geq 1\ M_\odot$ of a large sample of stellar associations in Bastian et al. (2010), which cover a diversity of physical conditions such as age, metallicity and total mass. However, this slope is slightly steeper than those for most clusters in Table 1, although in agreement with the ONC (considering the sample without age threshold by Da Rio et al. 2012) and with the intermediate-mass slope of Pleiades (Bouy et al., 2015). In order to check the possibility that our slope Γ_2 may be affected by missed massive members of 25 Ori in our PMS locus selection, we applied the Gaia DR2 criteria to all the brightest sources ($I_c \lesssim 10$ or $J \lesssim 10$ mag) in our optical catalog (from

UCAC4 and *Hipparcos*) and NIR catalog (from 2MASS). All the sources satisfying the adopted Gaia DR2 thresholds lie inside our PMS locus, which indicate we are including all massive members of 25 Ori in our candidate selection.

In the case of the slope for the very low-mass and BD regime, the value we obtained for 25 Ori is roughly consistent with most of the regions in Table 1 and in Table 4 of Mužić et al. (2017). The slope ranges between -0.3 and -0.8, which restricts the fall (in logarithmic scale of mass) of the number of very LMSs and BDs with mass in a star-forming region with respect to the review of Bastian et al. (2010). A significant steeper slope is reported in the ONC (Da Rio et al., 2012), but a flatter value consistent with the mentioned range is also obtained in that same cluster (Muench et al., 2002; Lucas et al., 2005). Also, we observe that the flattest slope reported in the contributions summarized in the mentioned tables is in NGC 1333 when considering masses up to 1 $M_{\odot}$ (Scholz et al., 2013) but, when considering masses $m < 0.6$ $M_{\odot}$ the slope is consistent with the range quoted here (Scholz et al., 2012). Thus, when comparing slope fits it is important to take care of the mass range that was considered in each study, specially if the fit extends for masses somewhat higher than the characteristic mass. In the case of 25 Ori, the slope for very LMSs and BDs do not present significant differences if the fit is done in any mass range with masses lower than 0.5 $M_{\odot}$, but it significantly flattens by roughly 50 per cent if higher masses are considered in the fit.

About the tapered power-law fit to our system IMF, it is roughly consistent with that reported in an extended sample of young clusters (25 Ori not included) by De Marchi et al. (2010) and Bastian et al. (2010), which has the parameters $\Gamma = 1.1 \pm 0.2$, $m_p = 0.23 \pm 0.10$ and $\beta = 2.4 \pm 0.4$. The m_p value is slightly higher in our system IMF but the differences are in agreement within the errors.

These comparisons indicate that the 25 Ori system IMF is similar to that of a diversity of stellar clusters, which supports the idea that the shape of the IMF is largely insensitive to environmental properties, as predicted by the models from Bonnell et al. (2006), Elmegreen et al. (2008) and Lee & Hennebelle (2018).

Also, we emphasize that the 25 Ori system IMF is a smooth function across the entire mass range, in the sense that we do not observe any bimodality behavior as in the ONC (Drass et al., 2016).

2.4.3 BD/star ratio

An alternative quantity that indicates the relative efficiency to form stellar and substellar objects is, precisely, the ratio between BDs and stars. We worked with the R_{ss} definition by Briceño et al. (2002), which is the ratio between BDs and stars considering objects with masses between 0.02 and 10 $M_{\odot}$ and the BD-star limit at 0.08 $M_{\odot}$. For the 25 Ori areas of 1.0, 0.7 and 0.5° radius, R_{ss} is 0.15 ± 0.03, 0.16 ± 0.02, 0.16 ± 0.02, respectively. Similar R_{ss} values are obtained for other radii between 0.4 and 1.1°.

The R_{ss} value representative of 25 Ori is 0.16 ± 0.03 i.e. for each 6 stars in 25 Ori we roughly expect 1 BD. This value is consistent with those found in regions with low stellar density as Blanco 1 (Moraux et al., 2007a) and with higher stellar density such as NGC 6611 (Oliveira et al., 2009), and is somewhat lower but consistent within the uncertainties, with those in higher stellar density regions such as the Trapezium (Muench et al., 2002; Thies & Kroupa, 2007), ONC (Kroupa & Bouvier, 2003), IC 348 (Scholz et al., 2013), Chamaeleon-I and Lupus-3 (Mužić et al., 2015). Also, the BD/star ratio we found in 25 Ori is consistent with that on the Galactic plane (Bihain & Scholz, 2016). The fact that such widely differing regions show similar ratios of BDs to stars suggests that the environment plays a small role, if any, in the formation of substellar and stellar

objects.

We point out that not all the mentioned BD/star ratios were estimated assuming the same mass ranges. In fact, we observed that most of the slightly higher reported values with respect to that obtained here considered masses lower than 1 $M_{\odot}$ (as suggested by Andersen et al. 2008), while we included sources up to 10 $M_{\odot}$ (as defined by Briceño et al. 2002). However, in the case of 25 Ori and considering the Andersen et al. (2008) definition, we obtained a BD/star ratio of 0.17 ± 0.03, which is very consistent with that we obtained using the Briceño et al. (2002) definition.

2.4.4 Spatial Distribution

Taking advantage of the large spatial coverage of our candidate sample, we examined the system IMF for possible variations with the radius. In Table 6 and Figure 10 we observe that the system IMFs for the different 25 Ori estimated areas are very consistent according to all the parameterizations. Similar results are obtained for other radii between 0.4 and 1.1° (2.5-6.8 pc), which suggests that the stellar and substellar populations of 25 Ori do not have any preferential spatial distribution.

Additionally, the similar R_{ss} values obtained in previous section are an indicative that the substellar and stellar population have similar spatial distribution over the full area of 25 Ori.

We can see in Figure 2 two stellar groups surrounding 25 Ori whose members could affect the determination of the 25 Ori system IMF. HR 1833 is a prominent overdensity in the spectroscopic study of Briceño et al. (2019) while ASCC 18, detected by Kharchenko et al. (2005), is not an obvious overdensity in Briceño et al. (2019) and is present very faintly in Zari et al. (2017). The reported radii of HR 1833 is 0.5° (Briceño et al., 2019) and 0.44° for ASCC 18 (Kharchenko et al., 2013). If we consider the 25 Ori area of 0.5° radius (Downes et al., 2014), neither HR 1833 nor ASCC 18 overlap 25 Ori, which allow us an analysis including only member candidates lying inside 25 Ori. Thus, the system IMF for this radius is representative of 25 Ori and do not present significant variations for radius up to 1.1°, where somewhat contamination by surrounding groups could be present.

2.4.5 Gravitational State of 25 Ori

As found by Lada & Lada (2003) and predicted by Bonatto & Bica (2011), most clusters are dissolved before they reach an age of 10 Myr; only less than 10% reach older ages and about 4% survive longer than 100 Myr. 25 Ori is just at this critical point and no conclusive results about its gravitational state have been presented (McGehee, 2006; Downes et al., 2014). Any cluster, to be gravitationally bound, its escape velocity, $v_{esc} = (2GM/R)^{1/2}$, must be larger than its velocity dispersion (Sherry et al., 2004).

Directly counting in the mass distributions shown in Figure 9, we obtained a total mass of 158 ± 18, 223 ± 21 and 324 ± 25 $M_{\odot}$ contained in 25 Ori inside areas of 0.5, 0.7 and 1.0° radius, respectively. The fraction of these masses contained in BDs is 1.42 ± 0.45, 1.41 ± 0.40 and 1.46 ± 0.35%, respectively. Similar values are obtained for other radius between 0.4 and 1.1°, which also indicates, as from the R_{ss} ratio, alike spatial distribution of the substellar and stellar population of 25 Ori.

Considering the total mass of 324 $M_{\odot}$ inside a radius of 1.0°, which corresponds to 6.2 pc at a distance of 356 pc, the resultant v_{esc} is 0.7 km s^{-1}. A similar v_{esc} is obtained if considering the total mass inside the 0.7 or 0.5° radii. This v_{esc} is about 3 times smaller than the velocity dispersion of 2 km s^{-1} in 25 Ori (Briceño et al., 2007), which indicates that 25 Ori is an unbound association. We estimated that to be a gravitationally bound cluster, 25 Ori should have about

10 times more mass than that estimated here, which implies an unrealistic number of more than 6000 members, or to have a significantly smaller velocity dispersion.

2.5 Summary and Conclusions

By combining optical and NIR photometry from DECam, CDSO, UCAC4 and *Hipparcos*, and VISTA and 2MASS, respectively, we selected a sample of 1687 photometric member candidates in an area of 1.1° radius in 25 Ori on the basis of their position in color-magnitude and color-color diagrams. This sample covers an I_c range between 5.08 and 23.30 mag, which corresponds to a mass range from 0.011 to 13.1 $M_\odot$. The completeness of the sample is at 0.012 $M_\odot$, which is just beyond the deuterium burning limit (0.013 $M_\odot$), and also includes the most massive stars in 25 Ori. We estimated a contamination of 20% for the LMS candidates, but it increases for the intermediate-mass candidates due to giant and subgiant stars and for BD candidates due to extragalactic sources.

Additionally, we discussed and/or considered, in the context of 25 Ori, the following uncertainties and biases to be taken into account when determining the mass distribution: spatial completeness, photometric sensitivity, IR excesses, chromospheric activity, unresolved binaries and missed members.

With the sample of member candidates we constructed the system IMF of 25 Ori for different areas, which is complete down to 0.012 to 13.1 $M_\odot$ and is one of the few system IMFs over the whole mass range of a stellar cluster (e.g. Collinder 69 by Bayo et al. 2011 and σ Ori by Peña Ramírez et al. 2012). This system IMF is a smooth function across the entire mass range. We parameterized the resultant system IMF using a two-segment power-law, a lognormal and a tapered power-law function to compare it with other studies. We observed that a lognormal function well-fitted to the peak of the mass distribution underestimates the BD population of 25 Ori.

The system IMF presented here shows a larger number of BDs than that reported by Downes et al. (2014). We found this difference can be mainly explained by issues related to the spatial resolution and completeness of the CDSO as well as differences in the procedures for computation of the system IMF. The updated system IMF presented in this work allows us to rule-out the possible low number of BDs suggested by Downes et al. (2014).

The 25 Ori system IMF does not present significant differences in comparison with other clusters having different physical properties, which suggests that the conversion of gas into stars and BDs has minimum influence by the environmental properties, as predicted by some models (e.g. Bonnell et al., 2006; Elmegreen et al., 2008; Lee & Hennebelle, 2018).

We estimated the BD/star ratio of 25 Ori, which has a representative value of 0.15 ± 0.03. This ratio is consistent with those in other regions with different stellar densities which is an indicative that the formation of BDs and stars occurs in a similar way in different environments.

There are no significant variations of the 25 Ori system IMF with radius and the BD/star ratio is similar for different radii between 2.5 to 6.8 pc (0.4-1.1°). These results indicate that the substellar and stellar objects do not have any preferential spatial distribution.

Comparing the escape velocity estimated for 25 Ori and its velocity dispersion, we found that 25 Ori is an unbound association. In fact, 25 Ori should have about 10 times more mass or a significantly smaller velocity dispersion to be considered as a gravitationally bound cluster.

The system IMF of 25 Ori we present in this work was constructed with photometric member candidates. To determine the membership of each candidate it is necessary a follow up spectroscopy. Thus, we could determine the distribution of the masses of the confirmed members. This kind of study requires the use of several multi-fiber spectrographs to have full coverage of the brightness range and spatial distribution. In this direction, we have an ongoing spectroscopic

survey about 85% complete, which will be part of a future work (Suárez et al. 2019, in preparation; Downes et al. 2019, in preparation).

3 Memberships and Analysis from Spectroscopy

3.1 Research Statement

The analysis in the previous section was carried out using photometric member candidates and dealing with the contamination present in the sample using statistical techniques. In order to truly determine the membership of each individual source, it is necessary to make a spectroscopic follow-up, which also allows a precise determination of physical parameters such as T_{eff}, A_V, surface gravity ($\log g$), mass and age. This is essential to study various astrophysical phenomena as mass distribution, age spread, evolution of circumstellar disks and the history of star formation. However, such a follow-up spectroscopy is an arduous observational task that implies the use of several world-wide facilities.

We have an ongoing spectroscopic survey to observed each 25 Ori member candidate in our sample, which consists of 1687 sources with masses from 0.012 to 13.1 $M_{\odot}$ distributed in an area of 1.1° radius in 25 Ori. In the following sections we describe our spectroscopic observations and summarize the current state of the survey.

3.2 OAN-SPM/MES for Intermediate/High-Mass Stars

3.2.1 MES Spectra

To observe the brightest 25 Ori candidates we used the Manchester Echelle Spectrograph (MES; Meaburn et al., 1984, 2003) attached to the 2.1m telescope of the Observatorio Astronómico Nacional at San Pedro Mártir (OAN-SPM) in Baja California, Mexico, which allows the acquisition of optical medium-high resolution spectra (R=18000 at 5000 Å). We obtained 24 nights of observing time distributed as follow: 6 nights on December 11-16, 2014 (PI: J. J. Downes), 6 nights on January 06-11, 2015 (PI: J. J. Downes), 6 nights on October 24-29, 2015 (PI: G. Suárez) and 6 nights on January 22-27, 2016 (PI: G. Suárez). In Table 7 we show the log of our MES observations.

3.2.1.1 Target Selection

The selection of the MES targets was done on the basis of their positions in the V vs $V-J$ and H vs $H-K$ diagrams using the UCAC4 and 2MASS catalogs. We defined the empirical isochrone traced by the spectroscopically confirmed members by Briceño et al. (2005, 2007); Downes et al. (2014) as well as the highly probable members by Kharchenko et al. (2005). Then, we defined the PMS locus as the region around the empirical isochrone that contains most of the confirmed and highly probable members, and selected the sources lying inside both loci. Additionally, we removed from the candidate selection the sources having low photometric and kinematics probability of being members according to Kharchenko et al. (2005). The final sample contains 80 member candidates covering an area of 3x3 deg^2 around 25 Ori and with V-band magnitudes from 4.9 to 12.1 mag, which corresponds to the mass range from 1.6 to 13.1 $M_{\odot}$ considering the PARSEC-COLIBRI 7 Myr isochrone.

3.2.1.2 Data Reduction

During our MES observations we obtained spectra for 77 of these member candidates (96% of the sample), including all those lying inside the 1.0° radius area of 25 Ori. Additionally, we obtained images for the calibration of the data (bias, flats, ThAr lamps and radial velocity standards). In

order to reduce the spectra we used standard IRAF[6] tasks to remove bias, flats and cosmic rays, and to extract the spectra, calibrate in wavelength and normalize the continuum. The final wavelength covered by the 32 Echelle orders (from 32 to 63) in each spectra ranges from 3600 to 7100 Å with a typical resolution of $R = 21000$ at H_α. In Figure 11 we show an example of a MES spectrum, focusing on some orders of interest.

3.2.2 Membership Assignment

In order to determine the RVs of the MES spectra we used the *fxcor* task of IRAF, which correlates the spectra with unknown radial velocity with a template spectrum with known radial velocity. For this correlation we considered the following absorption lines: H_α (in order 34), NaI$\lambda\lambda$5890, 5896 (in order 38), MgI$\lambda\lambda\lambda$5167, 5172, 5184 (in order 43), H_β (in order 46), CaIIλ3968 (in order 56) and CaIIλ3934 (in order 57). So far, we have obtained radial velocities for 22 targets of the sample (about 30%) which have values between 10 and 40 km s^{-1} (plus two targets with values of -10 and 50 km s^{-1}) and with typical uncertainties of 3 km s^{-1}.

In order to determine which of these targets are members of 25 Ori, we applied several criteria on the basis of their radial velocities, distances and spatial distribution as follows:

i) First, we cross matched our list of targets with Gaia DR2; 99% of all the MES targets have reliable parallaxes (errors lesser than 20%). To filter the sample according to their distances, we considered the 25 Ori distance of 356 ± 47 pc (Suárez et al., 2019) and selected the targets located around 25 Ori with a dispersion of 3σ. About 86% of the MES targets satisfies this criterion.

ii) Additionally, we selected the targets with radial velocities between 10 and 40 km s^{-1} to have consistency with 25 Ori (Briceño et al., 2007). From the 22 targets for which we have obtained radial velocities from the MES spectra, 14 sources satisfy the distance and radial velocity criteria. Because these sample of 22 targets is representative of the whole sample, we expect that more than 60% of our targets satisfy these criteria.

iii) Finally, we selected the sources lying inside the 25 Ori estimated area of 1.0° radius. From the 14 targets with distance and radial velocity consistent with 25 Ori, 10 of them are located inside the 25 Ori limits.

In summary, from the 22 targets with radial velocity from the MES spectra and with distances from Gaia DR2, 10 of them have spatial distribution, distances and radial velocities consistent with 25 Ori. Therefore, from the entire sample of MES spectra (77 targets) we roughly expect 35 intermediate/high-mass members of 25 Ori, which is consistent with the expected sources from the 25 Ori system IMF (Suárez et al., 2019).

3.2.3 Physical Parameters

We estimated T_{eff} of the member candidates observed with MES by interpolating their observed $G-J$ colors from Gaia DR2 and 2MASS in an updated version of the Kenyon & Hartmann (1995) relation, assuming the 25 Ori A_V obtained in this work (0.29 ± 0.26 mag). For the estimation of L_{bol}, mass and age we used the routine described in Section 3.3.2.3, working with the PARSEC-COLIBRI isochrones. The masses obtained for the sources range between 1.3 and 11 $M_\odot$.

[6]IRAF is distributed by the National Optical Astronomy Observatory, which is operated by the Association of Universities for Research in Astronomy (AURA) under a cooperative agreement with the National Science Foundation.

Table 7: OAN-SPM/MES observing log.

Target	RA (hh:mm:ss)	DEC (hh:mm:ss)	UT Date (yyyy-mm-ddThh:mm:ss)	Airmass	T_{exp} (s)	V (mag)	Comments
			2014B Runs				
25Ori_40	05:23:14.54	+02:01:06.9	2014-12-11T05:20:32	1.415	3000	11.627	tiny clouds
25Ori_65	05:23:45.91	+01:50:33.4	2014-12-11T06:43:46	1.189	2000	9.923	—
25Ori_93	05:24:16.19	+01:38:35.7	2014-12-11T08:31:15	1.168	3000	11.442	bad sky
25Ori_86	05:24:12.73	+01:34:12.1	2014-12-11T10:35:36	1.541	3000	10.645	—
25Ori_105	05:24:20.74	+01:35:26.6	2014-12-12T05:27:09	1.382	6000	9.793	—
25Ori_128	05:24:44.83	+01:50:47.2	2014-12-12T07:27:03	1.148	2000	4.878	a second spectrum
25Ori_256	05:26:11.98	+01:53:35.7	2014-12-12T09:13:14	1.233	3000	9.33	—
25Ori_157	05:25:11.65	+01:33:29.7	2014-12-12T10:37:16	1.571	3000	9.959	—
25Ori_134	05:24:54.56	+01:58:08.3	2014-12-12T11:53:37	2.428	2000	10.064	—
25Ori_265	05:26:19.93	+01:47:14.3	2014-12-13T08:52:49	1.203	3600	12.183	—
25Ori_235	05:26:03.68	+01:48:29.4	2014-12-13T11:03:39	1.792	3600	10.81	—
25Ori_66	05:23:50.20	+01:32:52.9	2014-12-14T05:07:48	1.43	3000	10.586	—
25Ori_123	05:24:38.92	+01:54:06.4	2014-12-14T06:54:42	1.163	3000	10.969	—
25Ori_135	05:24:55.01	+01:39:22.9	2014-12-14T08:24:08	1.172	3600	11.128	—
25Ori_99	05:24:18.17	+02:22:06.1	2014-12-14T09:59:35	1.402	3000	10.091	—
25Ori_95	05:24:17.61	+02:22:04.6	2014-12-14T10:57:04	1.766	2000	9.572	very close to 25Ori 99
			2015A Runs				
25Ori_487	05:28:45.29	+01:38:38.1	2015-01-07T08:21:37	1.381	3000	6.895	—
25Ori_547	05:29:33.53	+03:08:52.5	2015-01-07T09:44:31	1.912	3000	7.104	—
25Ori_668	05:31:29.89	+01:41:24.1	2015-01-10T03:50:59	1.34	1200	7.517	—
25Ori_447	05:28:15.70	+01:34:48.2	2015-01-10T04:43:42	1.202	1200	8.983	—
25Ori_390	05:27:20.59	+02:12:57.1	2015-01-10T05:37:06	1.144	5100	9.171	—
25Ori_512	05:28:59.36	+01:29:19.1	2015-01-10T08:18:19	1.418	2700	9.293	—
25Ori_586	05:30:08.82	+01:14:52.4	2015-01-10T09:20:03	1.831	2700	9.339	—
25Ori_119	05:24:36.10	+02:21:11.4	2015-01-11T03:55:13	1.283	600	6.307	—
25Ori_577	05:30:02.85	+01:06:33.3	2015-01-11T04:42:35	1.207	2700	9.577	—
25Ori_435	05:28:01.47	+01:17:53.7	2015-01-11T05:32:49	1.154	600	6.388	—
			2015B Runs				
25Ori_121	05:24:36.62	+01:48:03.5	2015-10-24T07:30:36	1.832	3000	8.948	—
25Ori_122	05:24:38.62	+01:48:38.8	2015-10-24T08:48:06	1.352	3000	8.311	—
25Ori_152	05:25:11.10	+01:52:01.6	2015-10-24T10:02:56	1.178	3000	9.86	—
25Ori_80	05:24:07.86	+01:38:00.1	2015-10-25T06:38:40	2.537	3000	9.339	—
25Ori_30	05:23:01.94	+01:41:48.9	2015-10-25T07:59:12	1.565	3000	8.135	—
25Ori_24	05:22:47.96	+01:43:00.2	2015-10-25T09:17:39	1.249	3000	9.641	—
25Ori_318	05:26:48.11	+02:04:05.8	2015-10-25T11:01:57	1.143	3000	8.503	—
25Ori_148	05:25:10.30	+01:15:31.3	2015-10-26T06:49:30	2.292	3000	9.839	—
25Ori_377	05:27:19.20	+01:36:22.4	2015-10-26T08:00:01	1.563	3000	8.88	—
25Ori_146	05:25:07.39	+00:56:00.7	2015-10-26T09:20:16	1.249	4800	9.587	tiny clouds
25Ori_69	05:23:51.38	+00:51:46.3	2015-10-26T11:03:19	1.158	3000	8.388	—
25Ori_569	05:29:54.77	+01:47:21.3	2015-10-26T12:04:15	1.199	900	5.749	—
25Ori_242	05:26:06.00	+00:50:02.4	2015-10-27T06:40:48	2.416	3000	8.298	—
25Ori_281	05:26:27.20	+00:50:21.2	2015-10-27T07:54:30	1.585	3600	9.892	—
25Ori_238	05:26:04.62	+00:43:38.9	2015-10-27T09:14:33	1.258	3600	9.215	—
25Ori_538	05:29:28.64	+01:43:09.7	2015-10-27T10:37:29	1.148	4500	10.215	—
25Ori_131	05:24:50.10	+00:45:58.6	2015-10-27T12:23:28	1.271	3000	8.71	—
25Ori_126	05:24:42.80	+01:43:48.2	2015-10-28T07:44:00	1.596	3600	10.258	—
25Ori_111	05:24:24.21	+01:41:33.3	2015-10-28T09:18:06	1.226	3600	10.233	—
25Ori_210	05:25:47.02	+00:31:12.9	2015-10-29T07:46:24	1.588	900	6.149	—
25Ori_425	05:27:54.23	+01:06:18.2	2015-10-29T08:14:59	1.432	1350	7.79	—
25Ori_570	05:29:55.56	+02:08:31.8	2015-10-29T08:54:10	1.312	1800	8.144	—
25Ori_211	05:25:48.66	+01:23:22.0	2015-10-29T10:07:23	1.161	2700	10.424	—
25Ori_468	05:28:34.15	+00:45:57.6	2015-10-29T11:09:37	1.166	900	9.719	low SNR
			2016A Runs				
25Ori_494	05:28:48.46	+02:09:53.0	2016-01-22T03:18:54	1.28	3000	7.136	—
25Ori_440	05:28:10.12	+00:47:14.0	2016-01-22T04:46:04	1.162	3000	8.35	—
25Ori_601	05:30:29.60	+01:46:55.4	2016-01-22T06:06:02	1.182	4000	10.214	—
25Ori_513	05:28:59.71	+03:21:48.6	2016-01-22T07:35:12	1.401	4000	10.343	—
25Ori_571	05:29:55.94	+02:12:34.0	2016-01-22T09:29:49	2.655	3000	10.36	—
25Ori_630	05:30:53.05	+01:36:47.0	2016-01-23T02:51:07	1.375	4000	10.512	—
25Ori_652	05:31:13.56	+01:23:12.0	2016-01-23T04:23:15	1.171	4000	10.561	—
25Ori_548	05:29:34.26	+01:53:50.5	2016-01-23T06:06:35	1.187	4000	10.633	—
25Ori_222	05:25:50.76	+00:47:48.9	2016-01-23T08:26:34	1.853	4000	10.737	tiny clouds
25Ori_473	05:28:36.30	+02:20:42.9	2016-01-24T03:00:01	1.31	4000	10.686	close companion
25Ori_466	05:28:31.17	+01:54:07.8	2016-01-24T04:34:53	1.151	4000	10.764	—
25Ori_428	05:27:57.33	+02:16:34.6	2016-01-24T05:42:52	1.161	4000	10.782	—
25Ori_454	05:28:18.74	+01:20:56.1	2016-01-24T08:32:11	1.909	4000	10.805	—
25Ori_486	05:28:44.05	+01:11:37.9	2016-01-25T02:44:04	1.371	4000	10.806	—
25Ori_542	05:29:30.65	+01:29:41.0	2016-01-25T04:11:24	1.171	4000	10.872	—
25Ori_137	05:25:00.18	+01:38:29.8	2016-01-25T05:58:41	1.197	4000	10.876	close companions
25Ori_396	05:27:33.26	+01:12:55.1	2016-01-25T06:52:28	1.322	6000	10.882	tiny clouds
25Ori_467	05:28:33.18	+01:45:55.9	2016-01-25T09:09:34	2.521	4000	10.964	tiny clouds
25Ori_472	05:28:35.44	+01:40:07.3	2016-01-26T02:55:07	1.311	4000	10.983	—
25Ori_469	05:28:34.40	+02:20:18.2	2016-01-26T04:41:44	1.141	4000	11.014	—
25Ori_554	05:29:38.03	+01:56:05.6	2016-01-26T06:01:41	1.197	4000	11.081	close companion
25Ori_445	05:28:15.32	+01:27:34.1	2016-01-26T07:36:17	1.524	5000	11.27	—
25Ori_309	05:26:46.56	+01:40:55.2	2016-01-26T09:02:14	2.496	3000	11.358	—
25Ori_94	05:24:17.49	+01:38:30.1	2016-01-27T02:58:00	1.279	4800	11.366	—
25Ori_492	05:28:47.46	+02:18:51.1	2016-01-27T04:20:38	1.148	4800	11.37	—
25Ori_239	05:26:04.90	+00:32:19.7	2016-01-27T06:25:23	1.28	4800	11.419	—
25Ori_308	05:26:45.90	+03:26:54.0	2016-01-27T07:45:46	1.574	4800	11.448	—

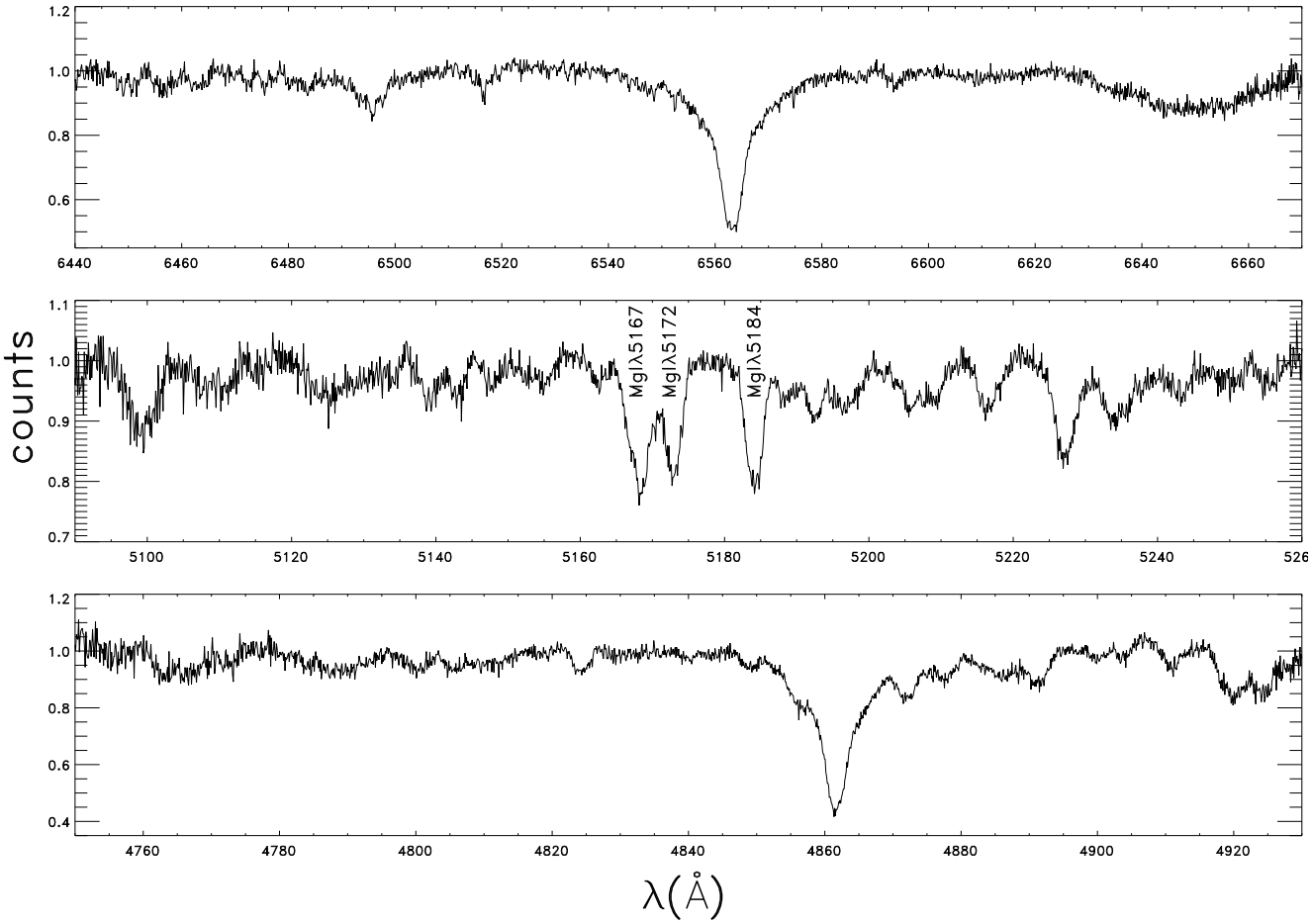

Figure 11: MES spectrum of a confirmed member of 25 Ori with a mass of 1.7 $M_{\odot}$. The panels show the absorption of the lines: H_{α} (in order 34; upper panel), MgI$\lambda\lambda\lambda$5167, 5172, 5184 (in order 43; middle panel) and H_{β} (in order 46; lower panel).

3.3 SDSS-IV/APOGEE-2 for Intermediate-Mass Stars

3.3.1 APOGEE-2 Spectra

In order to observe 25 Ori member candidates less massive that those observed with the MES spectrograph but more massive than the peak of the IMF (0.31 $M_{\odot}$; Suárez et al., 2019), we used the Apache Point Observatory Galactic Evolution Experiment 2 (APOGEE-2) spectrograph, mounted on the 2.5m SDSS telescope (Gunn et al., 2006; Blanton et al., 2017). As one of the SDSS-IV programs, APOGEE-2 uses a multi-fiber spectrograph that allows the acquisition of up to 300 moderate-to-high resolution ($R \sim 22500$) spectra at the H-band (1.51-1.70 μm) across a 1.5° radius circular FOV (Wilson et al., 2010; Majewski et al., 2017). We obtained the data as part of the APOGEE-2 Young Cluster Survey and divided into two high-priority fields with 10 visits dedicated to the observation of mainly 25 Ori targets. Our participation in this survey is thanks to the collaboration of UNAM in SDSS-IV. In Table 8 we summarize the details of these APOGEE-2 fields in 25 Ori.

Table 8: APOGEE-2 fields in 25 Ori.

Field Name	RA (°)	DEC (°)	Plate ID	Epoch (MJD)	UT Date (yyyy-mm-ddThh:mm:ss)	Seeing (arcsec)
Ori OB1ab-E	81.496	1.006	8900	2457648	2016-09-17T11:01:08.967	1.4
			8901	2457649	2016-09-18T11:24:21.106	1.4
			8901	2457650	2016-09-19T11:22:07.462	1.4
			8902	2457652	2016-09-21T11:59:29.344	1.4
			8902	2457653	2016-09-22T11:10:54.354	1.8
			8903	2457675	2016-10-14T10:17:16.340	1.6
Ori OB1ab-F	82.000	3.000	8904	2457676	2016-10-15T10:53:52.447	1.5
			8905	2457410	2016-01-23T04:27:33.611	1.5
			8906	2457411	2016-01-24T04:24:59.808	1.4
			8906	2457412	2016-01-25T04:55:00.687	2.1

3.3.1.1 Target Selection

The selection of the targets was based on IR excess, variability and color-magnitude criteria as well as including previously confirmed member and X-ray sources, as described in Cottle et al. (2018) and summarized as followed:

i) For a uniform selection of young stellar objects (YSOs) with IR excess, the Koenig & Leisawitz (2014) method was followed, considering NIR and mid-IR photometry from the 2MASS and WISE (Cutri & et al., 2013) catalogs, respectively, which provides an efficiency of about 80%, proven in σ Ori and λ Ori (Koenig et al., 2015).

ii) Additionally, to extend the uniform selection of YSOs, including diskless sources, we considered variable candidates, which is an effective method for the selection of PMS stars (Briceño et al., 2005, 2019), using the PanSTARRS catalog (Chambers et al., 2016).

iii) The number of YSOs selected from IR excess and variability criteria required to use about 10% of the available APOGEE-2 fibers, therefore, we filled the rest of the fibers with previously confirmed members by Briceño et al. (2005, 2007); Downes et al. (2014); Suárez et al. (2017c) as well as highly probable member from Kharchenko et al. (2005), X-ray sources from the 3XMM-DR5 catalog (Rosen et al., 2015) and member candidates selected on the basis of their position in I vs $I-J$ diagrams using photometry from the USNO (Monet et al., 2003) and 2MASS catalogs. For the selection of the latter group of member candidates we considered the sources lying inside the defined PMS locus, working with the empirical isochrone traced by several spectroscopically confirmed members and highly probable members of 25 Ori and Orion OB1a. In Figure 12 we show the CMDs used for the selection of photometric candidates observed with APOGEE-2 in 25 Ori.

In Table 9 we summarize the number of APOGEE-2 targets selected from the above criteria and keeping all of them with H-band magnitudes between 7. and 12.2 mag, in order to ensure signal-to-noise ratio (SNR) > 100 for a three-visit source with a total of 3h of exposure (Majewski et al., 2017). We prioritized the targets to first assign fibers to the uniformly selected sources and then to the rest of the candidates. After removing duplicates and 72" fiber collisions, we acquired 1185 unique APOGEE-2 spectra in both fields dedicated to 25 Ori. In Figure 13 we show the spatial distribution of these APOGEE-2 targets.

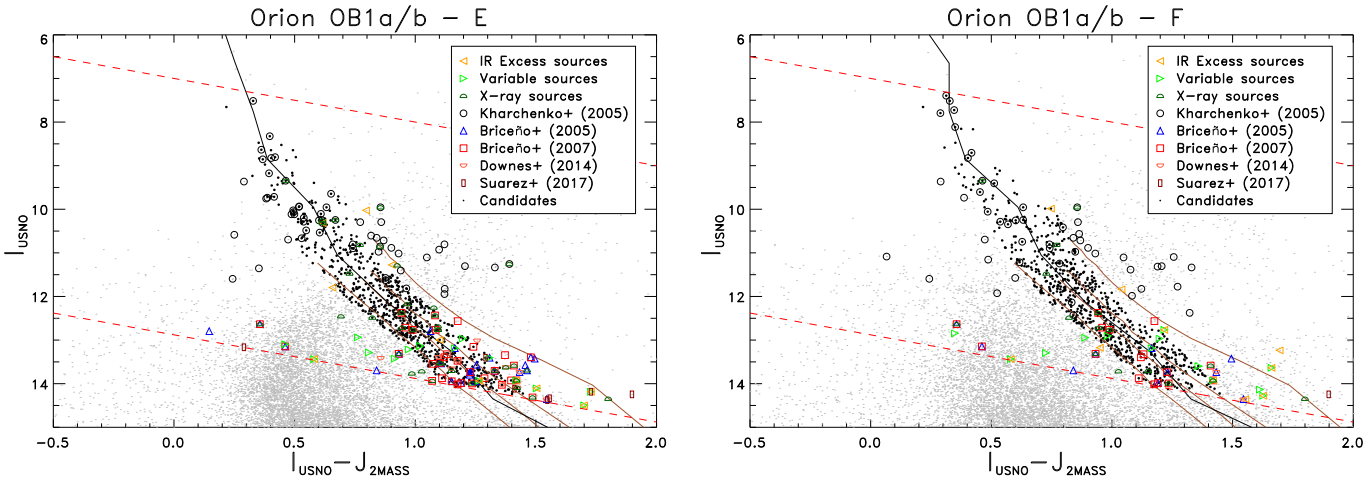

Figure 12: CMDs used to select member candidates (black points) for the APOGEE-2 fields dedicated to 25 Ori (OB1ab-E in left panel and OB1ab-F in right panel). The open symbols show confirmed members, highly probable members and member candidates of 25 Ori and Orion OB1a, as indicated in the label. The black solid curve corresponds to the empirical isochrone and the brown curves represent the BT-Settl isochrones for 1, 3, 5 and 10 Myr. The red dashed lines indicate the APOGEE-2 limits of 7 and 12.2 mag in the H-band. These plots are based on those in Cottle et al. (2018).

Table 9: APOGEE-2 targets in 25 Ori.

IR Excess		Variable		X-ray sources		Members[a]		Candidates	
Selected	Observed	Selected	Observed	Selected	Observed	Selected	Observed	Selected	Observed
23	20	28	25	40	38	216	92	1442	985

[a] Spectroscopically confirmed members considering the studies by Briceño et al. (2005, 2007); Downes et al. (2014); Suárez et al. (2017c).

3.3.1.2 Radial Velocities and Effective Temperatures

We retrieved the APOGEE-2 spectra from the Science Archive Sever (SAS), which are available for SDSS-IV members. These spectra were originally processed by the APOGEE Stellar Parameter and Chemical Abundances Pipeline (ASPCAP; García Pérez et al., 2016), which is an automated software for the determination of RV, T_{eff}, log g and chemical abundances with accuracies of ∼0.1 km s^{-1}, 2%, 0.1 dex and $\lesssim$ 0.05 dex, respectively, through a comparison of the observed spectra to libraries of theoretical spectra. However, ASPCAP is optimized for the analysis of spectra of red giant stars and can introduce biases when working with spectra of YSOs (Nidever et al., 2015). Therefore, these APOGEE-2 spectra were processed by Kounkel et al. (2018) using the pipeline developed by Cottaar et al. (2014), which is designed for spectra of PMS stars. This pipeline determines the T_{eff}, log g, RV, rotational velocity (v sin i) and H-band veiling (r_H) for each source by fitting the observed spectra to synthetic spectra and minimizing χ^2. The corresponding uncertainties are derived by the pipeline using Markov chain Monte Carlo simulations. After some comparisons between the results using the Coelho et al. (2005), Allard et al. (2012) and Husser et al. (PHOENIX; 2013) spectral libraries assuming solar metallicities, it was decided to adopt those from PHOENIX because produce the most self-consistent solutions and covers the widest T_{eff} range (2300-15000 K) (Kounkel et al., 2018). These fits were done for each visit spectrum

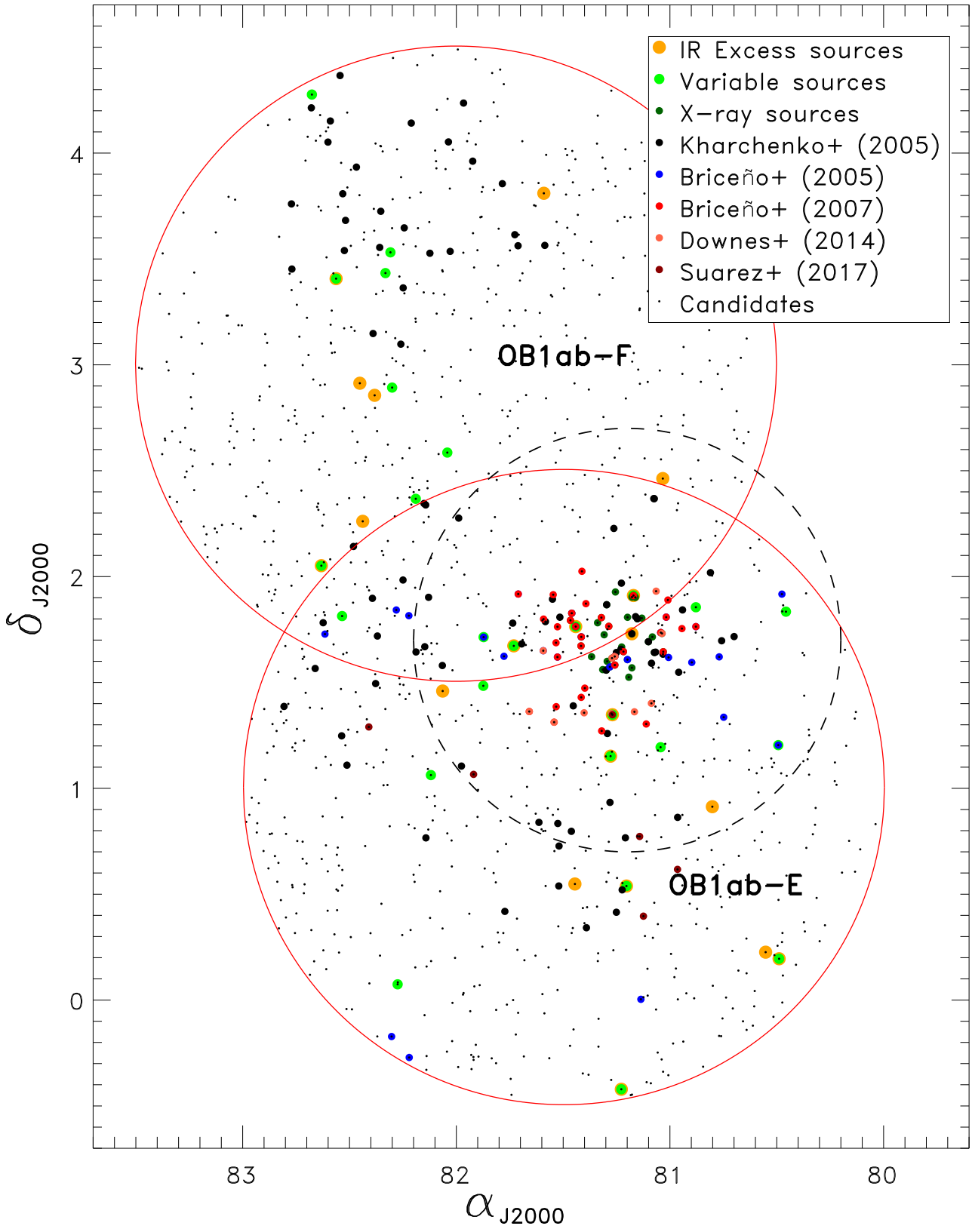

Figure 13: Spatial distribution of the targets observed by APOGEE-2 in the two fields dedicated to 25 Ori (red circles). The colored points represent the different kind of targets and the sizes indicate their priority, as shown in the label. The dashed circle shows the 1° radius area of 25 Ori.

and then, the reported parameters for each target are the weighted average of the parameters in all the visits for that specific target. Additionally to the use of this pipeline, we are working with a new code named TONALLI (Adame et al. 2018, in preparation) to fit the PHOENIX synthetic spectra to the observed spectra considering α element (O, Ne, Mg, Si, S, Ar, Ca and Ti) abundance ([α/Fe]) and [Fe/H] as additional free parameters. As this is still an ongoing work, for the analysis presented in this thesis we used the parameters derived by Kounkel et al. (2018).

Particularly, the parameters of interest for this project from the APOGEE-2 spectra are T_{eff} and RV. For the APOGEE-2 fields in 25 Ori, the typical T_{eff} uncertainties are 40 K but they significantly increase for sources with $T_{eff} > 6250$ K. In the case of the RV errors, the typical values are 0.5 km s^{-1}.

3.3.2 Spectra Analysis

3.3.2.1 Membership Assignment

The APOGEE-2 targets selection was not totally impervious to contamination from background and, in a lesser degree, from foreground field stars. For this reason, in order to select the 25 Ori members we applied distance, RV and spatial distribution criteria, similarly to those used for the MES spectra in Section 3.2.2, assuring consistent values with those expected for the 25 Ori population. About 90% of all the targets in the Ori OB1ab-E and OB1ab-F fields have reliable BJ18 distances (errors less than 20%) and there are 353 sources satisfying the distance and RV criteria, out of which 153 lie inside the 1° radius area of 25 Ori. This sample of 25 Ori members spans H-band mangitudes between 8.4 and 12.2. From these 153 members in 25 Ori, 56 of them were confirmed before through spectroscopic studies by Briceño et al. (18 sources; 2005), Briceño et al. (9 sources; 2007), Downes et al. (8 sources; 2014), Suárez et al. (3 sources; 2017c) and Briceño et al. (18 sources; 2019). All of these members have H-band magnitudes fainter than 10.6 mag (1.3 $M_{\odot}$). Therefore, we confirmed 97 new members of 25 Ori using APOGEE-2 spectra.

There are 9 additional previously confirmed 25 Ori members (2 from Briceño et al. 2005, 1 from Briceño et al. 2007, 1 from Downes et al. 2014 and 5 from Briceño et al. 2019) with APOGEE-2 spectra that we did not recover after applying our membership criteria; 2 of them because they have distances of 180 ± 2 and 545 ± 87 pc and the remaining 7 members because they do not have Gaia DR2 parallaxes (4 sources) or their parallaxes or RVs have errors larger than 20% (3 sources).

3.3.2.2 Radial Velocity Dispersion

With the sample of confirmed members from the APOGEE-2 spectra, we analyzed their radial velocities to obtain the velocity dispersion (σ_{RV}). In Figure 14 we show the radial velocity distributions of all the APOGEE-2 targets lying inside 25 Ori (1° radius area) and for the distance filtered targets as well as for the previously confirmed members. The most prominent peak corresponds to the 25 Ori population and has a mean value of 20.9 ± 2.0 km s^{-1}, considering the previously confirmed members with APOGEE-2 RVs or the APOGEE-2 targets filtered by their distances and removing those with RV larger than 28 km s^{-1}. This mean RV and velocity dispersion are very consistent with that obtained by Briceño et al. (19.7 ± 1.7 km s^{-1}; 2007, and references therein) working with a smaller sample of 47 members of 25 Ori. Also, the velocity dispersion from the RV study is consistent with the typical value of 1-3 km s^{-1} for a sample of 28 clusters and associations with ages of $\sim 1 - 5$ Myr by Kuhn et al. (2019).

The velocity dispersion we obtained in this section supports the confirmation of 25 Ori as a gravitationally unbound association in Section 2.4.5, when comparing its velocity dispersion with its escape velocity. With this velocity dispersion we also estimate that the crossing time,

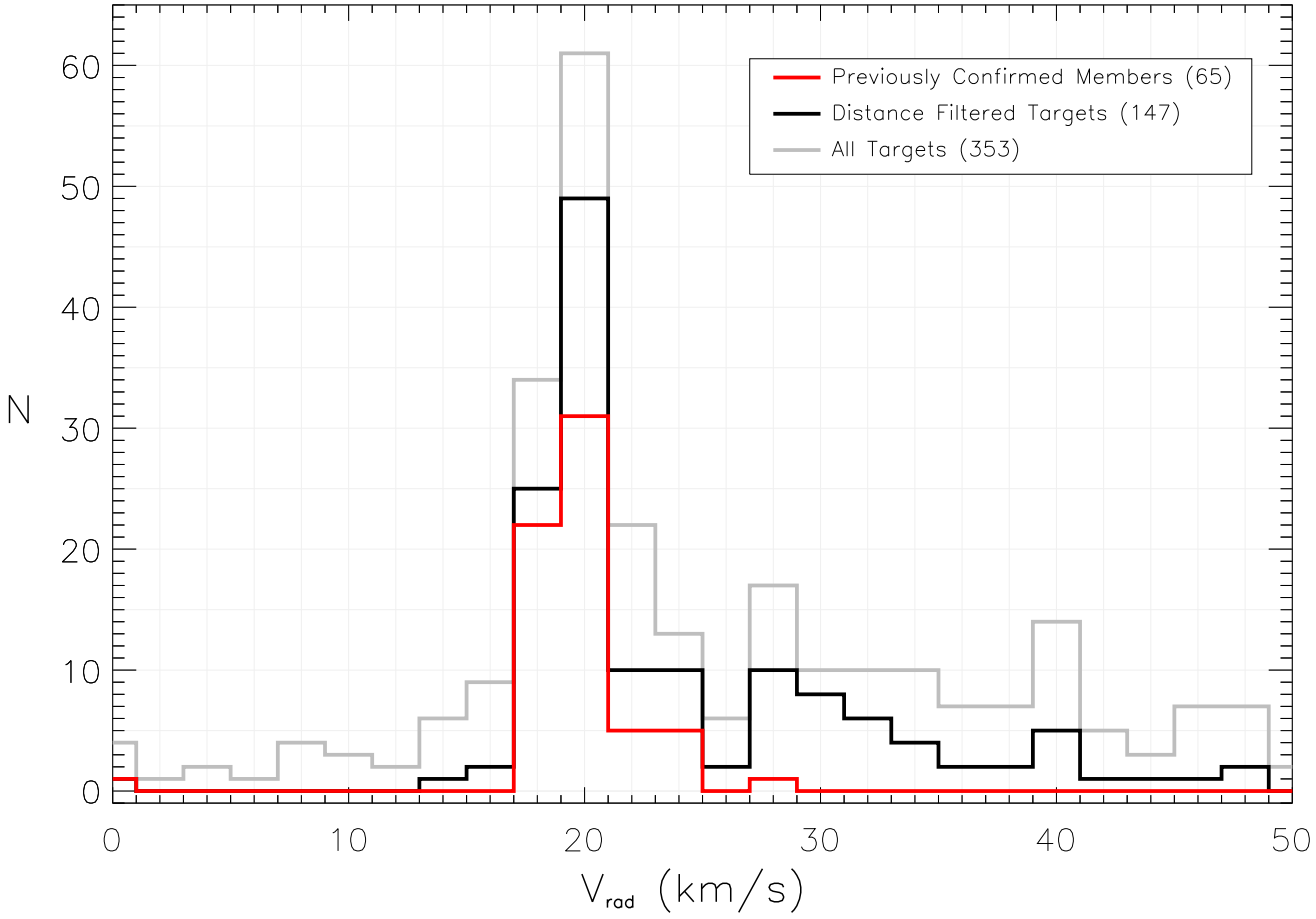

Figure 14: Radial velocity distributions of all the APOGEE-2 targets inside 25 Ori (gray histogram), of the targets after applying the distance criterion (black histogram) and of the spectroscopically confirmed members in the literature with RV from APOGEE-2 (red histogram).

$t_{cross} = 2r_{hm}/\sigma_{RV}$, of 25 Ori is 3.0 Myr, considering a half-mass radius $r_{hm} \approx 3$ pc, obtained from the system IMF we derived in Suárez et al. (2019). This crossing time corresponds to a relaxation time, $t_{relax} \simeq \frac{N}{8\ln N} t_{cross}$ (Binney & Tremaine, 2008), of about 32 Myr. As the 25 Ori age is ∼7 Myr, this implies that the groups is dynamically young and has not had time enough to relax through interactions between the members.

Additionally in Figure 14, we observed a second peak at about 28 km s^{-1} that can be due to the presence of dispersed OB1a population or even to overlapping members of OB1b (Orion C and D; Kounkel et al., 2018), which have RVs of ∼ 24 (Jeffries et al., 2006) and 30.1 ± 1.9 km s^{-1} (Briceño et al., 2007), respectively.

3.3.2.3 Physical Parameters

After we applied the membership criteria to the APOGEE-2 spectra in the OB1ab-E and OB1ab-F fields, we estimated the physical parameters of interest for the resulting 25 Ori members. For this purpose, we developed a custom computer program, which we describe below.

3.3.2.3.1 PHYPAR Routine

For the estimation of the bolometric luminosity (L_{bol}), mass and age of young stellar and substel-

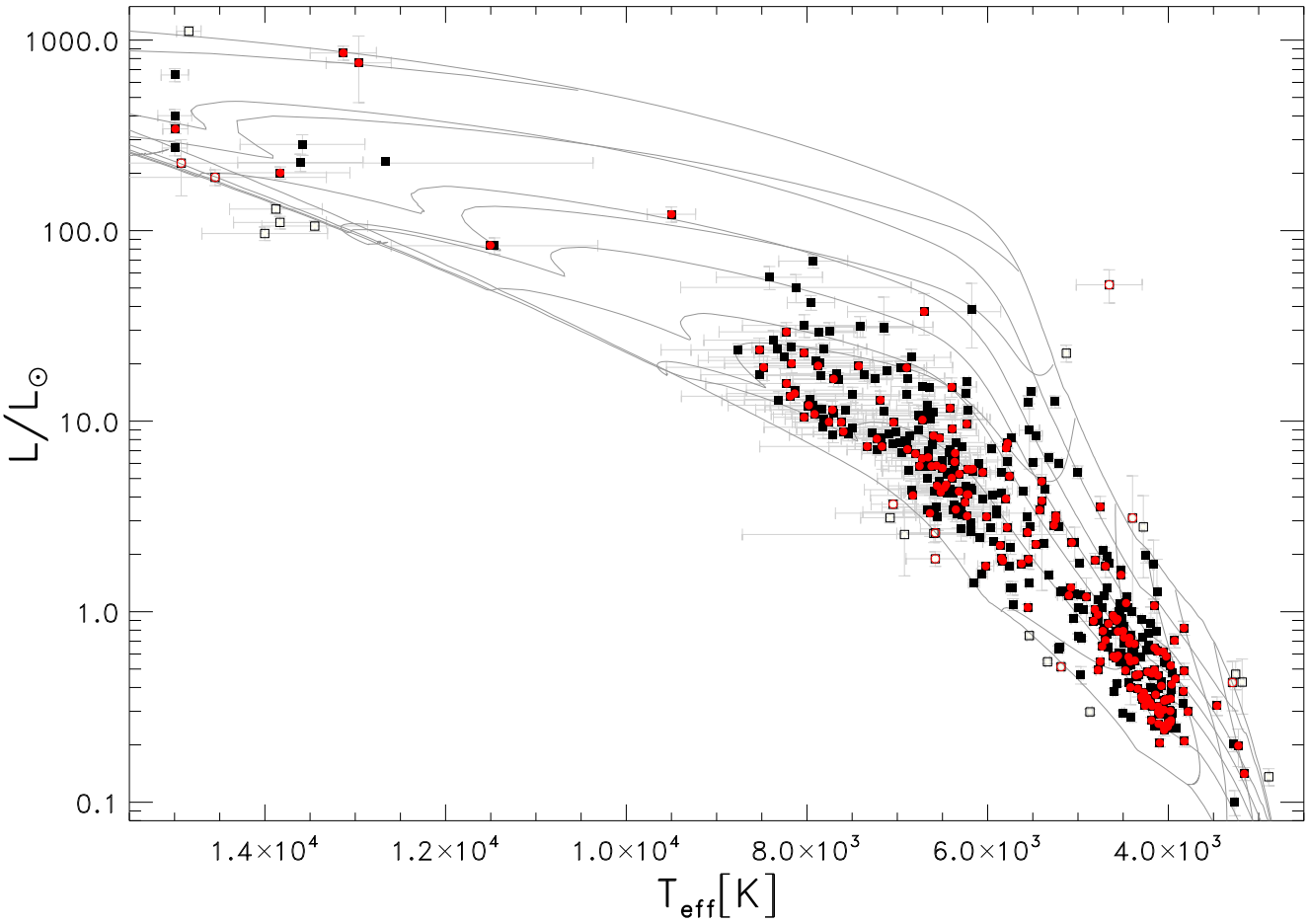

Figure 15: H-R diagram of the confirmed members in the APOGEE-2 OB1ab-E and OB1ab-F fields (black squares) and of the members lying inside the 25 Ori area of 1° radius (red circles). The gray curves represent the PARSEC evolutionary tracks for 0.3, 0.5, 0.7, 1.0, 2.0, 3.0, 4.0 and 5.0 $M_{\odot}$ and the PARSEC-COLIBRI isochrones for 0.5, 1, 2, 3, 5, 10 and 30 Myr. The open symbols indicate the members without mass and age estimates because they lie outside the model grid.

lar objects, I developed the PHYPAR IDL routine (see Appendix D), which has been succesfully used in several contributions (Suárez et al., 2017c; Kounkel et al., 2018; Ramírez-Preciado et al., 2018). The input parameters are distance, T_{eff}, A_V, and a photometric band magnitude together with their uncertainties. So far, the code works with magnitudes in the G, V, R, I, J, H or K photometric bands.

First, the magnitudes are dereddened using the input A_V and assuming the Cardelli et al. (1989) coefficients for all the photometric bands less that from Gaia or the coefficient $C_G = 0.9145$ (J. Hernández, private communication) for the G magnitudes. Then, the distance modulus is added to the dereddened magnitudes to obtain the absolute magnitudes. These magnitudes are then converted to bolometric magnitudes using the bolometric corrections obtained by interpolating T_{eff} in the Kenyon & Hartmann (1995) relation combined with the Luhman (1999), Briceño et al. (2002) and Luhman et al. (2003b) relations for the LMSs and BDs. Then, the bolemetric magnitudes are converted to L_{bol}. Finally, T_{eff} and L_{bol} are interpolated into stellar evolution models to obtain masses and ages for the sources lying inside a defined region of the model grid. This region is defined according to the expected masses and ages of the sources, which avoids

degeneracy when the stellar model also includes post-MS stages. The code uses the BT-Settl or PARSEC-COLIBRI isochrones, which allows to cover a wide mass range (from planetary masses to tend of solar masses) for sources in the PMS or MS.

The errors for each parameter are obtained as follows: *i*) when each of the above steps involve an equation, the uncertainties are computed by using the corresponding error propagation rule and *ii*) when an interpolation is done, the error is defined as the standard deviation of the resultant values from the interpolation of 10^3 artificially generated numbers drawn from a normal distribution centered at the parameter value and with a standard deviation equal to one third its error (this way 99.7% of the random values are within the uncertainties).

3.3.2.3.2 Parameters

Before using the PHYPAR code for the resulting confirmed members, we estimated A_V by using photometry from the Gaia DR2 and 2MASS catalogs and T_{eff} from the APOGEE-2 spectra. We compared the observed $G-J$ and $G_{BP}-G_{RP}$ colors with the intrinsic colors obtained by interpolating T_{eff} into the PARSEC-COLIBRI 7 Myr isochrone and then transforming the color excesses to A_V. When this resulted into a negative extinction, which can be due to the T_{eff} errors and/or magnitude uncertainties, we assigned null values. We computed the A_V uncertainties with the same method described in Section 3.3.2.3.1. For most of the sources, the A_V values obtained using only Gaia DR2 photometry are in agreement with those combining Gaia DR2 with 2MASS. The resultant A_V from the Gaia DR2 photometry are lower than 1.8 mag, but most of them ($\approx$75%) have values lesser than 1 mag. The mean extinction, $\bar{A_V}$, we obtained is 0.39 ± 0.40 mag, considering sources with values lower than 1 mag. This low extinction is consistent with previous works (Suárez et al., 2019, and references therein).

Then, the L_{bol}, mass and age of the APOGEE-2 members were obtained using the PHYPAR routine with distances from BJ18, T_{eff} from the APOGEE-2 spectra, A_V derived here from the Gaia DR2 photometry and G magnitudes from Gaia DR2 as well as the PARSEC-COLIBRI isochrones. In Figure 15 we show the H-R diagram of the members from the APOGEE-2 spectra. The masses of these members in 25 Ori ranges between 0.3 and 5.2 $M_\odot$. The mean age we obtained is 7.2 ± 3.6 Myr, which is very consistent with previous studies in 25 Ori (6.1±2.4 Myr by Briceño et al., 2019, and references therein).

3.4 SDSS-III/BOSS for Low-Mass Stars (Suárez et al., 2017c)

The following analysis constitutes the publication "New Low-Mass Stars in the 25 Orionis Stellar Group and Orion OB1a Sub-association from SDSS-III/BOSS Spectroscopy" by Suárez et al. (2017c), which was carried out as part of this dissertation.

Abstract. The Orion OB1a sub-association is a rich low mass star (LMS) region. Previous spectroscopic studies have confirmed 160 LMSs in the 25 Orionis stellar group (25 Ori), which is the most prominent overdensity of Orion OB1a. Nonetheless, the current census of the 25 Ori members is estimated to be less than 50% complete, leaving a large number of members to be still confirmed. We retrieved 172 low-resolution stellar spectra in Orion OB1a observed as ancillary science in the SDSS-III/BOSS survey, for which we classified their spectral types and determined physical parameters. To determine memberships, we analyzed the H_α emission, LiIλ6708 absorption, and NaI$\lambda\lambda$8183, 8195 absorption as youth indicators in stars classified as M-type. We report 50 new LMSs spread across the 25 Orionis, ASCC 18, and ASCC 20 stellar groups with spectral types from M0 to M6, corresponding to a mass range of $0.10 \leq m/M_\odot \leq 0.58$. This represents an increase of 50% in the number of known LMSs in the area and a net increase of 20% in the number of 25 Ori members in this mass range. Using parallax values from the Gaia DR1 catalog, we estimated the

distances to these three stellar groups and found that they are all co-distant, at 338±66 pc. We analyzed the spectral energy distributions of these LMSs and classified their disks by evolutionary classes. Using H-R diagrams, we found a suggestion that 25 Ori could be slightly older that the other two observed groups in Orion OB1a.

3.4.1 Introduction

Comprehensive studies of known OB associations in terms of their stellar populations and structural properties provide a firm basis to the understanding of how young star aggregations form and evolve until they eventually disperse to be part of the Galactic disk component. Particularly useful in this respect are the $\sim$ 10 Myr *fossil star forming regions* (FSFRs; Blaauw, 1991), where one would expect that: *i*) the dust and gas are largely dispersed, and extinction is generally low, permitting the detection of low mass stars (LMSs), *ii*) the members are still spatially concentrated and can be distinguished from the field population, *iii*) only a minority of stars retain optically thick circumstellar disks, *iv*) the active star formation was ceased but its products are still present, *v*) accretion is essentially over, so the objects have attained their final masses, and *vi*) the stars can be considered nearly coeval.

The properties of the LMSs in the FSFRs are of particular importance to understand/clarify the structure and dispersal processes acting on such stellar populations, the circumstellar disk evolution and the possible large-scale dynamical effects. In fact, such studies are not possible solely from the observation of massive stars, as the LMSs do have relatively large PMS phases, they are characterized by the presence of evolving disks, variable mass accretion and circumstellar and chromospheric activity. Furthermore, they make up the majority of all the stars formed in clusters in terms of number and mass (e.g., Bastian et al., 2010), and have long lifetimes ($> 10^{10}$ yr) in the MS.

The Orion OB1 association is one of the largest and nearest star forming regions (e.g. Genzel & Stutzki, 1989; Bally, 2008; Briceno, 2008) and contains four distinct sub-associations, which can be distinguished according to their ages and content of gas and dust (Blaauw, 1964). With an age of 7-10 Myr and a distance of $\sim$330 pc (e.g., Briceño et al., 2005), Orion OB1a is the oldest and closest of the Orion OB1 sub-associations. Considering the critical age of 10 Myr, Orion OB1a is an excellent region for studying the early evolution of LMSs. Particularly important is the 25 Orionis stellar group (25 Ori), one of the most numerous and spatially dense 7-10 Myr old populations (r$\sim$ 7 pc, $\Sigma \sim$ 128 stars deg^{-2}) known within 500 pc from the Sun (Briceño et al., 2007).

As mentioned in Downes et al. (2014), there are other associations of similar age to 25 Ori, but these regions cover relatively extended areas in the sky or are too distant to enable the detection of their LMSs. 25 Ori's unique combination of its distance, age, and area in the sky (360 pc, $\sim$ 7 Myr, and $\approx$ 3 deg^2; Briceño et al., 2005, 2007; Downes et al., 2014), makes it a particularly convenient region for studying the population of LMSs. Additionally, 25 Ori is almost free of extinction ($A_V \approx 0.30$ mag.; Kharchenko et al., 2005; Briceño et al., 2005, 2007; Downes et al., 2014).

Although 25 Ori is a clear spatial overdensity of young LMSs (Briceño et al., 2007; Downes et al., 2014), a level of contamination is expected close to 25 Ori from at least two other nearby 10 Myr old stellar groups, identified as ASCC 18 and ASCC 20 by Kharchenko et al. (2005, 2013). Thus, in order to disentangle these groups and identify the complete 25 Ori population, it is necessary to make a study that covers an area into those additional groups, beyond the proposed 25 Ori radius of 1° (Briceño et al., 2005, 2007).

Several spectroscopic studies have confirmed, to date, 160 LMS members of 25 Ori (Briceño

et al., 2005, 2007; Biazzo et al., 2011; Downes et al., 2014, 2015), which represent about 34% of its total estimated LMS members (Downes et al., 2014). In this paper, we analyze optical spectra obtained with the SDSS-III/BOSS spectrograph to confirm 50 additional young LMSs in Orion OB1a, of which 22 are inside the 25 Ori's estimated area (1° radius; Briceño et al., 2005, 2007). This increases the confirmed member sample of 25 Ori by about 20% in a mass range from 0.1 to 0.6 $M_\odot$. We characterize these new members according to their optical spectral types and spectral features, as well as infrared (IR) photometric signatures of circumstellar disks. The paper is organized as follows: In Section 3.4.2 we describe the optical and IR photometric data, and the optical spectroscopy from the SDSS-III/BOSS survey. In Section 3.4.3 we analyze the spectra and describe our results. In Section 3.4.4 we comment on particular objects and in Section 3.4.5 we discuss and summarize the results.

3.4.2 Observations

3.4.2.1 Optical Photometry

The V, R, and I photometry used in this work was obtained from the CIDA Deep Survey of Orion (CDSO) catalog (Downes et al., 2014), which was constructed by co-adding the multi-epoch optical observations from the CIDA Variability Survey of Orion (CVSO; Briceño et al., 2005; Mateu et al., 2012). The sensitivity limits of the CDSO covers the LMS and brown dwarf (BD) population of 25 Ori and its surroundings within the region $79.7° \lesssim \alpha \lesssim 82.7°$ and $0.35° \lesssim \delta \lesssim 3.35°$. The limiting magnitude of the CDSO photometry in this region is $I_{lim} = 22$ and the completeness magnitude is $I_{com} = 19.6$ (Downes et al., 2014), enough to assure an I band detection even for the faintest targets of our spectroscopic sample ($I \approx 17.0$).

Additionally, we used the u, g, r, i, and z photometry from the Sloan Digital Sky Survey (SDSS) catalog (Finkbeiner et al., 2004; Ahn et al., 2012). These values are listed in Table 10.

3.4.2.2 IR Photometry

The *Z, Y, J, H,* and *Ks* near-IR photometry used in this study was carried out by Petr-Gotzens et al. (2011) as part of the Visible and Infrared Survey Telescope for Astronomy (VISTA; Emerson et al., 2004) science verification surveys (Arnaboldi et al., 2010). The 5σ limiting magnitudes of the VISTA survey of the Orion star-forming region are $Z = 22.5$, $Y = 21.2$, $J = 20.4$, $H = 19.4$, and $Ks = 18.6$ mag, which are enough to have VISTA photometry even for the faintest objects in our spectroscopic sample ($J \approx 15.0$).

Additionally, we used near-IR photometry from the 2MASS catalog (Skrutskie et al., 2006) and mid-IR photometry from IRAC-*Spitzer* (Hernández et al., 2007a) and the WISE (Wide-field Infrared Survey Explorer) All-Sky catalog (Cutri & et al., 2013). This IR photometry is listed in Table 10.

3.4.2.3 Spectroscopy

The spectra used in this paper were obtained as part of the Baryon Oscillation Spectroscopic Survey (BOSS; Dawson et al., 2013), which is one of the four main surveys of SDSS (York et al., 2000) in its third phase (SDSS-III; Eisenstein et al., 2011). The BOSS spectrograph has plates with 1000 fibers of 2" diameter spanning a field of view of 3.0° in diameter and cover a wavelength range from 3560 Å to 10400 Å with a resolution of R=1560 at 3700 Å and R=2650 at 9000 Å(Gunn et al., 2006; Smee et al., 2013).

The spectra we analyzed were obtained as part of the *Star Formation in the Orion and Taurus Molecular Clouds* ancillary science program (Alam et al., 2015). The plate is centered around the B2 star 25 Orionis ($\alpha_{J2000} = 5^h24^m44^s.8$; $\delta_{J2000} = +1°50'47''.2$) and includes the stellar groups ASCC 16 (25 Ori), ASCC 18, and ASCC 20 (Kharchenko et al., 2013). The object selection process for this plate is described in detail in Section A2 by Alam et al. (2015) and is based on the cataloged optical and IR photometric properties (SDSS, WISE, 2MASS, Spitzer) of the objects. The integration time for the selected objects was 5 x 4500 s, achieving a typical S/N ratio of ∼20 for the faintest sources. The observation produced 677 spectra of which only 172 are stellar and the remaining 505 turned out to be spectra of galaxies and quasars, as explained in Section 3.4.3. In Figure 16 we show the spatial distribution of the targets observed in this plate (Alam et al., 2015), as well as the locations of the different stellar groups from Kharchenko et al. (2013). In Figure 17 we show the $u - K$ vs K-W3 color-color diagram including all the targets of the 25 Ori BOSS plate, where we can see that most of these targets have K-W3 colors redder than those expected from previously confirmed members. It is important to notice that this target selection implies a bias towards sources with IR excesses (e.g. stars with accretion disks, see Section 3.4.3.4).

The BOSS ancillary science programs made use of the `v5_7_2` version of the `idlspec2d` pipeline, which, together with `idlutils`, are the SDSS pipelines used for the data reduction[7]. A detailed explanation of the automated classification and the redshift measurements was provided by Bolton et al. (2012).

The calibrated wavelengths of the BOSS spectra are in the vacuum reference. In order to recognize spectral lines and to use stellar templates to analyze the BOSS spectra, it is needed to convert wavelengths from vacuum to air. We used the IAU standard transformations, as given in Morton (1991).

3.4.3 Analysis and Results

In Figure 18 we show the I vs $I - J$ color-magnitude diagram for all the targets of the 25 Ori BOSS plate, together with the confirmed members in 25 Ori and Orion OB1a from Briceño et al. (2005, 2007); Downes et al. (2014, 2015). We also included the 25 Ori members from Briceño et al. (2019), which were selected according to their position in optical-near-IR color-magnitude diagrams and confirmed on the basis of youth indicators (e.g. H_α emission and NaIλ6708 absorption) and radial velocities, when available. Additionally, we included the photometric candidates from Hernández et al. (2007a); Downes et al. (2014). In this diagram, the confirmed members form a very clear locus, nicely separated from the Galactic disk dwarf stars and giant star branches, as well as from extragalactic sources. This shows that the combination of optical and near-IR photometry in color-magnitude diagrams allow for a clear selection of photometric candidates in regions like Orion OB1a (e.g., Downes et al., 2014).

The BOSS spectra in the DR12 archive are provided with a spectral classification as well as an object classification (star, galaxy or quasar). The stellar templates used for this automated classification are mainly selected from The Indo-US Library (Valdes et al., 2004), which is focused on F- and early G-type stars. The library was supplemented for cool stars by theoretical atmosphere models computed using the MARCS models (Gustafsson et al., 2008). The M-type stellar templates in the database are representative of giant stars with effective temperature down to 3000 K, and a grid resolution of 500 K (Palacios et al., 2010). Thus, these templates are generally not suitable for the spectral type classification of young dwarf stars. Also, the grid resolution in effective temperature of the templates is not enough for the diversity of M-type stars present in our sample. Thus, to determine accurate physical parameters for the BOSS stars (extinction,

[7] *SDSS data processing software is publicly available at* `http://www.sdss.org/dr12/software/products/`

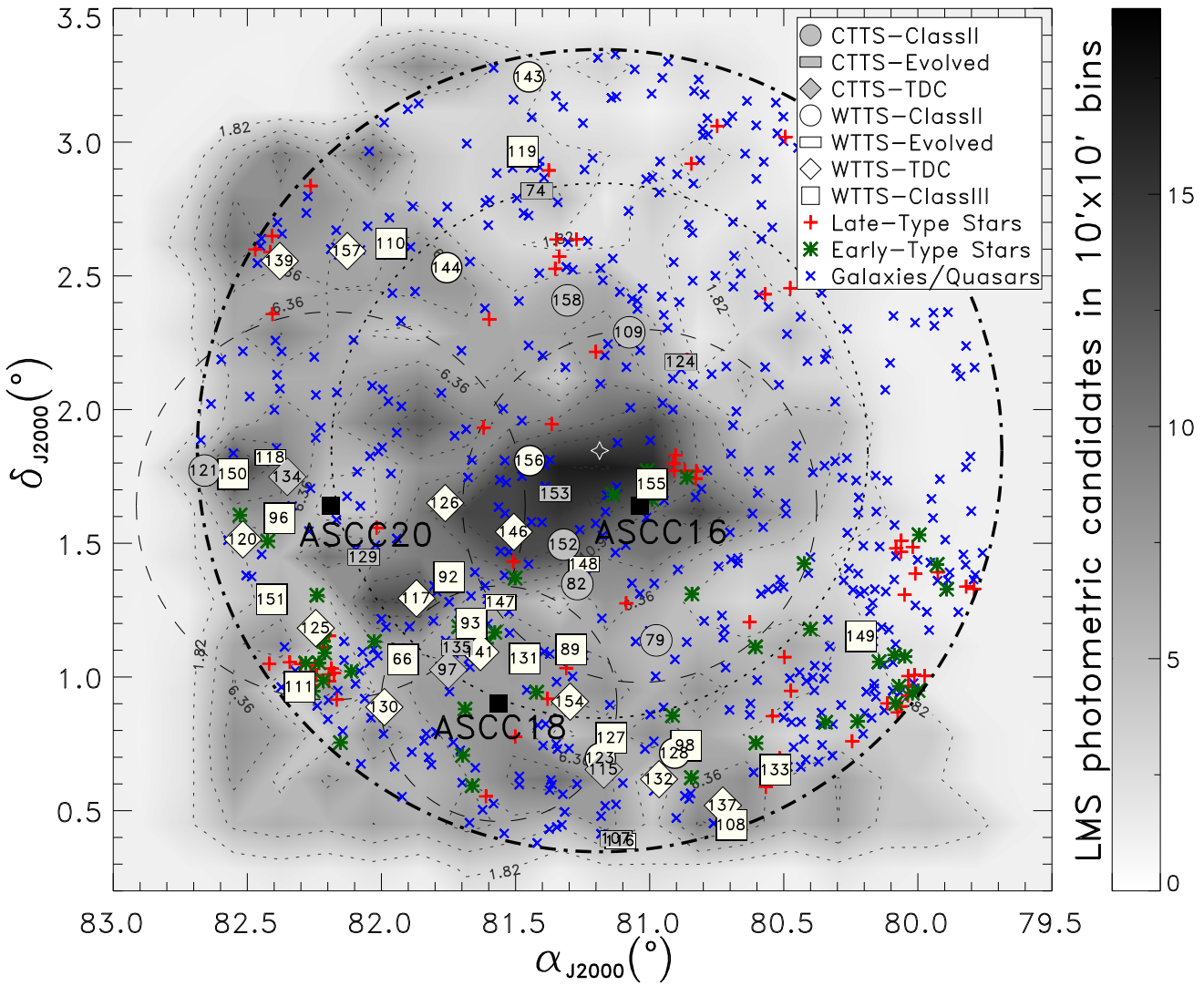

Figure 16: Spatial distribution of the confirmed members of 25 Ori or Orion OB1a classified as CTTSs and WTTSs on the BOSS plate dedicated to 25 Ori (thick dashed-dotted circle); see Sections 3.4.3.2 and 3.4.3.4. The labeled circles, horizontal bars, diamonds, and squares represent YSOs classified as Class II objects, evolved systems, TDC or Class III objects, respectively, as shown in the label box (see Section 3.4.3.5). The dotted circle represents the estimated area of 25 Ori (1° radius; Briceño et al., 2005, 2007). The red plus signs, green asterisks, and blue cross signs indicate, respectively, stars later than G spectral type, G-type or earlier stars, and the galaxy/quasar samples. The black filled squares and the dashed circles around them represent, respectively, the central position and estimated area of the labeled stellar groups from Kharchenko et al. (2013). The gray background map and the labeled isocontours indicate the LMS and BD photometric candidate density in 10'x10' bins from Downes et al. (2014). The white star sign at the center represents the position of the 25 Orionis star.

effective temperature, bolometric luminosity, age, and mass), it is important to verify the SDSS spectral type classification independently. We visually inspected all spectra on the 25 Ori BOSS plate, confirming all objects correctly classified as stars by SDSS, and also identifying those sources for which the SDSS classification was incorrect, either stars classified as galaxies or quasars or, conversely, galaxies or quasars as stars. Through this process, we found 172 stellar spectra out of

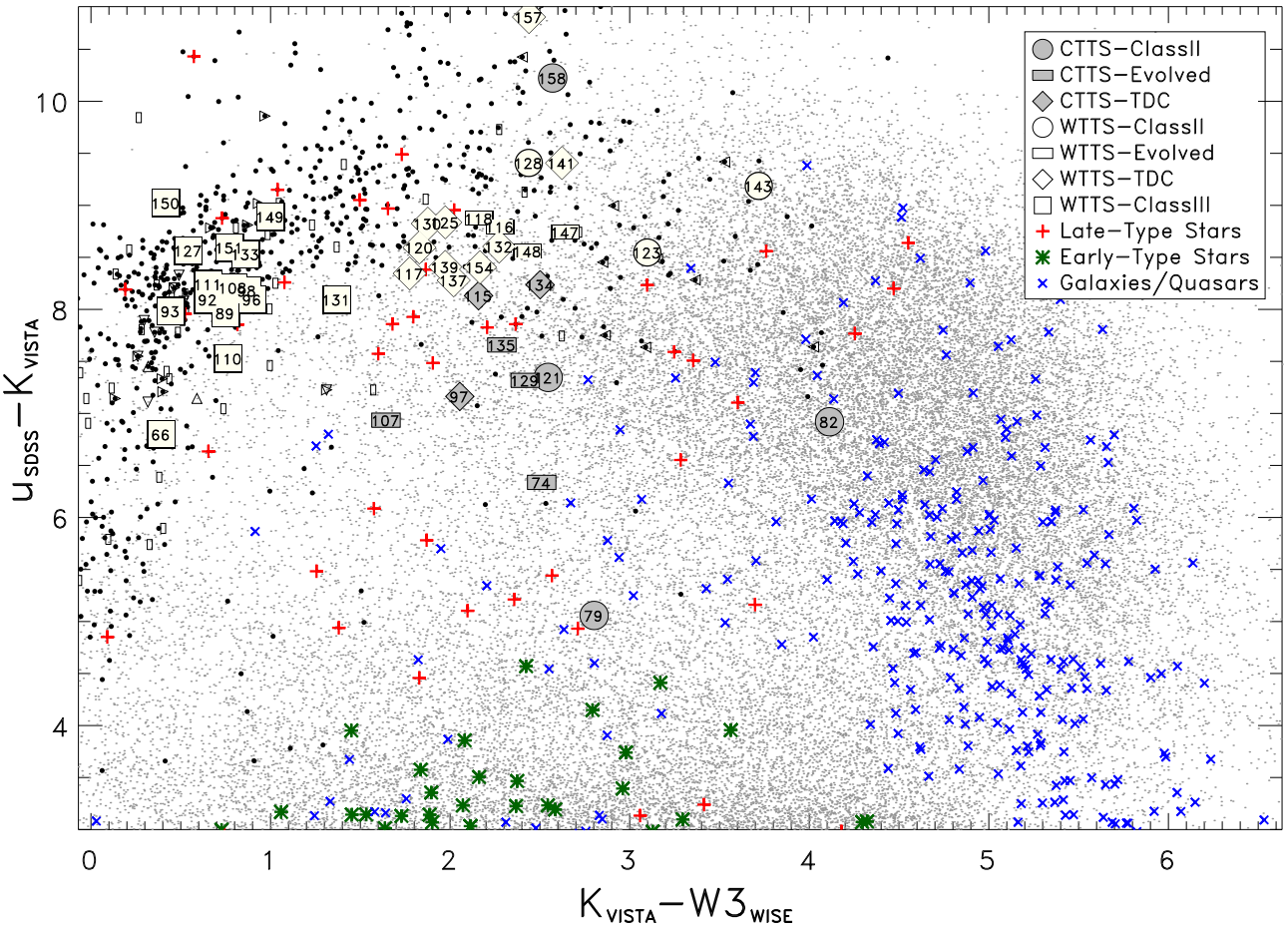

Figure 17: Color-color diagram showing the targets observed in the 25 Ori BOSS plate. The open upward triangles, downward triangles, rightfacing triangles, leftfacing triangles, and vertical bars indicate, respectively, previously confirmed members by Briceño et al. (2005, 2007); Downes et al. (2014, 2015); Briceño et al. (2019). The black points represent the LMS and BD photometric candidates from Downes et al. (2014), which were selected with an efficiency of $\sim 86\%$ from color-magnitude diagrams where a bias toward sources with IR excesses is not expected. The gray points show the SDSS+VISTA+WISE detections in the 25 Ori BOSS plate field of view. The rest of the symbols are indicated in the label. Note that the gray labeled symbols represent young stars showing intense H_α emission, as explained in Section 3.4.3.4.

a total of 677 targets observed on the 25 Ori BOSS plate. The 505 remaining spectra from this plate correspond to either galaxies or quasars, as shown in Figure 16.

3.4.3.1 Spectral Classification

We used the SPTCLASS[8] semi-automatic code (Hernández et al. 2004; extended to classify the M spectral type regime as published in Briceño et al. 2005) to derive spectral types for the 172 stars on the 25 Ori BOSS plate. The code uses empirical relations between the equivalent widths of several effective temperature-sensitive spectral features and the spectral types. Particularly, we are interested in the LMS regime, where the SPTCLASS code uses 10 TiO molecular bands in the wavelength range 4775-7150 Å and six VO molecular bands in the mid part of the spectra from

[8] *http://www.cida.gob.ve/~hernandj/SPTclass/sptclass.html*

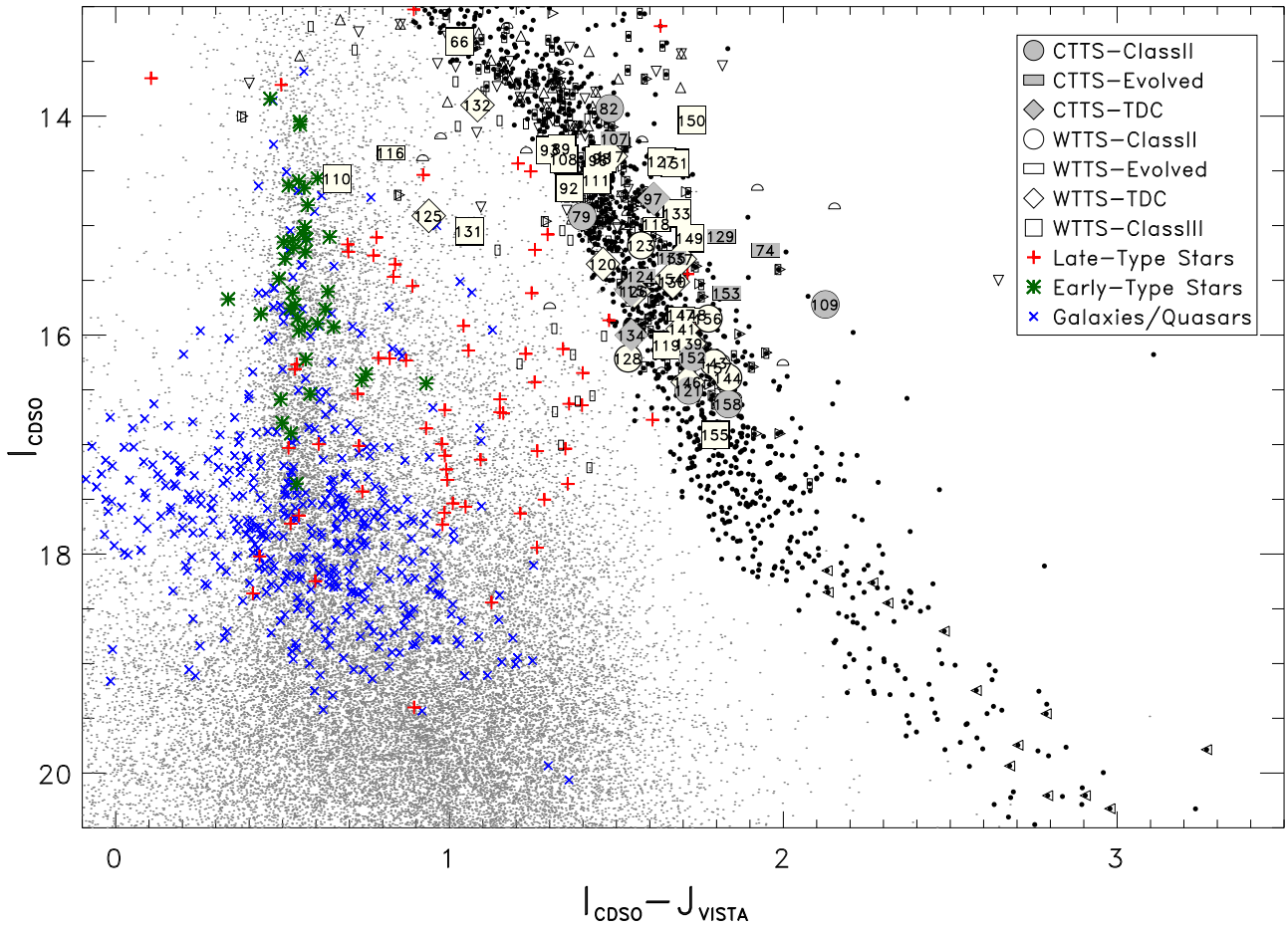

Figure 18: Color-magnitude diagram from the CDSO and VISTA catalogs. The black points and open small symbols are as in Figure 17. The open half circles represent the photometric candidates from Hernández et al. (2007a). The gray points show the CDSO+VISTA detections in the 25 Ori BOSS plate field of view. The rest of the symbols are indicated in the label.

7460 to 8880 Å. For the LMSs, the typical uncertainties from our spectral type classification are ±0.7 spectral sub-classes, while these increase up to ±5 spectral sub-classes for stars earlier than G-type. In Figure 19 we show the residuals between our spectral types using the SPTCLASS code and the spectral types assigned by the SDSS pipeline. Roughly 30% of the spectra have differences between these two spectral type classifications of more than three spectral sub-classes, especially for the stars with earlier spectral types. There seems to be a trend for stars later than M0, which is due to the fact that most of the M-type stars in our sample are classified as M5 by the SDSS automated classification algorithm. By visually comparing those spectra with the largest spectral type residuals against templates of young and old field stars from Luhman (2000), Briceño et al. (2002), Luhman et al. (2003b) Luhman (2004), and Kirkpatrick et al. (1999), respectively, we can confirm that our SPTCLASS classification is always more accurate than the SDSS classification. Therefore, for the rest of this work we use the spectral type classification from the SPTCLASS code, which has been extensively used and proven to be accurate and efficient for stars in the spectral type and age ranges considered in this work (e.g. Briceño et al., 2007; Hernández et al., 2007a; Downes et al., 2014). This classification covers a spectral type range from A5 to M6, with more than a half of the sample being M-type stars. Spectral types of our confirmed members of 25 Ori or Orion OB1a on the BOSS plate (see Section 3.4.3.2) are listed in Table 11. In Table 17

Table 10: Photometric catalog of the confirmed members of 25 Ori or Orion OB1a.

ID	α_{J2000}	δ_{J2000}	SDSS					CDSO		
			u	g	r	i	z	V	R	I
66	81.919314	1.065933	18.281	15.971	14.664	14.256	13.48	15.194	14.336	13.318
74	81.421671	2.818307	18.326	17.989	17.294	16.394	15.679	17.935	16.772	15.223
79	80.975436	1.136898	17.565	17.46	16.39	15.777	15.051	16.832	15.932	14.917
82	81.269534	1.347489	18.175	17.499	16.287	15.147	14.329	16.621	15.302	13.93
89	81.292164	1.102412	20.133	17.362	16.228	15.094	14.409	16.829	15.738	14.297
92	81.747728	1.373077	20.591	18.091	16.675	15.412	14.743	17.287	16.203	14.657
93	81.664785	1.200688	20.171	17.681	16.272	15.092	14.445	16.878	15.789	14.309
96	82.379687	1.594114	20.233	17.702	16.291	15.081	14.415	16.926	15.903	14.404
97	81.75054	1.026903	19.279	18.115	16.778	15.467	14.674	17.569	16.325	14.755
98	80.864815	0.743855	20.267	17.855	16.422	15.156	14.419	17.061	16.022	14.386

VISTA					2MASS			IRAC				WISE			
Z	Y	J	H	K	J	H	K	CH1	CH2	CH3	CH4	W1	W2	W3	W4
13.278	12.907	12.286	11.689	11.483	12.114	11.428	11.27	...	...	...	...	11.242	11.183	11.092	8.305
14.415	13.89	13.275	12.563	11.989	13.585	12.862	12.353	...	...	...	...	11.403	10.89	9.479	7.651
14.628	14.094	13.519	12.941	12.507	13.5	12.757	12.295	...	...	...	...	11.752	11.259	9.705	7.639
13.467	12.803	12.45	11.748	11.255	12.457	11.666	11.059	10.043	...	9.22	...	10.167	9.494	7.142	5.08
13.867	13.446	12.96	12.382	12.17	12.969	12.321	12.082	...	...	...	...	12.001	11.861	11.42	8.552
14.167	13.776	13.297	12.715	12.496	13.357	12.734	12.54	12.208	...	12.209	...	12.35	12.216	11.843	8.279
13.914	13.479	13.007	12.392	12.188	13.079	12.386	12.155	...	...	...	...	12.036	11.912	11.743	8.913
13.906	13.444	12.957	12.374	12.138	13.02	12.355	12.109	...	...	...	...	11.991	11.852	11.239	8.369
14.133	13.661	13.143	12.501	12.116	13.18	12.47	12.102	...	...	...	...	11.587	11.176	10.062	7.028
13.972	13.428	12.928	12.343	12.087	12.976	12.321	12.028	...	...	...	...	11.961	11.805	11.216	8.441

(The complete version of this table is available in the electronic version of the Suárez et al. 2017c publication.)

we list the spectral types of all the stars rejected as members on the 25 Ori BOSS plate.

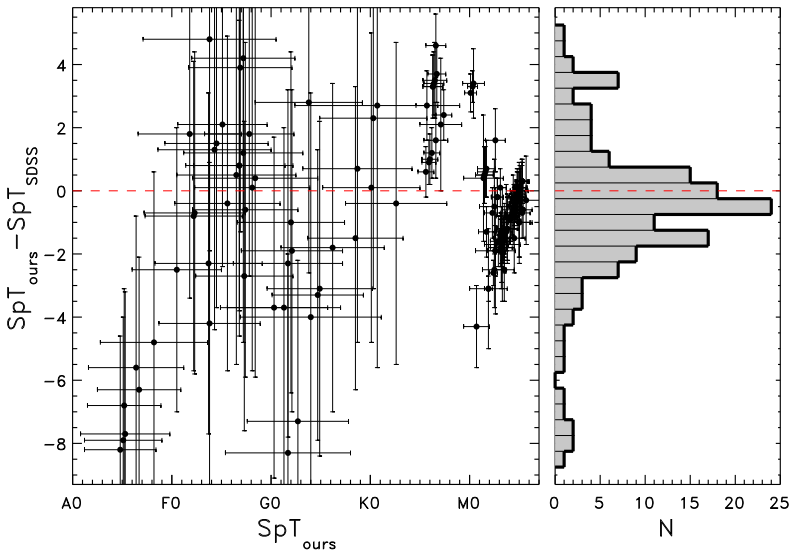

Figure 19: Residuals between our spectral type classification using the SPTCLASS code (Hernández et al., 2004) and the spectral type assigned by the SDSS pipeline. The associated errors are those estimated by the SPTCLASS code because the SDSS classification does not report spectral type uncertainties. The residuals are given in units of spectral subclasses.

3.4.3.2 Membership Determination for 25 Ori and Orion OB1a

Once the spectral type was determined for all the stars on the 25 Ori BOSS plate, several diagnoses were applied to determine their memberships, depending on their spectral types.

3.4.3.2.1 M-type Stars

The following criteria were used to assign the 25 Ori and Orion OB1a memberships of the M-type stars:

- H_α emission.

  The detection of strong H_α emission in young LMSs is due to both the chromospheric activity and accretion phenomena that produce narrow symmetric and broader asymmetric H_α line profiles (Muzerolle et al., 2005), respectively. We considered as possible M-type members those stars showing H_α emission. However, because at the age of 25 Ori most of the accreting circumstellar disks have dissipated (Calvet et al., 2005), not only those sources having strong emissions related to accretion are necessary members. Thus, additional criteria are needed to support the memberships of those objects showing weak H_α emission.

- LiIλ6708 absorption.

  For LMSs, the LiIλ6708 absorption is a well-known indicator of youth (Strom et al., 1989; Briceño et al., 1998). It is present in the stellar surface of LMSs because they are fully convective in the PMS phase and the mixing timescale is shorter than the time they need to reach the MS (Soderblom et al., 1993). Therefore, we used the presence of the LiIλ6708 absorption as an additional membership criterion for the LMSs.

- Weak NaI$\lambda\lambda$8183, 8195 doublet in absorption relative to a field star of the same spectral type.

  An additional youth indicator for the M-type stars is the NaI$\lambda\lambda$8183,8195 doublet in absorption, which is sensitive to surface gravity. Since the PMS stars are still contracting, they have lower surface gravity than MS stars with the same spectral type, such that the NaI$\lambda\lambda$8183, 8195 doublet is measurably weaker in PMS sources (Luhman et al., 2003a). We compared the BOSS M-type spectra with templates for young and old field stars with the same spectral type from, respectively, Luhman (2000), Briceño et al. (2002), Luhman et al. (2003b) and Luhman (2004), and Kirkpatrick et al. (1999), to determine if the NaI$\lambda\lambda$8183,8195 doublet is consistent with the weak absorption expected for a bona fide young star.

Summarizing these criteria, we confirm a M-type star as a 25 Ori or Orion OB1a member if it exhibits any level of H_α emission and either LiIλ6708 absorption or NaI$\lambda\lambda$8183, 8195 absorption whose profile agrees with a young stellar template of the same spectral type. Based on these criteria, we confirmed a total of 53 members of 25 Ori or Orion OB1a with spectral types from M0 to M6. Three of these members (148, 153, and 156) have already been confirmed as young members by Downes et al. (2014), so we can report the finding of a total of 50 new confirmed members of 25 Ori or Orion OB1a. In Table 11 we summarize the membership criteria for these confirmed members. About 87% of the M-type confirmed members have LiIλ6708 absorption equivalent widths W(LiI)>0.15 Å and the rest have a clear weak NaI$\lambda\lambda$8183, 8195 doublet. The 81% of the members have the NaI$\lambda\lambda$8183, 8195 doublet in absorption consistent with the young stellar templates and for most of the remaining members the NaI$\lambda\lambda$8183, 8195 is not conclusive but they show a clear LiIλ6708 absorption. As an example, in Figure 20 we show the spectrum of the member 157 with enlargements of the H_α emission, LiIλ6708 absorption and weak NaI$\lambda\lambda$8183, 8195 absorption youth indicators we used to assign its membership.

The 50 new confirmed members represent an increase of $\approx$ 30% the number of known sub-solar members of 25 Ori or Orion OB1a in the region covered by the considered BOSS plate (Briceño et al., 2005, 2007; Hernández et al., 2007a; Downes et al., 2014, 2015). Of these members, 22 are inside the Briceño et al. (2005, 2007) estimated area of 25 Ori (1° radius), which represents an increase of $\approx$ 14% in the number of 25 Ori confirmed members in the sub-solar mass range. Throughout this study, we conservatively worked with the 25 Ori estimated radius of 1°, which is greater than the 0.5° radius of the 25 Ori overdensity estimated by Downes et al. (2014).

3.4.3.2.2 K-type Stars

The H_α emission and LiIλ6708 absorption membership criteria discussed in Section 3.4.3.2.1 also apply for the K-type stars. Therefore, K-type stars were selected as YSOs when presenting H_α emission and LiIλ6708 absorption. From the 20 K-type stars in the BOSS stellar spectra, we did not confirm any K-type member. None present both LiIλ6708 absorption and H_α emission (only two stars have weak H_α emission, but those lack LiIλ6708 absorption).

3.4.3.2.3 Early-type Stars

The membership criteria discussed in Section 3.4.3.2.1 cannot be applied to stars earlier than K-type (43 stars of the sample). In fact, there is not a clear way to confirm these stars as young members with the available information. We checked the position of these stars in the I vs $I-J$ color-magnitude diagram. We found that not a single early-type star lies within the 25 Ori locus, even when considering the effects of variability. The position of these stars is consistent with the field stars.

The most robust membership diagnostic for stars earlier than K spectral type is their kinematics, though X-ray emission, IR excesses or variability are useful secondary indicators. The spectral resolution of BOSS is not high enough to provide precise radial velocities to determine kinematic memberships for these early type stars, so we checked the other criteria. None of these stars have X-ray counterparts in the 3XMM-DR5 database (Rosen et al., 2016) or in the Chandra Source Catalog (Evans et al., 2010). Additionally, none of these stars are high-probability variable stars according to the CVSO catalog or have IR excesses according to the photometric selection from Cottle et al. (2018), based on 2MASS+WISE photometry and the algorithm developed by Koenig & Leisawitz (2014). Therefore, the stars earlier than K spectral type on the 25 Ori BOSS plate are likely non-members.

3.4.3.3 Physical Parameters

As described in Luhman (1999), the I and J bands are preferred to estimate bolometric luminosities of young LMSs because the contamination from UV and IR excess emission is minimal. We used the I band from the CDSO and the J band from VISTA to determine the extinction and bolometric luminosity of our confirmed members.

3.4.3.3.4 Extinctions

The visual extinction (A_V) toward each confirmed member was calculated using the observed $I-J$ color, an assumed intrinsic $I-J$ color for a young star of the same measured spectral type and the extinction law from Fitzpatrick (1999), assuming $R_V = 3.1$. The adopted intrinsic $I-J$ color was obtained by interpolating the spectral type in the empirical relations from Kenyon & Hartmann (1995), Luhman (1999), Briceño et al. (2002), and Luhman et al. (2003a). These relationships were designed to match the Baraffe et al. (1998) tracks, as explained by Luhman et al. (2003b).

In Table 12 we list the extinctions we estimated toward each confirmed LMS member of 25 Ori or Orion OB1a. Removing the two members having the highest unexpected extinctions (member 74 and 109 with $A_V = 4.33^{+0.51}_{-0.98}$ and $A_V = 3.53^{+0.94}_{-1.01.}$ mag, respectively), we obtained a mean extinction $\bar{A_V}$=0.14 mag and a standard deviation $\sigma_{A_V} = 0.31$ mag toward the complete sample of confirmed members in 25 Ori and Orion OB1a, which is agreement with the mean extinction $\bar{A_V}$=0.16 mag, obtained by Downes et al. (2015). If we only consider the confirmed members inside the 25 Ori's estimated area, we obtain $\bar{A_V}$=0.21 mag and $\sigma_{A_V} = 0.43$ mag, which is also in

Table 11: Confirmed members and their youth indicators.

ID	SpT	WH_α (Å)	WLiIλ6708 (Å)	NaI
66	M0.3±0.5	-2.062	0.4257	0
74	M1.5±1.2	-161.8	0.2514	-1
79	M1.9±0.4	-247.7	0.3037	1
82	M2.4±0.4	-52.95	0.2569	1
89	M2.8±0.6	-5.843	0.1607	1
92	M3.1±0.5	-4.39	—	1
93	M3.1±0.5	-3.541	0.1659	1
96	M3.2±0.5	-4.448	0.3134	1
97	M3.2±0.5	-38.64	0.446	1
98	M3.2±0.6	-5.865	0.4586	1
107	M3.5±0.5	-39.31	0.2887	1
108	M3.5±0.6	-7.876	—	1
109	M3.5±1.0	-41.43	0.577	0
110	M3.5±1.1	-7.721	0.2379	1
111	M3.7±0.6	-4.347	0.4181	1
115	M4.1±0.7	-16.54	0.4601	1
116	M4.1±0.7	-6.188	0.4777	1
117	M4.2±0.7	-6.016	0.3093	1
118	M4.3±0.7	-9.375	0.412	1
119	M4.4±1.1	-14.06	0.3332	-1
120	M4.5±0.7	-5.663	—	1
121	M4.5±0.7	-62.18	0.0799	1
123	M4.5±0.6	-6.398	0.5469	1
124	M4.5±1.1	-47.26	0.6343	-1
125	M4.6±0.6	-7.454	—	1
126	M4.6±0.6	-8.915	0.3241	1
127	M4.6±0.5	-10.15	0.3781	0
128	M4.6±0.5	-3.17	0.5076	1
129	M4.7±0.5	-74.23	0.2364	1
130	M4.7±0.5	-6.109	0.5821	1
131	M4.7±0.5	-4.569	0.5341	1
132	M4.7±0.4	-12.02	0.5568	1
133	M4.7±0.5	-12.18	0.3165	1
134	M4.8±0.4	-21.34	0.1725	1
135	M4.8±0.5	-59.07	0.4103	1
137	M4.8±0.5	-10.11	0.5883	1
139	M4.8±0.9	-14.6	—	1
141	M5.0±0.6	-9.543	0.5009	1
143	M5.0±1.3	-14.41	0.8292	-1
144	M5.0±1.1	-14.36	0.8965	1
146	M5.1±0.6	-15.92	0.7128	1
147	M5.1±0.6	-12.69	0.6626	1
148	M5.1±0.7	-8.659	0.6687	1
149	M5.1±0.7	-11.33	0.593	1
150	M5.3±0.6	-13.43	0.354	0
151	M5.3±0.5	-14.57	0.3275	1
152	M5.3±0.7	-88.18	0.5188	1
153	M5.3±0.6	-32.65	0.534	1
154	M5.3±0.6	-12.34	0.7089	1
155	M5.3±0.7	-14.95	1.056	0
156	M5.3±0.8	-12.88	—	1
157	M5.4±0.9	-7.491	0.6515	1
158	M5.7±1.4	-29.84	1.712	0

For the NaI$\lambda\lambda$8183, 8195 absorption, the 1, -1, and 0 flags mean, respectively, if the feature is consistent with a young stellar template, an old stellar template or not conclusive.

agreement with previous extinction estimates in 25 Ori (0.27 mag, 0.28 mag, 0.29 mag, and 0.30 mag by Kharchenko et al., 2005; Briceño et al., 2005, 2007; Downes et al., 2014, respectively).

3.4.3.3.5 Effective Temperatures and Bolometric Luminosities

We estimated the effective temperatures of the confirmed members by interpolating their spectral types into the empirical relations from Luhman (1999).

To compute the bolometric luminosities of these members, we used newly available Gaia data (Gaia DR1; Gaia Collaboration et al., 2016) to establish distances for the 25 Ori, ASCC 18, and ASCC 20 stellar groups, where the confirmed members are located. In Table 13 we summarize the previous distances to these groups (Kharchenko et al., 2005; Briceño et al., 2005, 2007; Kharchenko et al., 2013; Downes et al., 2014), as well as our own estimates from the Gaia DR1 parallaxes for the higher probability Kharchenko et al. (2005) members of these groups. The Gaia-based distance estimates for the 25 Ori, ASCC 18, and ASCC 20 stellar groups are, within the uncertainties, essentially identical of 338±66 pc. We then used individual distance estimates derived from Gaia DR1 parallaxes to calculate the absolute I magnitudes (M_I) for the confirmed members projected inside these stellar groups. For members located outside these groups, we assumed the mean Gaia distance. Then we used the bolometric correction from Kenyon & Hartmann (1995) to obtain the bolometric luminosity, assuming $M_{bol_\odot} = 4.755$ (Mamajek, 2012). In Figure 21 we show the locations of the confirmed members in the H-R diagrams according to the stellar group where they lie or if they are outside of the groups indicated in Figure 16 and in Table 12 are listed the effective temperatures and bolometric luminosities we estimated for the confirmed members.

Table 12: Physical parameters of the 53 confirmed members.

ID	A_V (mag.)	e_A_V (mag.)	T_{eff} (K)	e_T_{eff} (K)	L ($L_\odot$)	e_L ($L_\odot$)	m ($M_\odot$)	e_m ($M_\odot$)	age (Myr)	e_age (Myr)	TTS	Disk Type	Location
66[a]	0.193	$^{+0.325}_{-0.203}$	3806.5	$^{+85.5}_{-72.5}$	0.286	$^{+0.125}_{-0.118}$	0.573	$^{+0.038}_{-0.073}$	4.175	$^{+10.597}_{-2.387}$	WTTS	ClassIII	ASCC18/ASCC20
74	4.33	$^{+0.513}_{-0.975}$	3632.5	$^{+174.0}_{-174.0}$	0.312	$^{+0.195}_{-0.221}$	0.425	$^{+0.101}_{-0.125}$	2.026	$^{+12.817}_{-1.338}$	CTTS	Evolved	Outside
79[a]	1.355	$^{+0.183}_{-0.366}$	3574.5	$^{+58.0}_{-58.0}$	0.111	$^{+0.028}_{-0.031}$	0.445	$^{+0.036}_{-0.045}$	8.959	$^{+5.93}_{-3.864}$	CTTS	ClassII	25Ori
82[a]	1.299	$^{+0.426}_{-0.426}$	3502.0	$^{+58.0}_{-58.0}$	0.276	$^{+0.09}_{-0.09}$	0.353	$^{+0.016}_{-0.052}$	1.79	$^{+1.686}_{-0.853}$	CTTS	ClassII	25Ori
89[a]	0.147	$^{+0.64}_{-0.538}$	3444.0	$^{+87.0}_{-87.0}$	0.126	$^{+0.087}_{-0.08}$	0.331	$^{+0.047}_{-0.031}$	4.189	$^{+10.642}_{-2.699}$	WTTS	ClassIII	25Ori/ASCC18
92	0.0	$^{+0.508}_{-0.0}$	3400.5	$^{+72.5}_{-72.5}$	0.081	$^{+0.036}_{-0.029}$	0.306	$^{+0.053}_{-0.024}$	6.79	$^{+8.043}_{-3.529}$	WTTS	ClassIII	ASCC20
93[a]	0.0	$^{+0.508}_{-0.0}$	3400.5	$^{+72.5}_{-72.5}$	0.117	$^{+0.074}_{-0.061}$	0.3	$^{+0.047}_{-0.019}$	3.808	$^{+11.07}_{-2.231}$	WTTS	ClassIII	ASCC18/ASCC20
96[a]	0.33	$^{+0.482}_{-0.406}$	3386.0	$^{+72.5}_{-72.5}$	0.119	$^{+0.052}_{-0.049}$	0.299	$^{+0.035}_{-0.034}$	3.704	$^{+7.801}_{-1.933}$	WTTS	ClassIII	ASCC20
97[a]	1.168	$^{+0.482}_{-0.406}$	3386.0	$^{+72.5}_{-72.5}$	0.139	$^{+0.062}_{-0.058}$	0.296	$^{+0.034}_{-0.031}$	2.977	$^{+6.142}_{-1.566}$	CTTS	TDC	ASCC18
98[a]	0.386	$^{+0.589}_{-0.487}$	3386.0	$^{+87.0}_{-87.0}$	0.13	$^{+0.077}_{-0.073}$	0.297	$^{+0.047}_{-0.051}$	3.271	$^{+11.597}_{-1.978}$	WTTS	ClassIII	Outside
107[a]	0.33	$^{+0.406}_{-0.406}$	3342.5	$^{+72.5}_{-72.5}$	0.156	$^{+0.082}_{-0.082}$	0.272	$^{+0.028}_{-0.058}$	2.208	$^{+6.233}_{-1.237}$	CTTS	Evolved	Outside
108	0.0	$^{+0.513}_{-0.0}$	3342.5	$^{+87.0}_{-87.0}$	0.113	$^{+0.066}_{-0.06}$	0.278	$^{+0.025}_{-0.076}$	3.513	$^{+11.273}_{-2.028}$	WTTS	ClassIII	Outside
109	3.533	$^{+0.939}_{-1.066}$	3342.5	$^{+145.0}_{-145.0}$	0.157	$^{+0.118}_{-0.118}$	0.271	$^{+0.075}_{-0.071}$	2.188	$^{+12.64}_{-1.683}$	CTTS	ClassII	25Ori
110	0.0	$^{+1.046}_{-0.0}$	3342.5	$^{+159.5}_{-159.5}$	0.096	$^{+0.086}_{-0.069}$	0.282	$^{+0.088}_{-0.084}$	4.537	$^{+10.338}_{-3.771}$	WTTS	ClassIII	Outside
111	0.0	$^{+0.487}_{-0.0}$	3313.5	$^{+87.0}_{-87.0}$	0.093	$^{+0.046}_{-0.04}$	0.263	$^{+0.037}_{-0.063}$	4.353	$^{+8.988}_{-2.617}$	WTTS	ClassIII	ASCC20
115[a]	0.046	$^{+0.62}_{-0.924}$	3255.5	$^{+101.5}_{-101.5}$	0.042	$^{+0.027}_{-0.029}$	0.207	$^{+0.088}_{-0.028}$	8.578	$^{+6.298}_{-5.968}$	CTTS	TDC	Outside
116	0.0	$^{+0.619}_{-0.0}$	3255.5	$^{+101.5}_{-101.5}$	0.13	$^{+0.083}_{-0.074}$	0.218	$^{+0.054}_{-0.039}$	2.19	$^{+8.071}_{-1.685}$	WTTS	Evolved	Outside
117	0.0	$^{+0.67}_{-0.0}$	3241.0	$^{+101.5}_{-101.5}$	0.122	$^{+0.07}_{-0.058}$	0.206	$^{+0.062}_{-0.04}$	2.204	$^{+5.67}_{-1.606}$	WTTS	TDC	ASCC20
118[a]	0.162	$^{+0.721}_{-0.924}$	3226.5	$^{+101.5}_{-101.5}$	0.076	$^{+0.044}_{-0.047}$	0.2	$^{+0.07}_{-0.049}$	3.528	$^{+11.281}_{-2.451}$	WTTS	Evolved	ASCC20
119	0.188	$^{+1.097}_{-1.401}$	3212.0	$^{+159.5}_{-154.5}$	0.029	$^{+0.028}_{-0.03}$	0.185	$^{+0.115}_{-0.085}$	10.461	$^{+---}_{-8.376}$	WTTS	ClassIII	Outside
120	0.0	$^{+0.822}_{-0.0}$	3197.5	$^{+101.5}_{-99.5}$	0.052	$^{+0.032}_{-0.026}$	0.192	$^{+0.058}_{-0.067}$	4.924	$^{+9.879}_{-3.435}$	WTTS	TDC	ASCC20
121[a]	0.391	$^{+0.823}_{-0.904}$	3197.5	$^{+101.5}_{-99.5}$	0.021	$^{+0.013}_{-0.014}$	0.173	$^{+0.067}_{-0.048}$	14.128	$^{+0.742}_{-9.579}$	CTTS	ClassII	ASCC20
123[a]	0.0	$^{+0.741}_{-0.0}$	3197.5	$^{+87.0}_{-86.0}$	0.068	$^{+0.038}_{-0.03}$	0.198	$^{+0.042}_{-0.06}$	3.635	$^{+7.512}_{-2.437}$	WTTS	ClassII	ASCC18
124	0.0	$^{+1.147}_{-0.0}$	3197.5	$^{+159.5}_{-153.5}$	0.049	$^{+0.044}_{-0.037}$	0.191	$^{+0.099}_{-0.091}$	5.272	$^{+9.602}_{-4.006}$	CTTS	Evolved	25Ori
125	0.0	$^{+0.792}_{-0.0}$	3183.0	$^{+87.0}_{-85.0}$	0.079	$^{+0.045}_{-0.036}$	0.192	$^{+0.038}_{-0.066}$	2.755	$^{+6.192}_{-1.742}$	WTTS	TDC	ASCC20
126	0.0	$^{+0.792}_{-0.0}$	3183.0	$^{+87.0}_{-85.0}$	0.042	$^{+0.024}_{-0.019}$	0.182	$^{+0.042}_{-0.056}$	5.805	$^{+8.994}_{-3.891}$	WTTS	TDC	ASCC20
127[a]	0.0	$^{+0.66}_{-0.0}$	3183.0	$^{+72.5}_{-71.5}$	0.14	$^{+0.069}_{-0.056}$	0.183	$^{+0.039}_{-0.045}$	1.118	$^{+2.595}_{-0.612}$	WTTS	ClassIII	ASCC18
128	0.0	$^{+0.66}_{-0.0}$	3183.0	$^{+72.5}_{-71.5}$	0.025	$^{+0.014}_{-0.013}$	0.171	$^{+0.036}_{-0.033}$	10.55	$^{+4.332}_{-6.362}$	WTTS	ClassII	Outside
129[a]	0.619	$^{+0.66}_{-0.64}$	3168.5	$^{+72.5}_{-70.5}$	0.09	$^{+0.044}_{-0.044}$	0.178	$^{+0.028}_{-0.053}$	1.966	$^{+5.167}_{-1.028}$	CTTS	Evolved	ASCC20
130[a]	0.0	$^{+0.66}_{-0.0}$	3168.5	$^{+72.5}_{-70.5}$	0.052	$^{+0.026}_{-0.021}$	0.18	$^{+0.021}_{-0.055}$	4.194	$^{+7.27}_{-2.586}$	WTTS	TDC	ASCC18
131	0.0	$^{+0.66}_{-0.0}$	3168.5	$^{+72.5}_{-70.5}$	0.08	$^{+0.04}_{-0.033}$	0.18	$^{+0.026}_{-0.055}$	2.371	$^{+4.579}_{-1.325}$	WTTS	ClassIII	ASCC18
132[a]	0.0	$^{+0.528}_{-0.0}$	3168.5	$^{+58.0}_{-57.0}$	0.215	$^{+0.112}_{-0.1}$	0.181	$^{+0.019}_{-0.043}$	0.623	$^{+1.55}_{-0.116}$	WTTS	TDC	Outside
133	0.0	$^{+0.66}_{-0.0}$	3168.5	$^{+72.5}_{-70.5}$	0.087	$^{+0.05}_{-0.044}$	0.179	$^{+0.028}_{-0.053}$	2.075	$^{+5.654}_{-1.17}$	WTTS	ClassIII	Outside
134	0.0	$^{+0.528}_{-0.0}$	3154.0	$^{+58.0}_{-56.0}$	0.03	$^{+0.013}_{-0.011}$	0.163	$^{+0.031}_{-0.037}$	7.27	$^{+7.53}_{-4.032}$	CTTS	TDC	ASCC20
135	0.0	$^{+0.66}_{-0.0}$	3154.0	$^{+72.5}_{-69.5}$	0.061	$^{+0.044}_{-0.036}$	0.173	$^{+0.027}_{-0.058}$	3.113	$^{+10.263}_{-1.943}$	CTTS	Evolved	ASCC18/ASCC20
137	0.0	$^{+0.66}_{-0.0}$	3154.0	$^{+72.5}_{-69.5}$	0.06	$^{+0.035}_{-0.031}$	0.173	$^{+0.027}_{-0.058}$	3.222	$^{+8.17}_{-1.924}$	WTTS	TDC	Outside
139	0.005	$^{+1.137}_{-1.117}$	3154.0	$^{+130.5}_{-123.5}$	0.03	$^{+0.026}_{-0.026}$	0.163	$^{+0.071}_{-0.064}$	7.27	$^{+7.593}_{-5.211}$	WTTS	TDC	Outside
141	0.0	$^{+0.792}_{-0.0}$	3125.0	$^{+87.0}_{-81.0}$	0.037	$^{+0.022}_{-0.019}$	0.152	$^{+0.048}_{-0.052}$	4.762	$^{+10.03}_{-2.779}$	WTTS	TDC	ASCC18
143	0.112	$^{+1.564}_{-1.873}$	3125.0	$^{+188.5}_{-168.0}$	0.027	$^{+0.035}_{-0.037}$	0.149	$^{+0.11}_{-0.069}$	6.993	$^{+---}_{-5.394}$	WTTS	ClassII	Outside
144	0.33	$^{+1.401}_{-1.437}$	3125.0	$^{+159.5}_{-146.0}$	0.026	$^{+0.029}_{-0.029}$	0.148	$^{+0.086}_{-0.066}$	7.309	$^{+---}_{-5.331}$	WTTS	ClassII	Outside
146	0.0	$^{+0.782}_{-0.0}$	3111.5	$^{+86.0}_{-81.0}$	0.021	$^{+0.018}_{-0.016}$	0.139	$^{+0.048}_{-0.04}$	8.428	$^{+6.447}_{-5.537}$	WTTS	TDC	25Ori/ASCC20
147	0.0	$^{+0.782}_{-0.0}$	3111.5	$^{+86.0}_{-81.0}$	0.041	$^{+0.034}_{-0.029}$	0.146	$^{+0.054}_{-0.047}$	3.998	$^{+10.89}_{-2.444}$	WTTS	Evolved	25Ori/ASCC18
148	0.0	$^{+0.914}_{-0.0}$	3111.5	$^{+100.5}_{-94.5}$	0.039	$^{+0.026}_{-0.022}$	0.146	$^{+0.054}_{-0.056}$	4.187	$^{+10.589}_{-2.437}$	WTTS	Evolved	25Ori
149	0.0	$^{+0.914}_{-0.0}$	3111.5	$^{+100.5}_{-94.5}$	0.075	$^{+0.056}_{-0.049}$	0.145	$^{+0.055}_{-0.045}$	1.714	$^{+10.208}_{-1.208}$	WTTS	ClassIII	Outside
150	0.0	$^{+0.761}_{-0.0}$	3084.5	$^{+84.0}_{-81.0}$	0.195	$^{+0.12}_{-0.103}$	0.162	$^{+0.031}_{-0.066}$	0.506	$^{+1.392}_{----}$	WTTS	ClassIII	ASCC20
151	0.0	$^{+0.63}_{-0.0}$	3084.5	$^{+69.5}_{-67.5}$	0.136	$^{+0.072}_{-0.063}$	0.15	$^{+0.027}_{-0.056}$	0.842	$^{+1.545}_{-0.334}$	WTTS	ClassIII	ASCC20
152	0.0	$^{+0.894}_{-0.0}$	3084.5	$^{+98.5}_{-94.5}$	0.027	$^{+0.019}_{-0.016}$	0.127	$^{+0.057}_{-0.036}$	5.486	$^{+9.401}_{-3.097}$	CTTS	ClassII	25Ori
153	0.0	$^{+0.762}_{-0.0}$	3084.5	$^{+84.0}_{-81.0}$	0.047	$^{+0.028}_{-0.024}$	0.128	$^{+0.053}_{-0.032}$	2.666	$^{+8.041}_{-1.183}$	CTTS	Evolved	25Ori
154	0.0	$^{+0.762}_{-0.0}$	3084.5	$^{+84.0}_{-81.0}$	0.057	$^{+0.036}_{-0.031}$	0.132	$^{+0.046}_{-0.036}$	2.18	$^{+7.117}_{-1.253}$	WTTS	TDC	ASCC18
155	0.0	$^{+0.894}_{-0.0}$	3084.5	$^{+98.5}_{-94.5}$	0.014	$^{+0.01}_{-0.008}$	0.119	$^{+0.051}_{-0.027}$	11.845	$^{+3.031}_{-7.036}$	WTTS	ClassIII	25Ori
156[a]	0.0	$^{+1.025}_{-0.0}$	3084.5	$^{+113.0}_{-105.5}$	0.038	$^{+0.03}_{-0.025}$	0.127	$^{+0.072}_{-0.046}$	3.463	$^{+11.422}_{-1.926}$	WTTS	ClassII	25Ori
157	0.0	$^{+1.148}_{-0.0}$	3071.0	$^{+126.5}_{-114.0}$	0.026	$^{+0.026}_{-0.021}$	0.12	$^{+0.072}_{-0.042}$	5.335	$^{+9.537}_{-3.422}$	WTTS	TDC	Outside
158	0.0	$^{+1.777}_{-0.0}$	3030.5	$^{+196.0}_{-167.5}$	0.019	$^{+0.032}_{-0.023}$	0.098	$^{+0.102}_{-0.026}$	6.334	$^{+---}_{-5.676}$	CTTS	ClassII	Outside

Note. Outside location label indicates the members not belonging to any stellar group defined by Kharchenko et al. (2013).
[a] > 99% probable variable star according to the CVSO study.

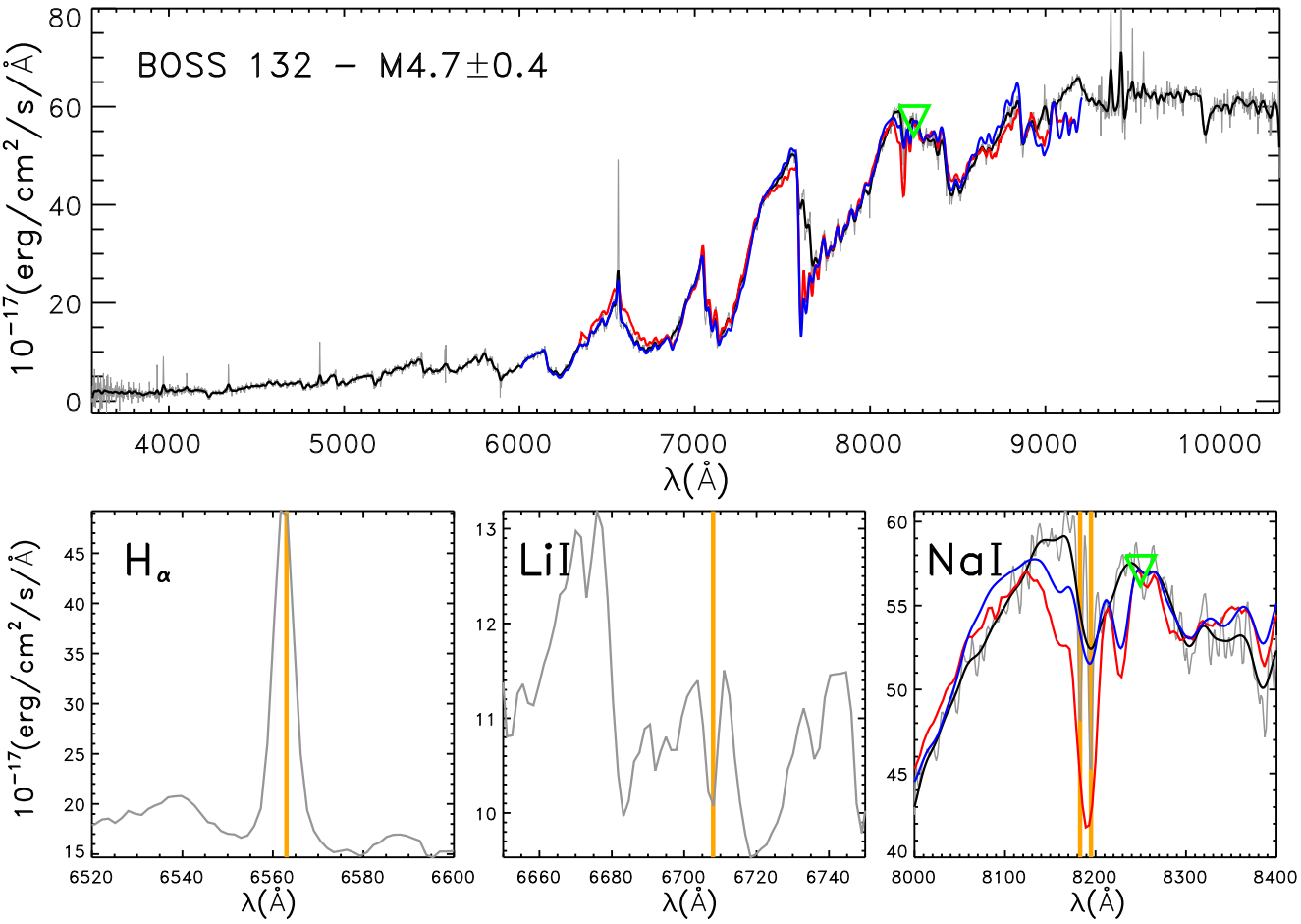

Figure 20: Example of one of the confirmed LMS members in Orion OB1a (member 132 from Table 11). **Upper panel:** BOSS spectrum with the original resolution of 1.4 Å (gray solid line) and with a convolved resolution of 16 Å (black solid line). The stellar templates with the same spectral type as this confirmed member are shown with a resolution of 16 Å for a field star from Kirkpatrick et al. (1999) (red line) and for a young star from the lists by Luhman (2000); Briceño et al. (2002); Luhman et al. (2003b) and Luhman (2004) (blue line). The green triangle indicates the normalization point of the stellar templates' fluxes, which is located in the pseudo-continuum of the NaI$\lambda\lambda$8183, 8195 doublet of the BOSS spectrum (Schlieder et al., 2012). **Lower panel:** Enlargements of the H_α emission, LiIλ6708 absorption and weak NaI$\lambda\lambda$8183, 8195 doublet youth indicators used to assign the memberships of the LMSs. The orange vertical solid lines show the wavelength range of the indicated features. For member 132, the spectrum presents H_α emission, LiIλ6708 absorption and the NaI$\lambda\lambda$8183, 8195 doublet consistent with the young stellar template. Therefore, this star was confirmed as a young LMS member.

3.4.3.3.6 Masses and Ages

As shown in Figure 21, all members are scattered, within the uncertainties, throughout the 1-10 Myr isochrones and 0.1-0.6 $M_\odot$ evolutionary tracks, adopting the PMS models from Baraffe et al. (2015).

To better estimate the masses and ages of the confirmed members, we interpolated their effective temperatures and bolometric luminosities into the Baraffe et al. (2015) models. When a confirmed member overlaps two stellar groups we adopted its mean bolometric luminosity. In Table 12 we show the mass and age we obtained for each confirmed member. The resulting masses for the 53

Table 13: Distances of the stellar groups partially covered by the 25 Ori BOSS plate.

Reference	Distance (pc)		
	25 Ori	ASCC 18	ASCC 20
Kharchenko et al. (2005)	460	500	450
Kharchenko et al. (2013)	397	313	394
Briceño et al. (2005, 2007)	330	...	...
Downes et al. (2014)	360	...	...
Gaia Collaboration et al. (2016)	336±30[a]	349±44[b]	330±39[c]

[a] for 17 high-probability members.
[b] for 7 high-probability members.
[c] for 15 high-probability members.

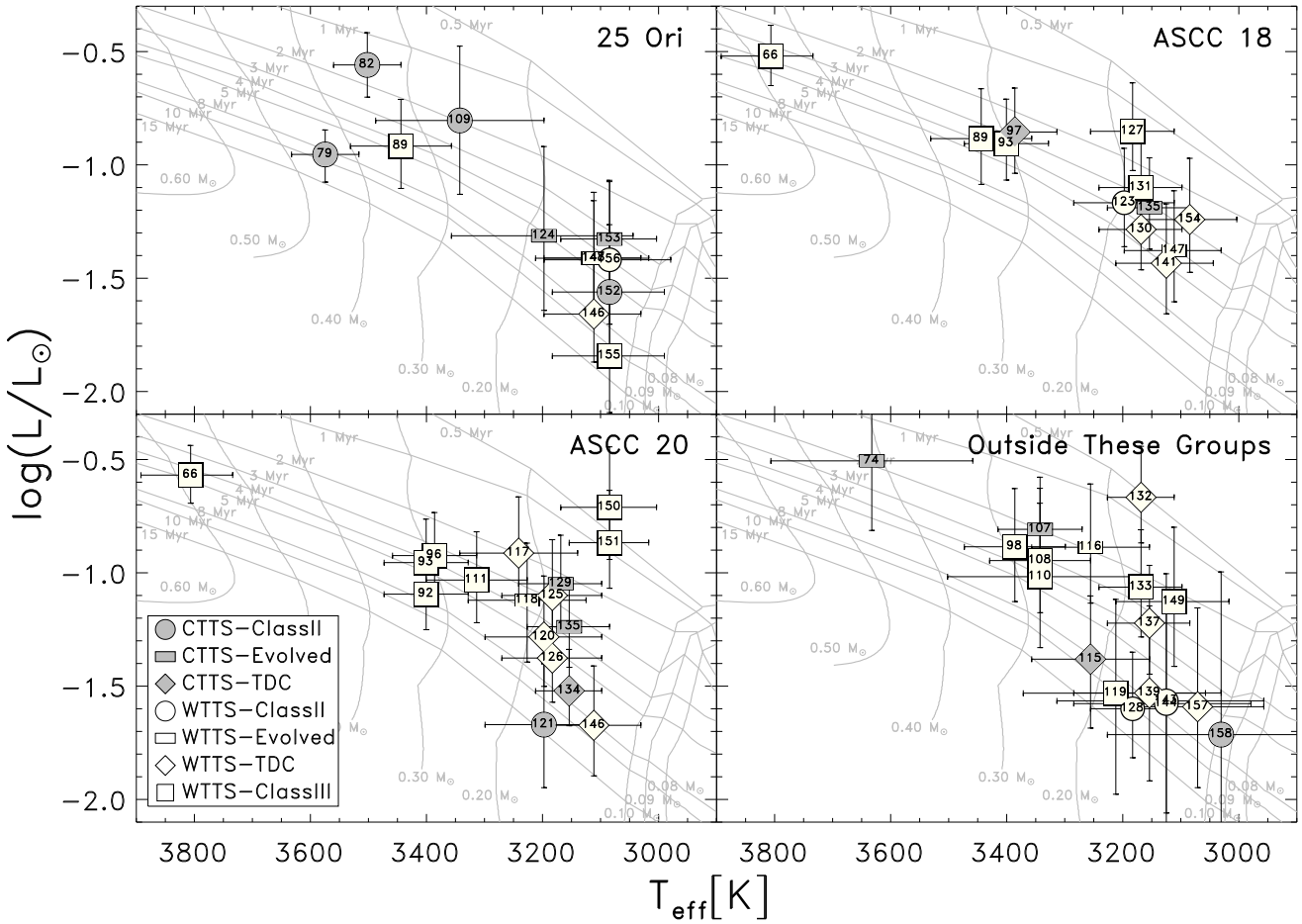

Figure 21: H-R diagrams of the confirmed members inside the labeled stellar groups or outside them, according to Kharchenko et al. (2013). The gray curves represent the PMS Baraffe et al. (2015) models. The members overlapping two of the stellar groups indicated in Figure 16 appear in both H-R diagrams.

confirmed members are in a range from 0.10 $M_\odot$ to 0.58 $M_\odot$, with 64% of the members having masses lower than 0.20 $M_\odot$. This implies that in this mass range we increased by a ≈ 50% the number of confirmed LMSs in the region covered by the BOSS plate, and by a ≈20% the number of LMSs in the estimated area of 25 Ori (1° radius; Briceño et al., 2005, 2007).

The ages we calculated for the confirmed members are roughly twice younger than those found

with similar methods in previous studies for the stellar groups where they are located (Kharchenko et al., 2005; Briceño et al., 2005, 2007; Kharchenko et al., 2013; Downes et al., 2014). This is due to the target selection bias in the 25 Ori BOSS spectra (see Section 3.4.2.3 and Figure 17).

For all the confirmed members we estimated the uncertainties in the derived values of the main physical parameters (extinction, effective temperature, bolometric luminosity, mass, and age) by considering the following factors: the error propagation that applies to each step described in this section and the errors associated to the interpolations. In Table 12 we show the resulting uncertainties for the extinction, effective temperature, bolometric luminosity, mass, and age values for the confirmed members. We also indicate to which stellar group they belong.

3.4.3.4 T Tauri Star Classification

The BOSS low-resolution spectra allowed us to measure the H_α equivalent width, which we used, together with the spectral types, to classify the confirmed members as either accreting young LMSs (classical T Tauri stars; CTTSs) or non-accreting young LMSs (weak T Tauri stars; WTTSs). To define the limit between both types of T Tauri stars (TTSs), we adopted the empirical saturation criterion by Barrado y Navascués & Martín (2003), in which stars with H_α emission above this limit are classified as CTTSs, and otherwise as WTTSs. In Figure 22 we show the TTS classification scheme and in Table 12 we show the resulting classification for the whole sample of confirmed members.

We confirmed a total of 15 CTTSs and 38 WTTSs among the 53 members in the BOSS sample. This corresponds to a very high fraction of CTTSs to WTTSs compared to the values of 5.6% and 3.8±0.4% found by Briceño et al. (2007) and Downes et al. (2014), respectively, which is due to the target selection bias toward sources with IR excesses.

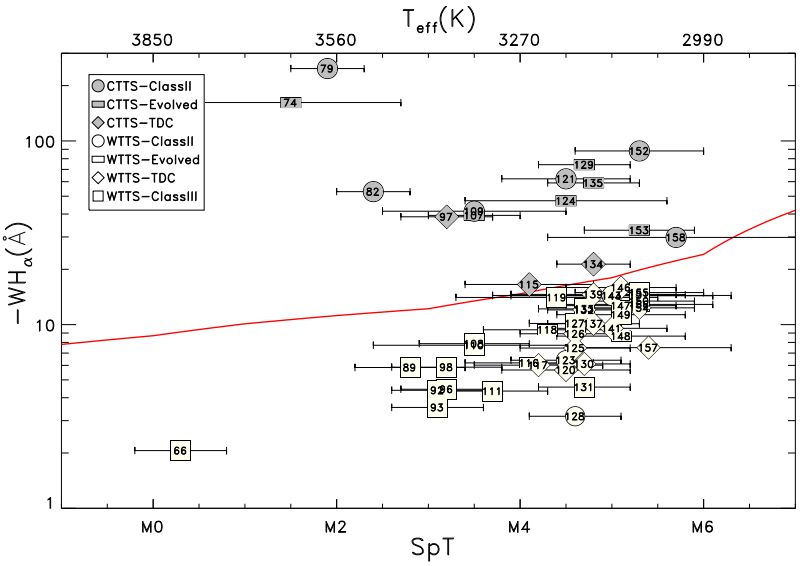

Figure 22: Relation between the H_α equivalent widths and spectral types for the confirmed members. The red solid curve indicates the saturation limit from Barrado y Navascués & Martín (2003), which allow us to separate WTTSs from CTTSs. The upper axis shows the effective temperature corresponding to the spectral types (Luhman et al., 2003b).

3.4.3.5 Spectral Energy Distributions

The circumstellar disks of the YSOs were classified according to their IR excess emissions at $\lambda > 2\ \mu$m. Objects having a flat or decreasing IR spectral energy distribution (SED) are considered Class II, while Class III objects have little or no near-IR excess (Lada & Wilking, 1984; Lada, 1987). An intermediate phase between the Class II and Class III objects contains the so-called "transitional disk systems" that present a decreasing SED slope in the near-IR that rises again in

the mid-IR. Finally, the "evolved disk systems" show a monotonically decreasing IR SED (e.g., Hernández et al., 2007a).

To classify the IR excesses of the confirmed members according to this scheme, we constructed their SEDs using the Virtual Observatory SED Analyzer (VOSA) tool (Bayo et al., 2008) and the photometric catalogs described in Sections 3.4.2.1 and 3.4.2.2, and listed in Table 10. We have a minimum of 10 and a maximum of 24 photometric bands for each confirmed member, covering a wavelength range from 0.36 μm to 22 μm.

The SEDs were dereddened using the visual extinction we estimated in Section 3.4.3.3.4 and assuming the extinction law reported by Fitzpatrick (1999) and subsequently improved by Indebetouw et al. (2005). To determine the corresponding IR excesses we proceeded iteratively as follows: First, we fitted the SEDs to the PMS LMS models from Baraffe et al. (2015), restricting the effective temperature range to the one obtained in Section 3.4.3.3.5. During this iteration we only considered the photometric bands where the IR excesses are not expected to occur ($\lambda < 2$ μm).

From the resulting fitted SEDs, VOSA automatically detects which bands present IR excesses by using an improved algorithm from that by Lada et al. (2006), which measures the slope of the IR points in the $\log(\lambda F_\lambda)$ vs $\log(\lambda)$ space. Basically, when the slope becomes greater than -2.56, the IR excesses are determined.

Then, a second fit to the Baraffe et al. (2015) models was performed, this time excluding those photometric bands showing IR excesses. In this way, we avoided false IR excess detections during the first iteration and maximized the number of photometric bands used for fitting the photospheres. The number of photometric bands used during the second iteration ran from 10 to 23 (except for the members 74 and 109 with 7 and 8 fitted bands, respectively). In Figure 23 we show the resulting SEDs for a selection of the confirmed members. The bolometric luminosities for the confirmed members corresponding to the total flux of the best Baraffe et al. (2015) model fit are in agreement, within the uncertainties, with those obtained using the I band, as explained in Section 3.4.3.3.5.

We classified the members as Class II if their IR SEDs resemble the median SEDs of Class II disks of the σ Orionis cluster (Hernández et al., 2007b) and the Taurus star-forming region (Furlan et al., 2006). The members showing lower IR excesses were considered evolved systems, while the members having IR SEDs consistent with the photospheric Baraffe et al. (2015) model fit were classified as Class III. The members showing a near-IR SED consistent with evolved systems or Class III objects, but having an unexpected strong excess at 22 μm were considered as transitional disk candidates (TDCs).

For the 14 members having available photometry in the [3.6] and [8.0] bands from IRAC, the slope in the [3.6]-[8.0] color (α, in the $\log[\lambda F_\lambda]$ vs $\log[\lambda]$ space) was analyzed to improve the disk classification as follows (Lada et al., 2006): Class II objects have slopes of $-1.8 < \alpha < 0$; evolved or "anemic" disk systems (Hernández et al., 2007b) have $-2.56 \leq \alpha < -1.8$ slopes; Class III objects have $\alpha < -2.56$. In Figure 24 we show the locations of the members in the IRAC color-color diagrams. All the CTTSs fall inside the CTTS locus defined by Hartmann et al. (2005), but four objects classified as WTTSs also fall inside this region (two having evolved disks, one is a TDC and the other one is bearing a Class II disk). All the members located in the IR excess region defined by Luhman et al. (2005) have Class II disks and only one of them has an evolved disk. The rest of the evolved systems and TDCs are located in the region between the Class II and Class III objects, as expected from the Hernández et al. (2007a) sample.

Of the 53 confirmed members we classified: *a*) 11 Class II objects, with SEDs consistent with the σ Orionis cluster and Taurus star-forming region median SEDs; *b*) 10 evolved disks, showing decreasing IR excesses but smaller than the aforementioned medians; *c*) 15 TDCs, having a sudden increase in their IR excesses at 22 μm; *d*) 17 Class III, with no detectable IR excesses. In Table 12

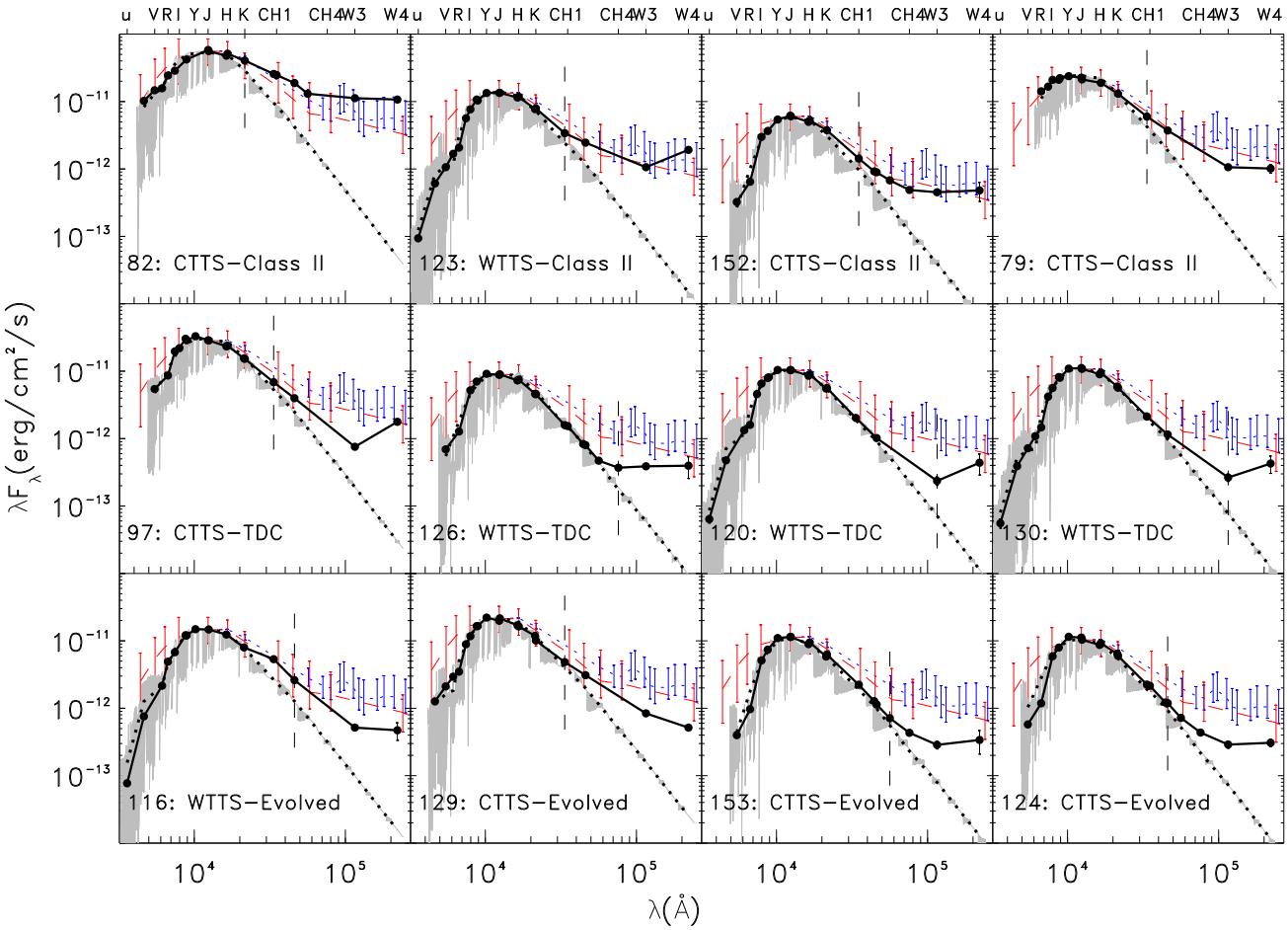

Figure 23: Dereddened SEDs for a sample of the confirmed members (black points and black solid curves). The gray spectra correspond to the best PMS LMS model from Baraffe et al. (2015) fitted to the dereddened data bluer than the point were the IR excesses start (vertical black dashed line). The black dotted curves show the fitted Baraffe et al. (2015) model spectra in a lower resolution. The red dashed curves and the blue dotted ones indicate, respectively, the median SEDs of Class II disks of the σ Orionis cluster (Hernández et al., 2007b) and the Taurus star-forming region (Furlan et al., 2006), normalized to the dereddened J-band flux of each member. The vertical red and blue solid lines represent the upper and lower quartiles for these median SEDs. Each SED has a label with the member ID and its TTS and disk classifications, as explained in Sections 3.4.3.4 and 3.4.3.5, respectively. The photometric errors are included but most of them are smaller than the corresponding symbols. All the SEDs of the confirmed members are available in the electronic version of the Suárez et al. 2017c publication.

we list the final disk type classification for the LMS members. For the sources showing IR excesses, those start at the WISE 3.4 μm band (for $\approx$ 42% of them) or longer wavelengths. Only for one member (member 82), the IR excess starts in the K band.

Considering both TTS and disk classifications for the 53 confirmed members: 17 out of the 38 WTTSs have disks of Class III, 12 are TDCs, 4 are evolved systems and 5 have Class II disks. All the 15 CTTSs show IR excesses, with 6 having Class II disks, 6 evolved systems and 3 TDCs.

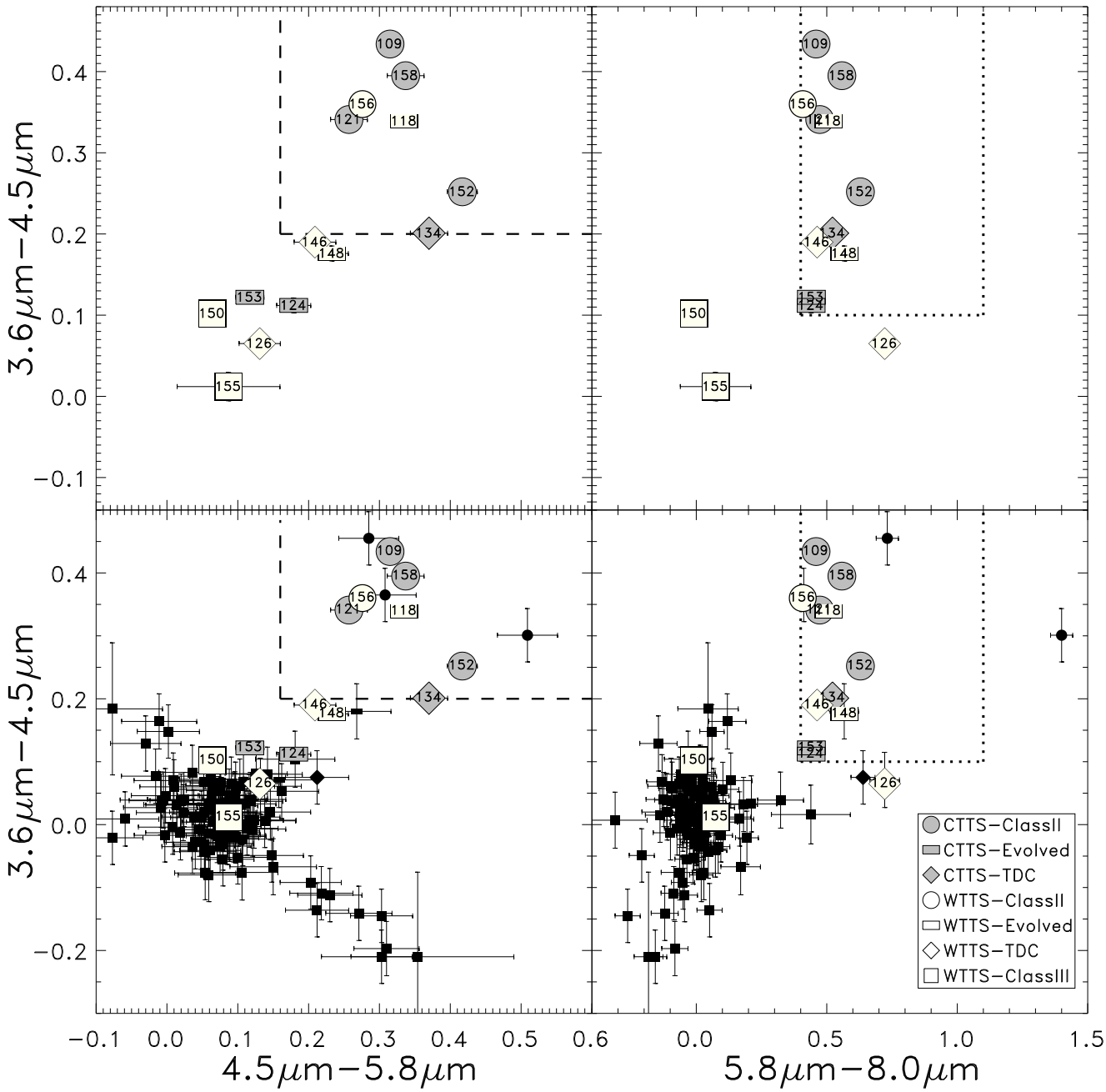

Figure 24: IRAC color-color diagrams for the confirmed members from this work (top panels) and including those from Hernández et al. (2007a) (bottom panels). The small black filled circles, diamonds, horizontal bars and square represent YSOs with Class II, transitional, evolved or Class III disks from Hernández et al. (2007a). The dashed lines delimit the region where M type objects with disk are expected, from the study by Luhman et al. (2005), and the dotted lines show the CTTS locus from Hartmann et al. (2005).

3.4.4 Peculiar Objects

3.4.4.1 Variable Members

Variability is an important effect than can be present in the member sample. It could modify their locations in the color-magnitude diagrams and affect the determination of physical parameters

such as extinction, bolometric luminosity, mass, and age. We expect that the variability in the I band should not have important effects in our confirmed member sample because we are using the CDSO photometric catalog, which lists mean magnitudes of multi-epoch observations with temporal spacing of about 4 yr. However, we are also working with multi-epoch VISTA photometry, which has temporal spacing of only 14 nights, where variability can be present. About 34% of the confirmed members have $> 99\%$ probability of being variable stars according to the CVSO catalog.

In the I vs $I - J$ color-magnitude diagram, members 110, 116, 125, and 131 fall outside the region defined by the YSO candidates. None of these members is listed as a high-probability variable stars in the CVSO catalog. However, they show the greatest $J_{\rm VISTA} - J_{\rm 2MASS}$ residuals (together with the high-probability variable stars 66, 74, and 118), with values of: 0.714, 0.357, 0.163, and 0.415 mag for members 110, 116, 125, and 131, respectively, which are, within the uncertainties, significantly larger than those for the rest of the members. These J-band differences explain well the deviated positions only for members 110 and 131. Members 110, 116, and 125 have close sources in the SDSS or 2MASS images, which may be contaminating their photometries, causing their deviations in the I vs $I - J$ diagram.

3.4.4.2 High-extinction Members

Considering that the mean extinction toward 25 Ori is $\bar{A_V}$ ≈0.28 mag (Kharchenko et al., 2005; Briceño et al., 2005, 2007; Downes et al., 2014), members 74 and 109 present significantly higher extinction values of $A_V = 4.33^{+0.51}_{-0.98}$ and $A_V = 3.53^{+0.94}_{-1.01.}$ mag, respectively. These members are not high-probability variable stars in the CVSO catalog, although they have the largest $I - J$ colors in the sample. Furthermore, members 74 and 109 were classified as CTTSs showing, respectively, an evolved disk system and a Class II disk. Additionally, the spectra of these two members show IR emissions more intense than those for the confirmed members with the same spectral types but with low extinction values. It may be that their high-extinction values are caused by dust in their disks, which are presented to us with an edge-on geometry. The positions of these members in the H-R diagram are, within the uncertainties, consistent with most of the members.

3.4.4.3 Highly Luminous Members

The deviant position of few members (132, 150, and 151) from the rest of the sample in the H-R diagrams can be naturally explained by their effective temperature and bolometric luminosity uncertainties. Only the member 132 is a $> 99\%$ probability variable star according to the CVSO catalog. Members 132 and 150 have a close companion in the SDSS or 2MASS images, which can be contaminating their photometries. The member 151 may be an isolated star without signals of variability, indicating that its position in the H-R diagram could be real.

3.4.5 Discussion and Conclusions

We determined the memberships of LMSs in the SDSS-III/BOSS spectra in 25 Ori and Orion OB1a on the basis of the presence of H_α emission and either LiIλ6708 or weak NaI$\lambda\lambda$8183, 8195 absorptions. We confirm 53 LMS members of 25 Ori or Orion OB1a, of which only three have been confirmed before by Downes et al. (2014). These members are located in regions associated with at least three different stellar groups belonging to Orion OB1a (25 Ori, ASCC 18, and ASCC 20; Kharchenko et al., 2005, 2013). The new LMS sample represents an increase of ≈50% in the number of M0-M6 spectral type spectroscopically confirmed members in the area of the 25 Ori

BOSS plate and a ≈20% increase in the number of LMSs known inside the 25 Ori's estimated area (1° radius; Briceño et al., 2005, 2007).

We did not confirm any K-type member in the 25 Ori BOSS plate on the basis of the H_α emission and LiIλ6708 absorption criteria. Furthermore, we found that the stars earlier than K-type are likely field stars after checking their position in the I vs $I-J$ color-magnitude diagram and looking for their X-ray emission, IR excesses or variability.

Parallaxes for high-probability members from the Kharchenko et al. (2005) list are available from Gaia DR1. Using these parallaxes, we derived distances of 336±30, 349±44, and 330±39 pc for 25 Ori, ASCC 18, and ASCC 20, respectively. Within the uncertainties, these stellar groups are located at the same distance (338±66 pc), but our estimates are based on a small number of high-probability members (17, 7, and 15 for 25 Ori, ASCC 18, and ASCC 20, respectively). With the next Gaia release we will have parallaxes for many more high-probability members and even for confirmed sub-solar members.

The mean extinction (excluding two outliers) we calculated toward the whole member sample is $\bar{A_V}$=0.14 mag. If we only consider the members inside the 25 Ori area, we obtained $\bar{A_V}$=0.21 mag, which is slightly lower than the one in previous studies (0.27 mag, 0.28 mag, 0.29 mag, and 0.30 mag by Kharchenko et al., 2005; Briceño et al., 2005, 2007; Downes et al., 2014). This small difference may be caused by the fact that our confirmed members in Orion OB1a span towards the south-east of the 25 Orionis star, where the Schlegel et al. (1998) extinction is even lower than in the area closer to the 25 Orionis star, as show in Figure 1 from Downes et al. (2014). Members 74 and 109 have extinctions of $A_V = 4.33^{+0.51}_{-0.98}$ and $A_V = 3.53^{+0.94}_{-1.01.}$ mag, respectively, which are much higher than the mean. A likely explanation could be that these members present edge-on disks, similar to the BD 4 member from Downes et al. (2015).

We constructed H-R diagrams for the confirmed members, assuming the distances determined from Gaia DR1 parallaxes. According to the PMS models from Baraffe et al. (2015), the mass range covered by the members is from 0.10 $M_\odot$ to 0.58 $M_\odot$. We do not find a clear separation over the isochrones for the members located in the different stellar groups. The ages we estimated for the confirmed members are younger by a factor of ~ 2 than those for the stellar groups in which they lie (Kharchenko et al., 2005; Briceño et al., 2005, 2007; Kharchenko et al., 2013; Downes et al., 2014). This is due to a bias in the target selection for the 25 Ori BOSS plate toward members with IR excesses. This bias is clear in Figure 17, where most of the BOSS targets have K-W3 colors redder than those expected from previously confirmed members.

Following the empirical saturation criterion by Barrado y Navascués & Martín (2003) for the TTSs classification of the confirmed members, we found 38 WTTSs and 15 CTTSs. This number of CTTSs is very high, considering that the fraction of CTTSs in 25 Ori has a mean value of 4.7% (Briceño et al., 2007; Downes et al., 2014), which is due to the bias in the selection of targets for the 25 Ori BOSS plate.

We constructed the SEDs of the TTSs and fitted the photospheric Baraffe et al. (2015) models in order to detect the IR excesses and classify their disks. We found: 11 Class II disks, with SEDs consistent with the median SEDs of Class II disks of the σ Orionis cluster (Hernández et al., 2007b) and the Taurus star-forming region (Furlan et al., 2006); 10 evolved disks, with falling IR SEDs showing excesses smaller than the medians SEDs; 15 TDCs, with falling near-IR SEDs with a sudden increase in the mid-IR; and 17 Class III disks, with SEDs with no detectable IR excesses, consistent with the photospheric Baraffe et al. (2015) models. For the members showing IR excesses, these start at wavelength longer that WISE 3.4 μm (only for the member 82 these start in the K band), which assure that the masses we assigned to the TTSs, working with the I and J bands, are not affected by the IR excesses.

The 34% of the confirmed members are > 99% probability variable stars in the CVSO catalog.

This effect, together with close sources to the members in the SDSS and 2MASS images, explained well most of the deviated members in the I vs $I-J$ color-magnitude diagram and H-R diagrams. Only the position of the member 151 in the H-R diagrams, that appears younger that expected, seems to be real. Additional analysis are necessary to reveal the nature of this object.

3.4.5.1 Chromospheric Activity

Due to the bias in the target selection for the 25 Ori BOSS plate, many of the confirmed members exhibit very strong Hα emission. This intense emission is due to strong chromospheric (magnetic) activity for the WTTSs and a combination of this phenomenon with ongoing accretion for the CTTSs. A number of recent studies have demonstrated that chromospheric activity in LMSs can alter their physical properties relative to the expectations of non-magnetic stellar models. In particular, strong activity appears to be able to inflate the stellar radius and to decrease the effective temperature (e.g. López-Morales, 2007; Morales et al., 2008). Typical amounts of radius inflation and effective temperature suppression are $\sim$10% and $\sim$5%, respectively (López-Morales, 2007).

For PMS LMSs, these effects can be quite important, causing the stars to appear to have lower masses and younger ages. For example, Stassun et al. (2012) developed empirical relations for the radius inflation and effective temperature suppression for a given amount of chromospheric Hα luminosity. These relations predict that the effective temperature suppression and radius inflation roughly preserve the bolometric luminosity. In addition, Stassun et al. (2014) showed that the effect of effective temperature suppression on ensembles of young LMSs and BDs is to skew the inferred initial mass function strongly toward lower masses.

In the case of the LMSs studied here, the individual ages we have determined for the entire sample are slightly younger than the mean estimated age of 25 Ori from previous studies. The combined effects of the effective temperature suppression from chromospheric activity as well as the bias in the target selection towards sources harboring disks, could explain such result. If so, then some of these stars could have higher masses and to be slightly older. This would have the effect of narrowing the age spread found here for these Orion OB1a groups. A detailed characterization of the mean ages of these regions is, however, beyond the scope of this work as it would require of a more robust sample of members.

3.5 MMT/Hectospec for Low-Mass Stars

3.5.1 Hectospec Spectra

In order to obtain spectra for 25 Ori member candidates with expected masses around the peak of its system IMF ($\approx 0.3\ M_{\odot}$), we used the Hectospec multifiber spectrograph on the 6.5m MMT telescope at the MMT Observatory (Fabricant et al., 2005). Hectospec is a 300 optical fiber-fed spectrograph with a FOV of 0.5° radius[9]. We were awarded one night of MMT observing time and we prepared the observation using the `xfitfibs` software[10] to create the fiber assigment of the Hectospec plates. The final design we considered consists of five Hectospec fields covering most of the 25 Ori region. Our observations were performed on two half-nights in 2016, one in October 4 and the other one in November 23 (PI: J. S. Kim). Only three of the five proposed fields were observed due to weather and instrument conditions. In fact, during the 2017B semester we could

[9] https://www.cfa.harvard.edu/mmti/hectospec/hecto_software_manual.htm
[10] https://www.cfa.harvard.edu/mmti/hectospec/xfitfibs/

Table 14: MMT/Hectospec observing log.

UT Date (yyyy-mm-ddThh:mm:ss)	Field	RA (hh:mm:ss)	DEC (hh:mm:ss)	Airmass	T_{exp} (s)	No. targets
2016-10-04T11:35:38	Plate 1	05:25:33.600	01:21:30.000	1.163	3x780	166
2016-11-23T09:35:54	Plate 2	05:23:32.400	02:08:00.000	1.188	2x600[a]	109
2016-10-05T12:09:28	Plate 3	05:26:46.330	02:12:10.000	1.151	3x900	125

[a] Less time than requested but the spectra have enough SNR for our analysis.

not perform another approved observing campaign due to the same issues. We show in Table 14 the log of our Hectospec observations and in Figure 25 the design of the plates.

In addition to these data, we have been granted with Hectospec observing time for semester 2018B to observe the remaining fields shown in Figure 25.

3.5.1.1 Target Selection

The candidates for the Hectospec observations were obtained from the selection by Downes et al. (2014), which was done using optical-NIR color-magnitude diagrams in a similar way to our selection done in Suárez et al. (2019), and from the selection we did using USNO and 2MASS photometry, as explained in Section 3.3.1.2. Also, because the availability of Hectospec fibers after adding the member candidates, we included previously confirmed members. With the three Hectospec plates we obtained 400 low-resolution spectra of targets with V-band brightness between 14.5 and 18.5 mag, corresponding to the mass range from 0.21 to 0.90 $M_{\odot}$, using the BT-Settl 7 Myr isochrone. In Figure 25 we show the spatial distribution of the observed candidates inside the three Hectospec fields, which roughly cover the estimated area of 25 Ori.

3.5.1.2 Data Reduction

The raw data were downloaded from the distribution area at CfA, which also includes the calibration files (biases, dome and twilight flats and comparison lamp exposures). To reduce the spectra we used the IDL-based HSRED pipeline[11] originally developed by Richard Cool (MMTO) to work with Hectospec spectra using IRAF tasks. The HSRED pipeline produces one-dimensional, wavelength calibrated, sky subtracted, red-leak removed, and velocity correlated spectra. The spectra have a coverage from 3700 to 9150 Å with a spectral resolution of $R \sim 1000 - 2000$. In Figure 26 we show an example of a Hectospec spectrum.

3.5.2 Spectra Analysis

3.5.2.1 Spectral Types

Spectral types of the Hectospec targets were determined using the SPTCLASS code, similarly than for the BOSS spectra in Section 3.4.3.1. The resulting spectral types range between K6.5 and M5.5, with an additional M7.0-type spectrum. The typical spectral type uncertainties for these sources are of 0.5 subclasses.

[11] http://www.mmto.org/node/536

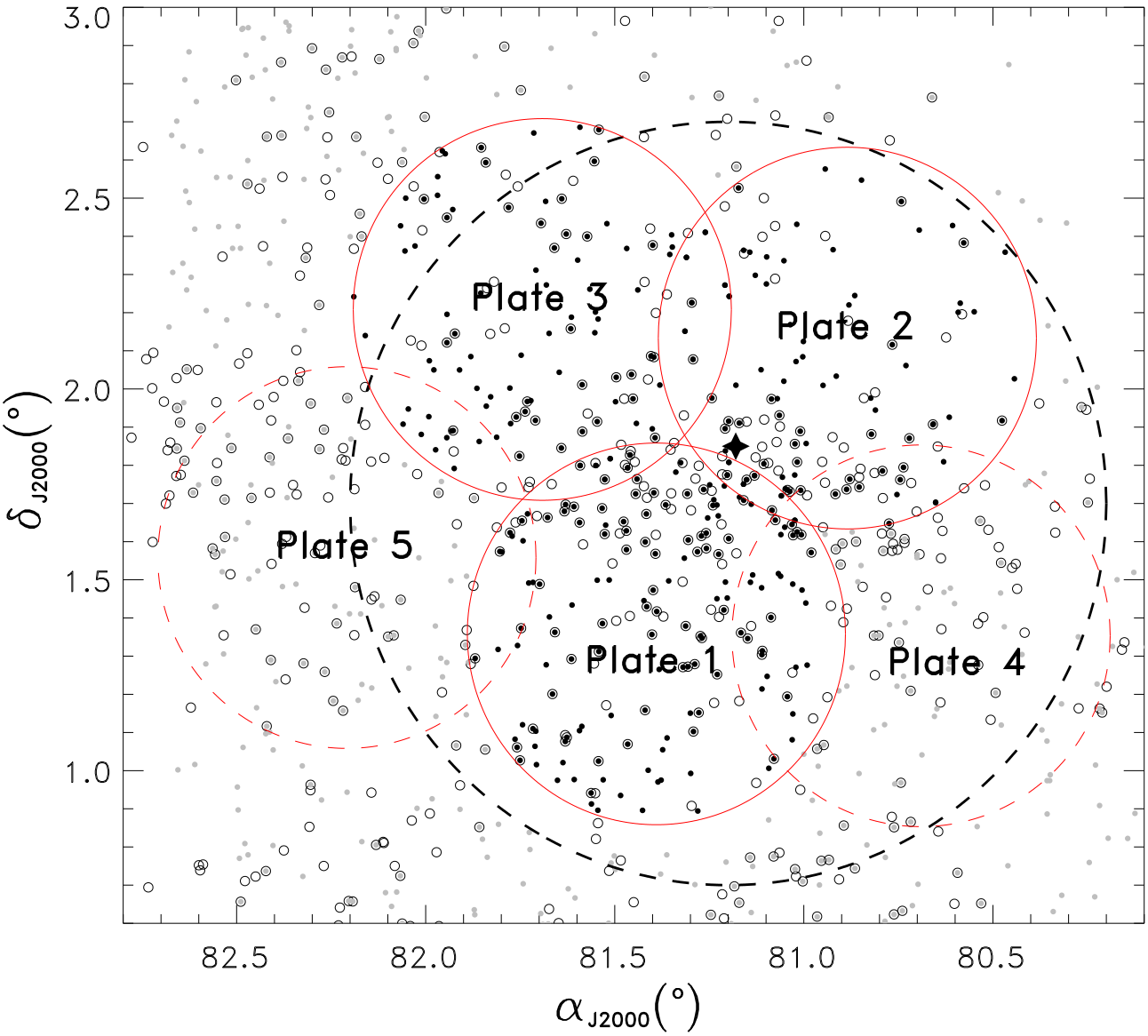

Figure 25: Proposed Hectospec fields (red circles) to observed young stellar candidates (14.5< V ≤18.5, 0.21≤ $m/M_{\odot}$ <0.90) mainly in 25 Ori. Due to weather conditions, only the three plates with the higher priority were observed (red solid circles). The black dots and the gray dots represent the observed candidates and the remaining candidates, respectively, in the indicated mass range. Open symbols represent spectroscopically confirmed members from previous studies. The dashed circle indicates the 1° radius area of 25 Ori. The star symbol shows the position of the 25 Ori star.

3.5.2.2 Membership Assignment

The membership of the Hectospec spectra were determined from the H_{α} emission, LiIλ6708 absorption and weak NaI$\lambda\lambda$8183, 8195 absorption youth indicators, described in Suárez et al. (2017c) (see Sections 3.4.3.2.1 and 3.4.3.2.2). The equivalent widths of each spectral feature was obtained by fitting a Gaussian function to the observed line profile using `IRAF` tasks and directly from the SPTCLASS code. Both set of values are consistent, as expected, because SPTCLASS uses IRAF tasks. So far, we have analyzed the spectra from Plate 2, resulting in 68 confirmed members, 52

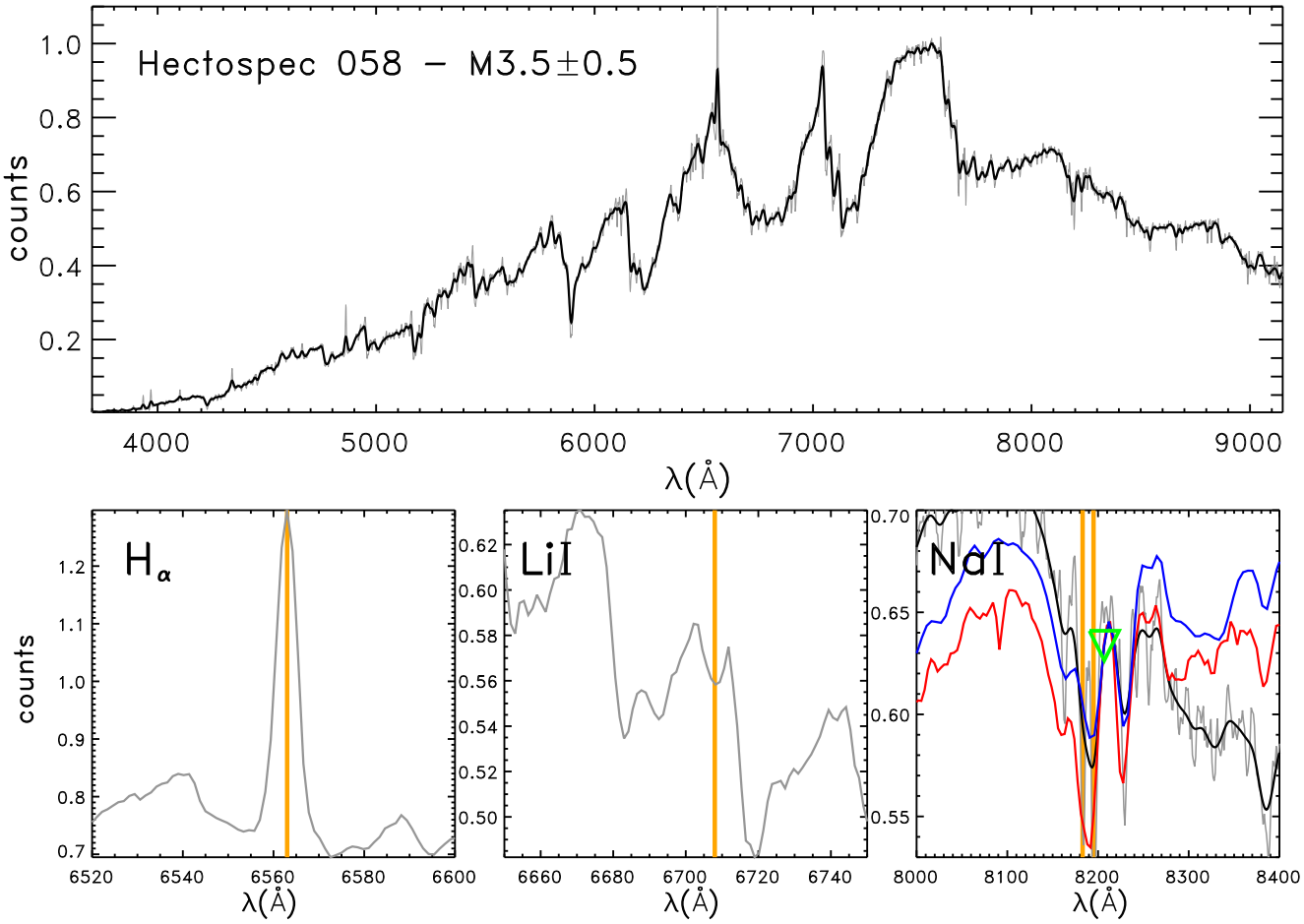

Figure 26: Hectospec spectrum of a confirmed member of 25 Ori. **Upper panel:** member spectrum with the original resolution of 6.0 Å (gray solid line) and with a convolved resolution of 16 Å (black solid line). **Lower panel:** Enlargements of the H_α emission, LiIλ6708 absorption and weak NaI$\lambda\lambda$8183, 8195 doublet youth indicators used to assign the memberships of the LMSs. The rest of the symbols and curves are similar to those in Figure 20. For this member, the spectrum presents H_α emission, LiIλ6708 absorption and the NaI$\lambda\lambda$8183, 8195 doublet consistent with a young stellar template. Therefore, this star was confirmed as a LMS member.

of them for the first time. All these new members lie inside the 1° radius area of 25 Ori. The remaining members already confirmed in the literature are: 1 from Briceño et al. (2007), 7 from Downes et al. (2014), 1 from Suárez et al. (2017c) and 7 from Briceño et al. (2019).

3.5.2.3 Physical Parameters

We estimated the T_{eff} of the confirmed members by interpolating their spectral types in the empirical relations from Kenyon & Hartmann (1995), Luhman (1999), Briceño et al. (2002) and Luhman et al. (2003b).

We obtained the A_V, L_{bol}, mass and age of the Hectospec confirmed members with the same techniques we used for the members from the APOGEE-2 spectra, as explained in Section 3.3.2.3.2. The mean A_V we obtained is 0.35±0.29, which is consistent with Suárez et al. (2019, and references therein) and with the value determined from the APOGEE-2 members. The mass range covered by these members is between 0.25 and 0.77 $M_\odot$. In Figure 27 we show the H-R diagram of these

resulting members. The mean age we obtained is 6.3±4.0 Myr, which is in agreement with previous studies (Briceño et al., 2019, and references there in) and with the members from the APOGEE-2 spectra.

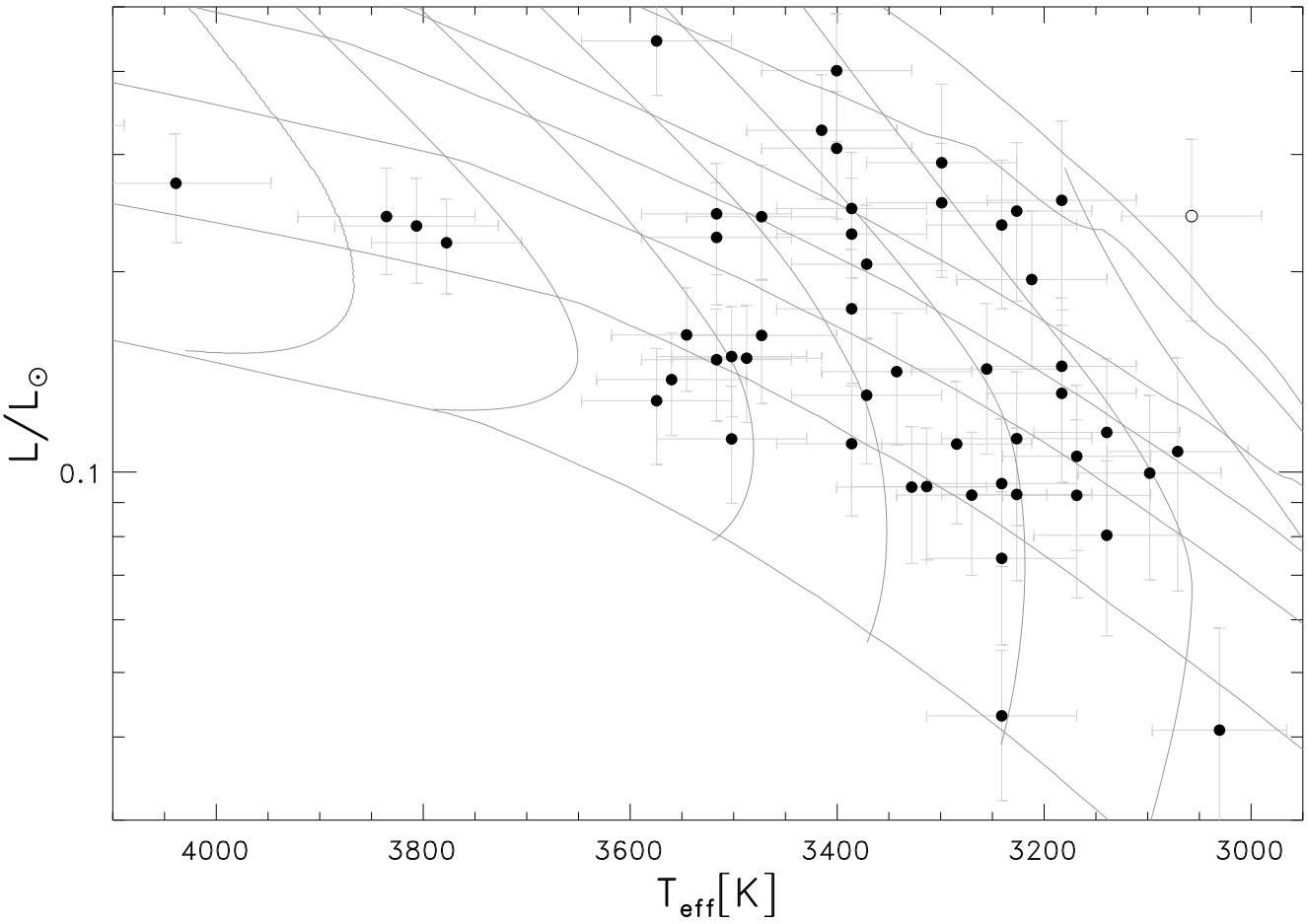

Figure 27: H-R diagram of the confirmed members from the Hectospec spectra. The gray curves represent the PARSEC evolutionary tracks for 0.2, 0.3, 0.4, 0.5, 0.6, 0.7 and 0.72 $M_{\odot}$ and the PARSEC-COLIBRI isochrones for 0.5, 1.0, 2.0, 3.0, 5.0, 10. and 30 Myr. The open symbol indicates the only member without mass and age estimates because lies outside the model grid.

This analysis of the Hectospec spectra was done in collaboration with the undergraduate student Sandy González as a project during the "XXVII Verano del OAN-SPM" summer research program under my supervision.

As from the analysis of the spectra in Plate 1 we obtained that ≈ 62% of the targets were confirmed as 25 Ori members and ≈ 76% of them were confirmed for the first time, we expect, assuming this sample as representative from the whole data, that from the remaining two Hectospec plates without analysis (Plate 1 and Plate 3), which include 291 spectra, to have 182 additional confirmed members of 25 Ori and 139 of them being confirmed for the first time.

3.6 GTC/OSIRIS for Brown Dwarfs

3.6.1 OSIRIS Spectra

In order to obtain spectra of the faintest member candidates of 25 Ori, which are expected to be BDs, we have ongoing observations with the Optical System for Imaging and low Resolution Integrated Spectroscopy (OSIRIS) instrument mounted on the 10.4m GTC at Observatorio Roque de los Muchachos. As a spectrograph, OSIRIS allows the acquisition of single long-slit or multiple object spectra in a FOV of 7x7 min^2 covering a wavelength range from 3650 to 10000 Å with a maximum spectral resolution of 5000 (Cepa et al., 2000, 2003). We worked with OSIRIS in the single long-slit mode (due to the low-density of targets in 25 Ori) with the R500R grism and a slit width of 1". The observations being part of this thesis project were performed in service mode during five observing seasons between December, 2014 and November, 2018 (PIs: G. Suárez and C. Román-Zúñiga) as part of the guaranteed Mexican time with GTC. Additionally, we have OSIRIS spectra of targets in 25 Ori and its surroundings taken during 2012 and 2013, which are part of the study by Downes et al. (2015). In Table 15 we show the log of all these OSIRIS observations.

3.6.1.1 Target Selection

For the OSIRIS observations performed during or before 2016, we selected the faintest sources from the Downes et al. (2014) candidate sample, which are expected to have spectral types between M6 and L1. This selection is based on the position on the sources in CMDs combining optical I_c-band photometry from the CDSO and NIR J, H and K-band photometry from VISTA. During these observational seasons, we obtained OSIRIS spectra from 52 member candidates.

For the more recent OSIRIS observations, we selected targets from the candidate sample by Suárez et al. (2019) in the range of expected spectral types (M6-L1). This sample is based on the position of the sources in the I_c vs $I-J$ diagram with photometry from DECam and VISTA that includes candidates with expected masses down to 12 M_{Jup}. We have obtained OSIRIS spectra for a total of 14 sources from this sample.

Considering all the observations with OSIRIS, we have spectra for 66 BD candidates, of which 55 lie inside the 1° radius area of 25 Ori. In Figure 28 we show the spatial distribution of these targets.

3.6.1.2 Data Reduction

The raw data were provided to us at the GTC FTP server together with calibration images (sky flats, dome flats, bias frames and comparison lamps) taken during the same night of observation. The spectra were reduced following standard IRAF routines, which consist of bias and cosmic ray subtraction, flat-fielding, instrumental response correction, spectrum extraction, elimination of atmospheric spectral features and wavelength calibration. The resulting spectral coverage is between 5780 to 10000 Å with a resolution of $R \approx 1300$ at H_α.

3.6.2 Spectra Analysis

3.6.2.1 Membership Assignment

In order to determine the spectral types of the BD candidates observed with OSIRIS, we worked with the SPTCLASS semi-automatic code. So far, we have classified 58 spectra (88% of the full sample), obtaining spectral types between M6 and M9.5.

Table 15: GTC/OSIRIS observing log.

Target	RA (hh:mm:ss)	DEC (hh:mm:ss)	UT Date (yyyy-mm-ddThh:mm:ss)	Airmass	T_{exp} (s)	Seeing (arcsec)	Observing conditions (atmosphere/moon)
			2012A Runs				
3	05:23:24.97	01:25:24.7	2012-03-12T21:02:06.050	1.3	3510	—	—
			2012B Runs				
8	05:23:09.86	01:42:50.8	2012-10-08T03:28:22.655	1.3	3440	1.10	Clear/Gray
9	05:23:24.07	01:47:27.4	2012-10-08T04:32:45.348	1.2	3440	1.10	Clear/Gray
10	05:23:34.65	01:50:47.5	2012-12-09T03:15:59.351	1.3	3440	<1.0	Spectroscopic/Dark
11	05:23:48.34	01:48:33.1	2012-12-17T01:06:16.672	1.1	3340	1.0	Photometric/Dark
12	05:24:58.48	01:44:00.1	2012-12-17T03:24:48.060	1.4	3340	1.0	Photometric/Dark
13	05:22:49.69	02:11:51.0	2012-12-21T21:25:13.901	1.6	3440	0.8	Spectroscopic/Gray
14	05:25:36.62	00:54:55.5	2012-12-22T03:38:46.893	1.6	4602	<0.8	Spectroscopic/Gray
			2013B Runs				
15	05:29:30.01	00:47:27.4	2013-10-13T05:02:08.778	1.1	3340	0.7	Clear/Dark
16	05:29:13.80	00:51:10.2	2013-10-13T05:02:08.778	1.1	3340	—	—
17	05:27:38.30	01:14:07.3	2013-10-14T05:01:06.925	1.1	3140	<0.9	Photometric/Bright
18	05:27:49.65	01:12:18.9	2013-10-14T05:01:06.925	1.1	3140	—	—
19	05:27:24.15	01:38:01.8	2013-11-06T05:05:57.362	1.2	3240	0.7	Spectroscopic/Dark
20	05:30:42.08	01:51:34.1	2013-11-05T04:39:54.909	1.2	3240	0.7	Spectroscopy/Dark
21	05:30:35.45	01:46:30.0	2013-11-05T04:39:54.909	1.2	3240	—	—
22	05:27:47.62	00:56:38.7	2013-11-06T01:50:38.996	1.3	3140	0.8	Spectroscopic/Dark
23	05:27:38.19	00:57:41.7	2013-11-06T01:50:38.996	1.3	3140	—	—
24	05:26:41.69	00:38:14.9	2013-11-06T04:15:15.002	1.1	3140	0.9	Spectroscopic/Dark
25	05:26:35.63	00:36:01.7	2013-11-06T04:15:15.002	1.1	3140	—	—
26	05:30:16.17	00:50:57.0	2013-11-07T02:23:33.637	1.2	3040	0.6	Spectroscopic/Dark
27	05:26:11.95	00:49:15.5	2013-10-30T06:02:09.175	1.3	2940	0.8	Clear/Dark
28	05:26:03.59	00:44:14.6	2013-10-30T06:02:09.175	1.3	2940	—	—
			2014B Runs				
29	05:23:34.66	01:50:47.9	2015-01-23T23:16:27.539	1.2	3906	0.7	Photometric/Dark
30	05:23:48.37	01:48:32.5	2015-01-23T23:16:27.539	1.2	3906	—	—
31	05:23:21.34	01:50:41.1	2014-12-26T01:27:10.108	1.2	4566	0.9	Clear/Dark
32	05:23:24.07	01:47:27.7	2014-12-26T01:27:10.108	1.2	4566	—	—
33	05:24:58.46	01:44:00.0	2015-01-21T23:17:01.712	1.2	3906	0.8	Clear/Dark
34	05:25:08.74	01:46:32.1	2015-01-21T23:17:01.712	1.2	3906	—	—
35	05:24:59.31	01:39:05.3	2014-12-29T02:10:27.281	1.4	3906	0.9	Spectroscopic/Dark
36	05:24:41.44	01:35:51.7	2014-12-29T02:10:27.281	1.4	3906	—	—
37	05:25:25.81	01:37:38.7	2014-12-29T00:50:12.894	1.2	3482	0.9	Spectroscopic/Dark
38	05:25:20.91	01:37:14.3	2014-12-29T00:50:12.894	1.2	3482	—	—
39	05:25:36.90	01:48:10.2	2014-12-26T03:04:16.605	1.6	4706	0.9	Clear/Dark
40	05:25:14.67	01:48:39.4	2014-12-26T03:04:16.605	1.6	4706	—	—
			2015B Runs				
41	05:26:16.21	02:02:21.0	2015-12-04T01:44:13.496	1.1	4536	0.7	Spectroscopic/Gray
42	05:26:12.99	02:06:26.0	2015-12-04T01:44:13.496	1.1	4536	—	—
43	05:25:15.23	01:56:05.5	2015-12-04T03:27:58.254	1.3	3936	0.7	Spectroscopic/Gray
44	05:25:28.85	01:59:49.0	2015-12-04T03:27:58.254	1.3	3936	—	—
45	05:24:30.57	01:51:09.6	2015-12-11T01:09:42.745	1.1	3936	0.8	Clear/Dark
46	05:24:28.27	01:53:27.5	2015-12-11T01:09:42.745	1.1	3936	—	—
47	05:24:22.77	01:47:05.4	2015-12-11T01:51:49.910	1.1	4536	1.2	Clear/Dark
48	05:24:07.87	01:48:01.7	2015-12-11T01:51:49.910	1.1	4536	—	—
49	05:24:06.64	01:37:20.8	2015-12-12T23:46:30.718	1.2	3736	0.7	Clear/Dark
50	05:24:04.32	01:35:18.4	2015-12-12T23:46:30.718	1.2	3736	—	—
51	05:25:26.63	01:19:22.1	2015-12-13T00:54:46.712	1.1	3736	0.8	Clear/Dark
52	05:25:24.66	01:21:26.5	2015-12-13T00:54:46.712	1.1	3736	—	—
			2016B Runs				
59	05:21:42.99	02:47:41.5	2016-10-02T05:16:09.819	1.1	3990	1.0	Clear/Dark
60	05:21:40.15	01:50:24.0	2016-10-11T05:13:19.736	1.1	3990	0.9	Clear/Dark
61	05:21:48.76	01:38:22.3	2016-10-12T04:48:46.378	1.1	3990	0.7	Clear/Dark
62	05:25:08.81	02:05:05.5	2016-11-24T03:38:30.210	1.2	3990	1.0	Clear/Dark
63	05:23:34.26	01:05:51.1	2016-11-21T03:08:23.768	1.1	4350	1.2	Spectroscopic/Dark
64	05:21:12.24	01:26:57.2	2016-12-06T00:20:53.845	1.2	4875	0.8	Clear/Dark
			2017B Runs				
65	05:22:18.67	02:05:53.2	2017-09-27T04:49:56.423	1.2	3375	—	—
66	05:22:18.69	01:42:59.9	2017-09-28T04:24:37.194	1.2	3765	—	—
67	05:22:23.84	01:42:25.2	2017-09-28T05:34:38.922	1.1	3675	—	—
68	05:24:03.62	01:13:35.0	2017-09-29T04:15:19.030	1.3	3675	—	—
69	05:26:01.78	01:39:15.5	2017-09-29T05:08:52.544	1.2	3675	—	—
70	05:26:05.31	01:41:30.2	2017-11-24T01:47:50.305	1.1	3675	—	—
71	05:26:43.16	01:31:23.6	2017-11-24T02:43:47.222	1.1	3375	—	—
			2018B Runs				
72	05:23:36.44	01:39:27.1	2018-10-03T04:46:47.796	1.2	3555	0.7	Clear/Dark
73	05:26:01.80	01:39:14.8	2018-10-06T05:03:53.361	1.1	3555	1.1	Spectroscopic/Dark
74	05:25:27.95	01:25:33.3	2018-10-15T05:08:56.785	1.1	3555	0.8	Clear/Dark
75	05:26:45.60	01:39:00.7	2018-10-15T06:03:02.663	1.2	3555	0.9	Clear/Dark
76	05:24:03.61	01:13:33.8	2018-10-16T05:50:14.268	1.2	3555	0.8	Clear/Dark
77	05:26:43.18	01:31:23.1	2018-11-04T03:43:46.686	1.1	3555	0.7	Clear/Dark
78	05:24:19.28	02:15:44.7	2018-10-31T05:21:56.865	1.2	3000	0.9	Clear/Gray

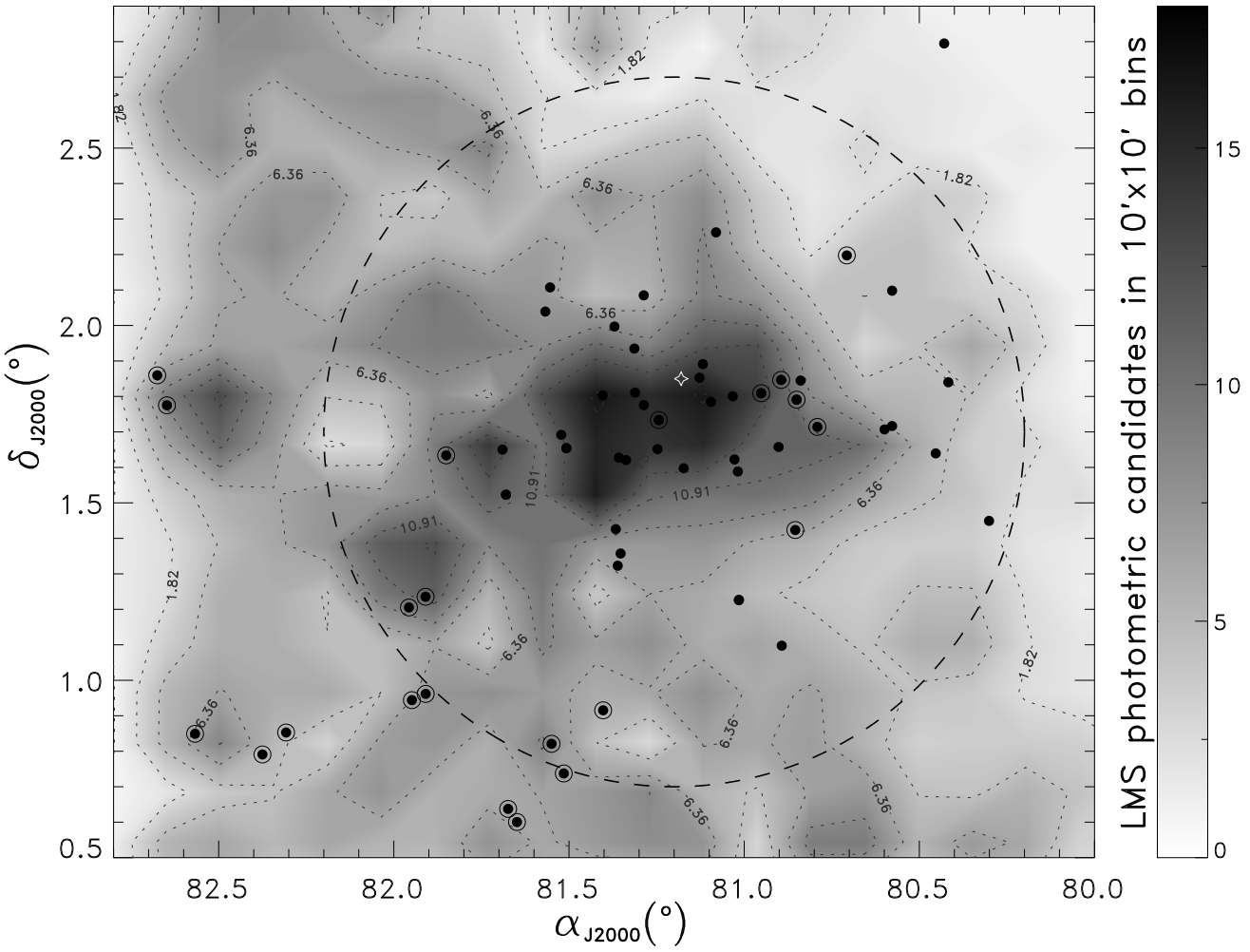

Figure 28: Spatial distribution of the targets observed with OSIRIS (black solid points). The open circles indicate sources with spectra analyzed by Downes et al. (2015). The dashed circle show the 1° radius area of 25 Ori. The white star symbol indicates the position of the 25 Ori star. The background map is the same as in Figure 2.

The membership for the sources observed with OSIRIS were assigned following the prescription by Downes et al. (2015): we focused on the CaH, VO, KI and NaI features demonstrated to be surface gravity sensitive in the optical spectra of BDs (Martin et al., 1996). The NaI$\lambda\lambda$8183, 8195 and the KI$\lambda\lambda$7665, 7699 doublets, and the CaH (λ6750 − λ7050) molecular band are weaker in young dwarfs than in the field stars of the same spectral type, while the VO$^{\rm I}$ (λ7300 − λ7500) and the VO$^{\rm II}$ (λ7800 − λ8000) molecular bands are stronger in the young dwarfs (McGovern et al., 2004). We compared our OSIRIS spectra with the young stellar templates from Luhman (2000), Briceño et al. (2002), Luhman et al. (2003b) and Luhman (2004), and the old field stellar templates from Kirkpatrick et al. (1999). Additionally, we measured the equivalent width of the H$_\alpha$ line, which, when present in emission, supports the membership assignment.

After applying the above criteria to the 58 spectral type classified targets, we confirmed 42 BD members, including the 15 BDs by Downes et al. (2015), of which 33 lie inside the area of 25 Ori. This includes 27 new confirmed BDs, 26 of them lying inside the 1° radius area of 25 Ori. Additionally, we expect to have 6 more BD members with the recent OSIRIS spectra we obtained in 2018B, all of them located inside the spatial extent of 25 Ori. In Figure 29 we show the OSIRIS

spectrum of one of these confirmed BDs in 25 Ori.

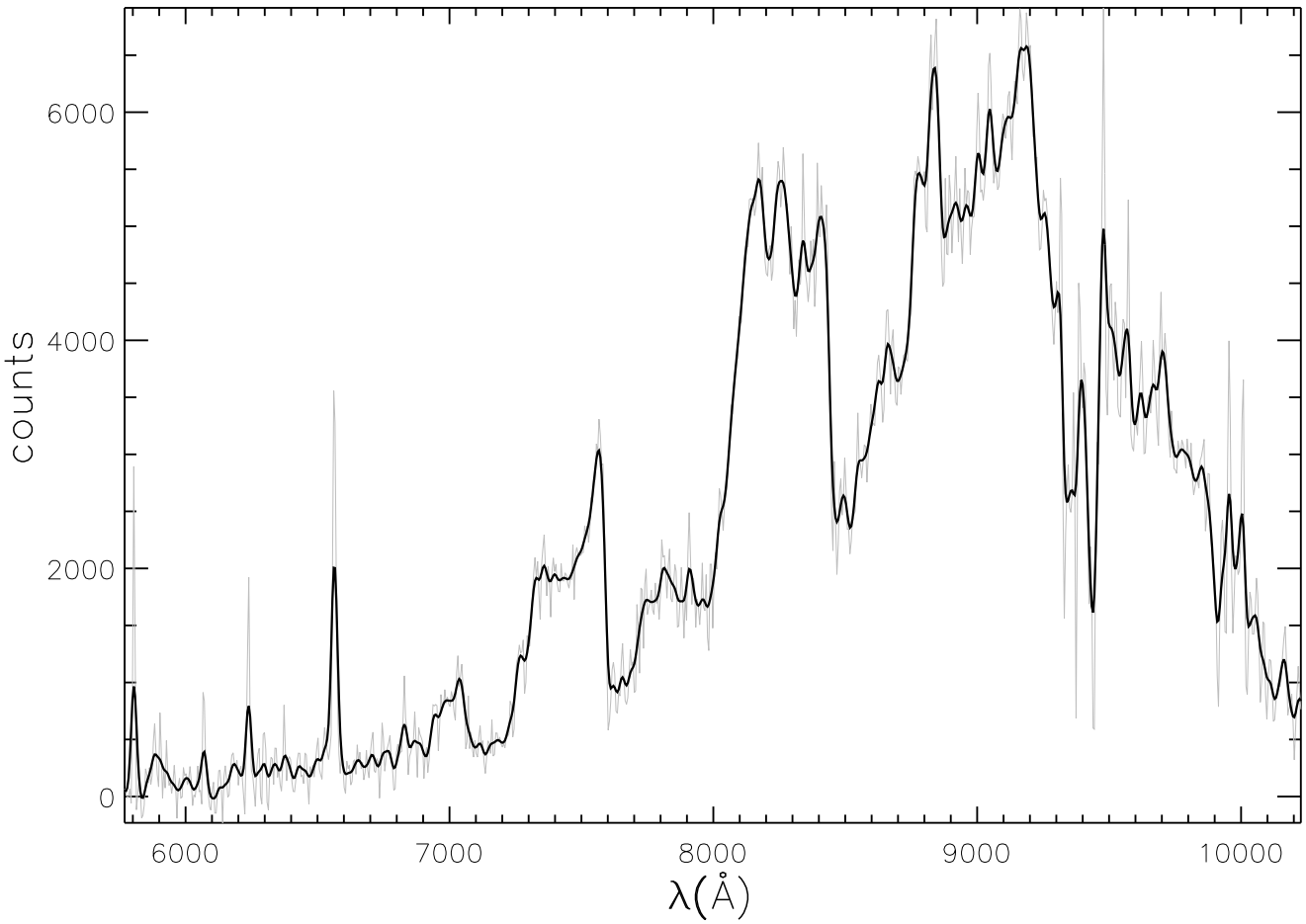

Figure 29: OSIRIS spectrum of a BD confirmed to be member of 25 Ori. The gray curve and the black curve represent the originally OSIRIS spectrum and the 16 Å smoothed spectrum of the BD, respectively.

3.6.2.2 Physical Parameters

We obtained the T_{eff} of the confirmed members by interpolating their spectral types in the relation by Pecaut & Mamajek (2013). For the estimation of A_V we compared the observed $I_c - J$ colors from DECam and VISTA with the intrinsic colors obtained by interpolating T_{eff} in the same mentioned relation to then convert the color excess to A_V considering the coefficients by Cardelli et al. (1989). To estimate L_{bol}, mass and age of the confirmed BDs we used the PHYPAR routine with the I_c-band magnitudes, assuming the 25 Ori distance obtained in this work (356 ± 47 pc) and working with the BT-Sett isochrones. In Figure 30 we show the H-R diagram of the confirmed members using spectra from OSIRIS. The obtained masses range between 15 and 88 M_{Jup}. The resulting mean age from these members is 10 ± 5 Myr, which is slightly older than that obtained from the other confirmed members in this work and in the literature, but consistent within the uncertainties.

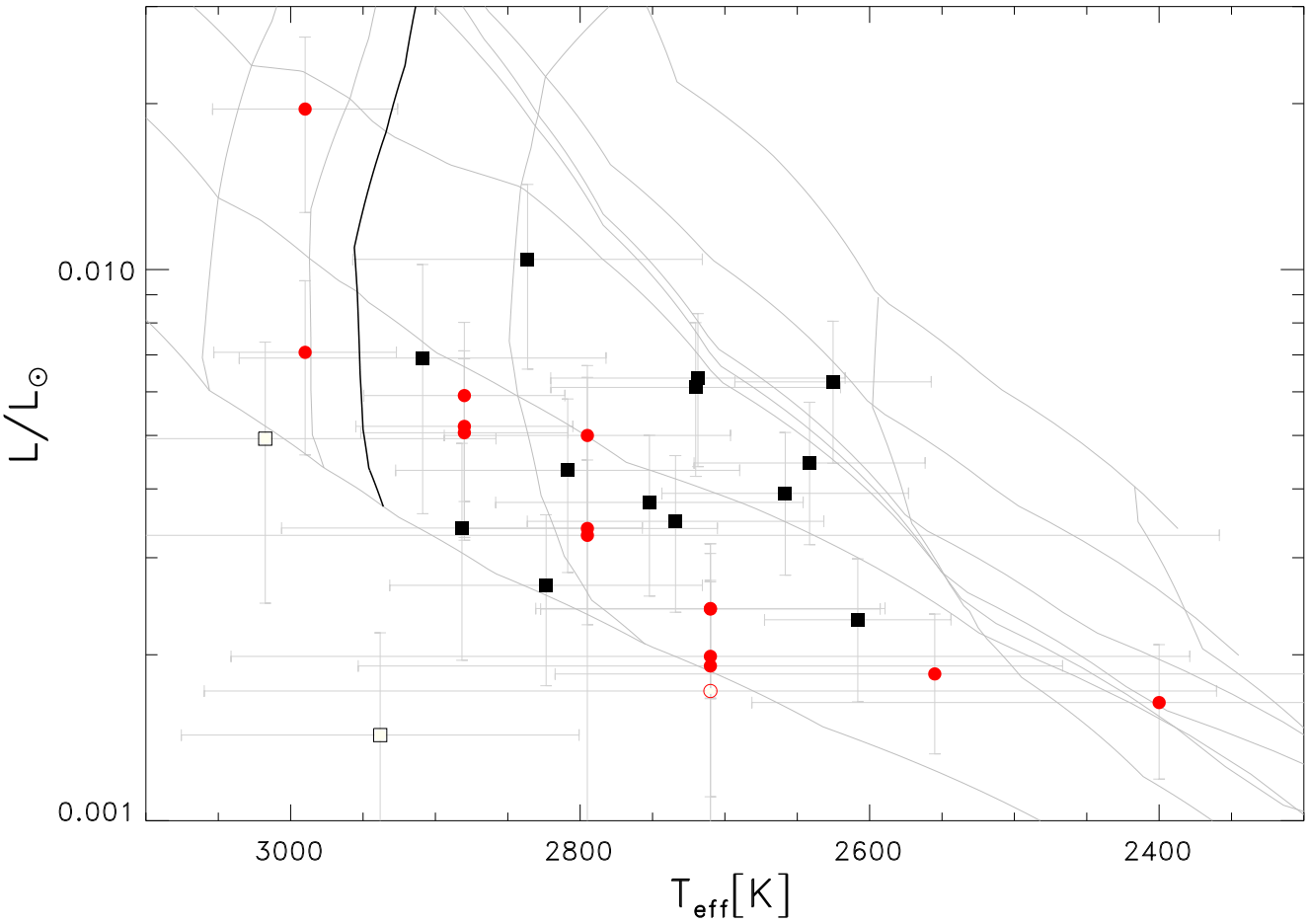

Figure 30: H-R diagram of the BDs confirmed in 25 Ori in this work (black squares) and by Downes et al. (red circles; 2015). The open symbols represent sources without mass and age estimates because lie outside the model grid. The gray curves show the BT-Settl evolutionary tracks of 0.011, 0.02, 0.05, 0.08 and 0.1 $M_{\odot}$ and isochrones of 0.5, 1, 2, 3, 5, 10 and 30 Myr. The black curve corresponds to the BT-Settl evolutionary track at the hydrogen burning limit mass (0.072 $M_{\odot}$).

3.7 Summary of the Spectroscopic Survey

In this section we summarize and put together all the members we have confirmed using spectra from several world-wide facilities. We also discuss the completeness of the survey in terms of the expected members from the 25 Ori system IMF derived in Section 2.

In Table 16 we list the different spectrographs we used in this survey and the number of targets for which we have spectra in the specified wavelength range and spectral resolution. Also, we include in the table the number of resulting members in the indicated mass range using the criteria summarized in this section. In Figure 31 we show the spatial distribution of all the observed targets.

Most of the targets were selected on the basis of their positions in CMDs combining optical and NIR photometry from different catalogs. In Figure 32 we show the I_c vs $I_c - J$ CMD of all the targets observed so far in the spectroscopic survey. Most of the targets lying outside the PMS locus were observed by BOSS (Alam et al., 2015) and are, in fact, field stars (Suárez et al., 2017c), as discussed in Section 3.4.3.2.

Table 16: Details of the spectroscopic survey in 25 Ori.

Spectrograph	λ range (Å)	R	Targets		Confirmed Members				m range ($M_\odot$)
			All	25 Ori[a]	All	25 Ori[a]	By First Time[b]	Expected in 25 Ori[c]	
MES	3600-7100	∼21000	77	50	$> 14^d$	$> 10^d$	$> 10^d$	35	1.3 - 11
APOGEE-2	15100-17000	∼22500	1185	353	353	153	97	97	0.3 - 5.2
Hectospec	3700-9150	∼1500	400	374	$> 68^e$	$> 68^e$	$> 52^e$	250	0.25 - 0.8
BOSS	3560-10400	∼2000	172	68	53	26	23	23	0.09 - 0.7
OSIRIS	5780-10000	∼1300	66	55	$> 42^f$	$> 33^f$	$> 26^f$	48	0.01 - 0.09

[a] Area of 1° radius (Briceño et al., 2005, 2007) centered at $\alpha_{J2000} = 81.2°$ and $\delta_{J2000} = 1.7°$.
[b] Not in the spectroscopic studies by Briceño et al. (2005, 2007); Downes et al. (2014, 2015); Suárez et al. (2017c); Briceño et al. (2019). For the members from BOSS spectra the comparison is not done with Suárez et al. (2017c) because it is the publication of those members.
[c] Considering also the spectra without membership determination.
[d] From the analysis of 22 spectra (29% of the sample).
[e] From the analysis of Plate 2, containing 27% of all our Hectospec spectra.
[f] From the analysis of 58 spectra (88% of the sample).

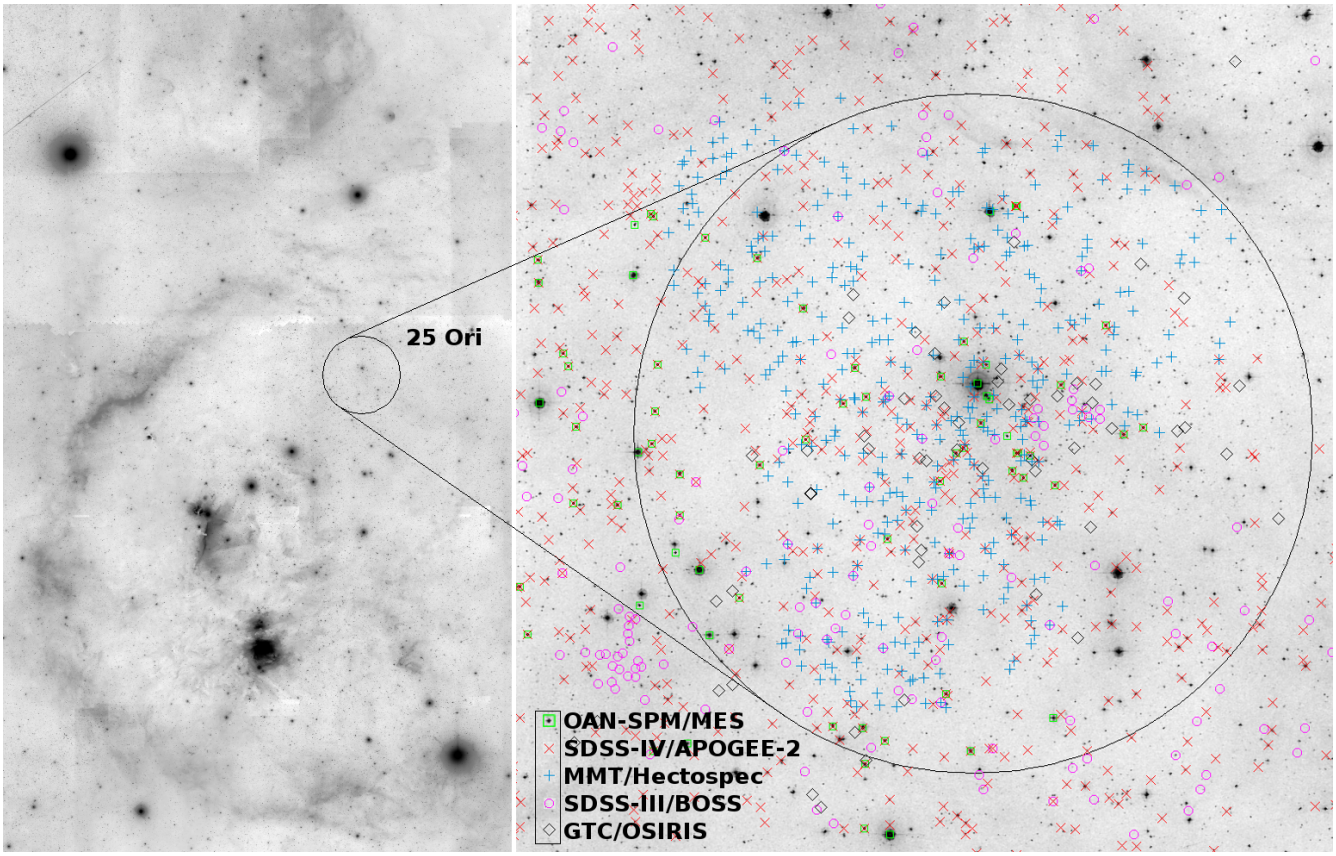

Figure 31: Spatial distribution of all the targets observed with the spectrographs indicated in the label. The black circle shows the 1° radius area of 25 Ori. The background image is from the Digitized Sky Survey (DSS).

As mentioned in Sections 3.4.3.1, 3.5.2.1 and 3.6.2.1, the spectral types of the optical spectra were determined using the SPTCLASS semi-automatic code, which uses empirical relations between the spectral types and several spectral features sensitive to T_{eff}. For the NIR spectra from APOGEE-2, the T_{eff} were obtained fitting synthetic spectra to the observed spectra (Kounkel et al., 2018).

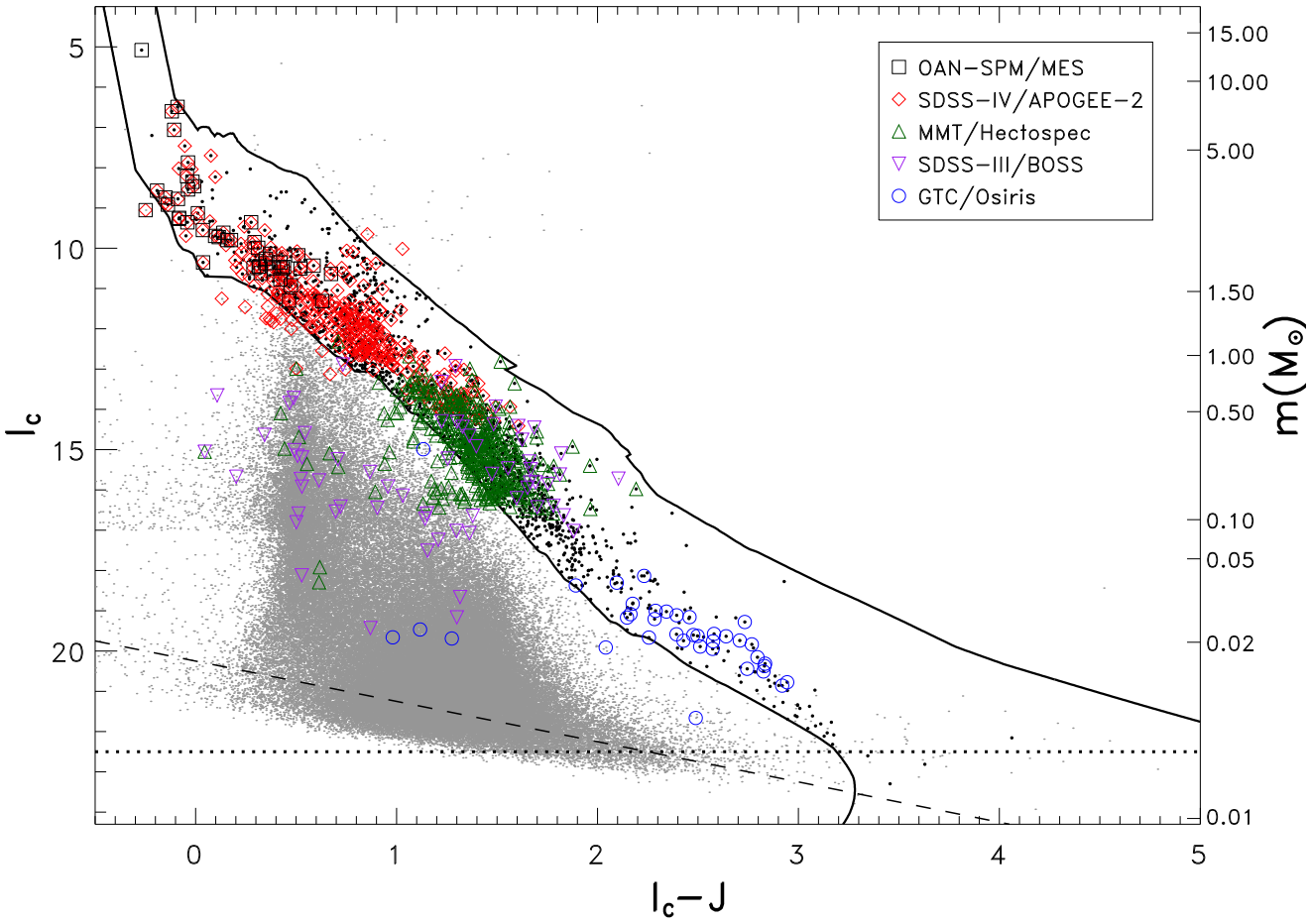

Figure 32: CMD of the targets observed using the facitilities indicated in the label. The black points show the member candidates selected in Section 2.3.1 as the sources lying inside the PMS locus (black solid curves). The dashed and the dotted curves are the same as in Figure 4.

The membership criteria we applied to the targets depend of their spectral types: *i*) For the earlier stars we considered radial velocities and distance criteria (see Section 3.2.2), *ii*) for the early M and K-type stars we analyzed the H_α emission and the LiIλ6708 and NaI$\lambda\lambda$8183, 8195 absorptions (see Section 3.4.3.2.1), and *iii*) for the late M-type stars we focused on surface gravity sensitive features (see Section 3.6.2.1). In Table 16 we indicate the number of confirmed members from the so far analyzed spectra and how many of them have been confirmed for the first time as well as the number of members we expect considering the remaining data.

To estimate the A_V of the confirmed stellar members we worked with the G_{BP} and G_{GP} photometry from Gaia DR2 and for the confirmed BD members with I_c and J photometry from the DECam and VISTA catalogs. For the estimation of L_{bol}, mass and age of all these members, we used the PHYPAR code described in Section 3.3.2.3.1 with the PARSEC-COLIBRI isochrones for members with masses larger than 0.2 $M_\odot$ and BT-Settl isochrones for lower masses.

In Figure 33 we summarize the general procedure followed to estimate the physical parameters of interest for most of the confirmed members and in Figure 34 we show the H-R diagram of all the so far confirmed members in our spectroscopic survey, including the member candidates observed using MES as well as the spectroscopically confirmed members in previous studies by Briceño et al. (2005, 2007); Downes et al. (2014, 2015); Briceño et al. (2019). We emphasize that this H-R diagram includes sources in a spectral type range between M9.5 and B1, which corresponds to

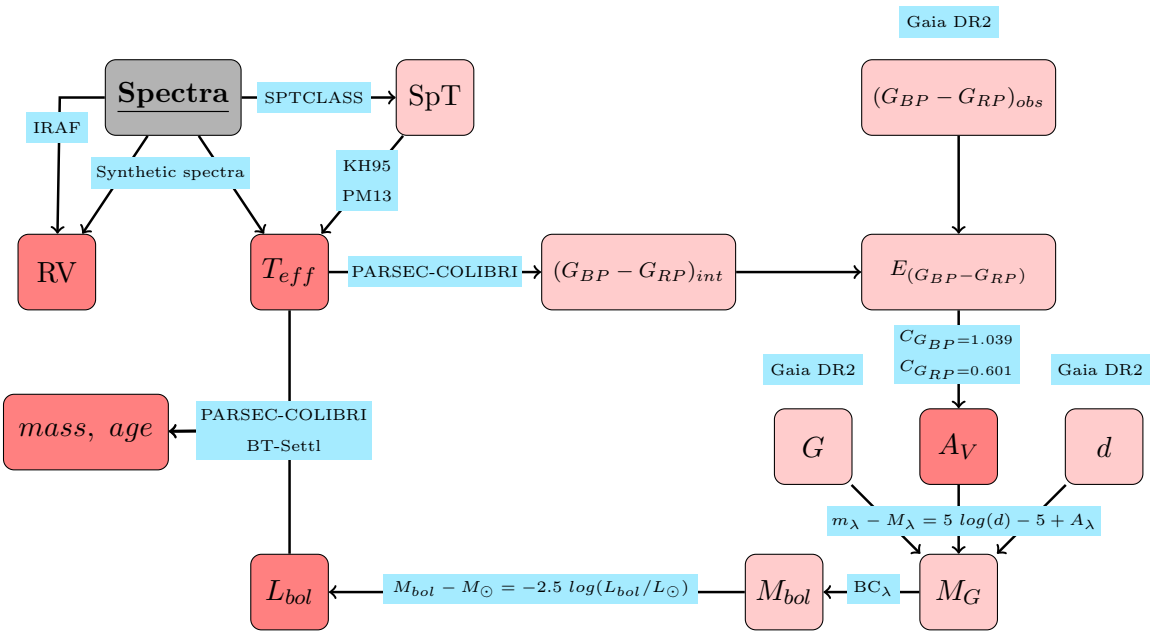

Figure 33: Summary flowchart of the general procedure followed to estimate the physical parameters of interest of the confirmed members in our spectroscopic survey.

T_{eff} between 2400 and 25000 K, considering the relation by Pecaut & Mamajek (2013). The total mass range covered by this sample runs from 0.015 to 11 $M_\odot$. The mean age we obtained from the whole sample of sources in this H-R diagram is 6.5 ± 2.5 Myr, which is very consistent with previous studies (6.1±2.4; Briceño et al., 2019, and references therein).

In Figure 35 we show the completeness of our spectroscopic survey in 25 Ori, also considering the members from the literature, according to the expected number of members from the tapered power law parameterization of its system IMF by Suárez et al. (2019). So far, the survey is $\sim 75\%$ complete, with most of the remaining unobserved targets in the very LMS and BD regime.

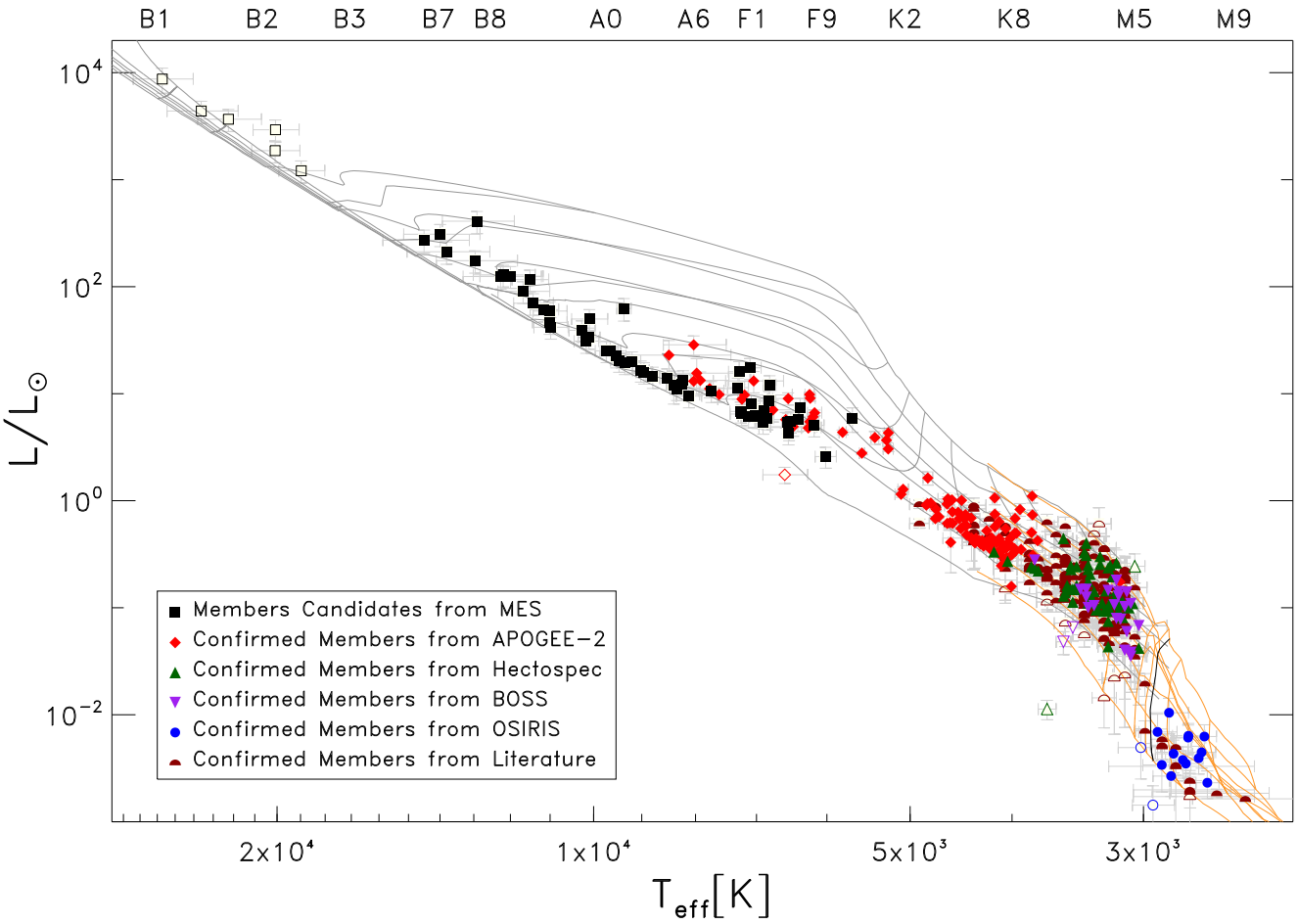

Figure 34: H-R diagram of the confirmed members using the spectra indicated in the label and of the member candidates observed using MES as well as of the previously confirmed members in the literature. The open symbols represent sources without mass and age estimates because lie outside the model grid. The gray curves represent the PARSEC evolutionary tracks of 0.3, 0.5, 0.7, 1, 1.5, 2, 3, 4, 5, 8 and 10 $M_{\odot}$ and the PARSEC-COLIBRI isochrones of 0.5, 1, 2, 3, 5, 10 and 30 Myr. The orange curves show the BT-Settl evolutionary tracks of 0.01, 0.02, 0.05, 0.08, 0.1 and 0.2 $M_{\odot}$ and isochrones of 0.5, 1, 2, 3, 5, 10 and 30 Myr. The black curve corresponds to the BT-Settl evolutionary track at the hydrogen burning limit mass (0.072 $M_{\odot}$). The upper axis shows the corresponding spectral types from Pecaut & Mamajek (2013).

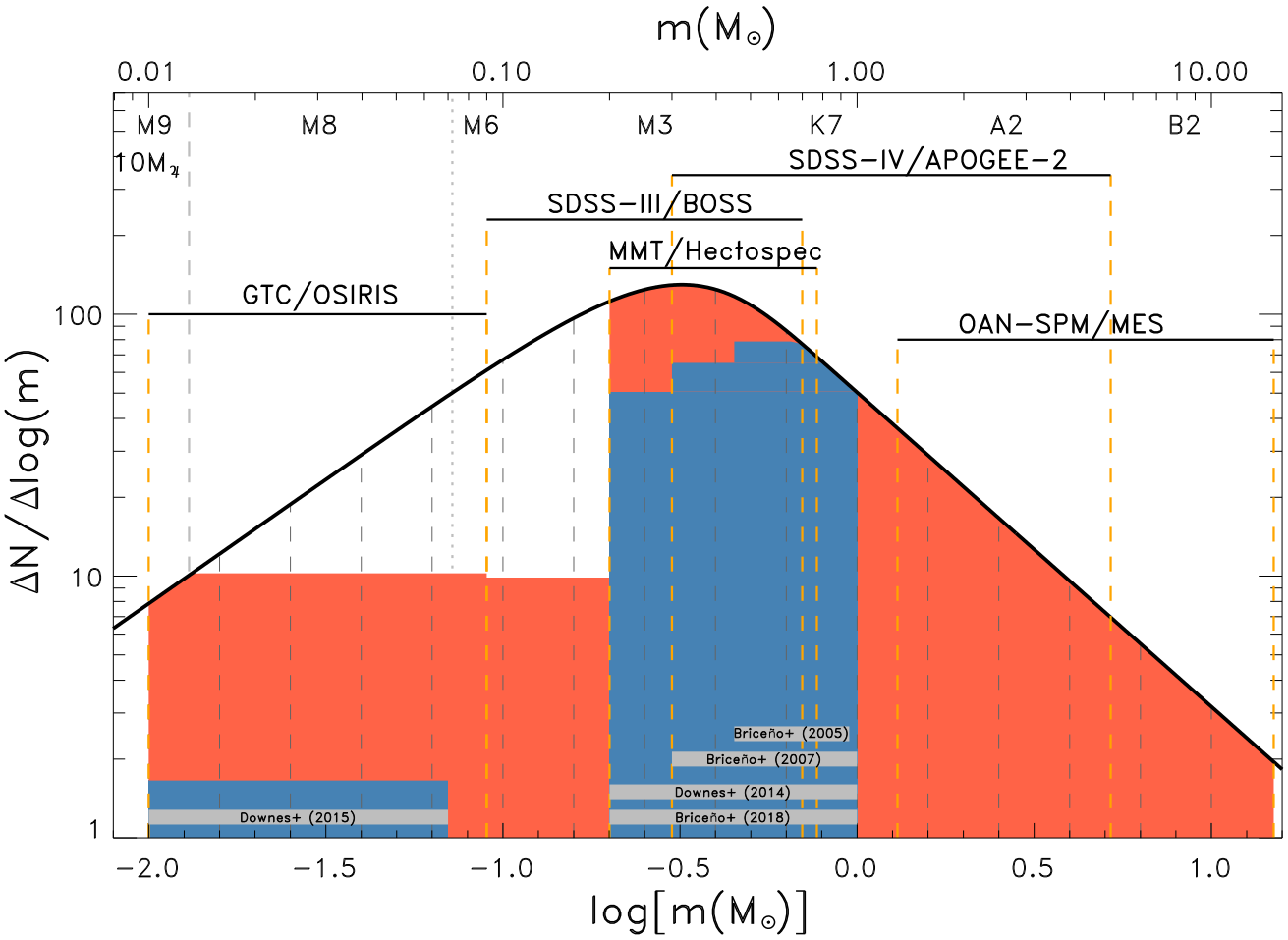

Figure 35: Completeness of the follow-up spectroscopy in 25 Ori according to the expected members from its system IMF. The black curve shows the tapered power law parameterization by Suárez et al. (2019). The yellow dashed lines indicate the mass range covered by our different spectroscopic surveys, as indicated in the plot. The orange and blue filled histograms show the expected member coverage in several mass ranges by our follow-up spectroscopy and by the members in the literature (indicated in the gray boxes), respectively. As reference, the black dashed lines show the edges of the 0.2 dex bins. The rest of lines and symbols are the same as in Figure 9.

4 Conclusions and Future Work

4.1 Conclusions

In this work we characterized the stellar and substellar population of 25 Ori through photometric and spectroscopic analysis. Here we list the main results obtained from this analysis:

- We selected, from a carefully defined PMS locus in color-magnitude and color-color diagrams combining optical and NIR photometry, a sample of 1687 member candidates in 25 Ori covering a mass range between 0.012 and 13.1 $M_{\odot}$ in a 1.1° radius area. The contamination present in this sample is ∼20% due to dwarfs of the field in the LMS regime but increases in the BD domain due to extragalactic sources and in the intermediate-mass range by giant and subgiant stars.

- With this sample of member candidates we constructed the 25 Ori system IMF from planetary-mass objects to intermediate/high-mass stars, which is one of the few IMFs over the whole mass range of a stellar group.

- We fitted a two-part power-law, a lognormal and a tapered power-law functions to the resultant system IMF to compare it with that in other stellar groups with a diversity of physical conditions. No significant differences were found, which suggests that the star formation process is largely insensitive to the enviromental conditions.

- We estimated that for each 6 stars in 25 Ori we can roughly expect one BD. This value is similar for different radii between 0.4 and 1.1°, which suggest that the substellar and stellar objects in 25 Ori have similar spatial distributions. Also, this BD/star ratio is consistent with that in other star-forming regions, which indicates that the formation of BDs and stars have a similar behavior in different environments.

- We analyzed the behavior of the system IMF when considering member candidates inside different areas. The variation of the IMF parameters are contained within the uncertainties for radii between 0.4 and 1.1° (2.5-6.8 pc). This indicates that the substellar and stellar objects in 25 Ori do not have any preferential spatial distribution.

- Considering the velocity dispersion and the total mass distribution of 25 Ori, we found that this group is very young to be dynamically relaxed.

- Comparing the escape velocity of 25 Ori with its velocity dispersion, we confirmed that 25 Ori is a gravitationally unbound stellar group that will be part of the Galactic Disk population.

- We have an ongoing spectroscopic survey to observe each of the 25 Ori member candidates using several world-wide facilities:

  i) 50 high-resolution spectra of intermediate/high-mass stars using MES at the OAN-SPM.

  ii) 353 high-resolution spectra of candidates with masses between 0.3 and 5.2 $M_{\odot}$ taken with APOGEE-2 from SDSS-IV.

  iii) 374 low-resolution spectra of targets with masses from 0.25 to 0.8 $M_{\odot}$ using Hectospec at the MMT

  iv) 68 low-resolution spectra of member candidates with masses ranging between 0.09 and 0.7 $M_{\odot}$ with BOSS from SDSS-III

v) 55 low-resolution spectra of BD candidates using OSIRIS at GTC.

- Considering several youth spectral features for the LMSs and BDs as well as distance and radial velocity criteria for the intermediate/high-mass stars, we have confirmed, so far, 290 members over the whole mass range of 25 Ori. 208 of these members are confirmed for the first time. Considering the remaining spectra without membership determination observed with MES, Hectospec and OSIRIS, we expect to have a total of 431 confirmed members in 25 Ori in our spectroscopic survey.

- We estimated the physical parameters (RV for the high-resolution spectra and T_{eff}, A_V, L_{bol}, mass and age for all the spectra). The mean RV (20.9 km s^{-1}), velocity dispersion (2.0 km s^{-1}), mean A_V (0.21-0.39 mag) and mean age (6.5 ± 2.5 Myr) we obtained are consistent with previous studies and are based on more robust statistic.

- From the sample of 53 confirmed members in 25 Ori and surroundings using spectra from BOSS, we analyzed their SEDs and classified their disks into evolutionary stages. We found that the IR excesses for sources harboring disks start at wavelengths larger than the *WISE* 3.4 μm band.

- So far, our spectroscopic survey is $\sim$ 75% complete, considering the confirmed member and those expected from the spectra without membership determination as well as those confirmed in the literature. Most of the targets to be observed have expected masses around the hydrogen burning limit.

4.2 Ongoing and Future Work

As a continuation of the scientific analysis derived from this thesis, we list the ongoing work and some of our plans for the near future:

- To complete the follow-up spectroscopy we are going to continue observing with OSIRIS. Additionally, we have ongoing Hectospec observations, where we are going to include some of the faint targets without spectra. Also, I plan to submit observational proposals to other facilities such as FLAMES on the VLT, COSMOS on the Blanco 4-m telescope and/or Goodman on the SOAR 4.1-m telescope.

- The mass distribution we presented in this work is the system IMF, which is not corrected by multiple system. We plan to work with binarity properties discussed in Duchêne et al. (2018) and those obtained in the Orion Complex (Kounkel et al. 2019, submitted) to study the effects of these systems in the determination of the single-star IMF.

- With the statistically complete sample of spectroscopically confirmed members I plan to:

  Construct, for the first time in a stellar association, the spectroscopic-based IMF across the entire mass spectrum of the population, from planetary-mass objects to intermediate/high-mass stars, and covering its whole spatial distribution.

  Analyze the kinematics, combining RVs from APOGEE-2 and MES with Gaia DR2, for the LMSs and intermediate/high-mass stars to try to disentangle the presence of other associations surrounding 25 Ori, as suggested by Kounkel et al. (2018); Briceño et al. (2019).

  Study the mass segregation effect in a relatively young group which could indicate the nature of this phenomenon; if it is a primordial property (Bonnell & Davies, 1998; Bonnell et al.,

2001) or due to dynamical evolution (Kroupa et al., 2001; Kroupa, 2001) of clusters. This kind of study is also important to understand the BD formation mechanism (Reipurth & Clarke, 2001; Padoan & Nordlund, 2002; Whitworth & Zinnecker, 2004).

Analyze the age dispersion of the members to contribute to the understanding of this phenomenon to know to what degree it can be explained by the corresponding uncertainties or if it is a real effect (Palla & Stahler, 1999, 2000). In case a real age spread exist, we can look for any suggestion about a preferential spatial distribution for younger and/or older stars (Beccari et al., 2017). Also, we can look for any tendency of the ages with respect to the mass as an indicative that the formation of objects with certain masses occurs first (Vázquez-Semadeni et al., 2017).

Study the frequency of the circumstellar disks in a wide mass range, from planetary-mass objects to intermediate/high-mass stars (Downes et al. 2019, in preparation).

Make a study of the chemical abundances from APOGEE-2 for the intermediate-mass members, which allow us to understand the chemical enrichment and to reconstruct the star forming histories of the Orion OB association.

A Additional Contributions

A.1 Collaborations

Part of the data to carry out this thesis project was obtained working in collaboration in several studies. Additionally, valuable experience on the analysis of photometric and spectroscopic data was obtained participating in these collaborations. In this appendix I describe my contribution in each collaboration and how it is related to my thesis project.

A.1.1 Kounkel et al. (2018)

As part of my collaboration with the APOGEE-2 Young Star Clusters working group, I contributed with the determination of the physical parameters (A_V, L_{bol}, mass and age) of the APOGEE-2 targets in the Orion Complex, which are distributed in several associations as λ Ori, Orion A, Orion B, Orion OB1a and Orion OB1b. These results are part of the Kounkel et al. (2018) study about the 6D-structure of the Orion Star-forming Complex.

From the 8991 unique APOGEE-2 targets in the Orion complex, I selected about 4200 sources as highly probable members of the different Orion associations on the basis of their kinematics considering radial velocities from the APOGEE-2 spectra (Kounkel et al., 2018) and proper motions from Gaia DR2, and their distances from Gaia DR2 parallaxes as well as their spatial distributions.

Working with the T_{eff} estimated in Kounkel et al. (2018) as well as the G_{BP} and G_{RP} photometries from Gaia DR2, I estimated the visual extinctions of the highly probable members of the Orion Complex. Also, I estimated A_V considering photometry from 2MASS. Additionally, I obtained the extinction values working with the dust maps from Schlegel et al. (1998), Gontcharov (2017), Green et al. (2018) and from dust emission maps from the Herschel space telescope. After some comparisons between these extinctions, we decided to work with those from the Gaia DR2 data. I compared these A_V from Gaia DR2 with those obtained by K. Stassun from spectral energy distribution fits and found not significant differences.

I estimated the L_{bol}, mass and age of the highly probable members of the Orion Complex using the PHYPAR routine with the T_{eff} from the APOGEE-2 spectra, the A_V we obtained using Gaia DR2 data and the distances and G magnitudes from Gaia DR2 and using the PARSEC-COLIBRI isochrones. Also, we obtained these parameters considering the H magnitudes from 2MASS instead of the G-band photometry from Gaia DR2. At the end, when possible, we averaged the masses and ages obtained from both bands. The final mass range covered by the sample is between 0.13 and 5.2 $M_\odot$ and the ages for the full sample are shown in Figure 13 from Kounkel et al. (2018).

After the identification of spatially and/or kinematically distinct stellar groups in Orion, the ages obtained as described here allowed the investigation of the star-forming history in this complex (Kounkel et al., 2018). The identified populations have ages between 1 to 12 Myr.

The physical parameters of the highly probable members of 25 Ori obtained in this collaboration constitute part of the spectroscopic survey for this dissertation.

A.1.2 Cottle et al. (2017)

In the Cottle et al. (2018) collaboration, I participated in the selection of the Orion targets that were observed with the APOGEE-2 spectrograph. Particularly, I selected about 4500 photometric member candidates of Orion OB1a and OB1b on the basis of their positions in the I vs $I-J$ and I vs $I-K$ diagrams using photometry from the USNO and 2MASS catalogs (see Figures 15, 16 and 17 from Cottle et al. 2018). I considered as candidates those sources lying inside the defined PMS locus assuming the empirical isochrone traced by several spectroscopically confirmed members

and highly probable members in the regions. Additionally, the target selection includes uniformly selected sources on the basis of IR excesses working with the 2MASS and WISE catalogs and variability from the PanSTARRS catalog as well as X-ray sources from the 3XMM-DR5 catalog. I worked in the design of the plates using a prioritization method to ensure the observation of the uniform selected sources, then of the X-ray sources and finally, to fill the remaining fibers, of the candidates from the CMDs.

For most of these targets, together with those in the λ Ori, Orion A and Orion B associations, we obtained APOGEE-2 spectra, which are part of the Kounkel et al. (2018) study.

The APOGEE-2 plates dedicated to 25 Ori (Ori OB1ab-E and OB1ab-F) were designed as part of this collaboration. These data are an important part of the 25 Ori ongoing follow-up spectroscopy in this thesis project.

A.1.3 Ramírez-Preciado et al. (2018)

My main contribution in the Ramírez-Preciado et al. (2018) study was to estimate the physical parameters (L_{bol}, mass and age) for a sample of 571 candidates to belong to young nearby moving groups (YNMGs) and to clean the sample by removing post-MS star contaminants. This sample was obtained from a collection of chromospheric active stars in the Radial Velocity Experiment (RAVE) catalog (Kunder et al., 2017).

For this purpose, I used the PHYPAR routine with T_{eff} and A_V from RAVE, distances from the Gaia DR2 parallaxes and J-band magnitudes from 2MASS as well as V-band photometry from the AAVSO Photometric All Sky Survey (APASS) DR9 catalog (Henden et al., 2016), as a comparison. The resulting mass range of the sample is between 0.5 and 1.6 $M_{\odot}$. About 50% of the candidates (290) have ages younger than 100 Myr, which is roughly consistent with the percentage of chromospheric active stars in RAVE that are known to be high H_{α} emitters (Žerjal et al., 2013). This allowed us to remove about a half of the candidates, which have $M_V \geq 4.5$ mag and lie in the post-MS in the H-R diagram. In Figure 8 from Ramírez-Preciado et al. (2018) we show the H-R diagram of the clear sample. This sample was used to identify YNMGs and/or to associate the candidates to previously identified YNMGs on the basis of kinematics criteria using a technique called the Cone Method (Ramírez-Preciado et al., 2018).

The experience I obtained working with this data allowed me to improve my own PHYPAR routine, which we are using for the estimation of the L_{bol}, mass and age of the resulting members of 25 Ori in our ongoing spectroscopic survey.

A.1.4 Richer et al. (2017)

I participated measuring the Full Width at Half Maximum (FWHM) of several spectral lines ([NII]$\lambda\lambda$6548,6583, HeIIλ6560, H_{α} and CIIλ6578) in high-resolution spectra of 76 planetary nebulae, most of them obtained from the San Pedro Mártir Kinematic Catalogue of Planetary Nebulae (López et al., 2012). These measurements were used in the Richer et al. (2017) study of the kinematics of the CIIλ6578 permitted line with respect to the other mentioned lines to contribute to the understanding of the well-known abundance discrepancy problem.

For the measurements of the FWHMs of the lines of interest, I worked with `IRAF` tasks to fit Gaussians to the observed line profiles. The experience I obtained from this study was applied to the analysis of the spectra in 25 Ori from the BOSS spectrograph (Suárez et al., 2017c). Also, this ability is being used to analyze the spectra from the rest of the spectroscopic survey.

A.1.5 Interdisciplinary Collaborations

Due to my contribution in the selection of APOGEE-2 targets in the Orion Complex and in the analysis of these spectra as well as to my participation in the meetings of the APOGEE-2 Young Star Clusters working group, I am coauthor in the following collaboration papers: *i*) 13th Data Release of SDSS (Albareti et al., 2017), *ii*) SDSS-IV (Blanton et al., 2017), *iii*) 14th Data Release of SDSS (Abolfathi et al., 2018), *iv*) 15th Data Release of SDSS (Aguado et al., 2018), *v*) Roman-Lopes et al. (2019) *vi*) Borissova et al. (2019, submitted) and *vii*) Kounkel et al. (2019, submitted).

A.2 Proceedings

A.2.1 XV Latin American Regional IAU Meeting

During the XV Latin American Regional IAU Meeting I presented my PhD thesis project and the status of the work, as described in Suárez et al. (2017a). Also, I presented the analysis of low-resolution spectra in 25 Ori from the BOSS spectrograph, which are part of the Suárez et al. (2017c) study.

A.2.2 Francesco's Legacy: Star Formation in Space and Time

I presented in the Suárez et al. (2017b) contribution, during the Francesco's Legacy: Star Formation in Space and Time conference, the advances of the photometric determination of the system IMF of 25 Ori, stressing the importance and difficulties of removing the extragalactic contamination in deep photometric studies in this kind of stellar associations that present minimum extinction.

A.2.3 Cool Stars 20

During the Cool Star 20 conference I presented in Suárez et al. (2018) the determination of the 25 Ori system IMF complete from 0.012 to 13.1 $M_{\odot}$. This presentation allowed to improve the discussion about the comparisons between this IMF and those in other clusters, as reported in Suárez et al. (2019).

B From Suárez et al. (2019)

B.1 Calibration of the DECam Photometry

To calibrate our DECam photometry we first added the zero point of 25.18 mag from the image headers to the instrumental magnitudes. Then, we compared these instrumental magnitudes with the i magnitudes in the DECam system obtained using the i and z-band photometry from SDSS according to Transformation 8[12].

$$i_{DECam} = i + 0.014 - 0.214 * (i - z) - 0.096 * (i - z)^2 \quad (8)$$

where i_{DECam} are in the DECam system and i and z magnitudes are in the SDSS system.

The comparison was done for sources having colors $i - z < 0.8$ mag (valid range of the transformation), considering sources not having a high probability of being variable stars according to the CIDA Variability Survey of Orion (Briceño et al., 2005; Mateu et al., 2012; Briceño et al., 2019)

[12] http://www.ctio.noao.edu/noao/content/Photometric-Standard-Stars-0#transformations

and for sources having i and z-band photometric errors lesser than 0.05 mag. The mean value of the resultant residuals is 0.637 mag. Thus, we added this value to our DECam photometry to calibrate it. In Figure 36 we show the residual between our calibrated photometry and that in the DECam system using the SDSS catalog. The typical residuals are -0.001 mag with a RMS of 0.038 mag.

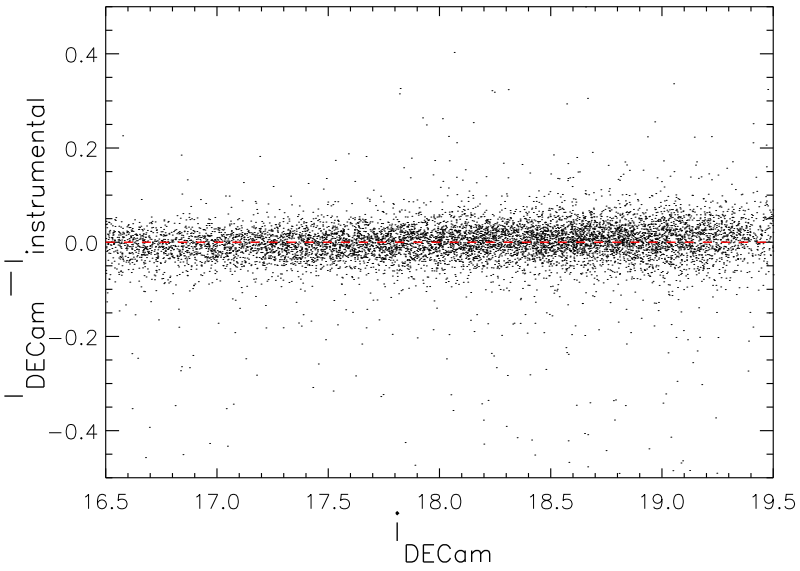

Figure 36: Residual between our calibrated photometry from DECam and the i-band photometry in the DECam system obtained using the SDSS catalog.

B.2 Transformation of the UCAC4 and DECam Photometry to I_c Magnitudes

We used transformations from Jordi et al. (2006) and empirical relations obtained directly from our data to convert the i-band magnitudes from the UCAC4 and DECam catalogs to the I_c-band magnitudes.

B.2.1 UCAC4 Data

As the transformations from Jordi et al. (2006) relate the SDSS and Cousins photometric systems, we first checked that the UCAC4 photometry are in the SDSS system.

The r and i-band photometry in UCAC4 came from the AAVSO [13] Photometric All-Sky Survey (Henden et al., 2016). These data were taken using the r' and i'-band filters from SDSS, whose magnitudes are on the AB system and are close to the r and i magnitudes of SDSS[14]. In Figure 37 we show the residuals between the r and i magnitudes from SDSS and UCAC4 as a function of the SDSS magnitudes. We did not consider the sources having $> 90\%$ probability of being variables according to the CVSO and only worked with sources having photometric errors lesser than 0.05 mag. In average, these residuals are basically zero for sources brighter than the SDSS saturation limit ($\sim$14 mag), which indicates that the r and i-band photometries from UCAC4 can be consider to be in the SDSS photometric system.

Thus, we worked with the following transformations from Jordi et al. (2006), which use the r and i-band magnitudes from SDSS:

[13] https://www.aavso.org
[14] http://www.sdss3.org/dr8/algorithms/fluxcal.php#SDSStoAB

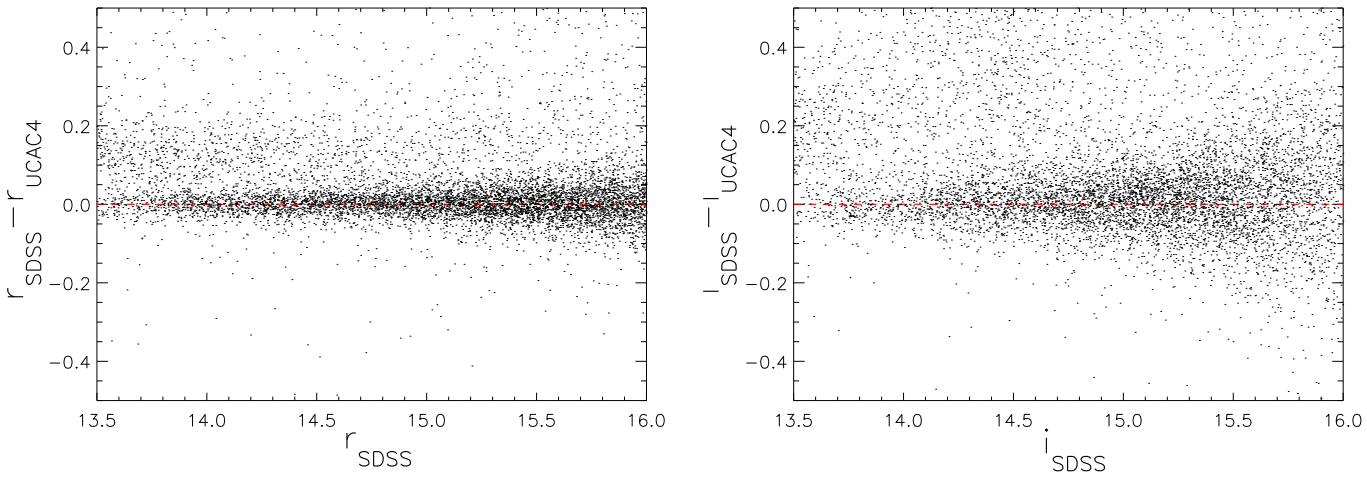

Figure 37: Residual between the SDSS and UCAC4 photometries as a function of the SDSS magnitudes in the r and i-bands (left and right panels, respectively).

$$R_c - r = -0.153 * (r - i) - 0.117 \tag{9}$$

$$R_c - I_c = 0.930 * (r - i) + 0.259 \tag{10}$$

Subtracting Transformation 10 from Transformation 9:

$$I_c - r = -1.083 * (r - i) - 0.376 \tag{11}$$

We used Transformation 11 to obtain the I_c magnitudes considering the r and i-band photometry from UCAC4. We compared the resultant I_c magnitudes with those from the CDSO, which are already in the Cousin system. In the left panel of Figure 38 we show the residual between the I_c magnitudes from the CDSO and UCAC4, where we can see that the peak of the residual distribution is somewhat deviated from zero. Therefore, we did slight modifications to the coefficients of Transformation 11 to have average residuals closer to zero. The resulting transformation is:

$$I_c - r = -1.323 * (r - i) - 0.353 \tag{12}$$

In the right panel of Figure 38 we show the I_c residuals between the CDSO and UCAC4 photometries after applying Transformation 12 to the UCAC4 data. The peak of the I_c residual histograms are essentially zero, with a RMS of 0.07 mag for all the sources within the CDSO saturation limit and the UCAC4 completeness limit (13-14.75 mag).

B.2.2 DECam Data

The i filter used in our DECam observations is similar to the i filter from SDSS (NOAO Data Handbook[15]). However, there is a color dependence to transform the DECam data to the SDSS system. As we only have DECam photometry taken with the i filter, in addition to these data we worked with the Z-band photometry from VISTA. This way, we will transform the DECam photometry only for the sources with VISTA counterpart, which is not an issue because for the selection of member candidates we used both catalogs. The Z-band photometry from VISTA is in the Vega system and to convert it to z'-band magnitudes in the AB system it is necessary to add

[15] http://ast.noao.edu/sites/default/files/NOAO_DHB_v2.2.pdf

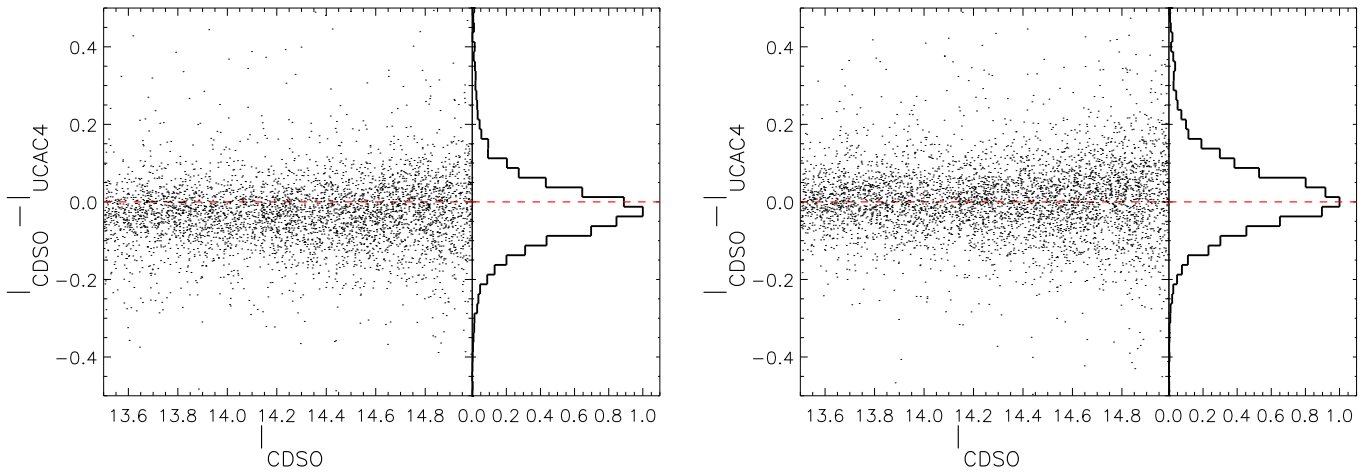

Figure 38: I_c-residuals between the CDSO and UCAC4 after applying Transformation 11 (left panel; Jordi et al., 2006) and Transformation 12 (right panel), which is a slight modification of Transformation 11.

the zero-point of 0.58 mag (Pickles & Depagne, 2010). These z'-band magnitudes are not exactly the same as the z-band magnitudes in the SDSS system, there is a small shift of 0.02 mag which should be subtracted[16]. Therefore, we added 0.56 mag to the Z-band photometry from VISTA to obtain the z-band magnitudes in the SDSS system. In Figure 39 we show the residuals between the z magnitudes directly from SDSS and from VISTA after the addition of the offset. We removed the sources with $> 90\%$ probability of being variable according to the CVSO catalog and we only considered sources with errors lesser than 0.05 mag. The average of the resultant residuals is -0.008 mag with a RMS of 0.04 mag.

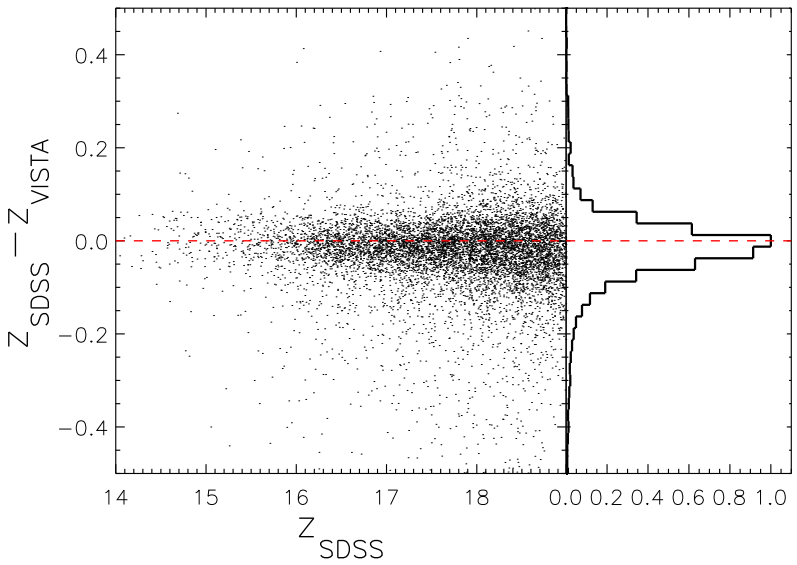

Figure 39: Residuals between the z magnitudes in the SDSS system directly from the SDSS catalog and from VISTA.

In left panel of Figure 40 we show the color dependence of the residuals between our calibrated DECam data and those from SDSS as a function of the $i - z$ color combining the calibrated photometry from DECam and the photometry from VISTA converted to the SDSS system. The second order function that best fits the residuals is:

[16] http://www.sdss3.org/dr8/algorithms/fluxcal.php#SDSStoAB

$$i - i_{DECam} = -0.008 + 0.194 * (i_{DECam} - z) + 0.381 * (i_{DECam} - z)^2 \quad (13)$$

where i_{DECam} are in the DECam system and i and z in the SDSS system.

We used Transformation 13 to convert our calibrated DECam photometry to the SDSS system. In right panel of Figure 40 we show the residuals between the i-band magnitudes in the SDSS system obtained directly from SDSS and from our calibrated DECam data. The average of the residuals is 0.002 mag with a RMS of 0.04 mag.

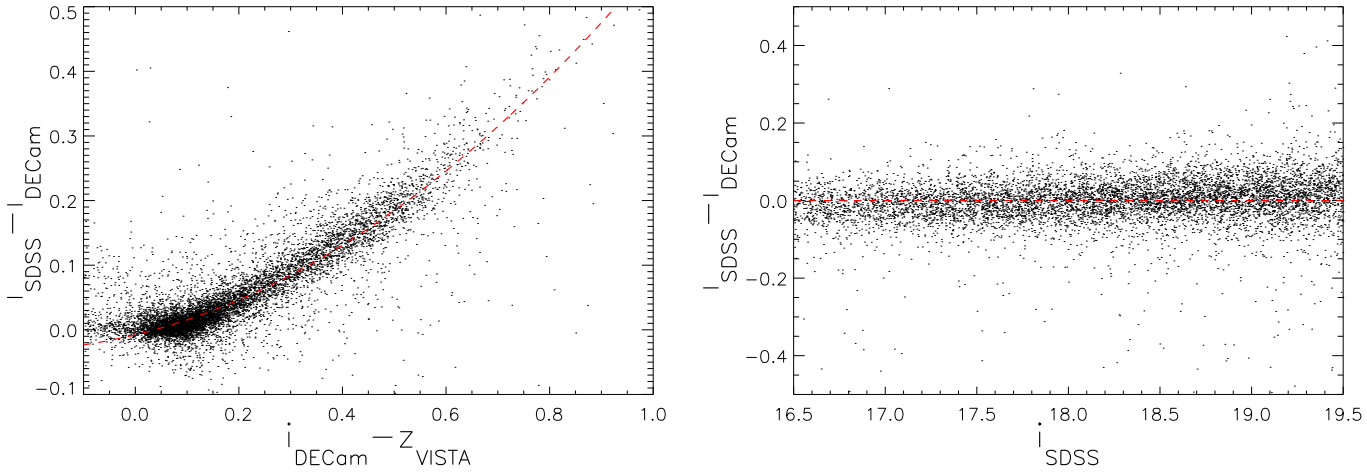

Figure 40: **Left panel:** Residuals between the i magnitudes from the SDSS catalog and from our calibrated DECam data as a function of the $i-z$ color from DECam and VISTA data in the SDSS system. The red dashed line indicate the second order function fitted to the residuals. **Right panel:** Residuals between the i-band photometries in the SDSS system directly from SDSS and from DECam after applying Transformation 13.

Finally, once we have both the i-band photometry from DECam and the Z-band photometry from VISTA in the SDSS system, we converted them to I_c magnitudes in the Cousins system. In left panel of Figure 41 we show the $i-z$ dependence of the residual between the I_c magnitudes from the CDSO survey and our DECam data in the SDSS system. The second order function fitted to the residual is:

$$I_c - i = -0.406 - 0.446 * (i - z) - 0.154 * (i - z)^2 \quad (14)$$

where I_c is in the Cousins system and i and z the SDSS system.

We used Transformation 14 to obtain the I_c magnitudes from our DECam and VISTA photometries in the SDSS system. In right panel of Figure 41 we show the residuals between the I_c magnitudes from the CDSO and those obtained from our DECam data. We did not consider neither the sources having $> 90\%$ probability of being variable stars in the CVSO catalog nor the sources with errors larger than 0.05 mag. The resultant residuals have an average of -0.001 mag with a RMS of 0.04 mag.

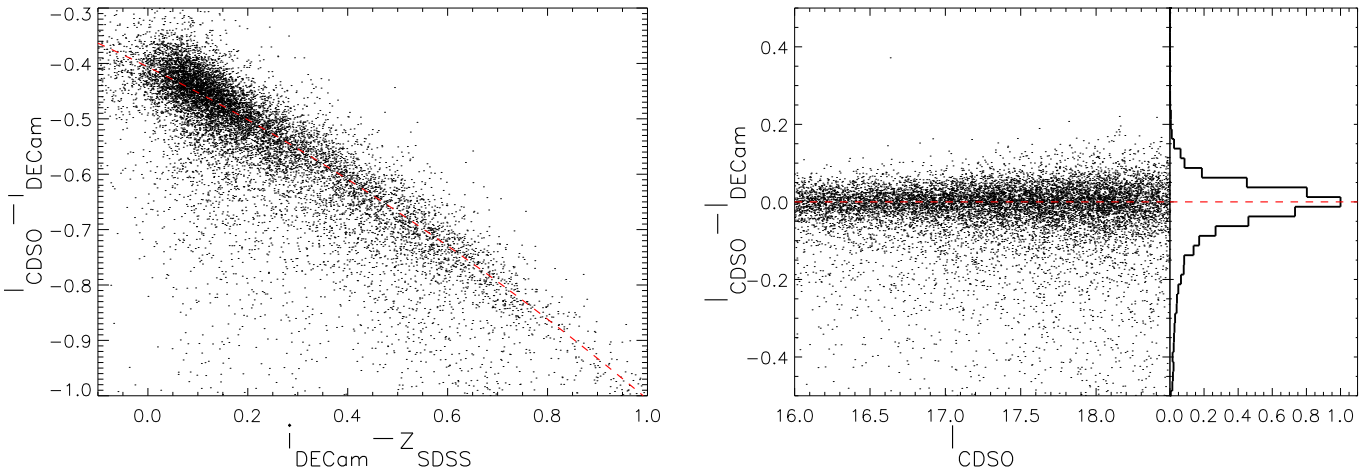

Figure 41: **Left panel:** Residuals between the I_c magnitudes from the CDSO and the i magnitudes from DECam as a function of the $i - z$ color from DECam and VISTA data in the SDSS system. **Right panel:** Residuals between the I_c-band photometries from the CDSO and DECam after applying Transformation 14.

B.3 Distance, Extinction and Proper Motion of 25 Ori

B.3.1 25 Ori Distance

To estimate the 25 Ori distance, we first compiled a list of 334 unique spectroscopically confirmed members of 25 Ori by Briceño et al. (2005, 2007); Downes et al. (2014, 2015); Suárez et al. (2017c); Briceño et al. (2019). Then, we cross-matched this list with Gaia DR2 and with the BJ18 catalog. 91% of the confirmed members have Gaia DR2 parallaxes with uncertainties of $\leq$ 20%. Using these parallaxes and the TOPCAT tool (Taylor, 2005) with the method implemented by Bailer-Jones (2015) and BJ18, we calculated the best distance estimates and the 25th and 75th percentile confidence intervals using the Exponentially Decreasing Space Density prior with a lenght scale of 500 pc. We consider these distance estimates as the distances of the compiled members and the percentiles as the uncertainties, which are very consistent with those obtained working with the inverse of the parallax as well as with the BJ18 distances.

In the left panel of Figure 42 we show the cumulative distribution of the distances of the confirmed members with parallax errors of $\leq$ 20%, which cover a range from 127 to 545 pc, but there is a clear concentration of members around the 25 Ori expected distance with 94% of them between 250 and 450 pc. From these distances we obtained that 25 Ori is 356±47 pc away, which is consistent with previous studies (Briceño et al., 2007; Downes et al., 2014; Suárez et al., 2017c; Briceño et al., 2019; Kounkel et al., 2018).

B.3.2 25 Ori Extinction

About 96% of the 334 confirmed members of 25 Ori by Briceño et al. (2005, 2007); Downes et al. (2014, 2015); Suárez et al. (2017c); Briceño et al. (2019) have reported visual extinctions obtained through spectroscopic analysis. In the right panel of Figure 42 we show the cumulative distribution of these extinctions, which go up to 1.88 mag (excluding two members with values of 3.53 and 6.29 mag) but more than 93% of the members with reported extinction have values lower than 1 mag. Considering values up to 1.88 mag, the mean visual extinction of the 25 Ori is 0.35±0.35

mag. If we consider values lower than 1 mag, the 25 Ori mean visual extinction is 0.29±0.26 mag. As expected, both values are consistent with previous studies (Kharchenko et al., 2005; Briceño et al., 2005, 2007; Downes et al., 2014; Suárez et al., 2017c; Briceño et al., 2019).

B.3.3 25 Ori Proper Motion

To estimate the proper motion of 25 Ori we used the list of 25 Ori confirmed members (Briceño et al., 2005, 2007; Downes et al., 2014, 2015; Suárez et al., 2017c; Briceño et al., 2019) having Gaia DR2 parallaxes with errors of $\leq$ 20%. We discarded 6 members with clearly discrepant proper motions and 17 members forming a possible distinct overdensity (perhaps ASCC 18). With the remaining 81% of the sample we estimated that the mean proper motion of 25 Ori is $\mu_\alpha = 1.33\pm0.46$ mas yr^{-1} and $\mu_\delta = -0.23 \pm 0.55$ mas yr^{-1}.

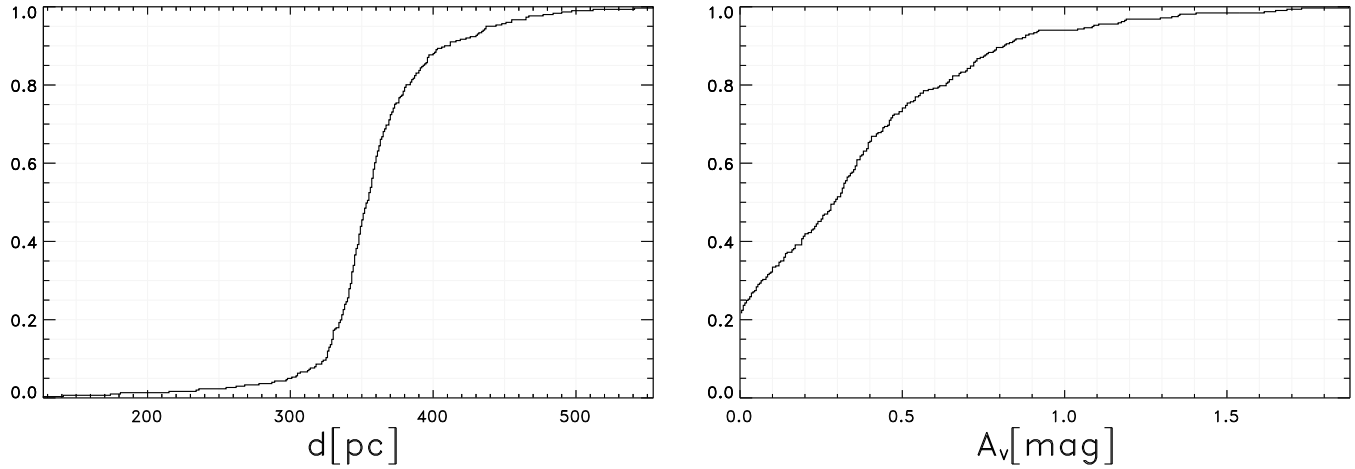

Figure 42: Normalized cumulative distributions of the distances (left panel) and extinctions (right panel) for the spectroscopically confirmed members of 25 Ori by Briceño et al. (2005, 2007); Downes et al. (2014, 2015); Suárez et al. (2017c); Briceño et al. (2019). The distances are from the Gaia DR2 parallaxes with uncertainties of $\leq$ 20%. The extinctions were mostly estimated through spectral analysis and combining optical and NIR photometry.

B.4 Distances and Extinctions for the Member Candidates and Contaminants

As we do not have distances and extinctions for all the member candidates (86% have distances and 18% have visual extinctions) and contaminants, we need to assign these values to the whole samples to have consistency with the 25 Ori members. The most common way to do this in photometric studies in the literature is to consider the mean distance and extinction of the cluster for all the member candidates. Here, we can take advantage of the Gaia DR2 parallaxes as well as of the previous spectroscopic studies in 25 Ori to use a statistically more robust technique. Considering the inversion of the normalized cumulative distribution of the BJ18 distances of the 25 Ori confirmed members (left panel of Figure 42), we created random realizations to assign distance values to all our member candidates and contaminants. We also assigned extinction values to these samples in a similar way, but considering the normalized cumulative distribution of the reported visual extinctions of the 25 Ori confirmed members (right panel of Figure 42).

This way, the distance and extinction values we assigned to each candidate and contaminant are consistent with those for the confirmed members of 25 Ori.

C From Suárez et al. (2017c)

C.1 Field Stars

The 119 objects resulting as field stars lack H_α emission and/or LiIλ6708 absorption, and show strong NaI$\lambda\lambda$8183, 8195 doublet in absorption. In Table 17 we list these stars rejected as confirmed members as well as their spectral types together with their I magnitudes and $I-J$ colors.

Table 17: Stars on the BOSS plate rejected as confirmed members of 25 Ori or Orion OB1a.

RA	DEC	SpT	I	$I-J$
80.842323	1.310326	A4.8 ±3.6	16.587	.494
82.423676	1.507883	A5.1 ±3.9	15.071	.562
81.696971	0.706731	A5.2 ±3.7	15.134	.530
82.240343	1.305623	A5.3 ±4.5	15.242	.568
80.048167	1.076809	A6.4 ±4.8	14.051	.551
82.15245	0.754426	A6.7 ±4.2	14.655	.565
82.527304	1.605351	A8.2 ±5.4	15.897	.605
80.51536	0.695541	F0[a]±—	16.268	.543
80.049821	1.307561	F0[a]±—	18.248	.598
81.607394	1.125553	F0.5 ±4.5	16.802	.499
79.928433	1.42041	F1.8 ±5.2	14.876	—
82.211707	1.089703	F2.2 ±4.9	15.305	.508
82.112572	1.021283	F2.3 ±5.1	15.757	.524

Note. The SDSS spectral type classification has not assigned the spectral type uncertainties.
[a] Spectral type assigned by the SDSS classification. Our SPTCLASS classification failed for this star.
(The complete version of this table is available in the electronic version of the Suárez et al. 2017c publication.)

D PHYPAR Routine

```
function phy_par, d, ed, T, eT, Av, eAv, Xmag, eXmag, BAND = band, MODEL = model, $
         MIN_AGE = min_age, MAX_AGE = max_age, MIN_MASS = min_mass, MAX_MASS = max_mass, $
         MAX_LBOL = max_Lbol

;+
; NAME:
;    phy_par()
; PURPOSE:
;    Estimate bolometric luminosity, mass and age of a set of targets
; EXPLANATION:
;    Using the distance, temperature, extinction and photometry of a set of
;    sources, compute their bolometric luminosity, mass and age together
;    with their uncertainties.
; CALLING SEQUENCE:
;    p    = phy_par(d, ed, T, eT, Av, eAv, Xmag, eXmag)
; INPUTS:
;    d        : distance in pc
;    ed        : distance uncertainties in pc
;    T        : temperature in K
;    eT        : temperature uncertainties in K
;    Av        : extinction in mag
;    eAv        : extinction uncertainties in mag
;    Xmag    : magnitude of the sources
```

```
;    eXmag    : magnitude uncertainties of the sources
; KEYWORD PARAMETERS:
;    band               : Photometric band of the input magnitude array. Options:
;        Vmag           : Vmag from Johnson
;        Rmag           : Rmag from Cousins
;        Imag           : Imag from Cousins
;        Gmag           : Gmag from Gaia
;        Jmag           : Jmag from 2MASS
;        Hmag           : Hmag from 2MASS
;        Kmag           : Kmag from 2MASS
;    model               : specify the models to be used.
;        PARSEC-COLIBRI    : isochrones from Marigo et al. (2017)
;        BT-Settl         : isochrones from Baraffe et al. (2015)
;    min_age               : youngest isochrone from the model (in yr)
;    max_age               : oldest isochrone from the model (to avoid the post-MS; in yr)
;    min_mass           : minimum mass to be used from the model (in Msun)
;    max_mass           : maximum mass to be used from the model (to avoid the
;                         evolution of massive stars; in Msun)
;    OPTIONAL
;        max_bol           : maximum Lbol from the model to be considered to avoid post-MS
;                         stages (when the model include them)
; OUTPUTS: an array containing Teff, Lbol, mass and age and their uncertainties
;
; EXAMPLE:
;    Obtain the Lbol, mass and age as well as their uncertainties for a set of targets, using the PARSEC-COLIBRI isochrones
;        p   = phy_par(d, ed, T, eT, Av, eAv, mag, emag, BAND = 'Vmag', MODEL = 'PARSEC-COLIBRI', min_age=age_mincut, $
;                    max_age=age_maxcut, min_mass=mass_mincut, max_mass=mass_maxcut)
;           T     = p[0,*]
;           eT    = p[1,*]
;           L     = p[2,*]
;           eL    = p[3,*]
;           mass  = p[4,*]
;           emass = p[5,*]
;           age   = p[6,*]
;           eage  = p[7,*]
;
; MODIFICATION HISTORY
;               by G. Suárez
;    11/09/18    Usage of the BT-Settl isochrones (Baraffe+2015)
;                Usage of the Rc and Ic bands
;    05/07/18    Usage of the Gmag from Gaia
;    03/19/18    Avoid the code stops when there is not any generated Teff, Lbol
;                inside the model grid. Mass and age errors are defined as 99.99.
;    03/17/18    Usage of the 2MASS bands.
;                Vmag not necessary in case of using 2MASS bands.
;    03/05/18    Output array has the same order as the input array.
;     02/22/18    Uncertainty estimation improvement when doing interpolations.
;     02/20/18    Improvement in the interpolation to obtain masses and ages.
;     07/31/15    Uncertainty estimates.
;     07/29/15    Development of the code by G. Suárez.

print,''
print,'%%%%%%%%%%%%%%%%%%%%%%%%%%%%%%%%%%%%%%%%%%%%%%%%%%%%%%%%%%%%%%%%%%%%%%%'
print,'%%%%%%%  Beginning of the phy_par code %%%%%%%%%%'
print,'%%%%%%%%%%%%%%%%%%%%%%%%%%%%%%%%%%%%%%%%%%%%%%%%%%%%%%%%%%%%%%%%%%%%%%%'
print,''

;#############################################################################
;#######################  FITTED PARAMETERS  #################################
;#############################################################################
                                                                              ;#
; Bolometric magnitude of the Sun.                                            ;#
Mbol_sun    = 4.755  ; (Mamajek 2012)                                         ;#
eMbol_sun    = 0.0004 ; error                                                 ;#
                                                                              ;#
; Extinction coefficients for the different filters.                          ;#
CI    = 0.751 ; A_R/A_V = 0.751 (Cardelli et al. 1989).                       ;#
CI    = 0.479 ; A_I/A_V = 0.479 (Cardelli et al. 1989).                       ;#
CJ    = 0.282 ; A_J/A_V = 0.282 (Cardelli et al. 1989).                       ;#
CH    = 0.190 ; A_H/A_V = 0.190 (Cardelli et al. 1989).                       ;#
CK    = 0.114 ; A_K/A_V = 0.114 (Cardelli et al. 1989).                       ;#
CG    = 0.9145; A_G/A_V = 0.9145 (J. Hernández private communication).        ;#
                                                                              ;#
```

```
;#########################################################################

; Extinction coefficients for the Xmag
if (band eq 'Vmag') then CXmag = 1.0
if (band eq 'Rmag') then CXmag = CR
if (band eq 'Imag') then CXmag = CI
if (band eq 'Jmag') then CXmag = CJ
if (band eq 'Hmag') then CXmag = CH
if (band eq 'Kmag') then CXmag = CK
if (band eq 'Gmag') then CXmag = CG

; Kenyon & Hartmann (1995) table.
filename_KH98    = 'files/Kenyon&Hartmann_1995_ApJ_101_117.cat'
readcol, filename_KH98, T_KH98, BCv_KH98, VR_KH98, VI_KH98, VJ_KH98, VH_KH98, VK_KH98, GJ_KH98, $
 format='x,x,x,f,f,x,x,f,x,f,x,f,f,f,x,x,x,x,f', comment='#'
    ; V-Xmag color
    if (band eq 'Vmag') then VXmag_KH98    = replicate(0.0, N_elements(T_KH98))
    if (band eq 'Rmag') then VXmag_KH98    = VR_KH98
    if (band eq 'Imag') then VXmag_KH98    = VI_KH98
    if (band eq 'Jmag') then VXmag_KH98    = VJ_KH98
    if (band eq 'Hmag') then VXmag_KH98    = VH_KH98
    if (band eq 'Kmag') then VXmag_KH98    = VK_KH98
    if (band eq 'Gmag') then VXmag_KH98    = VJ_KH98 - GJ_KH98

    if (band eq 'Gmag') then begin
        ind    = where(GJ_KH98 ne 9999) ; remove the late SpT without G-J estimates
            T_KH98        = T_KH98[ind]
            BCv_KH98    = BCv_KH98[ind]
            VXmag_KH98    = VXmag_KH98[ind]
    endif

; MODELS
; PARSEC-COLIBRI (Marigo et al. 2017) isochrones with the UBVRIJHK photometry
if(model eq 'PARSEC-COLIBRI') then begin
    print, 'reading PARSEC-COLIBRI isochrones...'
    root_model    = 'files/Marigo_et_al._2017_ApJ_835_77/'
    file_model    = root_model+'isochrones.cat'
    readcol, file_model, age_model, mass_model, logL_model, logT_model, Mv_model, Mj_model, $
     format='x,f,x,f,f,f,x,x,x,x,x,x,x,x,x,x,x,x,x,x,x,x,x,f,x,x,f,x,x', comment='#'

    L_model    = 10.^logL_model
    T_model    = 10.^logT_model

    ; cut the isochrones in the specified mass range
    ; keep ages between the specified range
    ; remove some weird points with logL=-9.999
    ind    = where(mass_model gt min_mass and mass_model lt max_mass and age_model ge min_age and $
                age_model le max_age and L_model gt 10.^(-9.) and Mv_model-Mj_model lt 7.0)
    ; also a luminosity cut to avoid post-MS stages
    if keyword_set(max_Lbol) then begin
        ind = where(mass_model gt min_mass and mass_model lt max_mass and age_model ge min_age and age_model $
                    le max_age and L_model gt 10.^(-9.) and Mv_model-Mj_model lt 7.0 and L_model le max_Lbol)
    endif
        age_model    = age_model[ind]
        mass_model    = mass_model[ind]
        L_model        = L_model[ind]
        T_model        = T_model[ind]
endif
; BT-Settl (Baraffe et al. 2015) isochrones with the VRIJHK photometry
if(model eq 'BT-Settl') then begin
    print, 'reading BT-Settl isochrones...'
    root_model    = 'files/BHAC15/'
    file_model    = root_model+'isochrones.CIT2.cat'
    readcol, file_model, age_model, mass_model, T_model, logL_model, Mv_model, Mj_model, $
     format='f,f,f,f,x,x,x,f,x,x,f,x,x,x,x,x', comment='#'

    age_model    = 1.e9*age_model ; yr
    L_model        = 10.^logL_model

    ; cut the isochrones in the specified mass range
    ; keep ages between the specified range
    ind    = where(mass_model gt min_mass and mass_model lt max_mass and age_model ge min_age and age_model le max_age)
        age_model    = age_model[ind]
```

```
        mass_model    = mass_model[ind]
        L_model        = L_model[ind]
        T_model        = T_model[ind]
endif

;+++++++++++++++++++++++++++++++++++
; Bolometric Luminosity
; deredden the observed magnitudes
Xmag_int    = Xmag - CXmag*Av

; convert intrinsic magnitudes to absolute magnitudes
MXmag    = Xmag_int - 5.0*alog10(d) + 5.0

; obtain the BCs interpolating Teff
BCv        = interpol(BCv_KH98, T_KH98, T)
VXmag    = interpol(VXmag_KH98, T_KH98, T) ; Vmag-Xmag intrinsic color
BCXmag    = BCv + VXmag ; BC of the X-band

; bolometric magnitude
Mbol    = MXmag + BCXmag

; bolometric luminosity
L    = 10.^((Mbol-Mbol_sun)/(-2.5)) ; (L/Lsun)

;+++++++++++++++++++++++++++++++++++
; Prepare sources to obtain masses and luminosities
; keep only the sources inside the model grid to avoid extrapolations
PARSECCOLIBRIiso    = age_model(uniq(age_model)) ; isochrones
PARSECCOLIBRIiso    = PARSECCOLIBRIiso(sort(PARSECCOLIBRIiso)) ; sort the list of isochrones
N_iso                = N_elements(PARSECCOLIBRIiso) ; number of different isochrones

; index of the youngest and oldest isochrones
iso_youngest    = where(age_model eq PARSECCOLIBRIiso(0))
iso_oldest        = where(age_model eq PARSECCOLIBRIiso(N_iso-1))

; get the corresponding Lbol of the sources in the youngest and oldest isochrones
L_iso_y    = interpol(L_model(iso_youngest), T_model(iso_youngest), T)
L_iso_o    = interpol(L_model(iso_oldest), T_model(iso_oldest), T)

; keep sources older than the youngest isochrone and younger than the oldest isochrone
ind_in    = where(L le L_iso_y and L ge L_iso_o, nind_in, complement=ind_out, ncomplement=nind_out)

print,''
print,'There are '+strcompress(N_elements(T),/remove_all)+' sources in the input array'
print,'of which '+strcompress(nind_out,/remove_all)+' lie outside the model grid'
print,''
if(nind_in eq 0) then begin ; stop the code when there is none source inside the model grid
    print, 'All sources are outside the model grid'
    print,''
    stop
endif
print,''

;+++++++++++++++++++++++++++++++++++
; MASS
; it is not necessary any sort of the model file
; the masses are the same (residual <0.035) using the isochrone file, track file or iso+track file.

; using the isochrones
; First triangulate the models' grids.
TRIANGULATE, alog10(T_model), alog10(L_model), tr_model
; determine mass interpolating T and L in the (logT, logL, m) grid of the model
mass_in    = GRIDDATA(alog10(T_model), alog10(L_model), mass_model, xout=alog10(T[ind_in]), $
            yout=alog10(L[ind_in]), TRIANGLES=tr_model, method='Linear') ; also NaturalNeighbor works well

;+++++++++++++++++++++++++++++++++++
; AGE
; using the isochrones
; determine mass interpolating T and L in the (logT, logL, m) grid of the model
age_in    = GRIDDATA(alog10(T_model), alog10(L_model), age_model, xout=alog10(T[ind_in]), $
            yout=alog10(L[ind_in]), TRIANGLES=tr_model, method='Linear') ; also NaturalNeighbor works well

; mass and ages for the input array in the same order
```

```
mass    = fltarr(N_elements(T)) ; mass array to include the sources in and out of the model grid
age       = fltarr(N_elements(T)) ; age array to include the sources in and out of the model grid

mass[ind_in]    = mass_in ; estimated mass
age[ind_in]       = age_in ; estimated age
if(nind_out gt 0) then begin
    mass[ind_out]    = 99.99 ; for sources outside the model grid
    age[ind_out]    = 99.99 ; for sources outside the model grid
endif

;++++++++++++++++++++++++++++++++++
; UNCERTAINTIES
; deredden magnitude uncertainties
eAmag        = CXmag*eAv ; uncertaintiy of the Xmag extinction
eXmag_int    = sqrt(eXmag^2 + eAmag^2)

; absolute magnitude uncertainties
eMXmag    = sqrt(eXmag_int^2 + (5.*ed/(d*alog(10.)))^2)

; compute the BCv and V-Xmag uncertainties as the standard deviation of the
; interpolated BCv and V-Xmag values from N-generated Teff for each source
eBCv        = fltarr(N_elements(BCv))
eVXmag         = fltarr(N_elements(BCv))
N_ran        = 1e3 ; generated points
sigma_fac    = 1.0/3.0 ; relation between eTeff and std dev of the normal distribution
sigma        = (1.0/3.0)*eT ; std dev of the normal distribution to generate N-Teff
for i=0, N_elements(BCv)-1 do begin
    ; BCv
    T_ran    = sigma(i)*randomn(seed, N_ran) + T(i) ; N-generated Teff with peak at the Teff of the source
                                                    ; and std dev related with the Teff uncertainties
    BCv_ran    = interpol(BCv_KH98, T_KH98, T_ran) ; corresponding BCv for the N-generated Teff
    eBCv(i)    = stddev(BCv_ran) ; eBCv as the std dev of the interpolated BCv from the generated T
    ; V-Xmag
    VXmag_ran    = interpol(VXmag_KH98, T_KH98, T_ran) ; corresponding V-Xmag for the N-generated Teff
    eVXmag(i)    = stddev(VXmag_ran) ; e(V-Xmag) as the std dev of the interpolated (V-Xmag) from the generated T
endfor

; BCXmag uncertainties
eBCXmag    = sqrt(eBCv^2 + eVXmag^2)

; bolometric uncertainties
eMbol    = sqrt(eMXmag^2 + eBCXmag^2)

; bolometric luminosity uncertainties
eL    = (alog(10.)/2.5)*L*sqrt(eMbol_sun^2 + eMbol^2)

; mass and age uncertainties with the same idea as for the BCv
; uncertainties but with two gaussians (for eT and eL)
emass_in    = fltarr(N_elements(mass_in))
eage_in        = fltarr(N_elements(age_in))
sigma_T        = sigma_fac*eT[ind_in]
sigma_L        = sigma_fac*eL[ind_in]
for i=0, N_elements(ind_in)-1 do begin
    T_ran        = sigma_T(i)*randomn(seed, N_ran) + T(ind_in[i])
    L_ran        = sigma_L(i)*randomn(seed, N_ran) + L(ind_in[i])
    ; keep only the (T, L) genereated points lying inside the youngest and oldest isochrone
    L_ran_iso_y    = interpol(L_model(iso_youngest), T_model(iso_youngest), T_ran)
    L_ran_iso_o    = interpol(L_model(iso_oldest), T_model(iso_oldest), T_ran)
    ; estimate the masses and ages for the (T, L) points inside the model grid
    ind    = where(L_ran le L_ran_iso_y and L_ran ge L_ran_iso_o, nind)
        if(nind gt 0) then begin
            mass_ran    = GRIDDATA(alog10(T_model), alog10(L_model), mass_model, xout=alog10(T_ran(ind)), $
                          yout=alog10(L_ran(ind)), TRIANGLES=tr_model, method='Linear')
            emass_in(i)    = stddev(mass_ran) ; mass uncertainties
            age_ran        = GRIDDATA(alog10(T_model), alog10(L_model), age_model, xout=alog10(T_ran(ind)), $
                             yout=alog10(L_ran(ind)), TRIANGLES=tr_model, method='Linear')
            eage_in(i)    = stddev(age_ran) ; age uncertainties
        endif else begin
            emass_in(i)    = 99.99
            eage_in(i)    = 99.99
        endelse
endfor
```

```
; mass and ages uncertainties for the input array in the same order
emass    = fltarr(N_elements(T)) ; mass array to include the sources in and out of the model grid
eage    = fltarr(N_elements(T)) ; age array to include the sources in and out of the model grid

emass[ind_in]    = emass_in ; estimated mass
eage[ind_in]    = eage_in ; estimated age
if(nind_out gt 0) then begin
    emass[ind_out]    = 99.99
    eage[ind_out]    = 99.99
endif
param    = fltarr(8, N_elements(T))
    param[0,*]    = T
    param[1,*]    = eT
    param[2,*]    = L
    param[3,*]    = eL
    param[4,*]    = mass
    param[5,*]    = emass
    param[6,*]    = age
    param[7,*]    = eage

print,''
print,'%%%%%%%%%%%%%%%%%%%%%%%%%%%%%%%%%%%%%%%%%%%%%%%%%'
print,'%%%%%%%%%%  End of the phy_par code  %%%%%%%%%%%%'
print,'%%%%%%%%%%%%%%%%%%%%%%%%%%%%%%%%%%%%%%%%%%%%%%%%%'
print,''

return, param

end
```

References

Abolfathi B., et al., 2018, ApJS, 235, 42

Adams F. C., Fatuzzo M., 1996, ApJ, 464, 256

Aguado D. S., et al., 2018, preprint, (`arXiv:1812.02759`)

Ahn C. P., et al., 2012, ApJS, 203, 21

Alam S., et al., 2015, ApJS, 219, 12

Albareti F. D., et al., 2017, ApJS, 233, 25

Allard F., Homeier D., Freytag B., 2012, Philosophical Transactions of the Royal Society of London Series A, 370, 2765

Alves J., Lombardi M., Lada C. J., 2007, A&A, 462, L17

Andersen M., Meyer M. R., Greissl J., Aversa A., 2008, ApJ, 683, L183

Arnaboldi M., et al., 2010, The Messenger, 139, 6

Ascenso J., 2011, in Alves J., Elmegreen B. G., Girart J. M., Trimble V., eds, IAU Symposium Vol. 270, Computational Star Formation. pp 89–97, doi:10.1017/S1743921311000226

Bailer-Jones C. A. L., 2015, PASP, 127, 994

Bailer-Jones C. A. L., Rybizki J., Fouesneau M., Mantelet G., Andrae R., 2018, AJ, 156, 58

Bally J., 2008, Overview of the Orion Complex. p. 459

Baraffe I., Chabrier G., Allard F., Hauschildt P. H., 1998, A&A, 337, 403

Baraffe I., Chabrier G., Barman T. S., Allard F., Hauschildt P. H., 2003, A&A, 402, 701

Baraffe I., Homeier D., Allard F., Chabrier G., 2015, A&A, 577, A42

Barrado y Navascués D., Martín E. L., 2003, AJ, 126, 2997

Bastian N., Covey K. R., Meyer M. R., 2010, ARA&A, 48, 339

Basu S., Gil M., Auddy S., 2015, MNRAS, 449, 2413

Baumgardt H., Kroupa P., 2007, MNRAS, 380, 1589

Bayo A., Rodrigo C., Barrado Y Navascués D., Solano E., Gutiérrez R., Morales-Calderón M., Allard F., 2008, A&A, 492, 277

Bayo A., et al., 2011, A&A, 536, A63

Beccari G., et al., 2017, A&A, 604, A22
Bertin E., Arnouts S., 1996, A&AS, 117, 393
Biazzo K., Randich S., Palla F., Briceño C., 2011, A&A, 530, A19
Bihain G., Scholz R.-D., 2016, A&A, 589, A26
Binney J., Tremaine S., 2008, Galactic Dynamics: Second Edition. Princeton University Press
Blaauw A., 1964, ARA&A, 2, 213
Blaauw A., 1991, in Lada C. J., Kylafis N. D., eds, NATO Advanced Science Institutes (ASI) Series C Vol. 342, NATO Advanced Science Institutes (ASI) Series C. p. 125
Blanton M. R., et al., 2017, AJ, 154, 28
Bolton A. S., et al., 2012, AJ, 144, 144
Bonatto C., Bica E., 2011, MNRAS, 415, 2827
Bonnell I. A., Davies M. B., 1998, MNRAS, 295, 691
Bonnell I. A., Bate M. R., Clarke C. J., Pringle J. E., 2001, MNRAS, 323, 785
Bonnell I. A., Clarke C. J., Bate M. R., 2006, MNRAS, 368, 1296
Bonnell I. A., Smith R. J., Clark P. C., Bate M. R., 2011, MNRAS, 410, 2339
Bouy H., et al., 2015, A&A, 577, A148
Bressan A., Marigo P., Girardi L., Salasnich B., Dal Cero C., Rubele S., Nanni A., 2012, MNRAS, 427, 127
Bressert E., et al., 2012, A&A, 542, A49
Briceño C., Hartmann L., Stauffer J., Martín E., 1998, AJ, 115, 2074
Briceño C., Luhman K. L., Hartmann L., Stauffer J. R., Kirkpatrick J. D., 2002, ApJ, 580, 317
Briceño C., Calvet N., Hernández J., Vivas A. K., Hartmann L., Downes J. J., Berlind P., 2005, AJ, 129, 907
Briceño C., Hartmann L., Hernández J., Calvet N., Vivas A. K., Furesz G., Szentgyorgyi A., 2007, ApJ, 661, 1119
Briceño C., et al., 2019, AJ, 157, 85
Briceno C., 2008, The Dispersed Young Population in Orion. p. 838
Caballero J. A., 2008, MNRAS, 383, 750
Calvet N., Briceño C., Hernández J., Hoyer S., Hartmann L., Sicilia-Aguilar A., Megeath S. T., D'Alessio P., 2005, AJ, 129, 935
Cardelli J. A., Clayton G. C., Mathis J. S., 1989, ApJ, 345, 245
Cepa J., et al., 2000, in Iye M., Moorwood A. F., eds, Society of Photo-Optical Instrumentation Engineers (SPIE) Conference Series Vol. 4008, Society of Photo-Optical Instrumentation Engineers (SPIE) Conference Series. pp 623–631
Cepa J., et al., 2003, in Iye M., Moorwood A. F. M., eds, Proc. SPIEVol. 4841, Instrument Design and Performance for Optical/Infrared Ground-based Telescopes. pp 1739–1749, doi:10.1117/12.460913
Chabrier G., 2001, ApJ, 554, 1274
Chabrier G., 2003a, PASP, 115, 763
Chabrier G., 2003b, ApJ, 586, L133
Chabrier G., 2005, in Corbelli E., Palla F., Zinnecker H., eds, Astrophysics and Space Science Library Vol. 327, The Initial Mass Function 50 Years Later. p. 41 (arXiv:astro-ph/0409465), doi:10.1007/978-1-4020-3407-7˙5
Chabrier G., Hennebelle P., 2010, ApJ, 725, L79
Chabrier G., Baraffe I., Allard F., Hauschildt P., 2000, ApJ, 542, 464
Chambers K. C., et al., 2016, preprint, (arXiv:1612.05560)
Chen Y., Girardi L., Bressan A., Marigo P., Barbieri M., Kong X., 2014, MNRAS, 444, 2525
Coelho P., Barbuy B., Meléndez J., Schiavon R. P., Castilho B. V., 2005, A&A, 443, 735
Cottaar M., et al., 2014, ApJ, 794, 125
Cottle J. N., et al., 2018, ApJS, 236, 27
Cutri R. M., et al. 2013, VizieR Online Data Catalog, 2328

D'Antona F., Mazzitelli I., 1998, in Rebolo R., Martin E. L., Zapatero Osorio M. R., eds, Astronomical Society of the Pacific Conference Series Vol. 134, Brown Dwarfs and Extrasolar Planets. p. 442
Da Rio N., Robberto M., Hillenbrand L. A., Henning T., Stassun K. G., 2012, ApJ, 748, 14
Dabringhausen J., Hilker M., Kroupa P., 2008, MNRAS, 386, 864
Dale J. E., Ercolano B., Bonnell I. A., 2015, MNRAS, 451, 987
Dawson K. S., et al., 2013, AJ, 145, 10
De Marchi G., Paresce F., Zwart S. P., 2005, in Corbelli E., Palla F., Zinnecker H., eds, Astrophysics and Space Science Library Vol. 327, The Initial Mass Function 50 Years Later. p. 77 (arXiv:astro-ph/0409601), doi:10.1007/978-1-4020-3407-7˙11
De Marchi G., Paresce F., Portegies Zwart S., 2010, ApJ, 718, 105
Dib S., Schmeja S., Hony S., 2017, MNRAS, 464, 1738
Dolan C. J., Mathieu R. D., 1999, AJ, 118, 2409
Downes J. J., et al., 2014, MNRAS, 444, 1793
Downes J. J., et al., 2015, MNRAS, 450, 3490
Drass H., Haas M., Chini R., Bayo A., Hackstein M., Hoffmeister V., Godoy N., Vogt N., 2016, MNRAS, 461, 1734
Duchêne G., Lacour S., Moraux E., Goodwin S., Bouvier J., 2018, MNRAS, 478, 1825
Eisenstein D. J., et al., 2011, AJ, 142, 72
Elmegreen B. G., Efremov Y. N., 1996, ApJ, 466, 802
Elmegreen B. G., Klessen R. S., Wilson C. D., 2008, ApJ, 681, 365
Emerson J. P., Sutherland W. J., McPherson A. M., Craig S. C., Dalton G. B., Ward A. K., 2004, The Messenger, 117, 27
Evans I. N., et al., 2010, ApJS, 189, 37
Fabricant D., et al., 2005, PASP, 117, 1411
Feigelson E. D., et al., 2013, ApJS, 209, 26
Finkbeiner D. P., et al., 2004, AJ, 128, 2577
Fitzpatrick E. L., 1999, PASP, 111, 63
Flaugher B., et al., 2015, AJ, 150, 150
Furlan E., et al., 2006, ApJS, 165, 568
Gaia Collaboration et al., 2016, A&A, 595, A2
Gaia Collaboration et al., 2018, A&A, 616, A1
García Pérez A. E., et al., 2016, AJ, 151, 144
Genzel R., Stutzki J., 1989, ARA&A, 27, 41
Getman K. V., et al., 2014, ApJ, 787, 108
Getman K. V., Kuhn M. A., Feigelson E. D., Broos P. S., Bate M. R., Garmire G. P., 2018, MNRAS, 477, 298
Gontcharov G. A., 2017, Astronomy Letters, 43, 472
Goodwin S. P., Bastian N., 2006, MNRAS, 373, 752
Gouliermis D. A., 2018, PASP, 130, 072001
Green G. M., et al., 2018, MNRAS, 478, 651
Gunn J. E., et al., 2006, AJ, 131, 2332
Gustafsson B., Edvardsson B., Eriksson K., Jørgensen U. G., Nordlund Å., Plez B., 2008, A&A, 486, 951
Hartmann L., Megeath S. T., Allen L., Luhman K., Calvet N., D'Alessio P., Franco- Hernandez R., Fazio G., 2005, ApJ, 629, 881
Henden A. A., Templeton M., Terrell D., Smith T. C., Levine S., Welch D., 2016, VizieR Online Data Catalog, 2336
Hennebelle P., Chabrier G., 2008, ApJ, 684, 395
Hennebelle P., Chabrier G., 2011, in Alves J., Elmegreen B. G., Girart J. M., Trimble V., eds, IAU Symposium Vol. 270, Computational Star Formation. pp 159–168 (arXiv:1011.2717), doi:10.1017/S1743921311000329
Hennebelle P., Chabrier G., 2013, ApJ, 770, 150

Hernández J., Calvet N., Briceño C., Hartmann L., Berlind P., 2004, AJ, 127, 1682
Hernández J., Calvet N., Hartmann L., Briceño C., Sicilia-Aguilar A., Berlind P., 2005, AJ, 129, 856
Hernández J., et al., 2007a, ApJ, 662, 1067
Hernández J., et al., 2007b, ApJ, 671, 1784
Hoffmann K. H., Essex C., Basu S., Prehl J., 2018, MNRAS, 478, 2113
Hopkins A. M., 2018, Publ. Astron. Soc. Australia, 35
Houk N., Swift C., 1999, in Michigan Spectral Survey, Ann Arbor, Dep. Astron., Univ. Michigan, Vol. 5, p. 0 (1999). p. 0
Husser T.-O., Wende-von Berg S., Dreizler S., Homeier D., Reiners A., Barman T., Hauschildt P. H., 2013, A&A, 553, A6
Indebetouw R., et al., 2005, ApJ, 619, 931
Jeffries R. D., 2012, in Reylé C., Charbonnel C., Schultheis M., eds, EAS Publications Series Vol. 57, EAS Publications Series. pp 45–89 (arXiv:1205.2966), doi:10.1051/eas/1257002
Jeffries R. D., Maxted P. F. L., Oliveira J. M., Naylor T., 2006, MNRAS, 371, L6
Jeffries R. D., et al., 2017, MNRAS, 464, 1456
Jordi K., Grebel E. K., Ammon K., 2006, A&A, 460, 339
Kenyon S. J., Hartmann L., 1995, ApJS, 101, 117
Kharchenko N. V., Piskunov A. E., Röser S., Schilbach E., Scholz R.-D., 2005, A&A, 440, 403
Kharchenko N. V., Piskunov A. E., Schilbach E., Röser S., Scholz R.-D., 2013, A&A, 558, A53
Kirkpatrick J. D., et al., 1999, ApJ, 519, 802
Koenig X. P., Leisawitz D. T., 2014, ApJ, 791, 131
Koenig X., Hillenbrand L. A., Padgett D. L., DeFelippis D., 2015, AJ, 150, 100
Kounkel M., et al., 2018, AJ, 156, 84
Kroupa P., 2001, MNRAS, 322, 231
Kroupa P., 2002, Science, 295, 82
Kroupa P., Bouvier J., 2003, MNRAS, 346, 369
Kroupa P., Tout C. A., Gilmore G., 1991, MNRAS, 251, 293
Kroupa P., Tout C. A., Gilmore G., 1993, MNRAS, 262, 545
Kroupa P., Aarseth S., Hurley J., 2001, MNRAS, 321, 699
Kroupa P., Weidner C., Pflamm-Altenburg J., Thies I., Dabringhausen J., Marks M., Maschberger T., 2013, The Stellar and Sub-Stellar Initial Mass Function of Simple and Composite Populations. p. 115, doi:10.1007/978-94-007-5612-0˙4
Kruijssen J. M. D., 2012, MNRAS, 426, 3008
Kuhn M. A., Hillenbrand L. A., Sills A., Feigelson E. D., Getman K. V., 2019, ApJ, 870, 32
Kunder A., et al., 2017, AJ, 153, 75
Lada C. J., 1987, in Peimbert M., Jugaku J., eds, IAU Symposium Vol. 115, Star Forming Regions. pp 1–17
Lada C. J., Lada E. A., 2003, ARA&A, 41, 57
Lada C. J., Wilking B. A., 1984, ApJ, 287, 610
Lada C. J., et al., 2006, AJ, 131, 1574
Larson R. B., 1973, MNRAS, 161, 133
Larson R. B., 1978, MNRAS, 184, 69
Larson R. B., 1994, in Clemens D. P., Barvainis R., eds, Astronomical Society of the Pacific Conference Series Vol. 65, Clouds, Cores, and Low Mass Stars. p. 125
Lee Y.-N., Hennebelle P., 2018, A&A, 611, A89
Levine J. L., 2006, PhD thesis, University of Florida
Lodieu N., 2013, MNRAS, 431, 3222
López-Morales M., 2007, ApJ, 660, 732
López J. A., Richer M. G., García-Díaz M. T., Clark D. M., Meaburn J., Riesgo H., Steffen W., Lloyd M., 2012, RMxAA, 48, 3
Lucas P. W., Roche P. F., Tamura M., 2005, MNRAS, 361, 211

Luhman K. L., 1999, ApJ, 525, 466
Luhman K. L., 2000, ApJ, 544, 1044
Luhman K. L., 2004, ApJ, 617, 1216
Luhman K. L., 2018, preprint, (arXiv:1811.01359)
Luhman K. L., Rieke G. H., Lada C. J., Lada E. A., 1998, ApJ, 508, 347
Luhman K. L., Briceño C., Stauffer J. R., Hartmann L., Barrado y Navascués D., Caldwell N., 2003a, ApJ, 590, 348
Luhman K. L., Stauffer J. R., Muench A. A., Rieke G. H., Lada E. A., Bouvier J., Lada C. J., 2003b, ApJ, 593, 1093
Luhman K. L., et al., 2005, ApJ, 631, L69
Maíz Apellániz J., Úbeda L., 2005, ApJ, 629, 873
Majewski S. R., et al., 2017, AJ, 154, 94
Mamajek E. E., 2012, ApJ, 754, L20
Marigo P., et al., 2017, ApJ, 835, 77
Martin E. L., Rebolo R., Zapatero-Osorio M. R., 1996, ApJ, 469, 706
Maschberger T., 2013, MNRAS, 429, 1725
Mateu C., Vivas A. K., Downes J. J., Briceño C., Zinn R., Cruz-Diaz G., 2012, MNRAS, 427, 3374
McGehee P. M., 2006, AJ, 131, 2959
McGovern M. R., Kirkpatrick J. D., McLean I. S., Burgasser A. J., Prato L., Lowrance P. J., 2004, ApJ, 600, 1020
Meaburn J., Blundell B., Carling R., Gregory D. F., Keir D., Wynne C. G., 1984, MNRAS, 210, 463
Meaburn J., López J. A., Gutiérrez L., Quiróz F., Murillo J. M., Valdéz J., Pedrayez M., 2003, RMxAA, 39, 185
Miller G. E., Scalo J. M., 1979, ApJS, 41, 513
Monet D. G., et al., 2003, AJ, 125, 984
Morales J. C., Ribas I., Jordi C., 2008, A&A, 478, 507
Moraux E., Bouvier J., Stauffer J. R., Cuillandre J.-C., 2003, A&A, 400, 891
Moraux E., Bouvier J., Stauffer J. R., Barrado y Navascués D., Cuillandre J.-C., 2007a, A&A, 471, 499
Moraux E., Lawson W. A., Clarke C., 2007b, A&A, 473, 163
Morton D. C., 1991, ApJS, 77, 119
Muench A. A., Lada E. A., Lada C. J., Alves J., 2002, ApJ, 573, 366
Mužić K., Scholz A., Geers V. C., Jayawardhana R., 2015, ApJ, 810, 159
Mužić K., Schödel R., Scholz A., Geers V. C., Jayawardhana R., Ascenso J., Cieza L. A., 2017, MNRAS, 471, 3699
Muzerolle J., Luhman K. L., Briceño C., Hartmann L., Calvet N., 2005, ApJ, 625, 906
Nidever D. L., et al., 2015, AJ, 150, 173
Offner S. S. R., Clark P. C., Hennebelle P., Bastian N., Bate M. R., Hopkins P. F., Moraux E., Whitworth A. P., 2014, Protostars and Planets VI, pp 53–75
Oliveira J. M., Jeffries R. D., van Loon J. T., 2009, MNRAS, 392, 1034
Padoan P., Nordlund Å., 2002, ApJ, 576, 870
Palacios A., Gebran M., Josselin E., Martins F., Plez B., Belmas M., Lèbre A., 2010, A&A, 516, A13
Palla F., Stahler S. W., 1999, ApJ, 525, 772
Palla F., Stahler S. W., 2000, ApJ, 540, 255
Parker R. J., Dale J. E., 2013, MNRAS, 432, 986
Parker R. J., Goodwin S. P., 2007, MNRAS, 380, 1271
Parravano A., McKee C. F., Hollenbach D. J., 2011, ApJ, 726, 27
Peña Ramírez K., Béjar V. J. S., Zapatero Osorio M. R., Petr-Gotzens M. G., Martín E. L., 2012, ApJ, 754, 30
Pecaut M. J., Mamajek E. E., 2013, ApJS, 208, 9
Perryman M. A. C., et al., 1997, A&A, 323, L49
Petr-Gotzens M., et al., 2011, The Messenger, 145, 29

Pickles A., Depagne É., 2010, PASP, 122, 1437
Prialnik D., 2000, An Introduction to the Theory of Stellar Structure and Evolution
Ramírez-Preciado V. G., Román-Zúñiga C. G., Aguilar L., Suárez G., Downes J. J., 2018, ApJ, 867, 93
Reipurth B., Clarke C., 2001, AJ, 122, 432
Richer M. G., Suárez G., López J. A., García Díaz M. T., 2017, AJ, 153, 140
Rieke G. H., Lebofsky M. J., 1985, ApJ, 288, 618
Robin A. C., Reylé C., Derrière S., Picaud S., 2003, A&A, 409, 523
Roman-Lopes A., et al., 2019, ApJ, 873, 66
Román-Zúñiga C. G., Roman-Lopes A., Tapia M., Hernández J., Ramírez-Preciado V., 2019, ApJ, 871, L12
Rosen S., et al., 2015, in Taylor A. R., Rosolowsky E., eds, Astronomical Society of the Pacific Conference Series Vol. 495, Astronomical Data Analysis Software an Systems XXIV (ADASS XXIV). p. 319
Rosen S. R., et al., 2016, A&A, 590, A1
Salpeter E. E., 1955, ApJ, 121, 161
Scalo J. M., 1986, Fundamentals Cosmic Phys., 11, 1
Schlegel D. J., Finkbeiner D. P., Davis M., 1998, ApJ, 500, 525
Schlieder J. E., Lépine S., Rice E., Simon M., Fielding D., Tomasino R., 2012, AJ, 143, 114
Schmidt-Kaler T., 1982, in Landolt-Bornstein, Group VI, Vol. 2, ed. K.-H. Hellwege (Berlin: Springer), 454
Schneider N., Csengeri T., Bontemps S., Motte F., Simon R., Hennebelle P., Federrath C., Klessen R., 2010, A&A, 520, A49
Scholz A., Xu X., Jayawardhana R., Wood K., Eislöffel J., Quinn C., 2009, MNRAS, 398, 873
Scholz A., Muzic K., Geers V., Bonavita M., Jayawardhana R., Tamura M., 2012, ApJ, 744, 6
Scholz A., Geers V., Clark P., Jayawardhana R., Muzic K., 2013, ApJ, 775, 138
Schweizer F., 2009, Globular Cluster Formation in Mergers. p. 331, doi:10.1007/978-3-540-76961-3˙78
Sherry W. H., Walter F. M., Wolk S. J., 2004, AJ, 128, 2316
Siess L., Dufour E., Forestini M., 2000, A&A, 358, 593
Sills A., Rieder S., Scora J., McCloskey J., Jaffa S., 2018, MNRAS, 477, 1903
Silverman B. W., 1986, Density estimation for statistics and data analysis
Skrutskie M. F., et al., 2006, AJ, 131, 1163
Smee S. A., et al., 2013, AJ, 146, 32
Soderblom D. R., Jones B. F., Balachandran S., Stauffer J. R., Duncan D. K., Fedele S. B., Hudon J. D., 1993, AJ, 106, 1059
Stassun K. G., Kratter K. M., Scholz A., Dupuy T. J., 2012, ApJ, 756, 47
Stassun K. G., Scholz A., Dupuy T. J., Kratter K. M., 2014, ApJ, 796, 119
Stauffer J. R., Schultz G., Kirkpatrick J. D., 1998, ApJ, 499, L199
Strom K. M., Wilkin F. P., Strom S. E., Seaman R. L., 1989, AJ, 98, 1444
Stutz A. M., 2018, MNRAS, 473, 4890
Suárez G., Román-Zúñiga C., Downes J. J., 2017a, in Revista Mexicana de Astronomia y Astrofisica Conference Series. pp 98–98
Suárez G., Román-Zúñiga C., Downes J. J., 2017b, Memorie della Societa Astronomica Italiana, 88, 844
Suárez G., et al., 2017c, AJ, 154, 14
Suárez G., Román-Zúñiga C., Downes J. J., Cerviño M., Briceño C., Vivas K., Petr-Gotzens M. G., 2018, System IMF of the 25 Orionis Stellar Group, doi:10.5281/zenodo.1419279, https://doi.org/10.5281/zenodo.1419279
Suárez G., José Downes J., Román-Zúñiga C., Cerviño M., Briceño C., Petr-Gotzens M. G., Vivas K., 2019, preprint, (arXiv:1903.05739)
Taylor M. B., 2005, in Shopbell P., Britton M., Ebert R., eds, Astronomical Society of the Pacific Conference Series Vol. 347, Astronomical Data Analysis Software and Systems XIV. p. 29
Taylor M. B., 2006, in Gabriel C., Arviset C., Ponz D., Enrique S., eds, Astronomical Society of the Pacific Conference Series Vol. 351, Astronomical Data Analysis Software and Systems XV. p. 666

Thies I., Kroupa P., 2007, ApJ, 671, 767
Valdes F., Gupta R., Rose J. A., Singh H. P., Bell D. J., 2004, ApJS, 152, 251
Valdes F., Gruendl R., DES Project 2014, in Manset N., Forshay P., eds, Astronomical Society of the Pacific Conference Series Vol. 485, Astronomical Data Analysis Software and Systems XXIII. p. 379
Vázquez-Semadeni E., González-Samaniego A., Colín P., 2017, MNRAS, 467, 1313
Ward J. L., Kruijssen J. M. D., 2018, MNRAS, 475, 5659
Weidner C., Kroupa P., 2005, ApJ, 625, 754
Weisz D. R., et al., 2015, ApJ, 806, 198
Whitworth A. P., Zinnecker H., 2004, A&A, 427, 299
Wilson J. C., et al., 2010, in Ground-based and Airborne Instrumentation for Astronomy III. p. 77351C, doi:10.1117/12.856708
Wright N. J., Mamajek E. E., 2018, MNRAS, 476, 381
York D. G., et al., 2000, AJ, 120, 1579
Zacharias N., Finch C. T., Girard T. M., Henden A., Bartlett J. L., Monet D. G., Zacharias M. I., 2013, AJ, 145, 44
Zapatero Osorio M. R., Béjar V. J. S., Pavlenko Y., Rebolo R., Allende Prieto C., Martín E. L., García López R. J., 2002, A&A, 384, 937
Zari E., Brown A. G. A., de Bruijne J., Manara C. F., de Zeeuw P. T., 2017, A&A, 608, A148
Zinnecker H., 1982, Annals of the New York Academy of Sciences, 395, 226
Zinnecker H., 1984, MNRAS, 210, 43
Zinnecker H., 2005, in Corbelli E., Palla F., Zinnecker H., eds, Astrophysics and Space Science Library Vol. 327, The Initial Mass Function 50 Years Later. pp 19–22, doi:10.1007/978-1-4020-3407-7˙3
de La Fuente Marcos R., de La Fuente Marcos C., 2000, Ap&SS, 271, 127
de Marchi G., Paresce F., 2001, in Schielicke E. R., ed., Astronomische Gesellschaft Meeting Abstracts Vol. 18, Astronomische Gesellschaft Meeting Abstracts.
Žerjal M., et al., 2013, ApJ, 776, 127